PRRC 03-20

Annual Technical Progress Report

IMPROVING CO_2 EFFICIENCY FOR RECOVERING OIL IN HETEROGENEOUS RESERVOIRS

DOE CONTRACT NO. DE-FG26-01BC15364

New Mexico Petroleum Recovery Research Center
New Mexico Institute of Mining and Technology
801 Leroy Place
Socorro, NM 87801
(505) 835-5142

Report Date:	October 31, 2003
Contract Date:	September 28, 2001
Completion Date:	September 27, 2004
DOE Award of Second year:	$337,000
Program Manager:	Reid B. Grigg
Principal Investigator:	Reid B. Grigg
Other Major Contributors:	Robert K. Svec Zhengwen Zeng Baojun Bai Laxman B. Bethapudi Sankish Ganda D.B. Gupta Yi Liu
Contracting Officer's Representative:	Paul West
Reporting Period:	Oct. 1, 2002–Sept. 30, 2003

DISCLAIMER

ABSTRACT

The second annual report of "Improving CO_2 Efficiency for Recovery Oil in Heterogeneous Reservoirs" presents results of laboratory studies with related analytical models for improved oil recovery. All studies have been undertaken with the intention to optimize utilization and extend the practice of CO_2 flooding to a wider range of reservoirs. Many items presented in this report are applicable to other interest areas: e.g. gas injection and production, greenhouse gas sequestration, chemical flooding, reservoir damage, etc. Major areas of studies include reduction of CO_2 mobility to improve conformance, determining and understanding injectivity changes in particular injectivity loses, and modeling process mechanisms determined in the first two areas.

Interfacial tension (IFT) between a high-pressure, high-temperature CO_2 and brine/surfactant and foam stability are used to assess and screen surfactant systems. In this work the effects of salinity, pressure, temperature, surfactant concentration, and the presence of oil on IFT and CO_2 foam stability were determined on the surfactant (CD1045^{TM}). Temperature, pressure, and surfactant concentration effected both IFT and foam stability while oil destabilized the foam, but did not destroy it.

Calcium lignosulfonate (CLS) can be used as a sacrificial and an enhancing agent. This work indicates that on Berea sandstone CLS concentration, brine salinity, and temperature are dominant affects on both adsorption and desorption and that adsorption is not totally reversible. Additionally, CLS adsorption was tested on five minerals common to oil reservoirs; it was found that CLS concentration, salinity, temperature, and mineral type had significant effects on adsorption. The adsorption density from most to least was: bentonite > kaolinite > dolomite > calcite > silica.

This work demonstrates the extent of dissolution and precipitation from co-injection of CO_2 and brine in limestone core. Metal tracers in the brine were used as markers to identify precipitation location and extent. This indicated possible causes of permanent permeability changes in the core and thus in a reservoir. Core segment porosity, permeability, chemical and back-scattered electron imaging, and chemical titrations were all used for qualitative and quantitative determination of compositional and injectivity changes. Also, injectivity effects of high flow rate near a wellbore and stress changes were shown on five different cores (two Berea sandstones, two Indiana limestones, and one Dakota sandstone).

TABLE OF CONTENTS

LIST OF TABLES

LIST OF FIGURES

INTRODUCTION

This report discusses the activity covering September 28, 2002 through September 27, 2003 that coincides with the project's second year fiscal year. A three-year contract for the project, DOE Contract No. DE-FG26-01BC15364, "Improving CO_2 Efficiency for Recovering Oil in Heterogeneous Reservoirs," was awarded and started on September 28, 2001. This project examines three major areas in which carbon dioxide (CO_2) flooding can be improved: fluid and matrix interactions, conformance control/sweep efficiency, and reservoir simulation for improved oil recovery. The second annual report presents results of laboratory studies with related analytical models for improved oil recovery. All studies have been undertaken with the express intention to optimize utilization and extend the practice of CO_2 flooding to a wider range of reservoirs. Items presented in this report are more often then not applicable to other interest areas: e.g. gas injection, gas production, greenhouse gas sequestration, chemical flooding, reservoir damage, etc. Benefits will include: increasing the range of reservoirs amenable to CO_2 flooding, improving efficiency and lowering cost of CO_2 foam systems, improving CO_2 flooding predictions, improving sweep efficiency, controlling production timing, and optimizing retention and injectivity changes.

Of the available advanced oil recovery methods, CO_2 injection has the greatest potential for improved oil recovery (IOR) from light oil reservoirs in the United States. Presently 11 states have CO_2 injection projects, with 75% found in west Texas and southeast New Mexico. Almost universally, CO_2 injection has been a technical success when applied, and has proven profitable in the majority of reported projects. New CO_2 projects commence yearly but many reservoirs are not considered for CO_2 flooding because of low fracture pressure, poor injectivity, and/or extreme heterogeneity. This project centers on crucial research to optimize CO_2 injection to maximize domestic hydrocarbon reserves. The results of this project will expand the range of reservoirs amenable to CO_2 flooding.

At reservoir conditions CO_2 is usually less dense and less viscous than reservoir brine or oil, resulting in high mobility, gravity override, and viscous fingering that causes early breakthrough and inefficient reservoir sweep. Chapters 1 through 3 in this report covers research related to improving conformance of CO_2 flooding through controlling CO_2 mobility. Water injection alternating with gas (WAG) is a routinely used technique for mobility control during CO_2 flooding. The WAG process often suffers more severe injectivity loss than expected through

relative permeabilities of multiphase flow. Knowing the mechanisms responsible for this WAG injectivity loss (WAGIL) is very important to improving CO_2 efficiency for recovering oil in heterogeneous reservoirs. Fluid-rock interactions, system stress, and flow changes are some of the causes of WAGIL and recent work in these areas is presented in Chapters 4 and 5. The phenomena of high mobility and WAGIL are intertwined because anything that is done to improve on conformance control will likely affect injectivity.

A Project Review Meeting was held in Midland, TX, on March 27, 2003. The meeting was attended by 34 individuals. The meeting was by invitation to optimize the audience size to promote good and open discussions. Besides the PRRC there were 17 other organizations represented: two governmental (PTTC and DOE/NPTO), three consultant firms, and 12 oil-producing companies (Amerada Hess, Oxy Permian, Bass, Kinder Morgan CO2, ChevronTexaco, JODCO, Denbury Resources, ExxonMobil, Pure Resources, Anadarko, Marathon Oil, and Energen Resources). Several engineers were invited to review current field practices in several areas; conformance problems, injectivity changes, and other effects. These were followed by presentations of what the PRRC is doing in these areas to understand or alleviate the problem. This was followed by open group discussions. This group was used as a sounding board to see if this project was addressing applicable subjects.

EXECUTIVE SUMMARY

The second annual report of "Improving CO_2 Efficiency for Recovery Oil in Heterogeneous Reservoirs" presents results of laboratory studies with related analytical models for improved oil recovery. All studies have been undertaken with the express intention to optimize utilization and extend the practice of CO_2 flooding to a wider range of reservoirs. Items presented in this report are often applicable to other interest areas: e.g. gas injection, gas production, greenhouse gas sequestration, chemical flooding, reservoir damage, etc. Chapters 1 through 3 in this report covers research related to improving conformance of CO_2 flooding through controlling CO_2 mobility. Water injection alternating with gas (WAG) is a routinely used technique for mobility control during CO_2 flooding. The WAG process often suffers more severe injectivity loss than expected. Possible causes for WAG injectivity loss (WAGIL) are fluid-rock interactions, system stress, and flow changes. Recent work in these areas is presented in Chapters 4 and 5.

Fundamental tests were performed to understand CO_2-foam and to screen potential foaming agents. Chapter 1 presents results of a foam stability apparatus, a bubble tube that is being used to screen surfactant candidates for CO_2 application and optimizing surfactant concentrations. The bubble tube/foam stability apparatus is used to determine the interfacial tension (IFT) between a high-pressure, high-temperature (HPHT) CO_2 and brine/surfactant solution using a drop weight method, the critical micelle concentration (CMC) by plotting IFT versus surfactant concentration, and CO_2 foam stability at reservoir temperature and pressure by observation. The effects of salinity, pressure, temperature, surfactant concentration, and the presence of oil on IFT and CO_2 foam stability were determined on the surfactant CD1045^{TM}. New findings for this system show indicate that IFT: (1) is insensitive to brine concentration over a wide range with a minimum near 10%, (2) increases with increasing temperature, and (3) decreases with increasing of pressure. Also, the stability of CO_2 foam: (1) is insensitive to brine concentration over a wide range of concentrations, (2) increases with increasing surfactant concentration, (3) decreases with increasing of temperature, (4) increases with increasing pressure, and (5) was destabilized but not destroyed by the presence of oil.

More surfactant is required to satisfy adsorption on rock than is used to create foam. Reduction of required surfactant and/or sacrificial agents is vital for foam flooding to be economically viable. Chapter 2 describes adsorption and desorption studies carried out with calcium lignosulfonate (CLS) on Berea sandstone. Adsorption/desorption isotherms were determined to assess the effects of CLS concentration, temperature, brine concentration and hardness, and injection rate on adsorption density the reversibility of the process. Results on Berea show: (1) increasing CLS concentration and brine salinity increases adsorption density, (2) increasing temperature decreases adsorption density, (3) increasing solution injection rate results in a small decrease in adsorption density, (4) adsorption and desorption process rates are different and desorption using brine was never complete and does not appear to be totally reversible, (5) increasing postflush salinity decreases CLS desorption rate, and (6) increasing temperature and pH during postflush had little effect on desorption.

Chapter 3 presents results of CLS adsorption onto five minerals common to oil reservoirs: silica, kaolinite, bentonite, calcite, and dolomite. Comparing CLS adsorption density onto different minerals will aid in predicting relative adsorption mass in a well-characterized reservoirs. A number of series of static batch adsorption experiments were carried out to study the effects on CLS adsorption density of CLS concentration; brine pH, salinity, and hardness; temperature; and mineral type. The results show that CLS adsorption density on silica was near zero under all tested conditions. For the other four minerals adsorption density: (1) increases with increasing CLS concentration, salinity and valence, (2) decreases with increasing

temperature, (3) is neutral at pH above 7, but below 7, increases with increasing pH for bentonite and kaolin clays and decreases for calcite and dolomite. Adsorption mechanisms that operate under the various conditions are also partially elucidated in Chapter 3; this work will aid in designing surfactant systems for specific reservoir types and conditions.

Chapter 4 reports dissolution/precipitation results of limestone coreflooding tests for co-injected CO_2 and brine at reservoir pressure and temperature. Metal chlorides were added as tracer components to the injection brine and appeared in quantities well above natural levels in deposited carbonates. This was done to attempt to verify location and quantity of precipitation suspected in earlier tests. Core segment porosity and permeability are reported during the course of the test to indicate dissolution and deposition. After completion, the core was sectioned and analyzed by chemical and back-scattered electron imaging (BSEI), and chemical titration for compositional changes. Porosity and permeability increased and decreased corresponding to suspected dissolution and precipitation. Qualitative and quantitative analyses confirmed the deposition of trace metals within deposited carbonate material, providing direct evidence of deposition. These phenomena can occur during CO_2 injection into carbonate geological formations and are a concern for permanent injectivity changes.

In the final study covered in this report, effects on stress, permeability, and non-Darcy flow are examined over a wide range of pressures and flow rates with the intent to examine them as possible mechanisms for WAGIL. Chapter 5 examines non-Darcy behavior at the near-wellbore region due to high flow rates. This part of the projects focuses on (1) confirming the effects of non-Darcy flow behavior, (2) investigating the non-Darcy flow parameters of five representative rocks under varied reservoir conditions, and (3) developing equations to predict the change of these non-Darcy flow parameters under varying reservoir conditions. The following has been achieved: (1) upgraded high-pressure, high-temperature, high-gas flow rate HPTR hardware, (2) developed experimental procedures and data processing for HPTR tests, (3) completed more than 200 HPTR flooding experiments with corresponding values of non-Darcy flow parameters on five representative rocks under typical reservoir conditions, (4) confirmed non-Darcy behavior in HPTR gas flooding for two different permeability samples each for limestone and Berea sandstone, and one Dakota sandstone sample, (5) defined and verified a criterion for non-Darcy behavior to determine the estimated error if non-Darcy flow behavior is ignored, (6) determined equations to correlate effective stress and non-Darcy flow parameters (permeability and non-Darcy flow coefficient), and (7) in the systems examined, non-Darcy flow parameters are dependent on effective normal stress, but seemed to be independent to shear stress, meaning that compaction is a more prevailing mechanism over deformation.

Work related to modeling mechanisms in each of the principle areas has started. As can be noted models are mentioned in the areas of adsorption and high flow rate behavior as found in Chapters 2, 3, and 5. Last year modeling work dissolution and deposition was started and shown to be applicable to these systems, but was deferred for more definitive proof of precipitation. This has know been accomplished in the work presented in Chapter 4 of this report. The foundation is set for significant advancements in each area during the next year.

ACKNOWLEDGEMENTS

The authors acknowledge the financial support of the US Department of Energy (contract no. DE-FC26-01BC-15364) and the State of New Mexico and the assistance for advisement, core samples, and support of a number of interested operators or potential operators of CO_2 field projects:

Amerada Hess
Anadarko
Bass
ChevronTexaco
ConocoPhillips
Denbury Resources
Devon
Energen Resources
ExxonMobil
JODCO
Kinder Morgan
Marathon Oil
Oxy Permian
Pure Resources

Acknowledge the following individuals for their contributions

New Mexico Petroleum Recovery Research Center

Reid B. Grigg, Principle Investigator, Senior Engineer
Robert K. Svec, Research Geophysicist
Zhengwen Zeng, Research Associate
Elizabeth Bustamante, Technical Information Associate
Baojun Bai and Yi Liu, PhD students
D.B. Gupta, Laxman B. Bethapudi, and Sankish Ganda, MS students
Yosuf Oni and Ghislain E. Fai-Yengo, Undergraduate student

New Mexico Bureau of Geology

Lynn Brandvold (analytical)
Lynn Heizler (BSEI)

Dave Martin and Associates, Inc.

F. David Martin

CHAPTER 1. SURFACTANT INTERFACIAL TENSION AND CO_2 FOAM STABILITY AT IN SITU CONDITIONS

Abstract

The foam stability apparatus, a bubble tube, is used to screen surfactant candidates for CO_2 application and optimizing surfactant concentrations. The interfacial tension (IFT) determined between a high-pressure, high-temperature (HPHT) CO_2 and brine/surfactant solution using a drop weight method, critical micelle concentration (CMC) determined by plotting IFT versus concentration, and CO_2 foam stability at reservoir temperature and pressure conditions determined visually are all done in this bubble tube apparatus. This system has been used to determine effects of salinity, pressure, temperature, surfactant concentration, and the presence of oil on IFT and CO_2 foam stability. All tests in this section were performed with the surfactant CD1045™. IFT has been determined to:

1. Be insensitive to brine concentration over a wide range with a minimum around 10%.
2. Decrease with surfactant concentration below the CMC and be essentially constant above the CMC.
3. Increase with the increase of temperature.
4. Decrease with the increase of pressure

Stability of CO_2 foam has been determined to:

1. Be insensitive to brine concentration over a wide range of concentrations.
2. Increase with surfactant concentration to the CMC.
3. Decrease with increase of temperature.
4. Increase with pressure increase.

In general, bubbles in stable foams are polyhedral, smaller and more homogeneous than in unstable foams. Foam volume in stable foams decreases with time from gravity drainage due to lamella thinning. In the presence of oil, CO_2 bubbles have irregular shapes and it appears that gravity drainage is impeded, even while the irregular bubbles coalesce.

Introduction

On the basis of laboratory displacement experiments, at pressures above the minimum miscibility pressure of carbon dioxide (CO_2) and reservoir oil, a developed miscibility flood could produce a large fraction of the oil remaining in the formation.[1-10] The use of CO_2 flooding for enhanced oil recovery (EOR) is increasing, because of the following properties of CO_2:

1. It remains a dense fluid over much of the range of pressures and temperatures found in many oil reservoirs.
2. This fluid is miscible or partial miscible with the hydrocarbon components of crude oil at reservoir conditions.
3. Dense CO_2 has an inherent advantage over immiscible fluids, like water, in the recovery efficiencies that are possible with its use.
4. Dense CO_2 has fairly low solubility in the water, thus an excessive amount of it is not lost to the process during the displacement.
5. As a displacement fluid, CO_2 costs are relatively low if found near an oil field.

The limited applications in the field are due to the quite low viscosity of dense CO_2.[11] The viscosity of dense CO_2 is from 1% to 20% of most crude oils at reservoir conditions. This low viscosity means that the mobility of the CO_2 is usually much higher than that of the oil that is being displaced. Because of this high mobility ratio, the displacement front is subject to instability when CO_2 displaces crude oil from a reservoir and causes premature breakthrough because of fingers of the displacing fluid.

The viscosity of CO_2 foam is higher than that of dense CO_2. Using surfactants will generate more stable CO_2 foam that will reduce viscous fingering, improve sweep efficiency, and if successful, improve oil recovery, compared to CO_2 and water. The CO_2 foam will increase the displacing fluid's viscosity and improve the oil recovery by mobility control. Thus, screening surfactant candidates and obtaining the optimum formation for CO_2 floods are important. The properties of foam generated by different surfactants were determined using a high-pressure test apparatus constructed in our laboratory.[12] The optimum surfactant

mixture and its concentration were determined by comparing the foaming ability and the foam stability of different surfactants.

The study of surfactant interfacial tension and CO_2 foam stability at in situ conditions will provide general information about the properties of CO_2 foam and the baseline properties of CD1045 over a wide range of pressure, temperature, salinity and the presence of oil. This data can be used to develop (work in progress) a CD 1045-co-surfactant system that has the appropriate physical properties and favorable economic potential for field application.

Experimental

IFT Definitions. The molecules at the surface of a liquid are subjected to an unbalanced force of molecular attraction as the molecules of the liquid tend to pull those at the surface inward while the vapor does not have as strong an attraction. This imbalance causes liquids to tend to maintain a minimum surface area. The magnitude of this force is called the surface tension (σ or “gamma"). Conventionally, the tension between the liquid and the atmosphere is called surface tension while the tension between one liquid and another is called interfacial tension.

IFT Measurement Methods. *Drop Weight Method*:[13-14] The drop weight method of measuring the interfacial tension of liquid with respect to air consists of determining the number of drops falling from a capillary. The drops are allowed to fall into a container until enough have been collected so that the weight per drop can be determined accurately. The principle of the method is that the size of the drop falling from a capillary tube depends on the surface tension of the liquid. The maximum amount of liquid weight W, which can hang from a capillary tube with radius r without falling, depends on the surface tension as

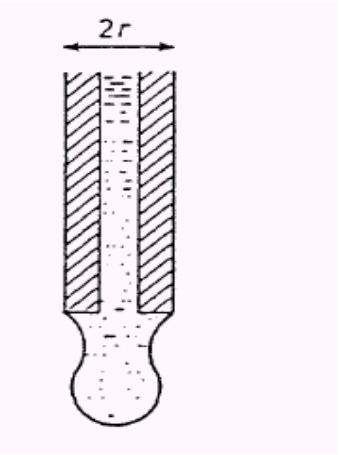

$$W = \Delta mg = 2\pi r\sigma \quad \ldots\ldots\ldots\ldots\ldots\ldots\ldots\ldots\ldots\ldots\ldots\ldots\ldots\ldots\ldots\ldots\ldots\ldots\ldots\ldots\ldots (1.1)$$

where

Δm = differential mass between the two fluids, g

G = gravitational force, cm/sec^2

r = needle radius, cm

σ = IFT (CO_2 and aqueous solution in this study), dynes/cm

Observations of falling drops show that a considerable portion of the drop (up to 40%) may remain attached to the capillary end. This effect will be compensated with a correction factor, f

$$\Delta mg = 2\pi r\sigma f \quad \text{(1.2)}$$

or

$$\frac{4}{3}\pi R^3(\rho_{surf} - \rho_{CO_2})g = 2\pi r\sigma f \quad \text{(1.3)}$$

where

R = average bubble radius, cm

ρ = fluid densities, g/cm^3

f = correction factor

The correction factor f is the Harking-Brown correction factor as described by Adamson.[14] This factor takes into account effects of attraction to the end of the tube and imperfections in the system and range form 0.5 to 1.0, see Fig. 1-1. Most of the results in this work range from 0.5 to 0.7. This is a fairly accurate method and perhaps the most convenient in the laboratory for measuring both gas-liquid and liquid-liquid interfacial tensions. Construction of the apparatus was based on this method.

Apparatus and Experimental Procedures. The foam stability apparatus built in the laboratory[12] was used for testing surfactant properties at high pressure, thus allowing the evaluation of these solutions for reservoir use. An earlier stability apparatus was modified with the following additions:

1. A protective frame was constructed,
2. The valves were fixed on a panel to reduce leaks, and
3. The whole system was simplified without changing its functions (Figs. 1-2–1-4).

The apparatus consists of a CO_2 source tank, a visual cell made from a transparent sapphire tube, an oil/surfactant-solution cylinder, a positive displacement pump and a cathetometer for

measuring the level of bubble decay versus elapsed time (Fig. 1-2). The CO_2 tank and the sapphire tube high-pressure cell are major parts of the system that are contained in a temperature controlled water bath (Fig. 1-3). The pump and the oil/surfactant-solution cylinder are installed outside the water bath and their temperatures are maintained at the test temperature through an independent temperature control system.

During the stability experiment, the sapphire visual cell was first filled with the solution to be tested. The aqueous system was brought to the desired pressure by means of the Ruska pump. The pressure difference between the CO_2 tank and the oil/surfactant-solution tank was determined by a Honeywell pressure transducer and brought to zero by fine adjustment of a Ruska positive displacement pump. At this point a valve at the bottom of the water tank was opened that allows flow of CO_2 into the surfactant as the pump is driven backward, causing the withdrawal of surfactant solution from the sapphire cell and into the oil/surfactant-solution tank. This drew the dense CO_2 upward through a needle at the lower end of the cell. Depending on the effectiveness of surfactants, the bubbles either formed a layer of foam-like dispersion at the top of the sapphire tube or coalesced into a clear layer of dense CO_2. After a standard volume of CO_2 (1.75 cc in one hour) was introduced into the sapphire tube, the pump was stopped and the duration of formed foam was measured. When the experiment was finished, the surfactant portion of the contents of the sapphire tube was discarded. The CO_2 portion was bled out into the atmosphere. Finally, the sapphire tube was thoroughly rinsed with distilled water.

Foam stability is defined as the fraction of the bubbles that stay intact as a foam layer at the top of the cell. The stability of the foam is obtained in terms of foam decay by measuring the change in the percentage of total injected CO_2 as foam versus time since CO_2 was bubbled through the surfactant solution. This test also provided the measurement techniques for calculating the interfacial tension between surfactants and dense CO_2. This was determined by counting the number of bubbles produced at the needle per volume of CO_2 injected.

Chemicals. ***Surfactants:*** Chaser CD1045 was the surfactant used, which was identified as one of the best foaming agents in several other studies.[20-22] It was supplied by Chaser

International as 46.7 wt% active aqueous solution. Calcium lignosulfonate (Lignosite 100™) was obtained from the Georgia-Pacific Corporation. This product is produced by sulfonation of softwood lignin and is provided in a powder form by the company. Research grade sodium chloride (NaCl) and calcium chloride ($CaCl_2 \cdot H_2O$) were obtained from the Aldrich Chemical Company, Inc. All aqueous solutions had the weight ratio of 3:1 NaCl:$CaCl_2 \cdot H_2O$ and unless stated otherwise were 2 wt% brines. The light mineral oil (paraffin oil, light) was obtained from Fisher Chemical, Fisher Scientific and had a density of 0.8429 g/cm^3 and molecular weight of 380 g/mole.

Results and Discussion

Interfacial tension. *Different Surfactant and Surfactant Concentration Effect:*

The surfactants were dissolved in synthetic brine and IFT values calculated using Eq. 1.3. For CD1045, IFT has been determined to decrease with surfactant concentration below the cricital micelle concentration (CMC) and to be essentially constant above the CMC (Fig. 1-5) at 25ºC (77ºF) and 1500 psig. The characteristic discontinuity in the plots of IFT against surfactant concentration can be observed. The corresponding surfactant concentration at this discontinuity corresponds to the CMC (see Fig. 1-5). The CMC of CD1045 is around 0.06 wt%. At surfactant concentration below the CMC, the surfactant molecules are loosely integrated into the water structure. In the region of the CMC, the surfactant-water structure is changed in such a way that the surfactant molecules begin to build up their own structures—micelles in the interior and monolayers at the interface. Micelles are surfactant aggregates formed in which the hydrophobic sections of the surfactant are stuck together due to the limited solubility of surfactants in aqueous phase. The number of monomers aggregated at the interface remains the same but the number of micelle will increase when surfactant concentration above the CMC is increased. IFT is related to the number of monomers aggregated at the interface and is independent to the number of micelle. Thus, IFT decreases with increase of surfactant concentration below the CMC and essentially constant above the CMC.

The IFT of calcium lignosulfonate is much high than that of CD1045 in 2 wt% brine. IFT

decreases with the concentration of lignosulfonate. When lignosulfonate solutions are mixed with 0.025 wt% CD1045, IFT increases with the lignosulfonate concentration (Fig. 1-6).[15]

Salinity Effect. A synthetic brine consisting of NaCl and $CaCl_2 \cdot H_2O$ with weight ratio 3:1 was used to dissolve surfactant CD1045. In order to determine the optimum range of salinity values, the interfacial tension between the dense CO_2 and the CD1045 solution were measured at different salinities and CD1045 concentrations at 1500 psig and 77 °F (25°C). Figure 1-7 shows the results of the IFT measurements. The IFT for the given surfactant concentration have been determined to be insensitive to brine concentration over a wide range with a minimum between 5 and 10 wt% brine, depending on surfactant concentration. The trends are similar for surfactant concentrations below and above the CMC.

Temperature Effect. Previous studies on the effect of temperature on interfacial tension indicate that observed trends will depend on the systems studied. This phenomenon has not previously been well explained. Experiments were conducted on aqueous CD1045 and a dense CO_2 system at different CD1045 concentrations. The temperature at which experiments were conducted ranged from 25ºC (77ºF) to 75ºC (167ºF) at 1500 psig. **T**he densities of the surfactant solution used in the calculating IFT were measured at atmospheric pressure. The results show that IFT increased with temperature for surfactant solutions and dense CO_2 systems (see Fig. 1-8). Also, Fig. 1-8 clearly shows that the CMC of CD1045 is between 0.05 wt% and 0.1 wt%.

Pressure Effect. Experiments were conducted on aqueous CD1045 and a dense CO_2 system at different CD1045 concentrations. The pressure at which experiments were conducted ranged from 800 psig to 2000 psig at 25ºC (77ºF). The results showed that IFT decreased dramatically at 800 psig compared to the higher pressures, 1100 psig and above (Fig. 1-9). This trend is mainly due to a reduced density difference between dense CO_2 and the aqueous phase at higher pressures.

Effects of Surfactant Concentration on CO_2 Foam Stability. For CD1045, the foams did

not collapse even when the concentrations were much lower than the CMC (see Fig 1-10). CO_2 foam stability of CD1045 is insensitive to surfactant concentration over a wide range, which indicates that CD1045 is a very good foaming agent for CO_2-brine systems. Figure 1-10 shows that the bubbles in foams are polyhedral. The bubble sizes are relatively smaller and homogeneous.

An interesting phenomenon is that the volume of the foam layer decreased with time (Fig. 1-10) even though the number of bubbles was constant in the foam (Figs. 1-10 and 1-11). This volume reduction occurs because liquid drains in the lamellae due to the force of gravity after foam generation. The liquid will drain by flowing downward through the liquid films. As the lamellae fluid drains and goes to drier foam the shape of the bubbles changes from spherical to polyhedral. Draining continues until capillary forces are equal to gravity forces. At the plateau borders (lamellae intersections) the gas-liquid interface curvature increases. The increased curvature generates a low-pressure region in the plateau border area. Because the interface is flat along the thin-film region, a higher pressure resides here. This pressure difference forces liquid to flow toward the plateau borders and causes thinning of the films and motion in the foam.

Oil Presence. The density of light mineral oil is higher than the dense CO_2 and less than CD1045 solution at 25ºC (77ºF) and 1500 psig. Three ml of light mineral oil was injected into the sapphire tube. The generated CO_2 had to pass through a layer of brine and then a layer of oil. The CO_2 would accumulate as distinct bubbles as a layer between the brine and oil then pass as a connected chain through the oil. Contrary to the way bubbles pass through the aqueous phase one by one, bubbles passed through the oil in a string (see Fig. 1-12). This was probably to maintain aqueous lamellae around a CO_2 bubble. It was difficult to determine CO_2 foam stability in the presence of oil. The CO_2 bubbles had irregular shapes and several clear, foam- free areas within the CO_2 foam. The content of these clear areas was uncertain, but believed to be dense CO_2 because as oil or water it would drain. Also, the oil appeared to impede drainage from the CO_2 foam, even while the irregular bubbles coalesced (see Fig. 1-13). Most of the CO_2 foam remained in the same structure for at least 90 min after

the end of CO_2 injection. Also, note that no obvious large areas without foam formed at the higher concentration of CD1045 shown in Fig. 1-13. This indicated an increased stability of the CO_2 foam at higher concentrations of CD 1045.

Salinity Effect. Bubble structure and size, gravity drainage, and foam stability were found to be insensitive to salinity for CD1045 solutions over a range of concentrations below and above the CMC, (Figs. 1-14 and 1-15). This implies that CD1045 can be used as stable foam over a wide range of field conditions.

Temperature Effect. Bubble structure and size, gravity drainage, and foam stability under the test conditions were insensitive to temperatures at 60ºC and below, as the three pictures in the top left of Fig. 1-16 show. Tests at 75ºC saw a marked decrease in stability with rapid decay for the CD 1045 solution concentration of 0.025 wt %; see top right photos in Fig. 1-16. Increasing the surfactant concentration (bottom of row of pictures in Fig. 1-16) resulted in increased foam stability. The results imply that the temperature dependence of stability versus CD 1045 concentrations must be considered when preparing a foam system.

Pressure Effect. Bubble structure and size, gravity drainage, and foam stability changed with pressure at the low surfactant concentration of 0.005 wt% (first two photos in Fig. 1-17). At 0.025 wt% surfactant the foam system was stable over the testing time (second two photos in Fig. 1-17).

Conclusions

In the past, stability and IFT have been used for screening surfactants to assess their suitability for use as foaming agents. Chapter 1 reviews how this is being done and in addition demonstrates the use of the bubble apparatus to assess the effect on foam for additional parameters: e.g. brine concentration, temperature, pressure, and presence of oil. Foam volume change due to film drainage versus bubble coalescence was also identified and quantified. These factors are and will be used to screen new surfactants/co-surfactants as well

as better define the applicability of surfactants that have been previously tested. Listed below are specific conclusions from the study this year.

IFT has been determined to:

a) Be insensitive to brine concentration over a wide range with a minimum around 10%.
b) Decrease with surfactant concentration below the CMC and to be essentially constant above the CMC.
c) Increase with the increase of temperature.
d) Decrease with the increase of pressure.

2) Stability of CO_2 foam has been determined to:
   a) Be insensitive to brine concentration over a wide range.
   b) Increase with surfactant concentration to the CMC.
   c) Decrease with increase of temperature.
   d) Increase with pressure increase
3) In general, bubbles in stable foams are polyhedral, smaller and more homogeneous than in unstable foams.
4) Foam volume in stable foams decreases with time from gravity drainage due to lamella thinning.
5) In the presence of oil, CO_2 bubbles have irregular shapes and it appears that gravity drainage is impeded, even while the irregular bubbles coalesce.

References

1. Moritis, G.: "2000 Worldwide EOR Survey," *Oil & Gas J.* (20 March 2000) **45**.
2. Brock, W.R. and Bryan, L.A.: "Summary Results of CO_2 EOR Field Tests, 1972-1987," paper SPE 18977 presented at the 1989 SPE Joint Rocky Mountain Regional/Low Permeability Reservoir Symposium and Exhibition, Denver, 6-8 March.
3. Hadlow, R.E.: "Update of Industry Experience with CO_2 Injection," paper SPE 24928 presented at the 1992 SPE Annual Technical Conference and Exhibition, Washington, DC, 4-7 October.

4. Grigg, R.B. and Schechter, D.S.: "State of the Industry in CO_2 Floods," paper SPE 38849 presented at the 1997 SPE Annual Technical Conference and Exhibition, San Antonio, Texas, 5-8 October.
5. Grigg, R.B. and Schechter, D.S.: "Improved Efficiency of Miscible CO_2 Floods and Enhanced Prospects for CO_2 Flooding Heterogeneous Reservoirs", Annual Report, Contract No. DE-FG26-97BC15047, U.S. DOE, Washington, DC (October 1999).
6. Christensen, J.R., Stenby, E.H., and Skauge, A.: "Review of WAG Field Experience," *SPERE* (April 2001) 97.
7. Gorrell, S.B.: "Implications of Water-Alternate-Gas Injection for Profile Control and Injectivity," paper SPE 20210 presented at the 1990 SPE/DOE Symposium on Enhanced Oil Recovery, Tulsa, 22-25 April.
8. Pariani, G.J. et al.: "An Approach To Optimize Economics in a West Texas CO_2 Flood," *JPT* (September 1992) 984; Trans., AIME, 293
9. Mamden, S.S.: "Foams in Porous Media," topical report, Contract No. AC03-81SF11564 (SUPRI TR49) U.S. DOE, Washington, DC(July 1986).
10. Heller, J.P. and Taber, J.J,: "Mobility Control for CO_2 Floods-A Literature survey," topical report, Contract No: DE-AC21-79b4ClC689 U.S. DOE, Washington, DC (Oct. 1980).
11. Chung, F.; Nguyen, H., "Carbon Dioxide Thermodynamic Properties [Computer] Program," National Institute for Petroleum and Energy Research: Bartlesville, OK, (1985).
12. Lee, H.O., Heller, J.P., and Hoefer, A.M.W.: "Change in. Apparent Viscosity of CO_2 Foam with Rock Permeability", *SPERE* (November 1991) 421-428.
13. Harkins, W.D.; Brown, J.J., "The determination of surface tension (free surface energy), and the weight of falling drops: the surface tension of water and benzene by the capillary height method," *Amer.Chem. Soc*, 41, 499, (1919).
14. Adamson, A. W., "Physical Chemistry of Surfaces", John Wiley & Sons, New York City (1982).
15. Syahputra, E.: "Experimental Evaluation of Lignosulfonate as a Sacrificial Agent in CO2-Foam Flooding", Thesis (August, 1999), NMIMT

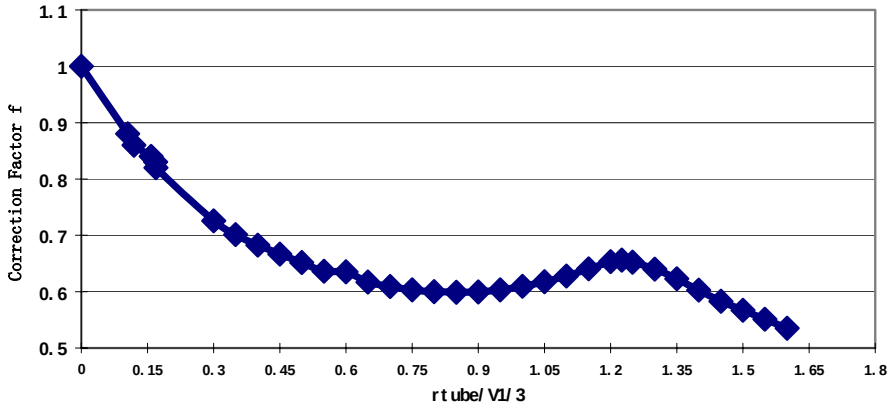

Fig. 1-1. Harkins-Brown correction factor for drop-weight method after Adamson.[14]

Fig. 1-2. Foam stability apparatus set-up.

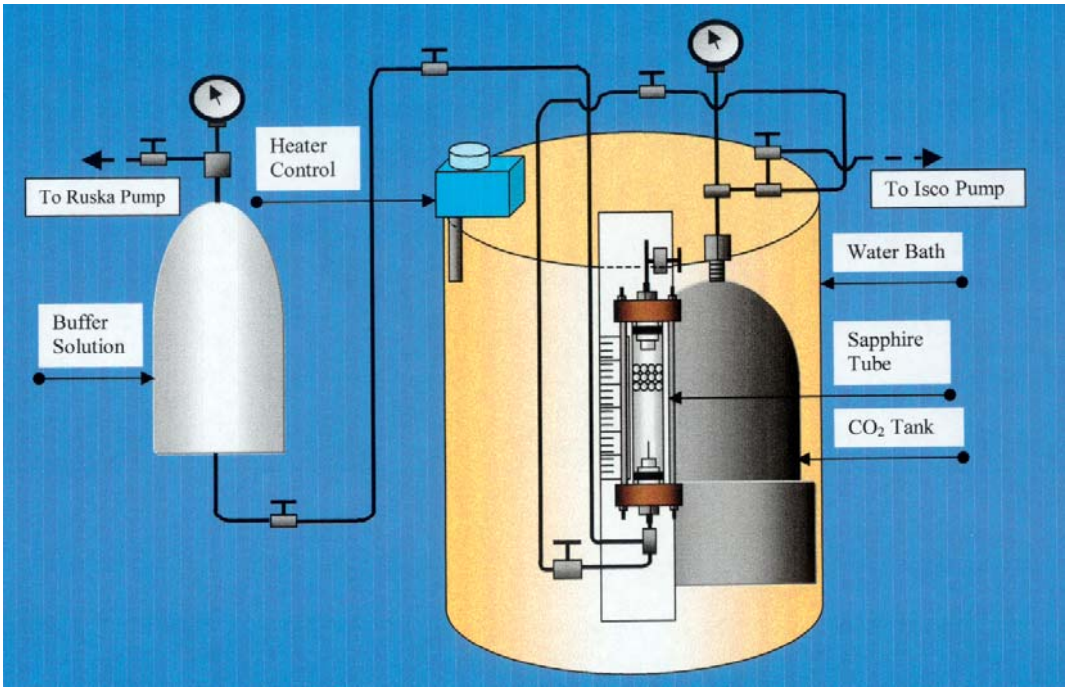

Fig. 1-3. Foam stability apparatus.

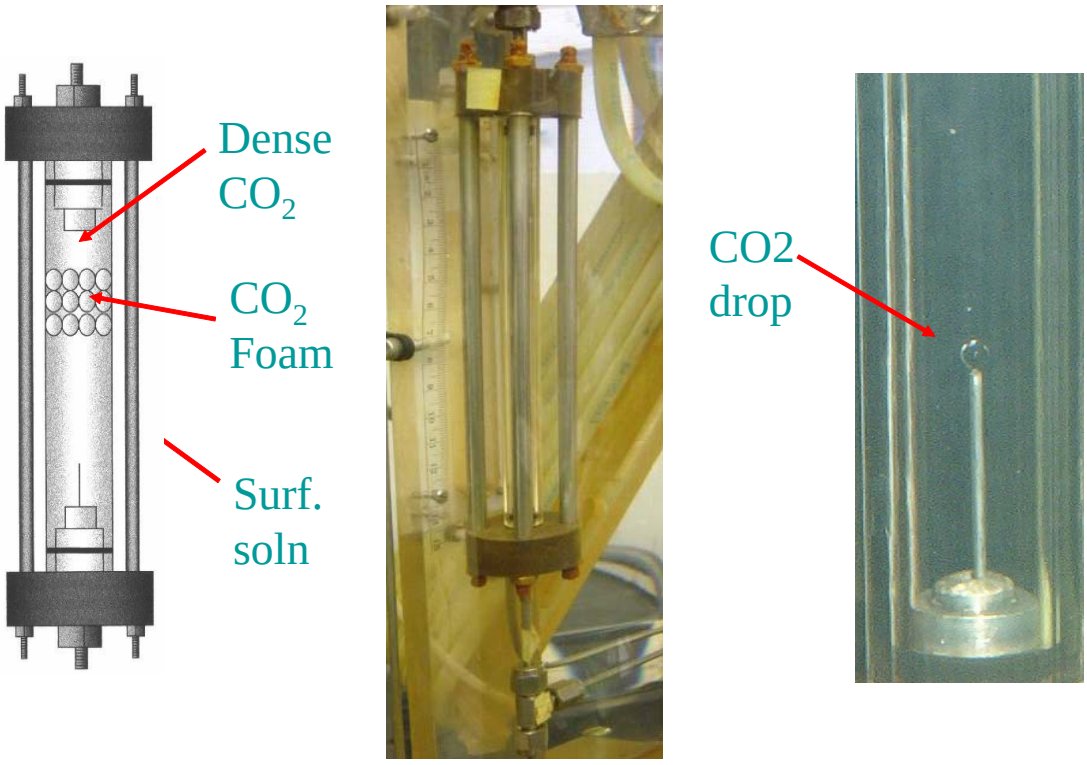

Fig. 1-4. The sapphire tube cell.

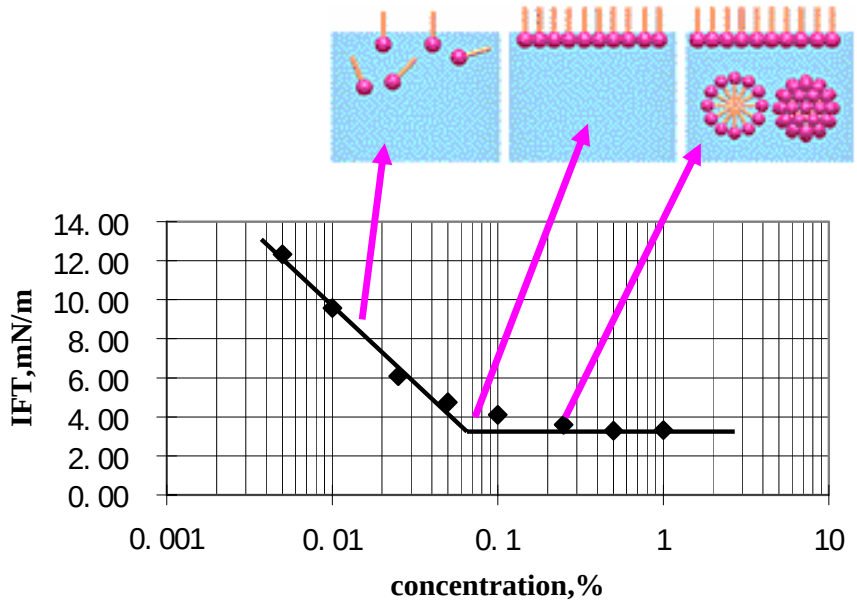

Fig. 1-5. CMC determination for CD1045.

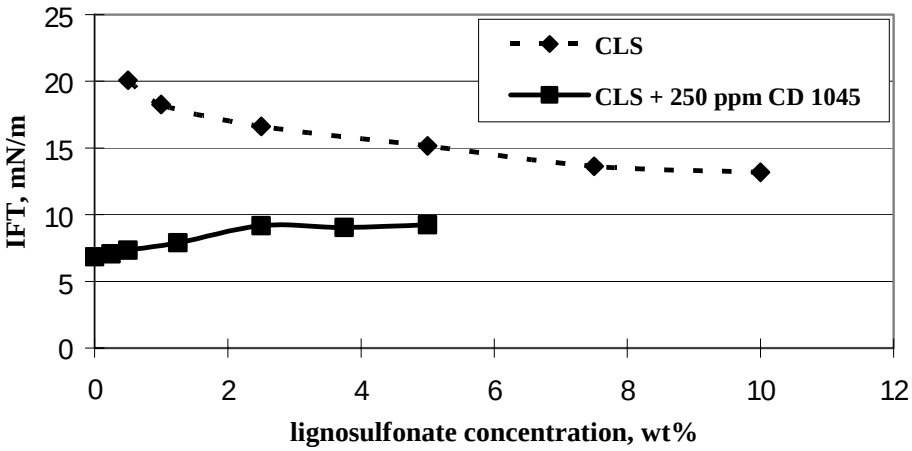

Fig. 1-6. IFT vs. lignosulfonate concentration in @ wt% brine.

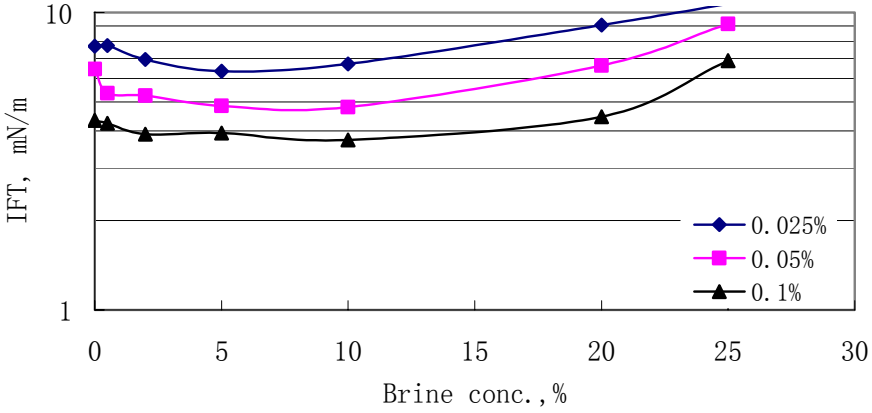

Fig. 1-7. IFT vs. brine concentration.

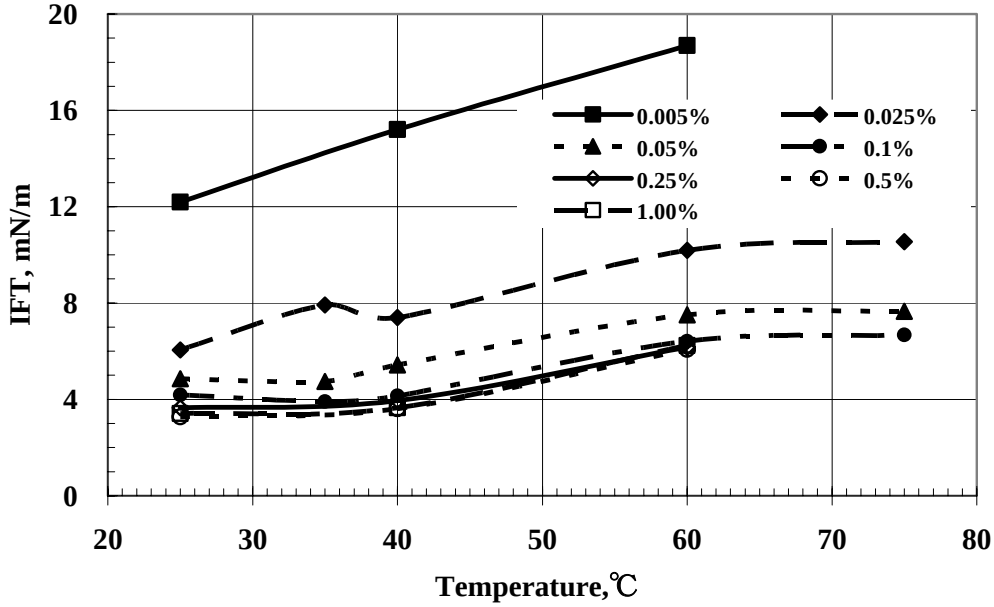

Fig. 1-8. IFT vs. temperature and surfactant concentration.

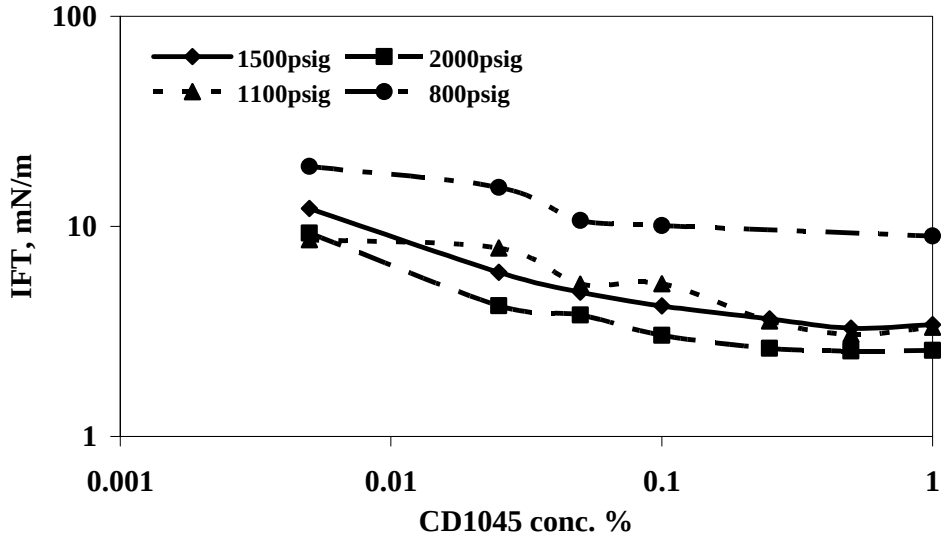

Fig. 1-9. IFT vs. pressure and surfactant concentration.

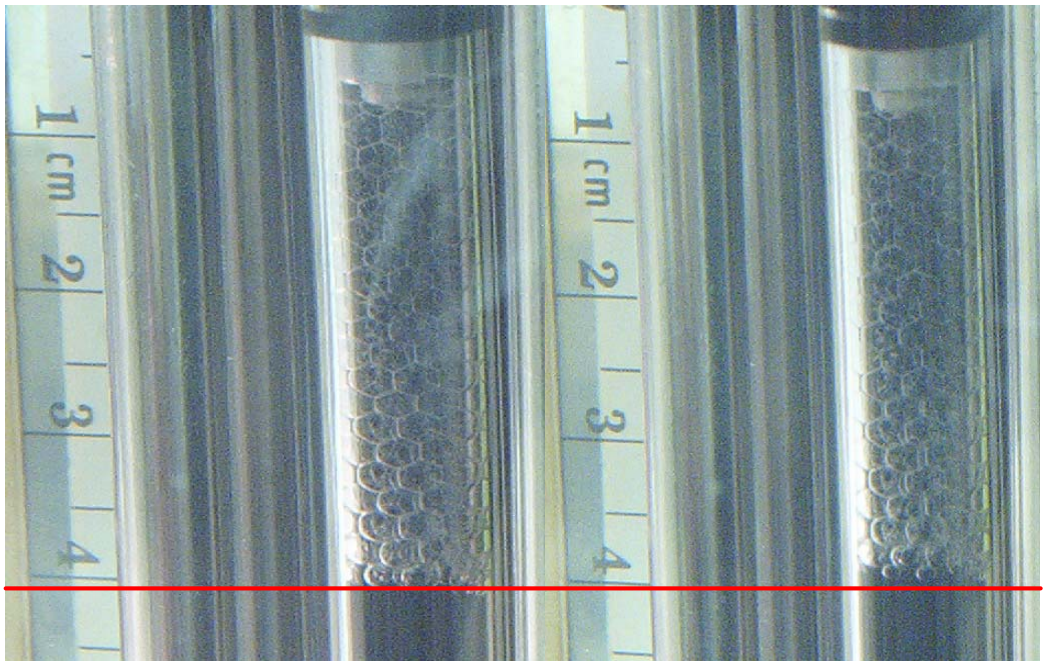

Fig. 1-10. Small volume changes occur with time from gravity drainage even for stable foams.

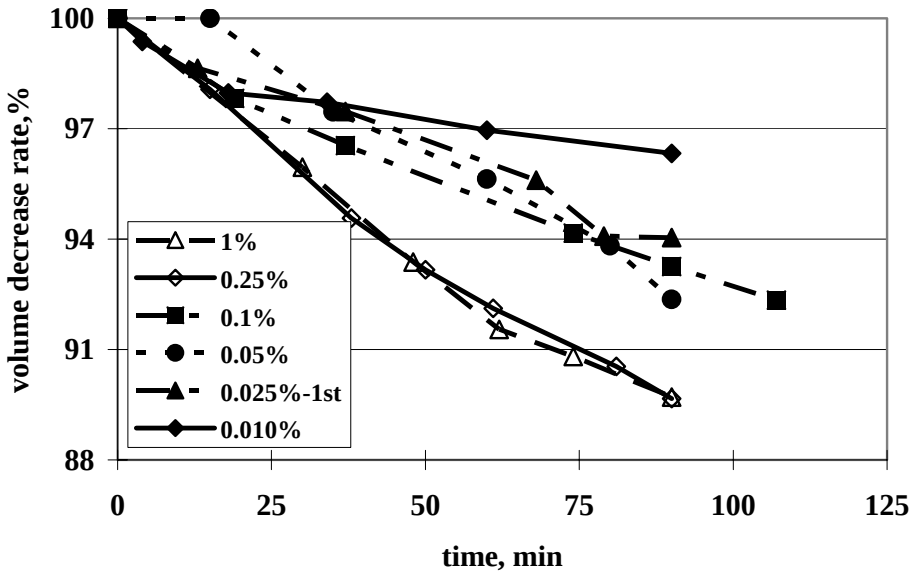

Fig. 1-11. Gravity drainage.

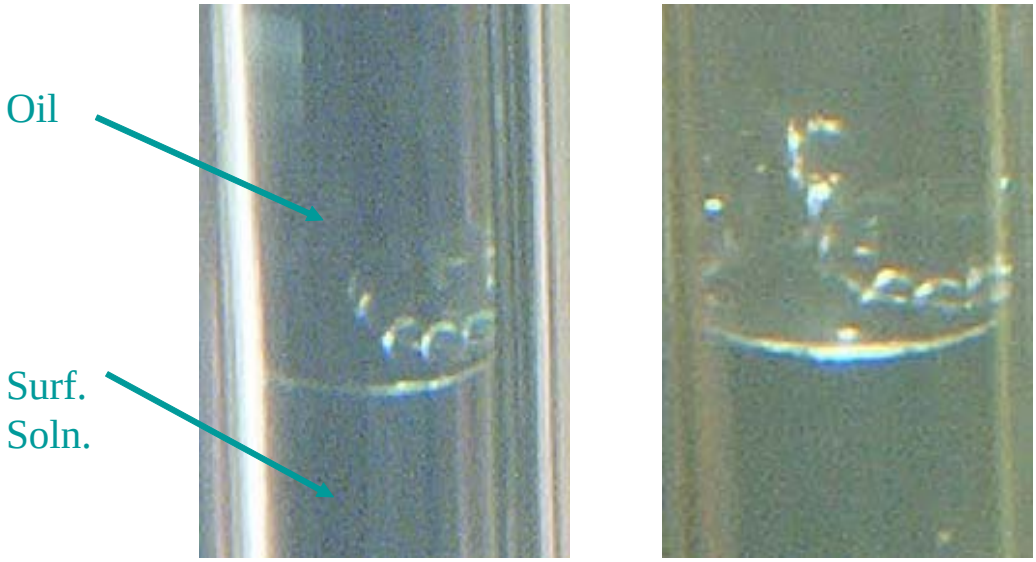

Fig. 1-12. CO_2 traversed the oil in a string of connected bubbles.

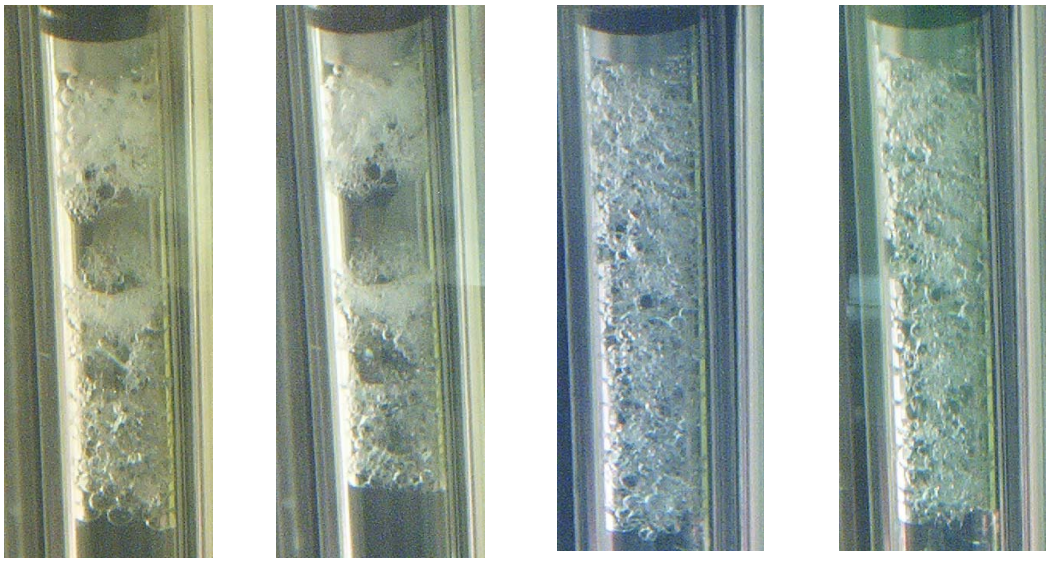

0.05wt%CD1045 **0.5wt%CD1045**

Time after generating bubbles

0 min **90min** **0min** **90min**

Fig. 1-13. Foam stability at different CD1045 concentrations.

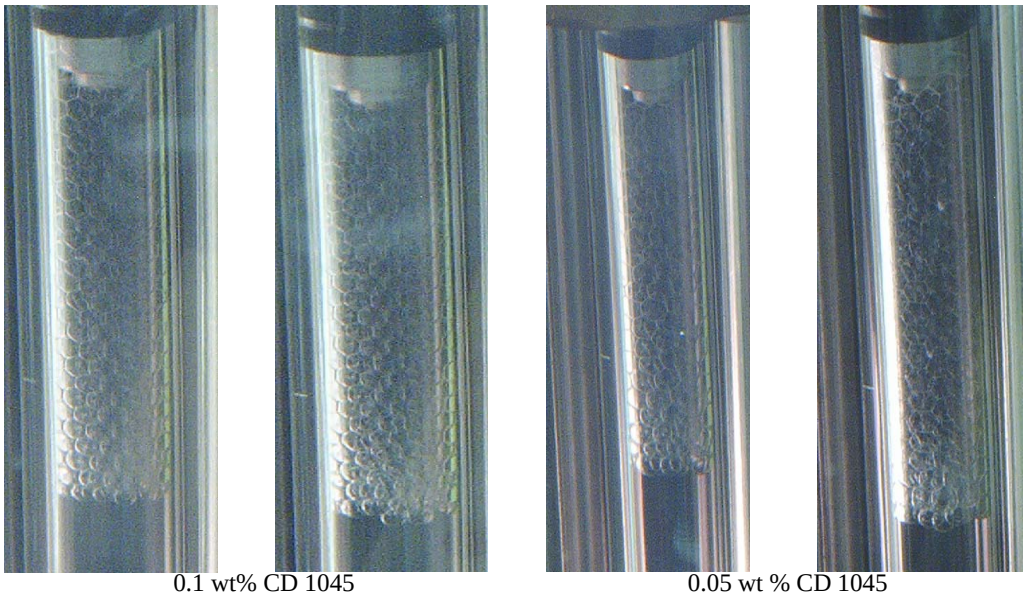

Fig. 1-14. Salinity versus CO_2 foam stability.

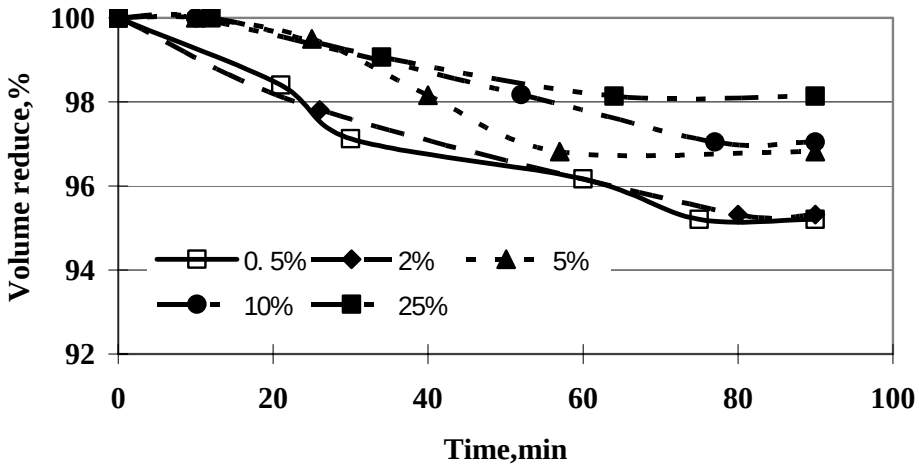

Fig. 1-15. Gravity drainage at different salinities.

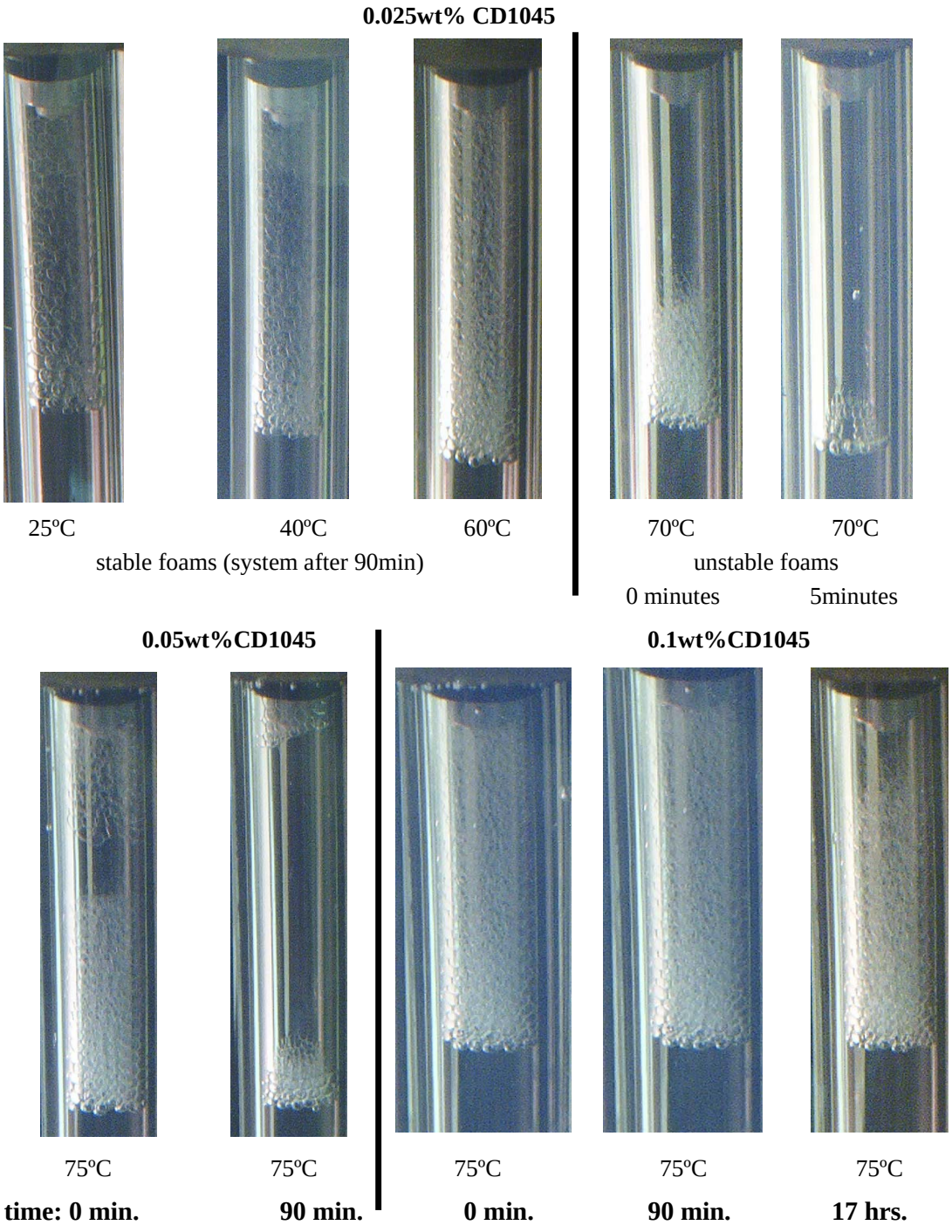

Fig. 1-16. Temperature effect on CO_2 foam stability.

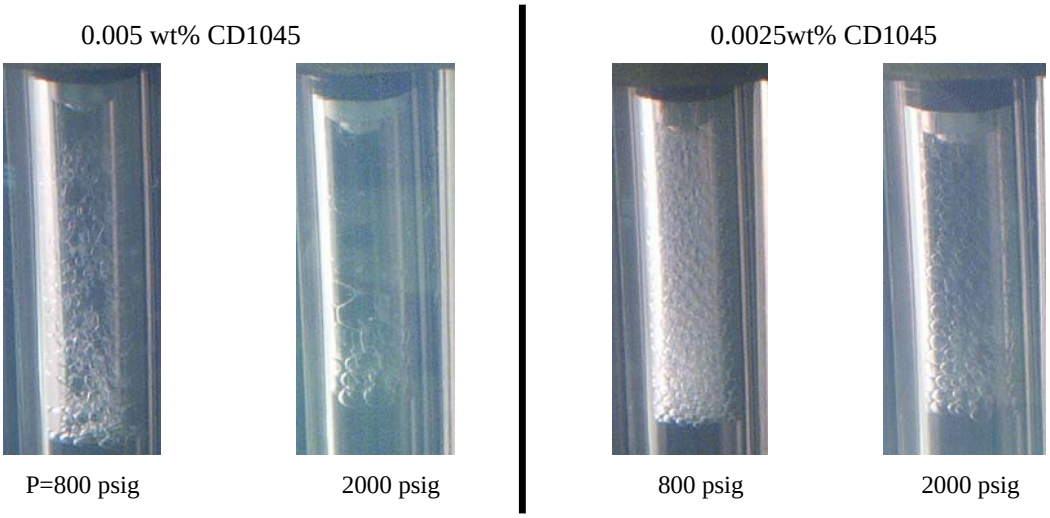

Fig. 1-17. Pressure effect on CO_2 foam stability.

CHAPTER 2. CALCIUM LIGNOSULFONATE ADSORPTION AND DESORPTION ON BEREA SANDSTONE

Abstract

Preflushing a reservoir with inexpensive chemicals in order to block the adsorption sites and reduce subsequent higher value surfactant adsorption is a concept that has prompted numerous studies. Lignosulfonate (LS), a cheap paper waste product, is thought to be an effective sacrificial agent for chemical flooding and foam flooding. In addition, as a co-surfactant it can reduce the high value surfactant requirement for stable foam by as much as 80%.

This paper describes adsorption and desorption studies carried out with calcium LS (CLS) on Berea sandstone. Circulation experiments were carried out to determine the CLS adsorption isotherm and to determine the effects of CLS concentration, temperature, salinity, brine hardness, and injection rate on adsorption density. Flow-through experiments were done to assess the reversibility of CLS adsorption and the influence of postflush rate, brine concentration and hardness, brine pH, and temperature on the desorption process.

Our experimental results concerning the effects of CLS adsorption and desorption on Berea sandstone show that:

1. Increasing CLS concentration and salinity increases CLS adsorption density;
2. Increasing temperature will decrease adsorption density;
3. Injection rate of CLS solution will slightly decrease CLS adsorption density,
4. Post-flush rate of brine influences the CLS desorption process;
5. The adsorption and desorption process rates are different and total desorption using only brine was never completely achieved and thus does not appear to be totally reversible;
6. Increasing postflush salinity decreases CLS desorption rate; and
7. Temperature and pH of postflush had little effect on desorption in our tests.

From these results, we deduce that CLS adsorption isotherm on Berea sandstone follows the Freundilich Isotherm Law; that is, diffusion is a principle mechanism controlling lignosulfonate transportation through sandstone.

Introduction

In recent years increasing interest in surfactant-based enhanced oil recovery processes has focused on the application of foam mobility control. [1-5] Propagation of foam partially depends on the propagation of the surfactant, which in turn is strongly affected by adsorption losses at the solid/liquid interface. Surfactant loss in a reservoir due to its adsorption in porous media represents the largest use of chemicals and is thus a major feature governing the economic viability of CO_2-foam flooding.

In general, there are three kinds of adsorption: ion exchange adsorption, physical adsorption and chemical adsorption.[6–11] Exchange adsorption is the result of electrostatic attraction. The charge of the ion is the determining factor (the trivalent ion is attracted much more strongly to a site of opposite charge). Physical adsorption is a result of van der Waals force. The adsorbed molecule is not affixed to a specific site at the surface but is free to undergo translational movement within the interface. It is predominantly a low temperature phenomenon, characterized by a relatively low energy of adsorption. Physical adsorption is usually a reversible process; an increase in temperature causes a decrease in adsorption efficiency and capacity. In chemical adsorption, in this case the surfactant undergoes chemical interaction with the mineral surfact. This bonding leads to a change in the chemical form of the adsorbed compounds, and is therefore not reversible.

Adsorption of surfactants at the solid/liquid interface is strongly influenced by the following factors[12–23]:

1. The type of surfactant and the specific properties of the molecule;
2. The solvent conditions, such as pH, salinity (Na^+, Cl^-) and hardness (Ca^{2+}, Mg^{2+});
3. The surface nature of the adsorbing substrate, such as surface area, type of surface (silica, calcium carbonate, clay, etc), and surface charge; and
4. The environment of the aqueous phase, temperature, redox environment, and flow rate in the reservoir.
5. Three approaches may be used to minimize surfactant adsorption [24]:
6. Matching surfactant type to specific reservoir rock by surface charge,
7. Application of surfactant mixtures, and
8. Sacrificial adsorbent.

The use of sacrificial agents is one of most important methods for reducing surfactant adsorption loss. They have been widely studied, and different kinds of inorganic and organic sacrificial agents have been shown to reduce surfactant adsorption sites in reservoir rocks.[25–28]

Lignosulfonate, an inexpensive modified waste byproduct from the paper industry, has been studied as a sacrificial agent to reduce surfactant adsorption. The use of lignosulfonate as a sacrificial agent in CO_2-foam application was first reported in a patent by Kalfoglou, et al.[28] They found lignosulfonate reduced a foaming agent's adsorption on limestone crushed rock samples by 16 to 35%. Hong *et al.* evaluated lignosulfonate as a sacrificial adsorbent in preparation for a surfactant flooding field test in a Glenn Pool reservoir.[29,30] In laboratory tests, the lignosulfonate reduced surfactant adsorption by 39%. Tsau *et al.* showed that lignosulfonate could reduce the adsorption of a primary foaming agent-CD1045 by 24-60% in Berea core and 15-29% in Indiana limestone core samples.[31-33] However, these studies concentrated on whether lignosulfonate could reduce primary surfactant adsorption loss based on surfactant-enhanced oil recovery processes. There has been little work concerned with CLS adsorption and desorption behavior. This section of the Annual Report demonstrates factors that affect lignosulfonate adsorption onto Berea sandstone by dynamic adsorption experiments and shows practical methods to control lignosulfonate adsorption and desorption.

Experimental

Chemicals. Lignosulfonate used in this study is Lignosite®100 calcium lignosulfonate, which was obtained from the Georgia-Pacific Corporation. The product provided is a powder produced by sulfonation of softwood lignin. Its basic properties (listed in Table 2-1) were provided by the Georgia-Pacific Corporation. All lignosulfonate solutions in this work were prepared in 2 wt% brine (1.5 wt% NaCl and 0.5 wt% $CaCl_2$) unless otherwise indicated. A spectrophotometer was used to determine the concentration of CLS. A 283 nm wavelength was used in all measurements to analyze the CLS concentration because it has a maximum absorbance in the neighborhood of 283 nm. To calculate CLS concentration, a standard calibration curve of CLS was established (as shown in Fig. 2-1). CLS had to be diluted to less than 400mg/L before its concentration was measured, because its concentration and adsorption showed a good straight line only if its concentration was below 400mg/L.

Adsorbents. Two Berea cores were used as adsorbents to determine dynamic adsorption. Their properties are summarized in Table 2-2.

Experimental methods of lignosulfonate adsorption on Berea core. Two dynamic methods, circulation and flow-through experiment, were used to study CLS adsorption and desorption onto Berea sandstone. The amount of CLS adsorbed is expressed as the unit: mass of CLS adsorbed/volume of rock (mg/cm^3).

Figure 2-2 shows a schematic diagram of the flow-through method apparatus. The source fluid is pumped from a beaker through the pump and into the core holder containing Berea core. Fluid effluent samples were collected versus time and the concentrations of CLS were analyzed by spectrophotometer.

Figure 2-3 shows a flow chart of the circulation experiment. As shown in this figure, the circulation experimental apparatus consists of:

1. A given solution having a known weight in a flask;
2. A core of known volume and weight; and
3. A metering pump.

A known concentration lignosulfonate solution was circulated through Berea core at constant temperature and injection rate until adsorption equilibrium was achieved. Circulation experiments were carried out to mainly establish CLS desorption and desorption isotherm and study the effect of salinity, brine hardness, temperature and injection rate on CLS adsorption density on sandstone porous media.

Experimental procedures: Results from Core 1 using the circulation method were used to determine CLS adsorption and desorption isotherm and study the effects of temperature, salinity, ionic strength, and injection rate on CLS adsorption density onto Berea sandstone. In addition, some desorption procedures were performed to determine the influence of flow interruption, post-flush rate, and postflush brine temperature influence on desorption rate. Table 2-3 summarizes the parameters used for all the experiments in Core 1. Core 2 was used to analysis the effect of CLS concentration in the injectant on adsorption and desorption processes and the effect of postflush rate, salinity, and pH on desorption. Table 2-4 summarizes all experiments in Core 2.

Results and Discussion

Adsorption/Desorption Isotherm. Four adsorption/desorption profiles were established using the circulation method on Core 1 (Runs 1–4, see summary in Table 2-3). The objectives of these experiments were to establish CLS adsorption isotherms and to determine the extent that CLS adsorption is reversible. First, brine was circulated through the core at a constant rate of 60 cm^3/hr. The total volume of circulated fluid was 100 cm^3, including the volume in flask, tube and core volume. After 12 hrs of circulation, brine in the flask was replaced with the same volume of 2500 ppm CLS solution. After another 12 hrs of circulation, a 2.5 ml sample of solutions was removed from the flask for analysis of CLS concentration and was replaced in the flask with 2.5 ml. of 100,000 ppm CLS. The cycle of sampling and replacement was repeated 10 times. This procedure was used to establish the adsorption isotherm. In order to determine desorption rate, solution was removed from the flask and replaced with same volume of brine. After the addition of the brine, the solution was circulated for another 12 hrs. This was repeated 15 to 20 times times. After each sample was removed it was tested for CLS concentration to calculate desorption to that point. The cycle of sampling and replacement was repeated until circulated CLS solution concentration was below 100 ppm. After 15-20 repeats, brine was injected continuously through the core until negligible surfactant remained in the effluent. This last process was a flow-through experiment. See Fig. 2-4 for the plot of the first adsorption/desorption profile.

Figures 2-5 and 2-6 present four consecutive CLS adsorption and desorption profiles, respectively, for the same Berea core. The data plotted in Fig. 2-5 assumes none of the CLS is left adsorbed from the previous test. The large difference in the adsorption profiles is easier to see if only two profiles are plotted at once as in Fig. 2-7. As can be seen in Fig. 2-6, none of the tests returned to zero. This hysteresis is easier to understand if adsorption is assumed to be irreversible. Figure 2-8 shows the difference of the first and third profiles. When the adsorption remaining from the previous tests is included, the four adsorption tests are much closer, as shown in Fig. 2-9.

As shown, adsorption density is a function of CLS concentration in the measured concentration range with increasing adsorption with the increase of lignosulfonate concentration. The desorption curve does not superimpose onto the adsorption curve. In each case the two curves appear to be reversible at higher concentrations. At a concentration below 3000 ppm the

desorption curve deviates and is higher in CLS adsorbed onto the core than during the adsorption process. We suspect different adsorption mechanisms at lower and higher concentrations. It is hypothesized that at higher concentrations, CLS forms aggregates on the porous surface, behaving as local monolayers, local bilayers, or something between them. CLS molecular attraction in aggregates is small and thus molecules can escape from one another. But at lower concentration, lignosulfonate adsorbs on Berea core as individual molecules and aggregates are not formed. The attraction between lignosulfonate molecules, the attraction between lignosulfonate molecules and rock sites is much stronger, thus it is not easy to remove them from the core surface. Another reason could be due to desorption site differences. At higher CLS concentration, advection, which occurs in effective flow paths, is predominant in the desorption process, adsorption equilibrium is easily established in flow paths (there may be only monolayer adsorption in small non-flow pores because of the small space). At lower CLS concentration, advection and diffusion contribute together to the desorption process, and if the diffusion rate is very slow, the desorption isotherm would not achieve equilibrium. In other words, it would be difficult to achieve equilibrium during this process in our experimental time frame.

As shown in Figs. 2-6 and 2-8, adsorbed CLS was not completely desorbed from the core, and some residual lignosulfonate was left in the core after each postflush. Table 2-5 lists the CLS density remaining after each desorption profile. If the remaining CLS is added into the adsorption mass of next profile, we obtain Fig. 2-9. This figure is very instructive because the four new adsorption profiles almost overlay. That means the total adsorption mass does not change at a constant CLS concentration whether the porous media is pre-adsorbed or not. Figure 2-9 compares the four new desorption profiles, which were obtained from the results of adding residual lignosulfonate in the former profiles to the measured desorption profile. Some residual lignosulfonate remained after each tests.

A number of equations to fit the adsorption isotherm are found in the literature.[34] In this work the Langmuir and Freundlich adsorption equations were used to fit the CLS adsorption and desorption isotherms shown in Figs. 2-9 and 2-10. Figures 2-11 and 2-12 show a fair fit of the CLS adsorption isotherm by applying Langmuir and Freundlich adsorption equation respectively. As shown in the two figures, both equations fit the adsorption isotherm fairly, with the relative coefficient square R2=0.9538 and R2=0.9733. From the Langmuir method, the following equation is used:[35]

$$q = \frac{6.0755C}{12322 + C} \quad \text{..... (2-1)}$$

Equation 2-1 can be rearranged to give:

$$q = \frac{6.0755\frac{1}{12322}C}{1 + \frac{1}{12322}C} \quad \text{..... (2-2)}$$

that can be rewritten as the Langmuir equation, Eq. 2-3

$$q = \frac{q_m K_a C}{1 + K_a C} \quad \text{..... (2-3)}$$

This finds a maximum adsorption density of 6.0755mg/cm3, and $K_a = 8.116\,\mathrm{X}\,10^{-5}$. The results are shown in Fig. 2-11.

Figure 2-12 is a fit of the adsorption data to the Freundlich equation.[36] As with the Langmuir equation the fit is fair. The Langmuir does not fit the desorption well but using two slopes the Freundlich equation fits fairly well for desorption. Figure 2-13 shows curves fit to the first and the third desorption profile using the Freundlich equation. As shown in this figure, desorption density data fit two different log-log linear relationship for each desorption profile that were fit using two different power equations with distinct slopes. The crosspoint value of the two lines is about 2600 ppm for each profile. The two distinct slopes can be explained by different adsorption mechanisms: single layer adsorption and bilayer or multilayer adsorption, as explained above.

Effect of Temperature on Adsorption Density. The adsorption experiments in Runs 5 and 6 of Table 2-3 were used to evaluate the temperature effect on CLS adsorption density onto Berea core. Figure 2-14 presents the adsorption density of 5,000 ppm and 10,000 ppm CLS solution at 30, 40 and 50ºC. Increasing temperature decreases CLS adsorption density for each of the solution concentrations. Adsorption decreased more than 50% when the temperature was raised from 30ºC to 50ºC for 5,000 ppm CLS solution. These results indicate that physical adsorption is probably one of the principle mechanisms controlling CLS adsorption onto Berea core. Because physical adsorption reaction is normally exothermic, the extent of adsorption generally increases with decreasing temperature.

Effect of Salinity on Adsorption Density. The adsorption experiments in Runs 7 through 9 (shown in Table 2-3) were performed to study the effect of salinity on CLS adsorption density on Berea core. The results are shown in Fig. 2-15. Comparing different brine concentrations, Fig. 2-15 indicates that ionic strength and species affect adsorption. The 5% NaCl + 5% $CaCl_2$ and 10% $CaCl_2$ brines have higher adsorption densities than the 10%NaCl brine, which indicates that $CaCl_2$ in CLS solution has a greater influence on CLS adsorption density than NaCl. This does not explain why the 5% NaCl + 5% $CaCl_2$ CLS solution has about the same adsorption density as that of the 10% $CaCl_2$ solution.

Reservoir brine composition and concentration vary over a wide range and if an oilfield has been waterflooded, salinity gradients often exist within the same pool. Therefore, it is very important to know the effect of brine concentration and hardness on lignosulfonate adsorption.

Effect of Injection Rate on Adsorption Mass. Run 5 in Table 2-3 was performed to study the effects on adsorption density of rates that varied over an order of magnitude, 2 to 20 Darcy feet per day or 0.5 to 5.0 ml/min. Increasing the injection rate from 0.5 to 2 ml/min resulted in an adsorption decrease of 0.07 mg/cc (about a 5%). Above 2 ml/min, no change in adsorption was noted up to 5.0 ml/min flow rate. Overall injection rate is not considered a significant factor in adsorption density. Since the pressure gradient is dependent on the flow rate, the pressure gradient should show a similar function.

For sandstone reservoirs without fractures or severe channels, at typical reservoir flow rates away from the wellbore, rate dependency should not be a concern. But for reservoirs with fractures or channels, the rate effect on adsorption might be considered due to the severe heterogeneity of those reservoirs.

Comparison of Adsorption/Desorption Profile for Different Concentrations of CLS Solutions. Runs 1 and 2 in Table 2-4 were performed to analysis CLS concentration effect on adsorption and desorption process. As shown in Fig. 2-17, adsorption equilibrium time does depend on CLS concentration, but in either case shown, over 90% of the final adsorption occurs in the first two PV injected. The great difference is the adsorption of the last 10%. Solutions at lower CLS concentrations take longer to achieve adsorption steady state. Figure 2-18 shows that desorption is also a slower process for the lower concentration system, but again both desorb 90% in the first couple of PV. In a field application, if the injection surfactant slugs and

sacrificial agent slugs are alternating, an oversized surfactant slug could minimize the effect of the sacrificial agent.

Postflush Rate and Interruption Effect on the Desorption Process. The desorption experiment described as Run 3 in Table 2-4 was conducted to study the postflush rate effect on desorption. Figure 2-19 shows the results. It can be seen that the effluent lignosulfonate concentrations are influenced by the brine flow rate. When flow rates changed from high to low, the effluent sample concentration increased. Zhang et al. found the same trend when they studied the mechanism of scale inhibitor adsorption on sandstone. [37] They attributed the observed results to the difference of fluid transit time and the equilibrium time of the chemical/rock system. The fluid transit time was shorter than the kinetics of desorption of the chemical/rock system, and thus did not have the opportunity to reach equilibrium. In the reservoir where the fluid has considerably more time in contact with rock and adsorbents, equilibrium is more likely to be approached as it was with the slowing rates in this test.

To further study CLS desorption versus the extent of non-equilibrium, a flow interruption experiment was performed. In this test flow was stopped for a time, allowing more time for desorption, and then the flow was resumed. Figures 2-20 and 2-21 present the interruption test results on desorption for Run 9 of Core 1 and Run 3 of Core 2, respectively. During Run 3 of Core 2, flow was stopped at 24PV, 27PV and 37PV for 4 hours each time. During Run 9 of Core 1, flow was stopped at 7PV, 147PV and 21PV for 12 hours each time. Both figures showed that after the interruption the effluent solution concentration increased while the solution was displaced. Brusseau et al.[34] found the same trend in bi-porous media and they attributed the physical non-equilibrium to diffusion time (diffusive mass transfer between mobile and immobile zones).

In summary, changing post-flush rate and interruption experiments show that under our tested conditions, CLS equilibrium is not achieved during flow conditions. Zhang *et al*. and Brusseau *et al.* indicated different explanation for the slow equilibrium time. Zhang suggested it is chemical or kinetics of desorption at the rock/chemical interface, while Brusseau *et al*. suggested that in their tests, diffusion time or physical non-equilibrium was the limiting process. It is difficult to consider if either or both mechanism predominate for CLS desorption from Berea core. When looking at cores on a microscopic scale, none are homogenous in composition or permeability. Berea core is made up of a number of minerals[18]: silica, bentonite, kaolinite,

dolomite, calcite, illite and other tracer components. Clay, such as bentonite and kaolinite, will form micropores in the core. In general, micropores are immobile zones, and macropores that are formed by silica bonds are mobile zones. From this, Berea core might be considered as a dual-porosity system. Another series of experiments that will be discussed in the following section show that CLS adsorption on silica is essential zero and adsorption on Berea is contributed to the clays in the core.

The question is whether the limiting process can be attributed to desorption kinetics or diffusion. Going from multilayer to monolayer adsorption and thus different kinetic mechanisms is supported by the change in Freundlich equation coefficients seen in Fig. 2-13. Diffusion after desorption could also be slow when considering the dual-porosity model just described. Further experiments and theoretical study will help determine if either or both mechanisms are significant.

Postflush Brine Concentration Effect on the Desorption Process. The desorption experiment of Run 4 in Table 2-4 was performed to determine brine concentration effect on desorption. The postflush brine was injected in the following flowing order: 4 PV 2% brine → 9 PV 10% brine → 9 PV 2% brine → 4 PV 10% brine → 2% brine injected until no CLS was being displaced from the core. The 10% brine was composed of 5% NaCl and 5% $CaCl_2$. As shown in Figure 2-22, the change of brine concentration influenced CLS desorption. After the first 4 PV of 2% brine was injected, the effluent concentration was about 60 ppm. But when brine concentration was increased by 10%, no more CLS was produced. After 9 PV of 10% brine was injected, injected brine concentration was decreased back to 2%, and the effluent concentration rapidly increased to 22 ppm. The same procedure was repeated and again the CLS concentration in the effluent returned to near zero and rebounded when returned to 2% brine.

Postflush Brine pH Effect on Desorption Process. The desorption test of Run 5 listed in Table 2-4 was performed to analyze brine pH effect on desorption. The postflush brine was injected in the following order: 4 PV of 2% brine (pH=7) → 8 PV of 2% brine (pH=4) → 2% brine (pH=7) injected until no CLS was displaced from the core. As shown in Fig. 2-23, the change of pH from 7 to 4 appears to affect CLS desorption trends.

Postflush Brine Temperature Effect on Desorption Process. The desorption experiment (Run 8) for Core 1 was performed to determine brine temperature effect on desorption. In this test, after about 16 PV of 2% brine were injected, the brine temperature was decreased from 40ºC to 20ºC. Figure 2-24 shows no significant change in the effluent concentration due to temperature change.

Comparison of CLS Recovery. Figure 2-25 summarizes five CLS recovery results from desorption experiments. Although some postflush conditions were changed in these desorption experiments, the recovery curves are smooth, indicating that the condition changes had little influence on the final recovery. In fact, although some conditions changes influenced desorption, the experiments were mainly post-flushed with 2% brine, except for a few PV. Therefore, the results are accurate when compared to each other. From these smooth curves, we also can infer that core conditions during adsorption have the principle influence on CLS recovery. Table 2-6 lists the core conditions before each desorption experiment was performed and recovery results after 20 PV of postflush and test termination. Figure 2-25 and Table 2-6 show the dependence core conditions. The recoveries of Runs 9 and 7 of Core 1 are below 20% because the core was saturated with 10% brine (10% $CaCl_2$ and 5% NaCl + 5 % $CaCl_2$, respectively) with final CLS adsorption densities of 32.9 mg/cm^3 and 30.73 mg/cm^3, respectively. For Run 8 of Core 1 and Run 2 of Core 2, their saturated fluid and the CLS solution before desorption are the same, the only difference being that Run 8 was preflushed with 10 PV 10% NaCl brine before the adsorption experiment was performed. Comparing these two results shows that Run 2 of Core 2 had the higher recovery of 84.08 %, leaving only 3.43 mg/cm^3 adsorption density remaining on the core.

Conclusions

It is not uncommon that over 90% of a component in a chemical process in a reservoir is required to satisfy adsorption on the rock. Thus the understanding of adsorption and desorption processes are critical in assessing transport of chemicals and to accurately assess chemicals required for a successful operation. In Chapter 2, CLS has been used to look at the effects on sorption of a number of parameters for a single rock type, Berea sandstone. Each of these can significantly affect the required chemical and thus the cost of a project.

Based on the results of CLS adsorption and desorption experiments onto Berea sandstone, the following conclusions can be drawn:

1) The CLS adsorption density on Berea core was influenced by CLS concentration, temperature, salinity, and injection rate. The results show that for Berea core:
   a) Increasing CLS concentration (to at least 25,000 ppm) increases adsorption density on Berea core.
   b) The adsorption isotherm can be fit using Langmiur and Freundlich adsorption models.
   c) That increasing temperature will decrease adsorption density is an indication that physical adsorption occurs and that it is a principal mechanism controlling CLS adsorption.
   d) Increasing brine and divalent concentration will increase CLS adsorption density.
   e) Increasing flow rate results in a slight decrease in adsorption density.
2) On the systems tested, postflush brine concentration, temperature, pH and injection rate have the following effects on CLS desorption:
   a) Desorption isotherm curves were fit by two Freundlich adsorption isotherm equations with different slopes. The two distinct slopes are an indication of different adsorption/desorption mechanisms.
   b) Temperature and pH have little effect on CLS desorption. Increasing brine concentration will reduce CLS desorption mass, and even stop desorption, thus leaving more CLS adsorbed onto the rock.
   c) Changing postflush flow rates and intermittent stoppage of injection significantly changed the effluent concentration of CLS. This indicates that equilibrium is not reached and the kinetics and/or diffusion are slow compared to the flow rates.
3) The adsorption and desorption are not completely reversible in the time frame of the experiments and desorption rates lag well behind adsorption rates below 2500 ppm for CLS solution concentrations.
4) The core condition before desorption experiments were carried out is a principle factor influencing the recovery of CLS from Berea sandstone.

References

1. Tsau, J. S. and J.P. Heller: "Evaluation of Surfactants for CO_2-Foam Mobility Control," paper SPE 24103, presented at the 1992 SPE Permian Basin Oil and Gas Recovery Conference, Midland, March 18–20.
2. M.I. Kuhlman, M.I., Lau, H.C., and Falls, A.H.: "Surfactant criteria for successful carbon dioxide foam in sandstone reservoirs", *SPERE*, Feb, 2000.
3. Grigg, R., Tsau, J-S, and Martin, F.D: "Cost Reduction and Injectivity Improvement for CO_2 Foam for Mobility Control," paper SPE 75178 presented at the 2002 SPE/DOE Improved Oil Recovery Symposium, April 13–17.
4. Mannhardt, K., Schramm, L.L. and Novosad, J.J.: "Effect of Rock Type and Brine Composition on Adsorption of Two Foam-Surfactants," paper SPE 20463 presented at the 1990 SPE Annual Technical Conference and Exhibition, New Orleans, Sep. 23–26.
5. Smith, D.H., *Surfactant-Based Mobility Control*, ISBN 0-8412-1491-3, American Chemical Society, 1988.
6. Willhite, G.P., Okoye, D.M., and Looney, M.D.: "A Study of Oil Displacement by Microemulsion Systems-Mechanisms and Phase behavior," *SPE*J (Dec. 1980) 457-72.
7. Rosen, M. J.: *Surfactants and Interfacial Phenomena*, New York: Wiley, c1989.
8. Schramm, L.L: *Foams: Fundamentals and Applications in the Petroleum Industry,* American Chemistry Society, Washington, DC, 1994.
9. Austad, T.: "A Review of Retention Mechanism of Ethoxylated Sulfonates in Reservoir Cores," paper SPE 25174 presented at the 1993 SPE International Symposium on Oilfield Chemistry, New Orleans, March 2-5,
10. Trogus, F.J., Sophany, T., Schechter, R.S. and Wade, W.H..: "Static and Dynamic Adsorption of Anionic and Nonionic Surfactants", paper SPE 6004 presented at the 1976 SPE Annual Technical Conference and Exhibition, New Orleans, Oct. 3–6.
11. Smith, L., Malmberg, E.W., nad Kelley, H.W.: "Measurement of Surfactant Loss in Porous Media," paper SPE 5306 presented at the 1975 SPE International Symposium on Oilfield Chemistry, Dallas, Jan. 16–17.
12. Tabatabai, A., et al.: "Reducing Surfactant on Carbonate Reservoir," *SPERE* (May 1993) 117–122.

13. Liu, D. B., Castanier, L. M., and Brigham, W. E.: "Displacement by Foam in Porous Media," paper SPE 24664, presented at the 1992 Annual Technical Conference and Exhibition, Washington, DC, Oct. 4-7.
14. Mannhard, K., Schramn L.L., and Novosad, J.J.: "Effect of Rock Type and Brine Composition on Adsorption of Two Foam-Forming Surfactants," paper SPE 20463, presented at the 1990 SPE Annual Technical Conference and Exhibition, New Orleans, Sept. 23-26.
15. Bae, J.H. and Petrick, C.B.: "Adsorption/Retention of Petroleum Sulfonates in Berea Cores," *SPEJ* (Oct.1977) 353-57.
16. Wang, F.H.L.: "Effects of Reservoir Anaerobic Reducing Conditions on Surfactant Retention in Chemical Flooding," *SPERE* (May 1993) 108-16.
17. Viswanathan, K.V.: "Abstraction of Sulfonates and Dodecane by Alumina ," paper SPE 10602 presented at the 1982 International Symposium on Oilfield and Geothermal Chemistry, Dallas, Jan. 25–27.
18. Eicke, H.: *Interfacial Phenomena in Apolar Media*, 1987.
19. Huang, A. Y., and Novosad, J.J.: "Modeling of Adsorption of Foam-Forming Surfactants in Porous Media," Fundamentals of Adsorption Engineering Foundation New York, 1986.
20. Shalaby, M.N.: "Adsorption Isotherm of Some Commercial Surfactants on Clay. Comparisons with Synthesis Surfactant," *J Dispersion Science Technology*, (Nov. 2000) **21**, No. 7, pp. 839-855.
21. K. Mannhardt, Schramn L.L., and Novosad, J.J: "Effect of Rock Type and Brine Composition on Adsorption of Two Foam-Surfactants," paper SPE 20463, presented at the 1990 SPE Annual Technical Conference and Exhibition, New Orleans, Sept. 23-26.
22. Nevskaia, D.M. et al.: "Adsorption of Polyxyethylenic Nonionic and Anionic Surfactants From Aqueous Solution: Effects of Induced by the Addition of NaCl and CaCl2," J. Colloid Interfaces Sciences, (Sep. 1 1998) Vol 205, No. 1, p 97-105,
23. Gale, W.W and Sandvik. E.I.: "Teriary Surfactant Flooding: Petroleum Sulfonate Composition Efficacy Studies," *SPEJ* (Aug. 1973) 191-199.
24. Gall, B.: "Use of Sacrificial Agents to Reduce Carboxymethylated Ethoxylated Surfactant Loss During Chemical Flooding," DOE/NIPER-447, 1989.

25. Surkalo, H. and Pouska, G.: " Analysis of Reservoir Pretreatment in Chemical Flooding: a Literature Review," Dept. of Energy Report No. DOE/BC/10027-11, 1980.
26. Surkalo, H. and Pouska, G.: "Experimental Evaluation of Reservoir Pretreatment in Chemical Flooding," Dept. of Energy Report No. DOE/BC/10072-12, Feb 1981.
27. Tabatabai, A.: "Reducing Surfactant Adsorption on Carbonate Reservoirs," *SPERE* (May 1993) 117–122.
28. Kalfoglou, G., Prieditis, J. and Paulette, G.S.: "Sacrificial Agents for Carbon Dioxide Foaming Agents," Canadian Patent 2,185,499.
29. Hong, S. A., and Bae, J. H.: "Field Experiment of Lignosulfonate Preflushing for Surfactant Adsorption Reduction," *SPERE*, 11,467-474 (1990).
30. Hong, S. A., et al.: "An Evaluation of Lignosulfonate as a Sacrificial Adsorbate in Surfactant Flooding," *SPERE*, 2, 17-27(1987).
31. Tsau, J-S., Syahputra, A. E, Yaghoobi, H., and Grigg, B.R.: "Use of Sacrificial Agents in CO_2 Foam Flooding Application," paper SPE 56609, presented at the 1999 SPE Annual Technical Conference and Exhibition, Houston, Oct. 3–6.
32. Syahputra, A.E., Tsau, J-S., and Grigg, R.B.: "Laboratory Evaluation of Using Lignosulfonate and Surfactant Mixture in CO2 Flooding," paper SPE 59368, presented at the 2000 SPE/DOE Improved Oil Recovery Symposium, Tulsa, April 3–5.
33. Tsau, J.S., Syahputra, A.E., and Grigg, R.B.: "Economic Evaluation of Surfactant Adsorption in CO_2 Foam Application," paper SPE 59365, presented at the 2000 SPE/DOE Improved Oil Recovery Symposium, Tulsa, April 3–5.
34. Knaelbel, K.S.: "Adsorption Selection," Adsorption, Inc., Dublin, Ohio, www.adsorption.com/publications/adsorbentSel1B.pdf.
35. Shu, B-Y.: "Surfactant Adsorption at Solid-Liquid Interfaces," *Advances in Colloid and Interface Science*, (1991), **37**, 1–32.
36. www.geo.utexas.edu/courses/387e/PDF/sorption.pdf
37. Zhang, H. Sorbie, K.S.: "Non-Equilibrium Adsorption and Precipitation of Scale Inhibitors: Corefloods and Mathematical Modelling," paper SPE 64755 presented at the 2000 SPE International Oil and Gas Conference and Exhibition in China, Beijing, Nov. 7–10.
38. Brusseau, M.L., Rao,R.E. and Davidson, J.M. : "Flow Interruption: a Method for Investigating Sorption Nonequilibrium". *J. Contam. Hydrol*, vol 4, 1989:223-240.

Table 2-1. Properties of Lignosite®100

Properties	**Descriptions**
PH	< 2.0-4.0
Insolubles(w/w%)	1.5% MAX
Reducing Substances	11% MAX
Moisture	8% MAX
Molecular Weight by GPC (%)	19200
Calcium (%)	4.0-5.5
Chromium (%)	-
Iron (%)	-
Sodium	0.02

Table 2-2. Properties of Berea Core Samples

No.	Permeability (md)	Porosity (%)	Length (cm)	Diameter (cm)
1	138.77	18.0	5.83	3.75
2	320.28	19.20	6.10	3.75

Table 2-3. Experiment Series for Core 1

Run #	**Adsorption (Circulation)**	**Desorption (flow-through)**
1-4	Establish adsorption and desorption isotherm, the detail procedures can be seen in the text.	
5	(1) Core saturated with 2%brine. (2) Circulated 10,000 ppm CLS-2% brine solution at 1 ml/min at 30-40-50-30ºC. (3) Circulated 10,000 ppm CLS-2% brine solution at 30ºC at 0.5-1-2-3-5-1 ml/min.	(1) Inject 2% brine to flush it at different post-flush rate. (2) Inject 400cm^3 THF to clean the core.
6	(1) Core saturated with 2% brine. (2) Circulated 5,000 ppm CLS-2% brine solution at 30-40-50-30ºC.	(1) Flushed with 2% brine at 0.5 ml/min. (2) Cleaned with 400 ml THF.
7	(1) Core saturated with 10,000 ppm CLS-10% brine (5%NaCL + 5%CaCL2) solution. (2) Circulated same solution at 1 ml/min at 30-40-50-30ºC.	(1) Flushed with 2% brine. (2) Cleaned with 400 ml THF.
8	(1) Core saturated with 10,000 ppm CLS-10% NaCl brine. (2) Circulated same solution at 1 ml/min at 30-40-50-30ºC.	(1) Flushed with 2% brine at different temperatures. (2) Cleaned with 400 ml THF.
9	(1) Core saturated with 10,000 ppm CLS-10% $CaCl_2$ brine. (2) Circulated same solution at 1 ml/min at 30-40-50-30ºC.	(1) Flushed with 2% brine at different post-flush rates. (2) Cleaned with 400 ml THF.

Table 2-4. Experiment Series for Core 2

Run #	Adsorption (flow-through)	Desorption (flow-through)
1	(1) Core saturated with 2% brine. (2) Injected 10,000 ppm CLS solution until effluent concentration is equal to the injection fluid concentration.	(1) Flushed with 2% brine. (2) Cleaned with 400 ml THF.
2	(1) Core saturated with 2% brine. (2) Injected 200 ppm CLS solution until effluent concentration is equal to the injection fluid concentration.	(1) Flushed with 2% brine. (2) Cleaned with 400 ml THF.
3	(1) Core saturated with 2% brine. (2) Injected 10,000 ppm CLS solution at the rate of 1cm^3/min.	(1) Flushed with 2% brine at different postflush rate (2) Cleaned with 400 ml THF.
4	(1) Core saturated with 2% brine. (2) Injected 10,000 ppm CLS solution at the rate of 1cm^3/min.	(1) Flushed with varied brine conc. (2) Cleaned with 400 ml THF.
5	(1) Core saturated with 2% brine. (2) Injected 10%brine (5%NaCl+5%$CaCl_2$) to preflush the core (3) Injected 10,000 ppm CLS solution at the rate of 1cm^3/min	(1) Injected 2% brine with different pH to flush the core (2) Cleaned with 400 ml THF.

Table 2-5. The remaining CLS after Each Desorption Profile

Profile NO.	1st	2nd	3rd	4th
Remaining CLS (mg/g)	0.67	0.55	0.28	0.27

Table 2-6. Recovery Summary of Several Desorption Experiments

Run	Core condition			Adsorp. Den. (mg/cm^3)	Final		Rec. % at 20PV
	Saturated fluid	Preflush fluid	Injected fluid before desorption		Injected postflush fluid, (PV)	Rec. (%)	
9, Core 1	10,000 ppm CLS in 10% $CaCl_2$.	-	Same	32.9	94.91	13.79	11.29
7, Core 1	10,000 ppm CLS, 5%$CaCl_2$ + 5%NaCl	-	Same	30.73	62.81	14.89	13.93
8, Core 1	10,000 ppm CLS, 10% NaCl	-	Same	6.00	101	74.41	71.17
2, Core 2	2% brine	-	10,000 ppm CLS	3.43	30	84.08	83.23
6, Core 2	2% brine	5% $CaCl_2$ + 5%NaCl	10,000 ppm CLS	5.112	29	65.5	65.34

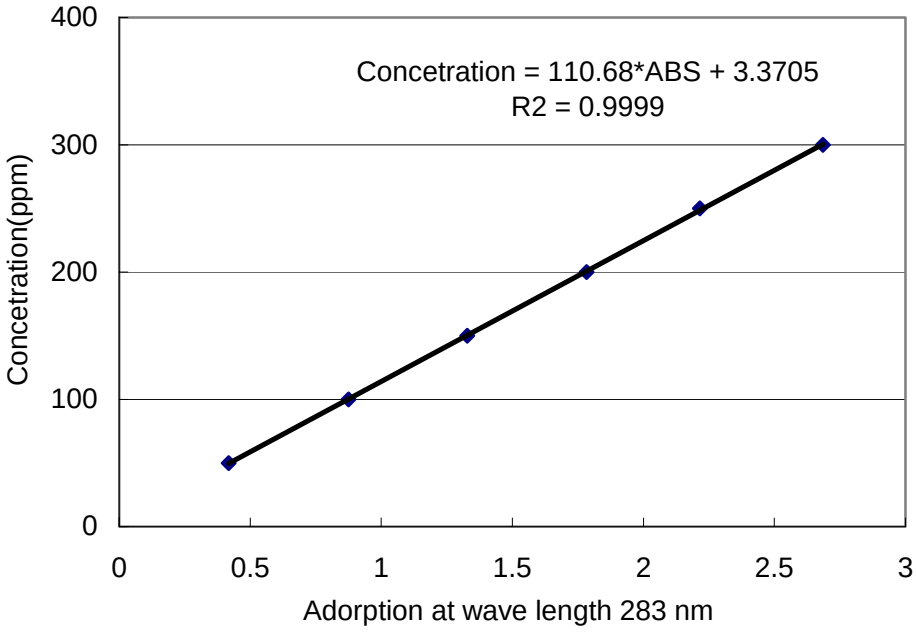

Fig. 2-1. CLS standard curve with wavelength 283nm.

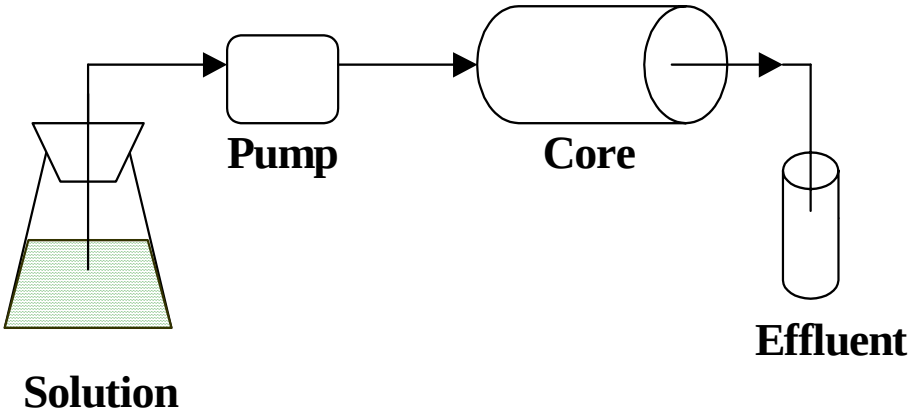

Fig. 2-2. Schematic diagram of flow-through method.

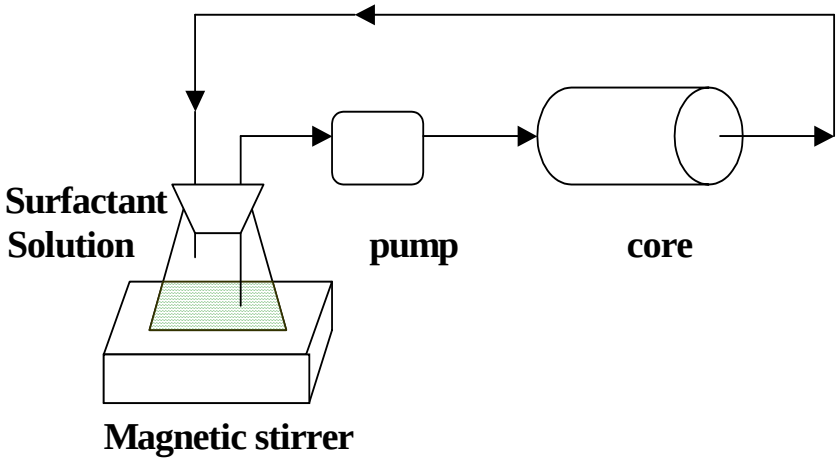

Fig. 2-3. Schematic diagram of circulation method.

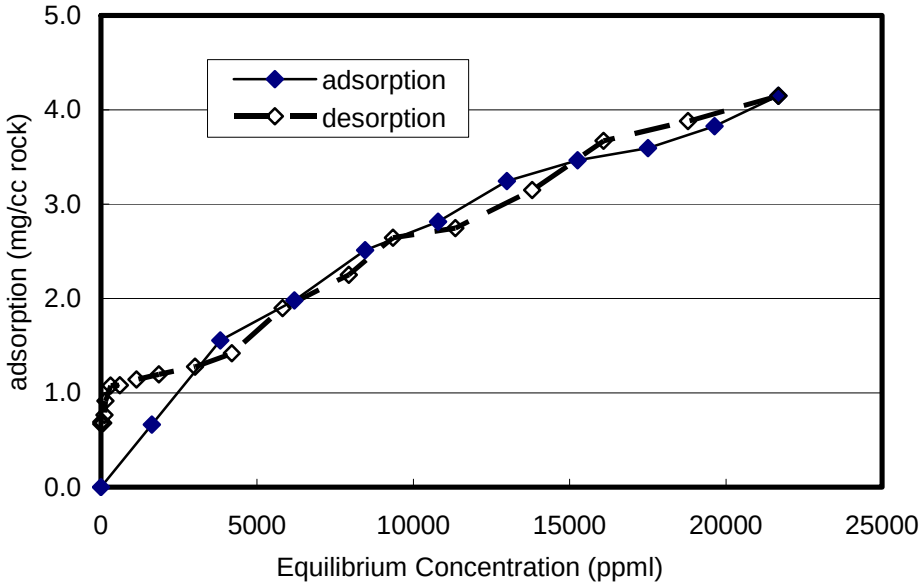

Fig. 2-4. The first profile of CLS adsorption and desorption.

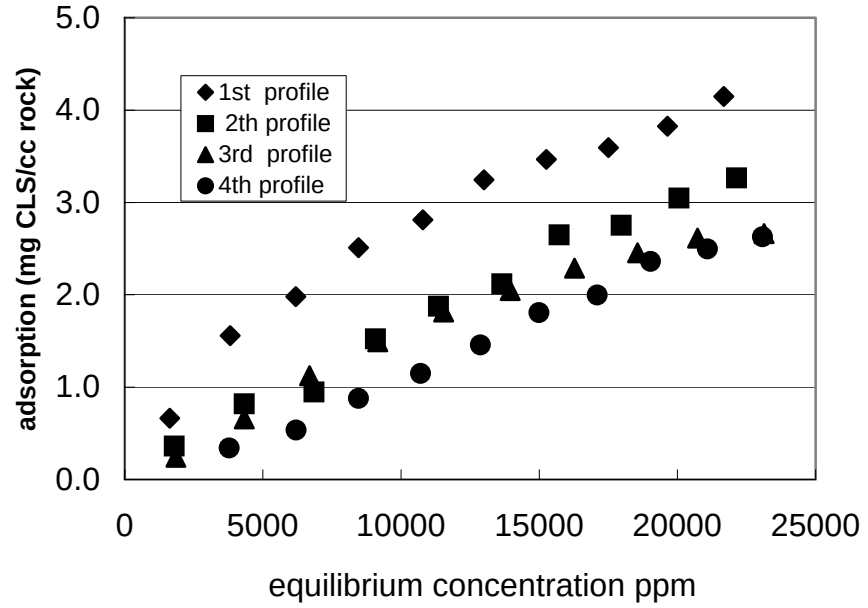

Fig. 2-5. Comparison of four CLS adsorption profiles.

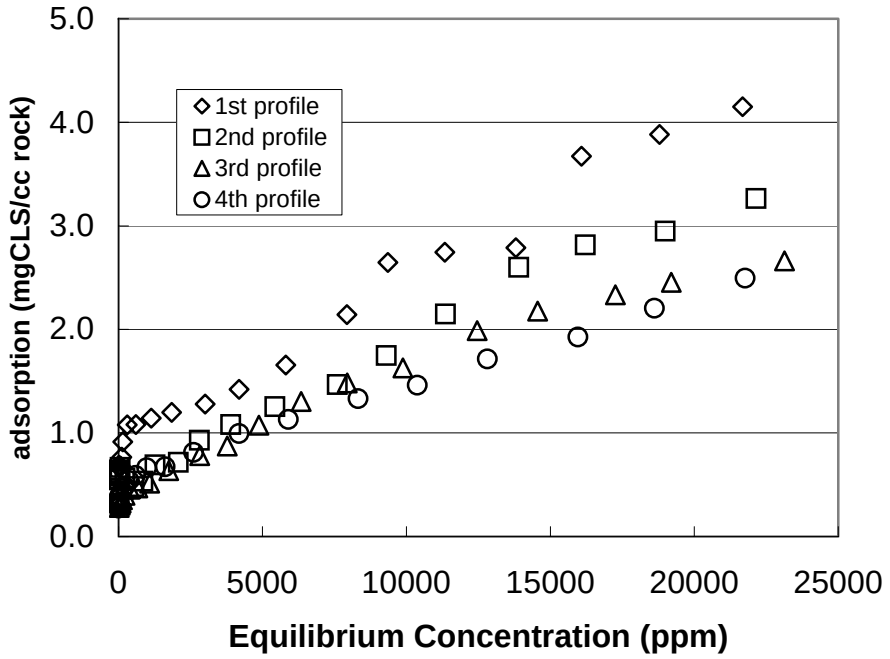

Fig. 2-6. Comparison of four CLS desorption profiles.

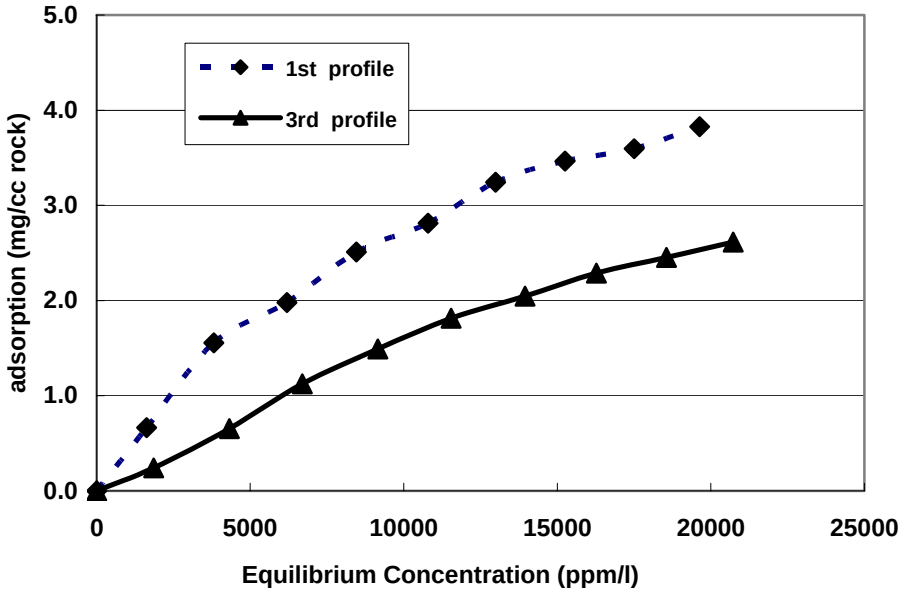

Fig. 2-7. Comparison of the first and third CLS adsorption profile**.**

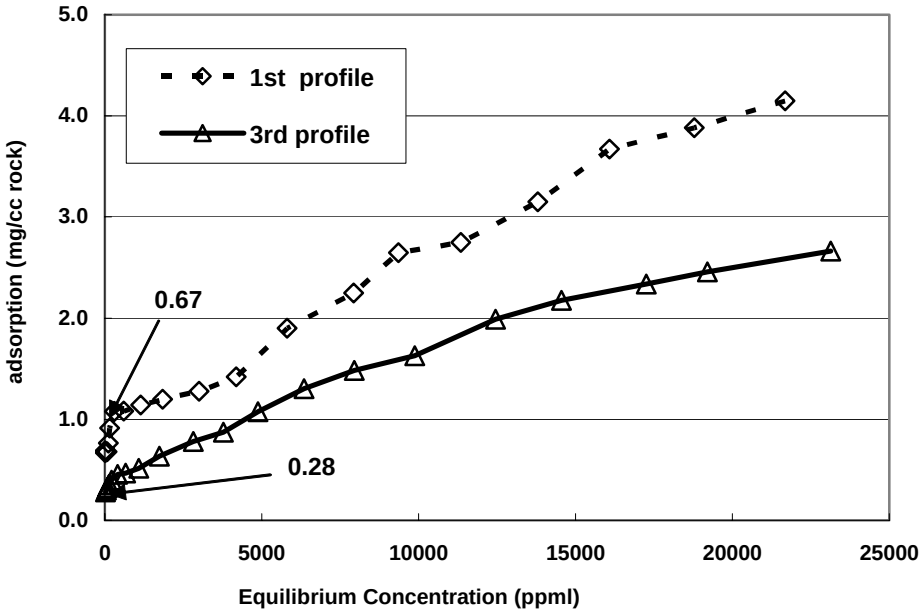

Fig. 2-8. Comparison of the first and third CLS desorption profile.

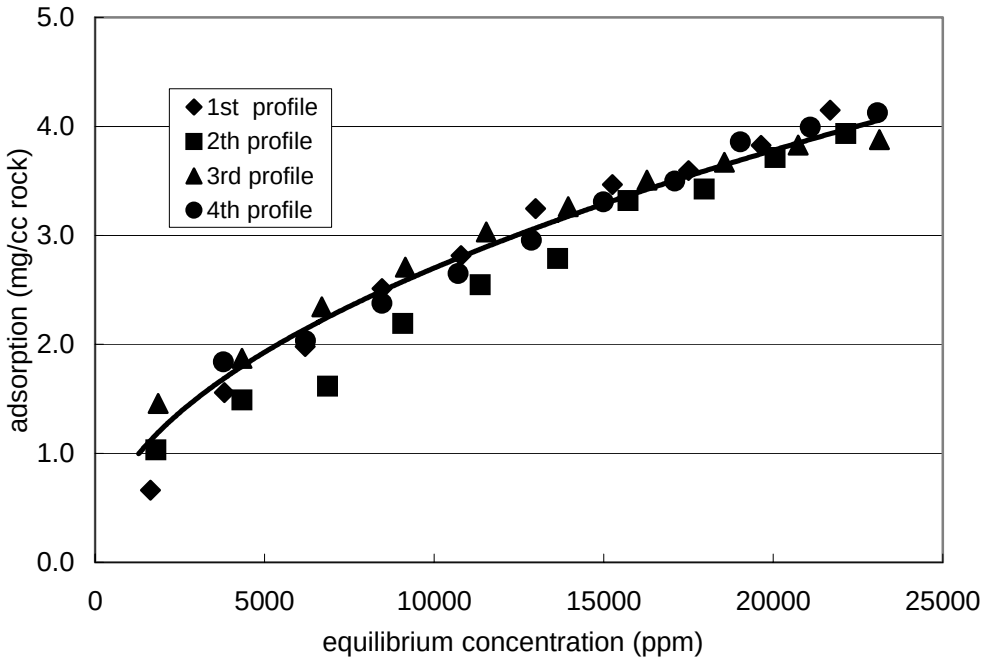

Fig. 2-9. CLS adsorption isotherm with the residual CLS density from the previous tests included**.**

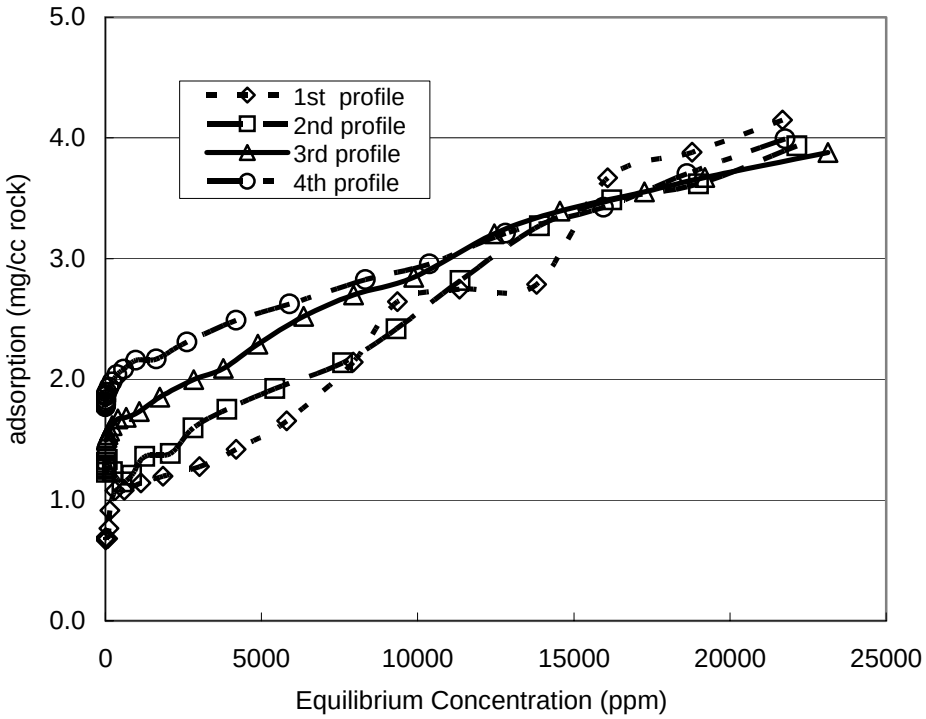

Fig. 2-10. Lignosulfonate desorption curves with the residual CLS density from the previous tests included.

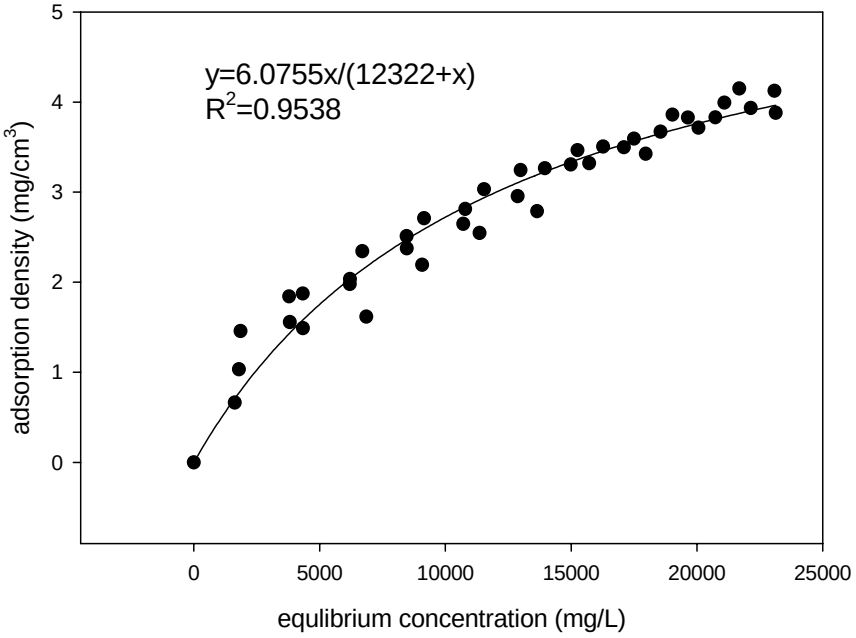

Fig. 2-11. CLS adsorption isotherm fit curve using Langmiur equation.

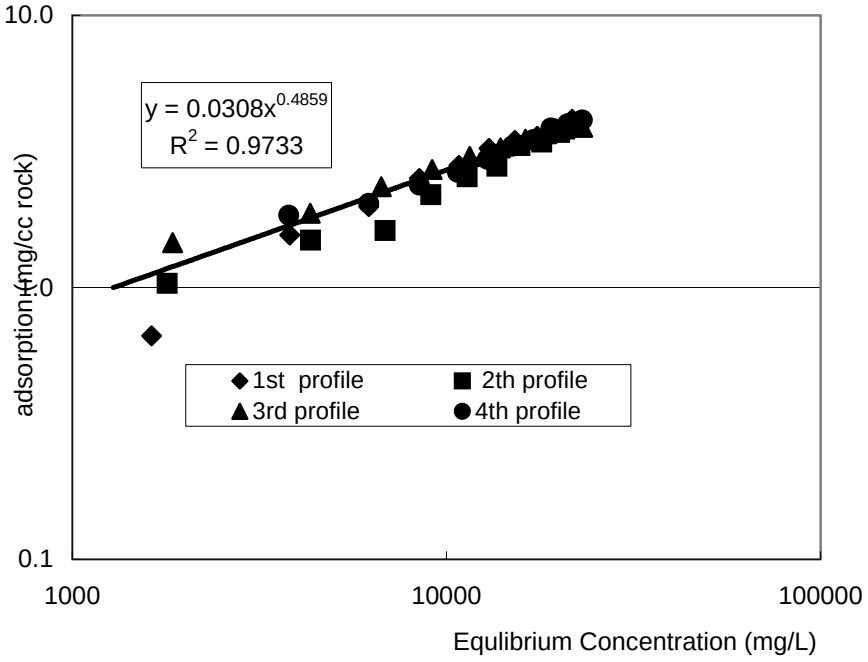

Fig. 2-12. CLS adsorption isotherm fit curve using Freundlich equation.

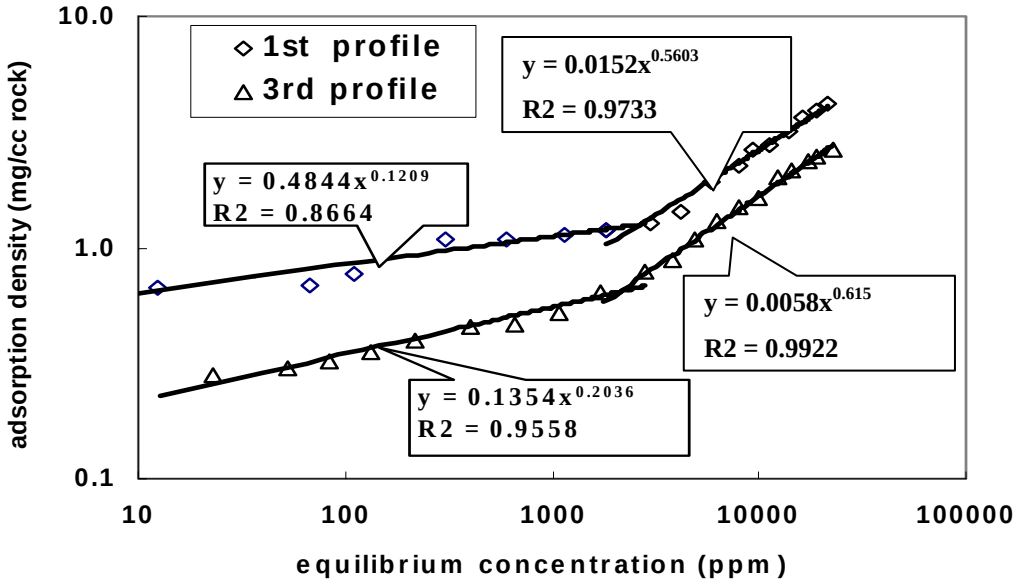

Fig. 2-13. CLS desorption isotherm fit curve using Freundlich equation.

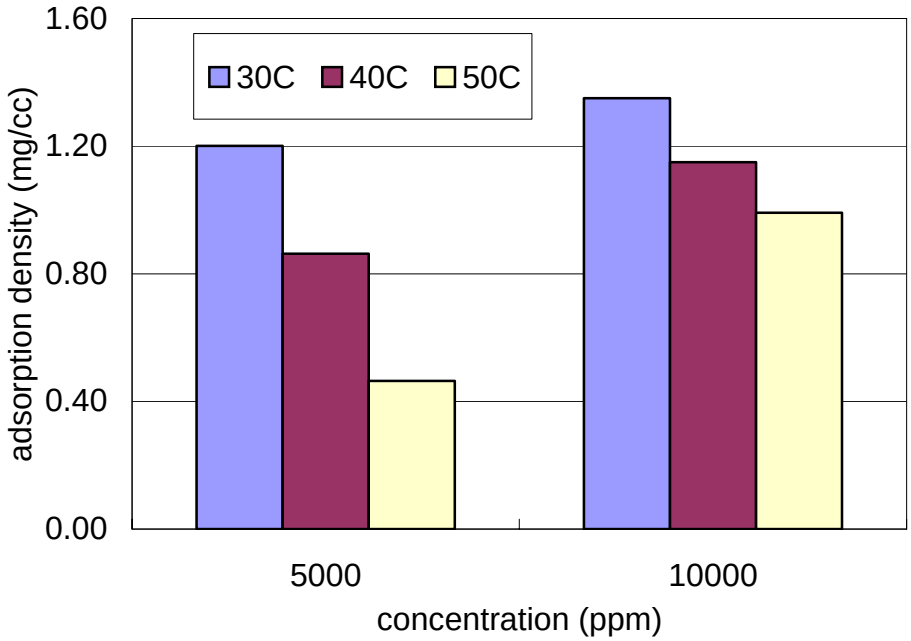

Fig. 2-14. Effect of temperature on CLS adsorption density.

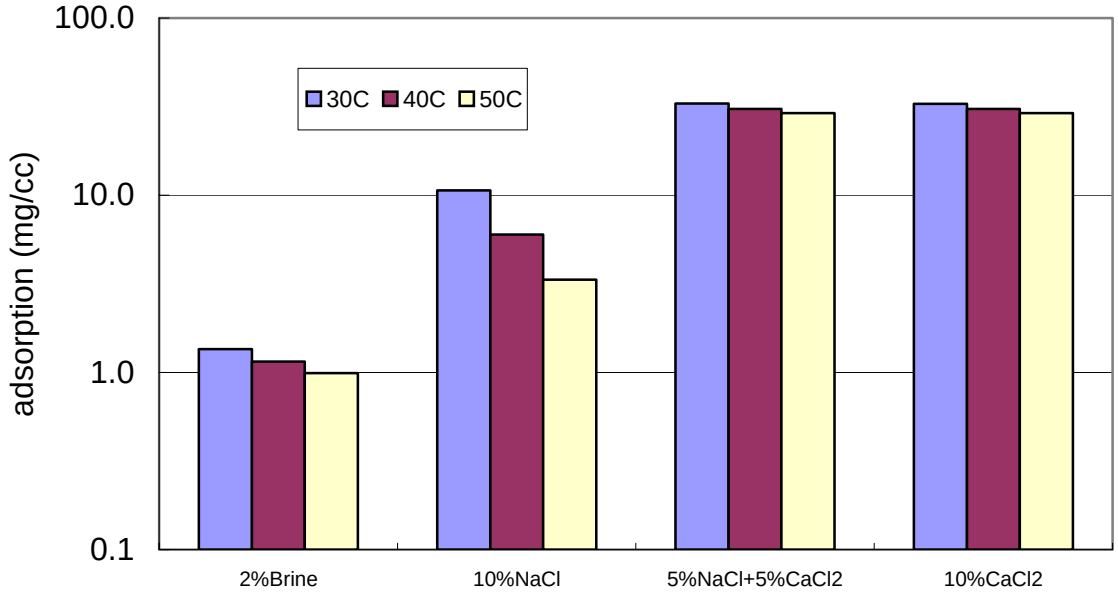

Fig. 2-15. Effect of brine concentration on adsorption mass.

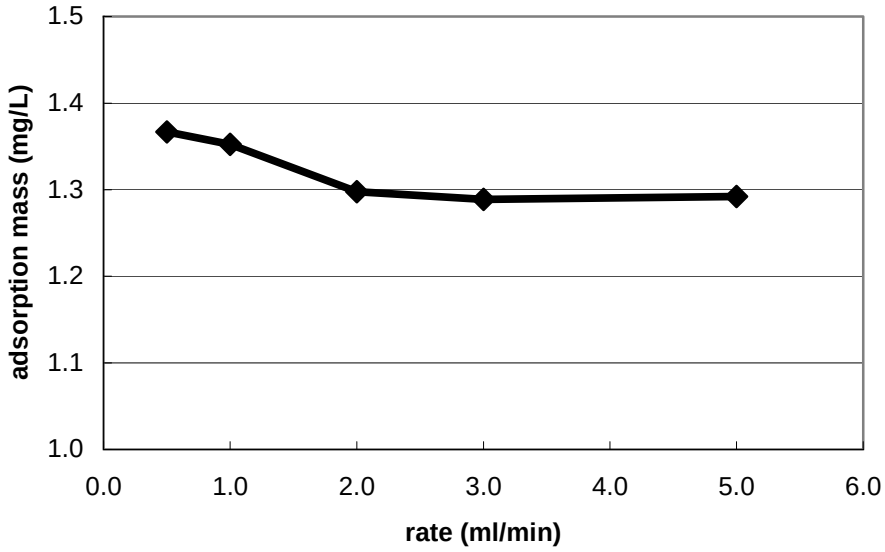

Fig. 2-16. Effect of injection rate on lignosulfonate adsorption (Berea core, C=10000mg/l, T=30C).

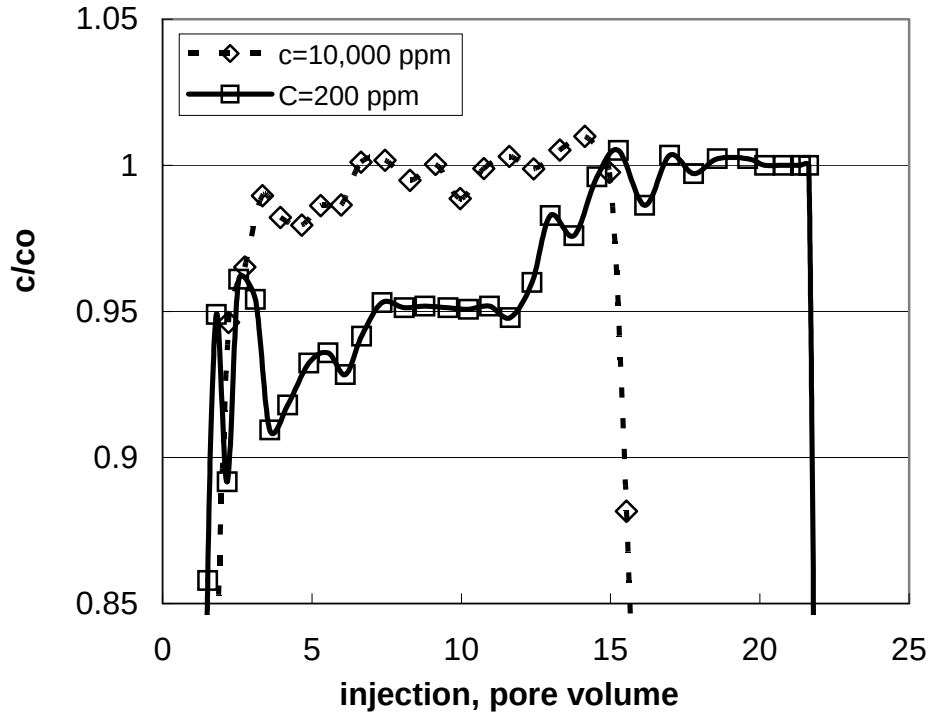

Fig. 2-17. Comparison of adsorption profiles at different CLS concentration.

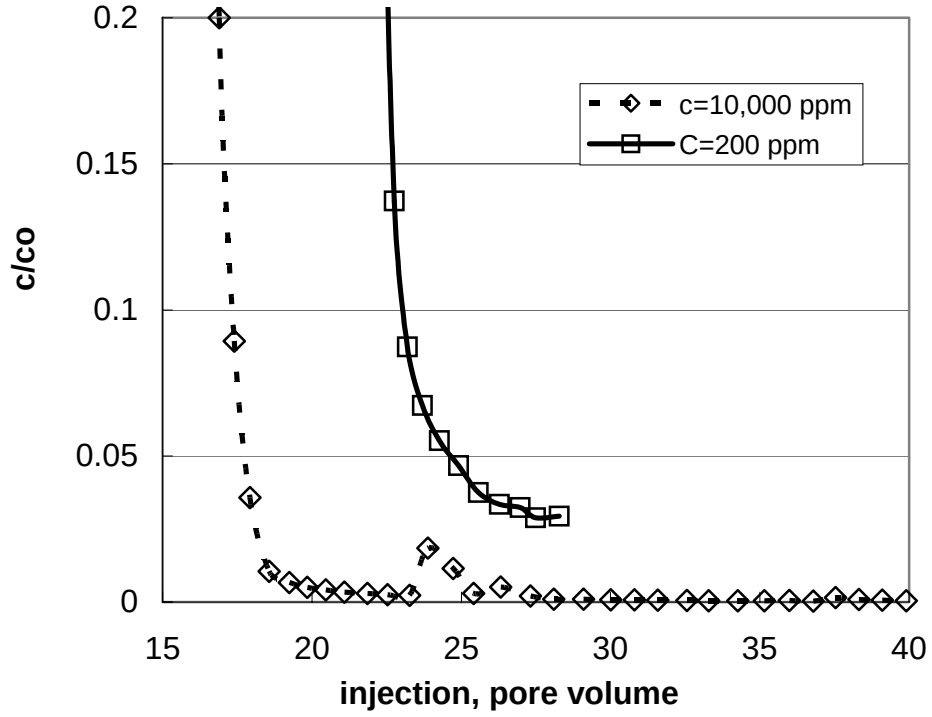

Fig. 2-18. Comparison of desorption profiles at different CLS concentration.

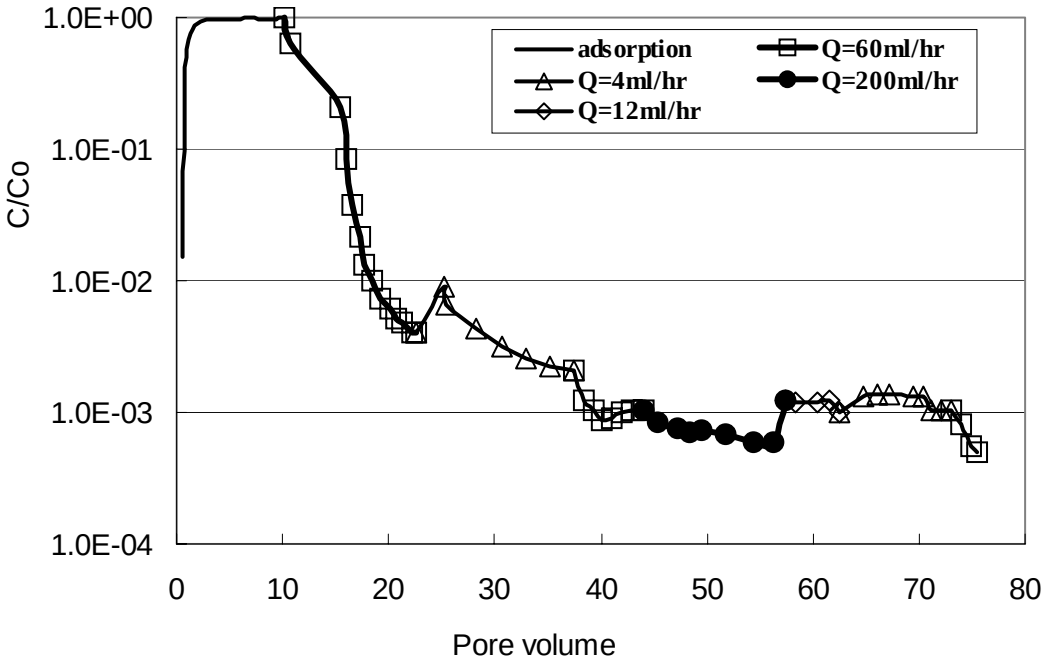

Fig. 2-19. Effect of postflush rate on desorption.

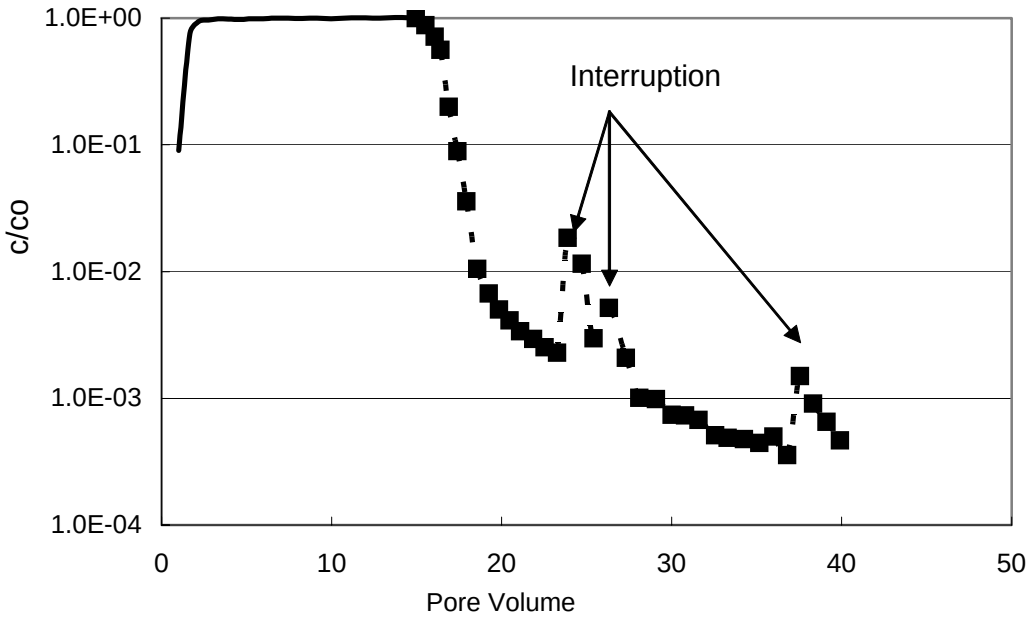

Fig. 2-20. Flow interruption experiment results (Run 3 of Core 2).

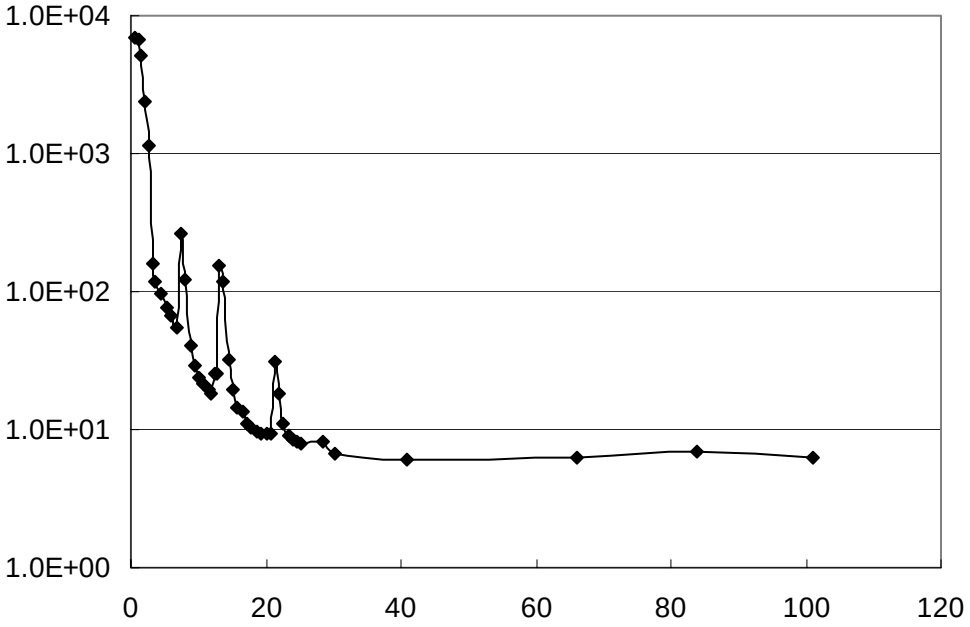

Fig. 2-21. Flow interruption experiment results (Run 9 of Core 1).

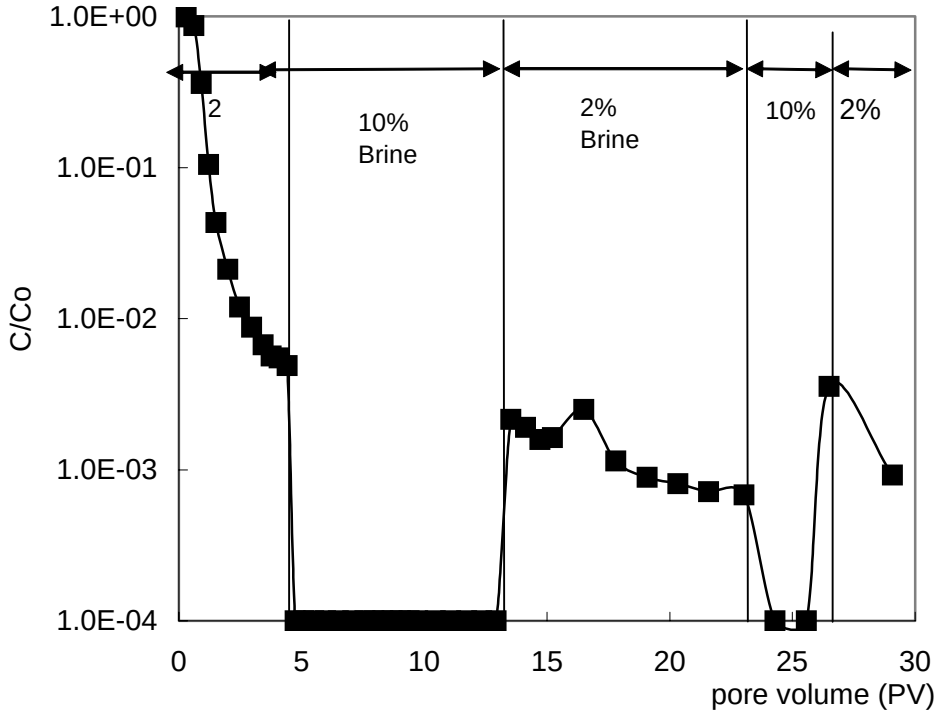

Fig. 2-22. Effect of postflush brine concentration on desorption.

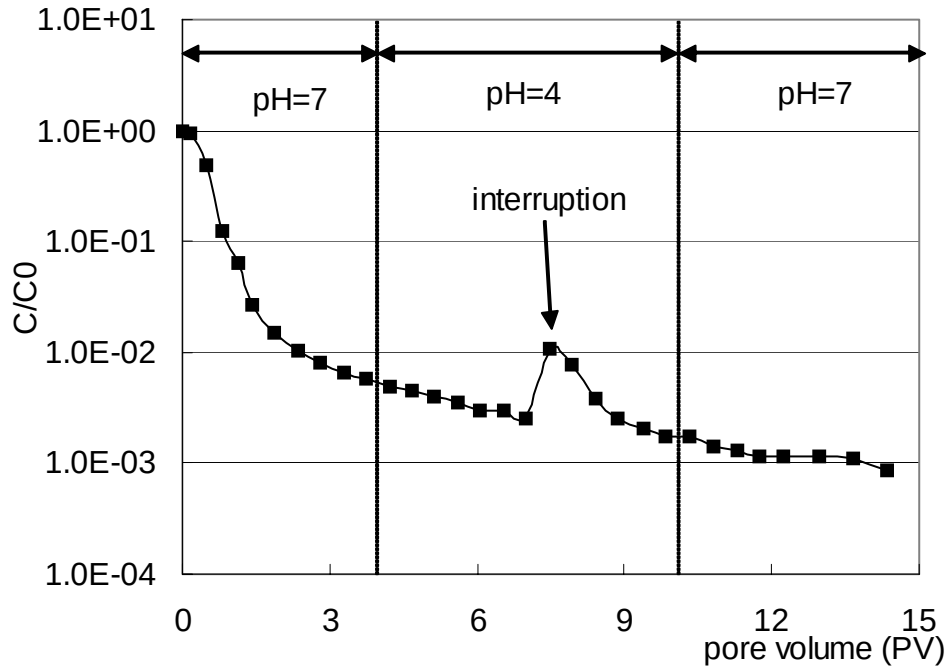

Fig. 2-23. Effect of postflush brine pH on desorption.

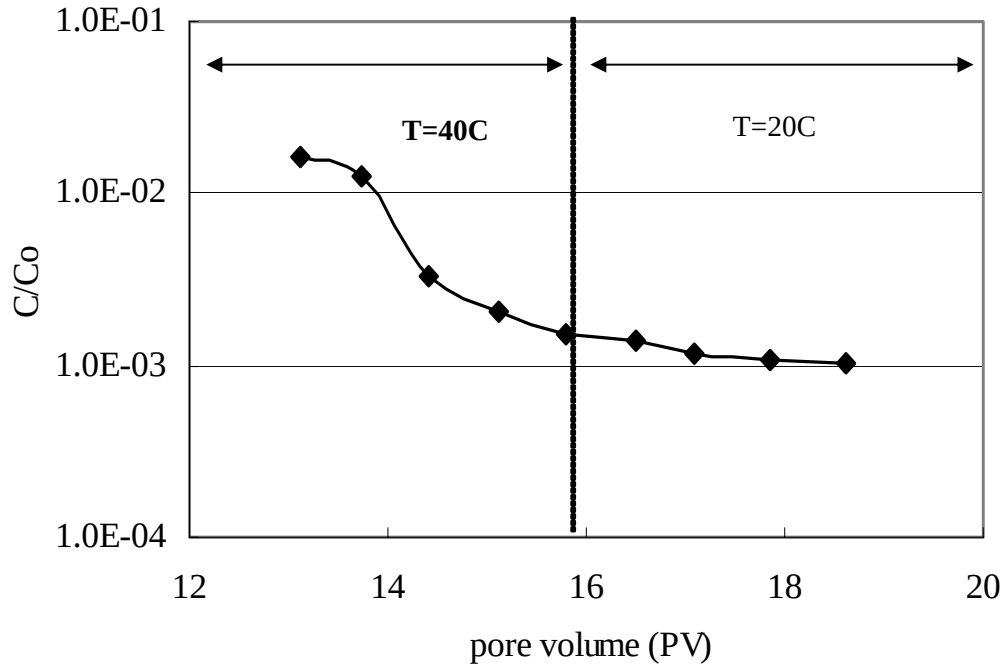

Fig. 2-24. Effect of postflush brine temperature on desorption.

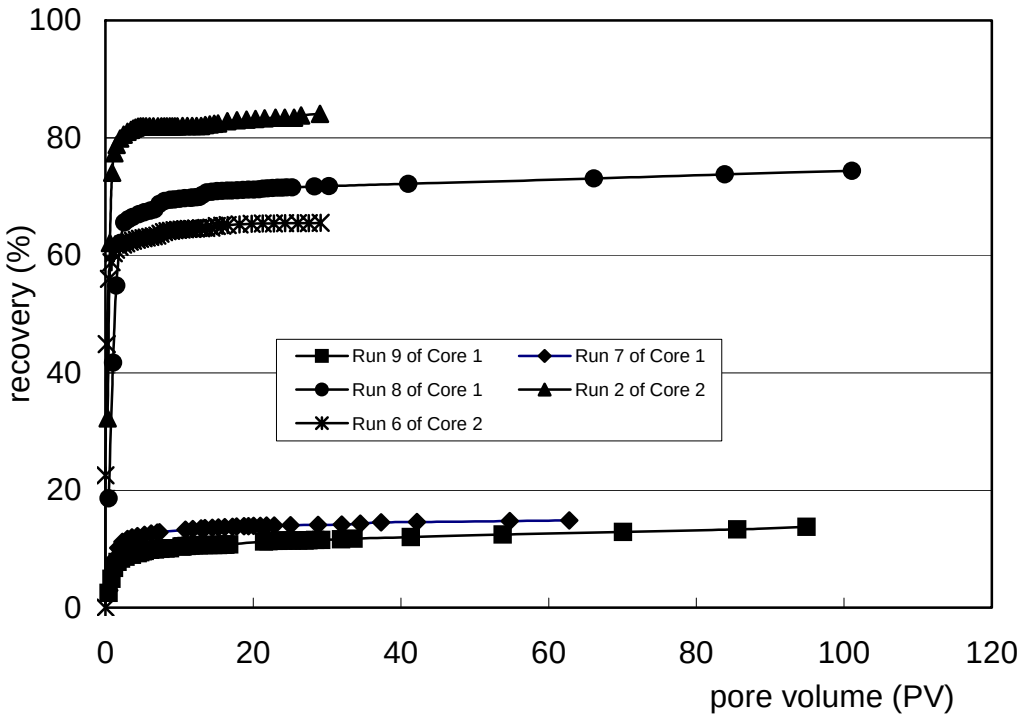

Fig. 2-25. Recovery comparison of different desorption experiments.

CHAPTER 3. PARAMETERS EFFECTING AND MAGNITUDE OF ADSORPTION OF CALCIUM LIGNOSULFONATE ONTO FIVE MINERALS

Abstract

Lignosulfonate (LS), a paper waste product, has been used as a sacrificial agent and proposed as a co-surfactant for improved oil recovery (IOR). Its effectiveness mainly depends on its adsorption properties onto mineral sites. This paper presents results of calcium lignosulfonate (CLS) adsorption onto minerals common to oil reservoirs: silica, kaolinite, bentonite, calcite, and dolomite. Comparing CLS adsorption density onto different minerals will be an aid in estimating relative adsorption mass in a well-characterized reservoir.

A number of series of batch static adsorption experiments were carried out to study the effects of CLS concentration, pH, salinity, brine hardness, and temperature on CLS adsorption density onto five minerals. For silica adsorbent, CLS adsorption density is near zero at all tested conditions. For the other four, adsorption density increases with the increase of CLS concentration, salinity and valence, and decreases with increasing temperature. At pH above 7, adsorption is neutral for the four systems; but at pH below 7, adsorption density increases with increased pH for bentonite and kaolin clay, and decreases with increasing pH for calcite and dolomite.

In this paper, adsorption mechanisms that operate under the various conditions are also partially elucidated. This study will aid in designing surfactant systems for specific reservoir types and conditions.

Introduction

In recent years more interest in surfactant-based enhanced oil recovery process has focused on the application of foam mobility control.[1-5] Propagation of foam partially depends on the propagation of the surfactant, which in turn is strongly affected by adsorption losses at the solid/liquid interface. Surfactant loss in reservoir due to its adsorption in porous media has been one of the most important features governing the economic viability of foam flooding process.

Sacrificial agents, one of most important methods to minimize surfactant adsorption loss, have been widely studied, and different kinds of inorganic and organic sacrificial agents have been shown to reduce surfactant adsorption sites in reservoir rocks.[6–9]

Lignosulfonate, an inexpensive modified waste byproduct from the paper industry, has been studied as a sacrificial agent to reduce surfactant adsorption. The use of lignosulfonate as a sacrificial agent in CO_2-foam application was first reported in a patent by Kalfoglou, et al.[9] They found lignosulfonate reduced a foaming agent's adsorption on limestone crushed rock samples by 16 to 35%. Hong et al evaluated lignosulfonate as a sacrificial adsorb in preparation for a surfactant flooding field test in a Glenn Pool reservoir.[10,11] In laboratory tests, the lignosulfonate did reduce surfactant adsorption by 39%. The results of Tsau et al showed that lignosulfonate could reduce the adsorption of a primary foaming agent-CD1045 by 24-60% in Berea core and 15-29% in Indiana limestone core samples. [12–14]

In general, effectiveness of sacrificial adsorbents mainly depends on whether the sacrificial agent adsorbs onto the same adsorption sites as the surfactant. Each reservoir rock is a complicated mixture composed of different minerals. However, the adsorption mass of sacrificial agents will be different on different minerals.[15] In addition, pore structures of any natural reservoirs rock are complex and heterogeneous. Knowing adsorption density of each component will not only aid in estimating adsorption mass in a well-characterized reservoir, but it will also aid in analyzing adsorption and transportation mechanisms.

This chapter reports on static adsorption experiments of calcium lignosulfonate on five minerals that were carried out in this project. The effects of pH, salinity, concentration and temperature on adsorption were studied for different minerals. The aim of this work was to study the differences in the CLS adsorption behavior on five different minerals and to determine the effect of CLS concentration, salinity, pH, and temperature on adsorption density for each adsorption system. The chosen five minerals are silica, kaolinite, bentonite, calcite, and dolomite because these types of materials are frequently found in oil reservoirs.

Experimental

Chemicals and Analysis Methods. Calcium lignosulfonate, brine, and analysis methods are the same as discussed in the previous section.

Adsorbents. Five minerals common in oil reservoirs are used as adsorbents: silica, kaolinite, bentonite, calcite, and dolomite. Table 3-1 lists the source and chemical composition. The chemical composition of Kaolinite is $2Al_2Si_2O_5(OH)_4$ or $2SiO_4.Al_2O_3.2H_2O$ per unit cell. There are no isomorphous substitutions in kaolinite. The water in kaolinite exists as hydroxyl groups. Kaolinite consists of sheets of SiO2 tetrahedra bonded to sheets of Al_2O_3 octahedra that are continuous in the *a* and *b* directions and stacked one above the other in the *c* direction. Figure 3-1. shows the component structure of Kaolinite.

Wyoming bentonite is composed primarily of sodium montmorillonite. The term is usually reserved for hydrous aluminum silicates approximately represented by the formula: $4SiO_2.Al_2O_3.2H_2O$+water; but with some of the aluminum cations, AL^{3+}, being displaced by magnesium cations, Mg^{2+}. This replacement of Al^{3+} by Mg^{2+} causes the montmorillonite structure to have an excess of electrons. This negative charge is satisfied by loosely held cations from the associated water. The name sodium montmorillonite refers to a clay minerals in which the loosely held cation is the Na^+ ion.[16] As seen in Fig. 3-2, the sodium bentonite has a 2:1 expanding crystal lattice. It consists of superimposed layers composed of two Si-O tetrahedral sheets framing an AL-O-OH octahedral sheet. The structure of bentonite is due to the isomorphic substitution of Si and Al in the crystalline lattice with cations of lower valence.[17] In aqueous dispersion, water can penetrate into the infra-layer space, causing swelling of bentonite. The result of the swelling process is a dispersion of colloidal, plate-shaped particles bearing two clearly differentiated interfaces[18]: the faces, which are always negatively charged and neutralized by a layer of mobile and exchangeable cations (usually Na+), and the edges, which constitute ~5% of total surface area and carry a positive, negative or neutral charge as a function of pH, ions in solution, etc.

Calcite and dolomite are carbonate minerals with similar structures. Calcite is formed by alternate layers of calcium ions and carbonate ion groups. Dolomite is composed of alternate layers of calcium ions, magnesium ions, and carbonate ions. Both solids are salt type minerals; therefore, the solubility in water is higher than for oxides and silicates.

Experiment Methods. CLS adsorption mass onto these five minerals was measured by the static experiment method. Static adsorption isotherms are obtained by measuring depletion in solute concentration after equilibrating solutions of known initial concentration with weighed quantities of the dry solids. In our experiments, a 12 ml solution at the desired CLS concentration was

pipetted into the bottle. The bottle was kept in a thermostatic shaker bath to allow the solution to equilibrate at the chosen temperature. A 4 g sample of bentonite or crushed core was then added to the bottle, which was shaken by hand vigorously for about half a minute. The samples were shaken in the thermostatic shaker bath for 24 hrs and then left undisturbed for another 48 hrs. Following equilibration, these samples were centrifuged at 2000 rpm for 20 min, and the supernatant solutions were separated by decantation from the vial of the solids after gravity sedimentation. At the same time, each individual stock solution was also analyzed for the initial lignosulfonate concentration. The concentration difference between the stock and the sample was used to evaluate the adsorption mass. Figure 3-3 shows the schematic diagram of the static experiment.

Results and Discussion

Adsorption Isotherm of CLS on Five Minerals. All adsorption isotherm experiments were carried out at 30ºC, and all CLS solutions were prepared by 2 wt% brine. The adsorption isotherm of CLS on bentonite is shown in Fig. 3-4. Compared with a typical adsorption isotherm curve,[8] which exhibits four identifiable regions, the adsorption isotherm can be classified into three regions.

Region I corresponds to low surface coverage by adsorbed lignosulfonate monomers. In this region, also known as the Henry's law region, there is a linear relationship between the lignosulfonate equilibrium concentration and adsorption density. The mechanism responsible for its adsorption is mainly the electrostatic attraction between the charged surface of the solid and the charged head group of the lignosulfonate molecular.

Region II is characterized by a sharp increase in the adsorption due to the formation of aggregates on the solid surface. Since the surface is heterogeneous, aggregation first takes place on the most energetic sites of the surface, resulting in formation of local monolayer or bilayer aggregates in patches on the surface. Hydrophobic bonding between the lignosulfonate tail groups makes a significant contribution to the aggregation phenomenon in this region. In Region III, the forces influencing adsorption are the same as those in Region II; the Region II/Region III transition is identified by a decrease in the slope of the adsorption isotherm and may be either

distinct or gradual, The slope of the isotherm is less in Region III because the remaining surface patches are less attractive than those covered in region II and, also, aggregate-aggregate interactions are becoming more prominent. Region IV, which begins at the CMC of the surfactant, does not appear in this CLS isotherm curve because the designed maximum lignosulfonate concentration is lower the than the CMC of CLS.

Figure 3-5 comprises the adsorption isotherms of CLS onto five minerals. CLS adsorption density onto silica is essentially zero. The order of CLS adsorption at equal concentrations onto these five minerals is: bentonite>kaolin>dolomite>calcium>silica. The differences depend on mineral composition and surface area.

Effect of Brine Salinity and Divalent Ion Content. Adsorption of EOR surfactants has generally been found to increase with increasing salt concentration and increasing divalent ion content. In some systems, however, only a small dependence of adsorption on salt concentration has been found, and some studies have indicated that inorganic monovalent ions may lower surfactant adsorption by competing with the surfactant for the surface or by shielding the surface charge on the solids.[4]

The effect of brine salinity and divalent cations on CLS adsorption onto kaolin is shown in Fig. 3-6, which provides a comparison of adsorption levels of different brine concentration and divalent contents. The adsorption in different concentrations of brine with the same salt ratio shows an increase of CLS adsorption on kaolin clay with an increase in brine concentration, but the slope of increase slows with increasing brine concentration. For equal CLS concentrations, a solution prepared with divalent salt had a higher adsorption density. Figure 3-7 presents the results of CLS adsorption on five minerals. For silica, CLS adsorption density is essentially zero. For the other four systems, the effect of brine concentration has a similar trend for same salt solution. CLS adsorption on calcite and dolomite, prepared in 2 wt% $CaCl_2$ brine is higher or almost the same as that prepared in a 10% NaCl brine solution. This indicates that divalent ions have a stronger effect on CLS adsorption.

The effect of salts on CLS adsorption has been attributed to several mechanisms. An increase in salt concentration may increase CLS adsorption by decreasing the solvent power of the aqueous phase for CLS, thus driving the CLS to the interface, or by decreasing headgroup-headgroup electrostatic repulsion in the adsorbed layer. Increasing the electrolyte concentration compresses the electric double layer, the resulting change in adsorption depending on the sign of

the charges of the solid surface and CLS. While monovalent inorganic ions change the magnitude of the solid's surface charge by compression of the electric double layer without changing the sign of the charge, multivalent ions may specifically adsorb to a surface of opposite charge and reverse the sign of the surface charge. On the other hand, the presence of inorganic salts affects the CLS behaviors. CLS molecular tends to stretch in low salt concentration solution, but it becomes curly in high salt concentration.

Effect of Temperature. Figure 3-8 presents the effect of temperature on CLS adsorption onto bentonite clay at the condition with different brines. Increasing temperature will decrease CLS adsorption density onto bentonite for any solution prepared by different brine. Figure 3-9 presents adsorption results of CLS onto five minerals at 30ºC and 40ºC, which shows the same decreasing trend as Fig. 3-8. All these result further indicate physical adsorption is a principle mechanism controlling CLS adsorption on the studied minerals.

Effect of PH. Anionic polyelectrolytes are contained in CLS. In general, adsorption of this kind of ionic polymer is strongly dependent on solid surface charge. The surface charge mainly depends on solution pH and zero point of charge (pHzpc), where the total charge from the cations and anions at the surface is equal to zero. Above this pH the surface has a net negative charge; below it the surface charge is positive. Table 3-2 lists the pHzpc of the five minerals in fresh water.[19]

The adsorption of CLS on five minerals was also measured at 30ºC as a function of changing pH concentration. CLS solution concentration was 10,000mg/L. Figure 3-10 shows a comparison of results for the five systems. The adsorption of CLS onto all five minerals essentially stayed constant at pH below 7. But when pH was above 7, CLS adsorption density was higher than that at pH below 7 for silica, dolomite and calcite, and increased with increased pH for bentonite and kaolin clay. As the pH increased, bentonite and kaolinite surfaces became more negatively charged, and the adsorption of CLS with negative charge decreased.

Conclusions

Both the surfactant and rock type affect the adsorption density. To develop transport and sorption models and to better predict chemical requirement, adsorption density of pure components has been determined in Chapter 3 for five common reservoir rock minerals with varied parameters.

This information can be used for qualitative assessment of chemical requirements in reservoir flooding processes.

Based on a series of batch static adsorption experiments of calcium lignosulfonate onto five minerals common to reservoirs: silica, bentonite, kaolinite, dolomite and calcite, the following conclusions were drawn:

1. For silica, CLSX adsorption density was essentially zero at all tested conditions,
2. For the other four; adsorption:
    a. Increased with increasing concentration,
    b. Decreased with increasing temperature,
    c. Increased with increasing salinity and valence,
    d. At pH below 7–neutral for all systems; above 7–increased with increased pH for bentonite and kaolin clay, and decreased for increasing pH for calcite and dolomite.
3. The order of CLS adsorption density onto the five minerals is:

    bentonite >kaolinite>dolomite>calcite>silica

References

1. Tsau, J. S. and Heller, J.P.: "Evaluation of Surfactants for CO_2-Foam Mobility Control," paper SPE 24103 presented at the 1992 SPE Permian Basin Oil and Gas Recovery Conference, Midland, March 18–20.
2. M.I. Kuhlman, M.I., Lau, H.C., and Falls, A.H.: "Surfactant criteria for successful carbon dioxide foam in sandstone reservoirs", *SPERE*, Feb, 2000.
3. Grigg, R.B., Tsau, J-S., and Martin, F.D.: "Cost Reduction and Injectivity Improvement for CO_2 Foam for Mobility Control," paper SPE 75178, presented at the 2002 SPE/DOE Improved Oil Recovery Symposium, Tulsa, April 13–17.
4. Mannhardt, K., Schramm, L.L., and Novosad, J.J.: "Effect of Rock Type and Brine Composition on Adsorption of Two Foam-Surfactants," paper SPE 20463 presented at the 1990 SPE Annual Technical Conference and Exhibition New Orleans, Sept. 23–26.
5. Smith, D.H., *Surfactant-Based Mobility Control,* American Chemical Society, 1988.
6. Surkalo, H. and Pouska, G.: "Analysis of Reservoir Pretreatment in Chemical Flooding: a Literature Review," Dept. of Energy Report No. DOE/BC/10027-11, 1980.

7. Surkalo, H. and Pouska, G.: “Experimental Evaluation of Reservoir Pretreatment in Chemical Flooding,” Dept. of Energy Report No. DOE/BC/10072-12, Feb 1981.
8. Tabatabai, A.: “Reducing Surfactant Adsorption on Carbonate Reservoirs,” *SPERE* (May 1993) 117–122.
9. Kalfoglou, G., Prieditis, J. and Paulette, G.S.: “Sacrificial Agents for Carbon Dioxide Foaming Agents,” Canadian Patent 2,185,499.
10. Hong, S. A., and Bae, J. H.: “Field Experiment of Lignosulfonate Preflushing for Surfactant Adsorption Reduction,” *SPERE*, 11,467-474 (1990).
11. Hong, S. A., et al.: “An Evaluation of Lignosulfonate as a Sacrificial Adsorbate in Surfactant Flooding,” *SPERE*, 1987, 17-27(1987).
12. Tsau, J.S., Syahputra, A. E, Yaghoobi, H., and Grigg, B.R.: “Use of Sacrificial Agents in CO_2 Foam Flooding Application,” paper SPE 56609 presented at the 1999 SPE Annual Technical Conference and Exhibition, Houston, October 3–6.
13. Syahputra, A.E., Tsau, J.S. and Grigg, R.B.: “Laboratory Evaluation of Using Lignosulfonate and Surfactant Mixture in CO_2 Flooding,” paper SPE 59368 presented at the 2000 SPE/DOE Improved Oil Recovery Symposium, Tulsa, April 3–5.
14. Tsau, J.S., Syahputra, A.E., and Grigg, R.B.: “Economic Evaluation of Surfactant Adsorption in CO_2 Foam Application,” paper SPE 59365 presented at the 2000 SPE/DOE Improved Oil Recovery Symposium, Tulsa, April 3–5.
15. Churcher, P.L. et al.: “Rock Properties of Berea Sandstone, Baker dolomite, and Indiana Limestone,” paper SPE 21044 presented at the SPE International Symposium on Oilfield Chemistry held in Anaheim, California, February 20-22, 1991.
16. Bourgoyne, A. et al.: *Applied Drilling Engineering*. SPE Textbook Series, 1986.
17. Van Olphen, H., *An Introduction to Clay Colloid Chemistry*, John Wiley & Sons, NY (1963) 57-82
18. Rabaioll, M.R. et al.: “Physical/Chemical Studies on the Surface Interactions of Bentonite with Polymetric Dispersing Agents,” paper SPE 25179 presented at the 1993 SPE International Symposium on Oilfield Chemistry, New Orleans, March 2-5.
19. Schramm, L. L: “Foams: Fundamentals and Applications in the Petroleum Industry,” American Chemistry Society, Washington, DC, 1994.

Table 3-1. Source and Main Composition of Five Minerals

Mineral	Source	chemical composition
Bentonite (Sodium Wyoming bentonite)	Wyo-Ben Incorporation	4SiO2·Al2O3·2H2O+water
Kaolin	Acro Organics, New Jersey	$Al_2Si_2O_5(OH)_4$ or $SiO_4 \cdot Al_2O_3 \cdot 2H_2O$
Silica (glass bead)	Mo-sci corporation	SiO_2
Calcite carbonate powder	Life extension foundation buyers club, Inc	$CaCO_3$
Dolomite powder	Naturaceutial Corp	$CaMg(CO_3)_2$

Table 3-2. The Isoelectric Point of Five Minerals

Minerals	**Isoelectric point (pHzpc)**
Silica	**2.9-3.0**
Bentonite	**<2-3**
Kaolinite	**2-4.6**
Dolomite	**7~9.5**
Calcite	**8-9**

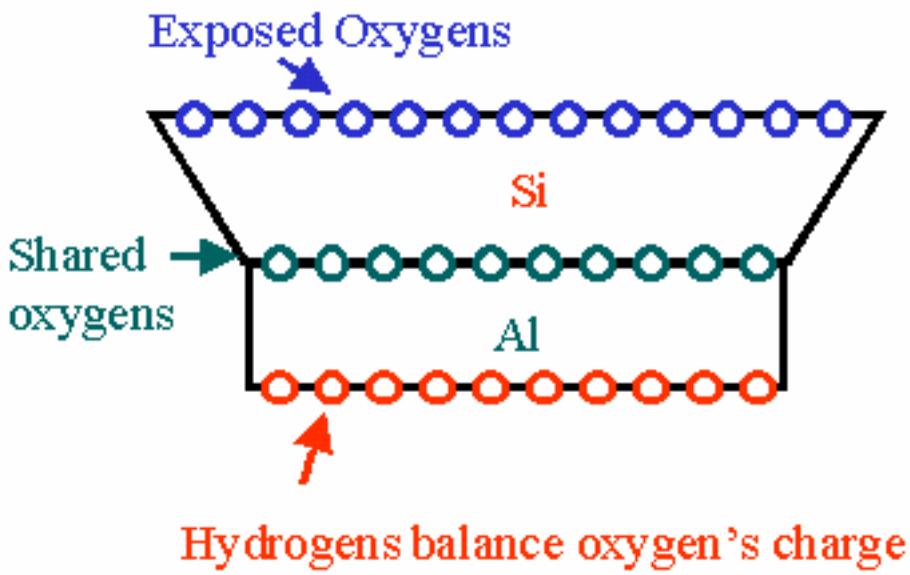

Fig. 3-1. Kaolinite structure.

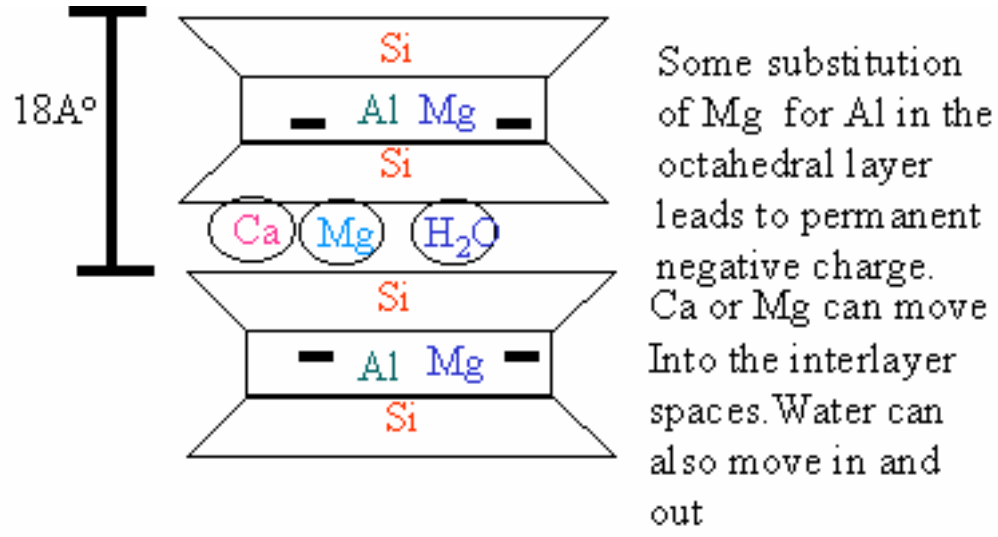

Fig. 3-2. Bentonite (montmorillonite) structures.

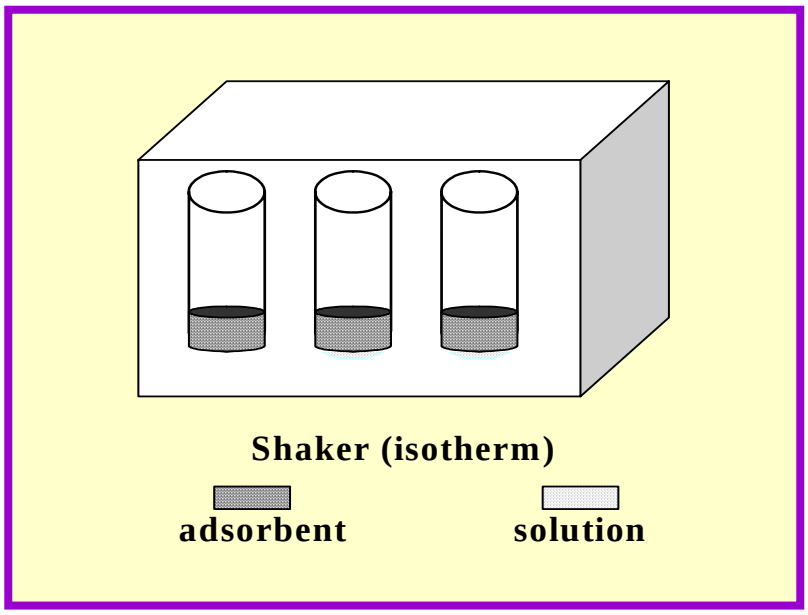

Fig. 3-3. Schematic diagram of static adsorption.

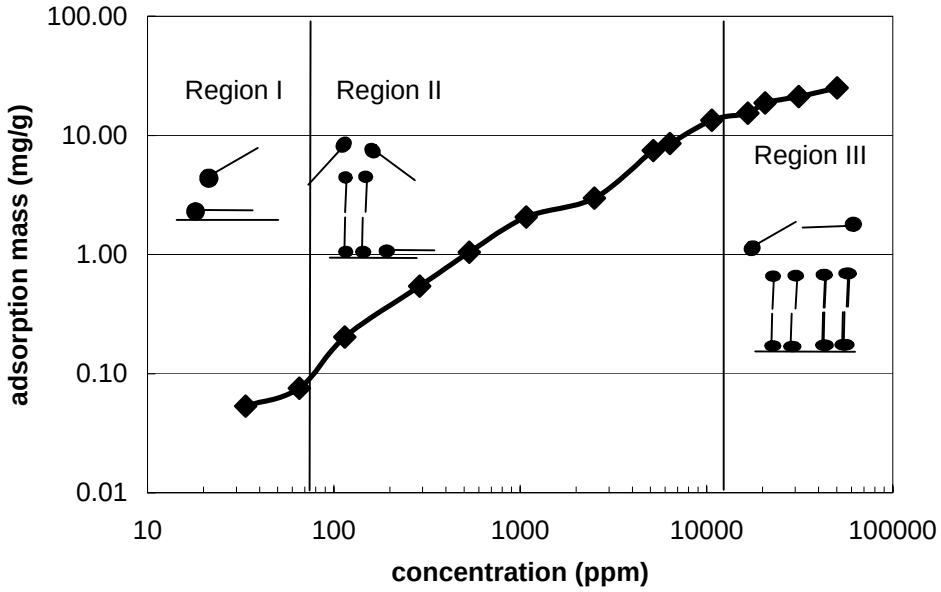

Fig. 3-4. Adsorption isotherm of CLS onto bentonite.

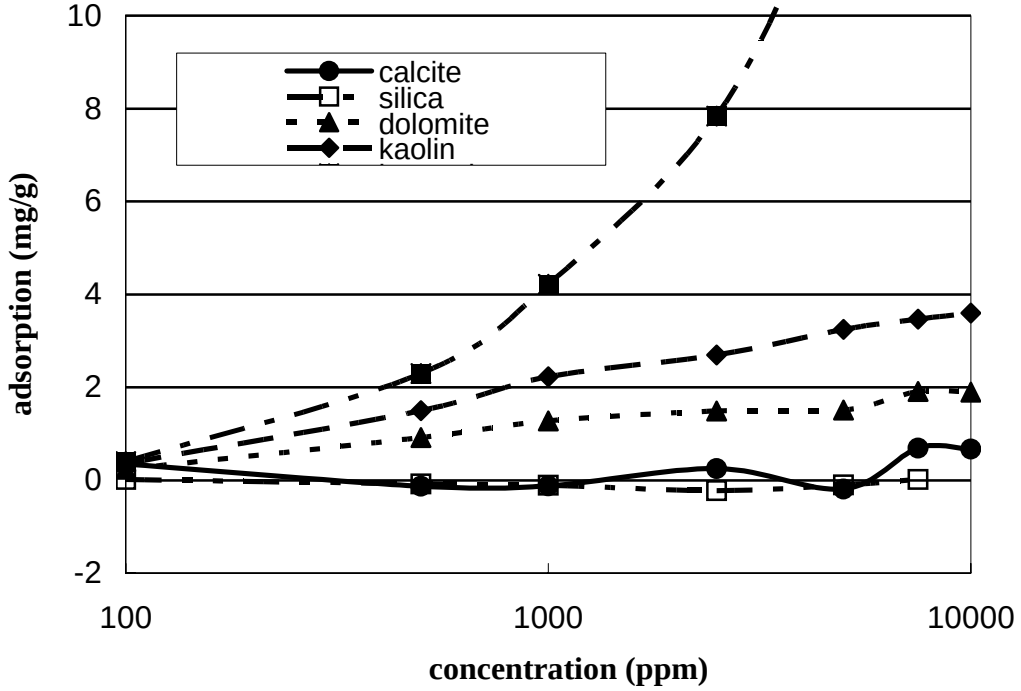

Fig. 3-5. Comparison of CLS adsorption on five minerals.

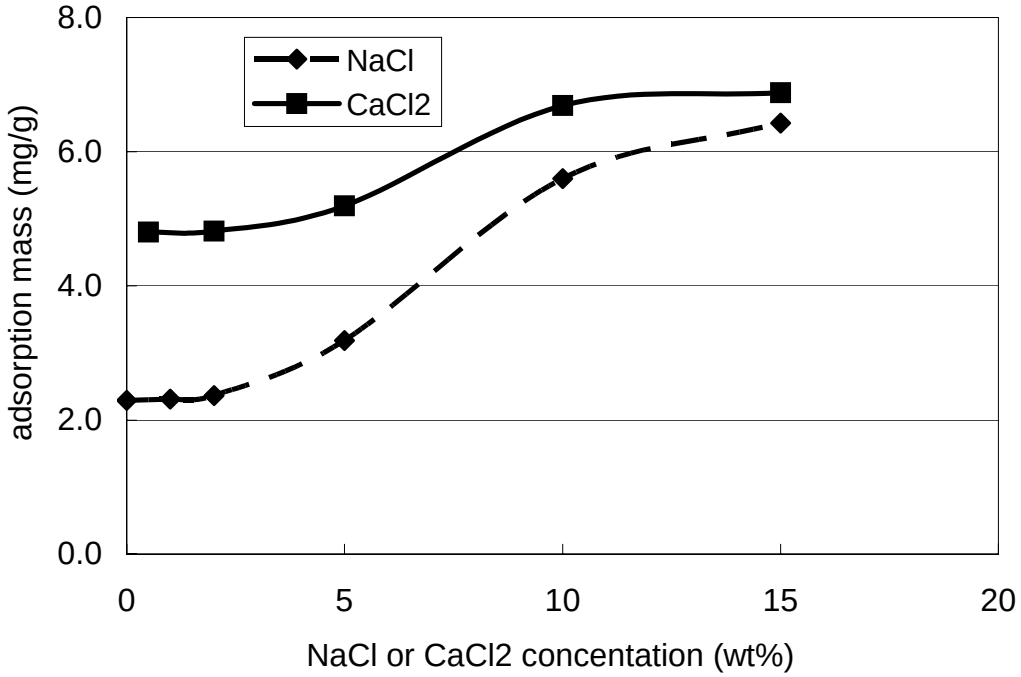

Fig. 3-6. Effect of NaCl and $CaCl_2$ concentration on adsorption (Kaolin, 30ºC).

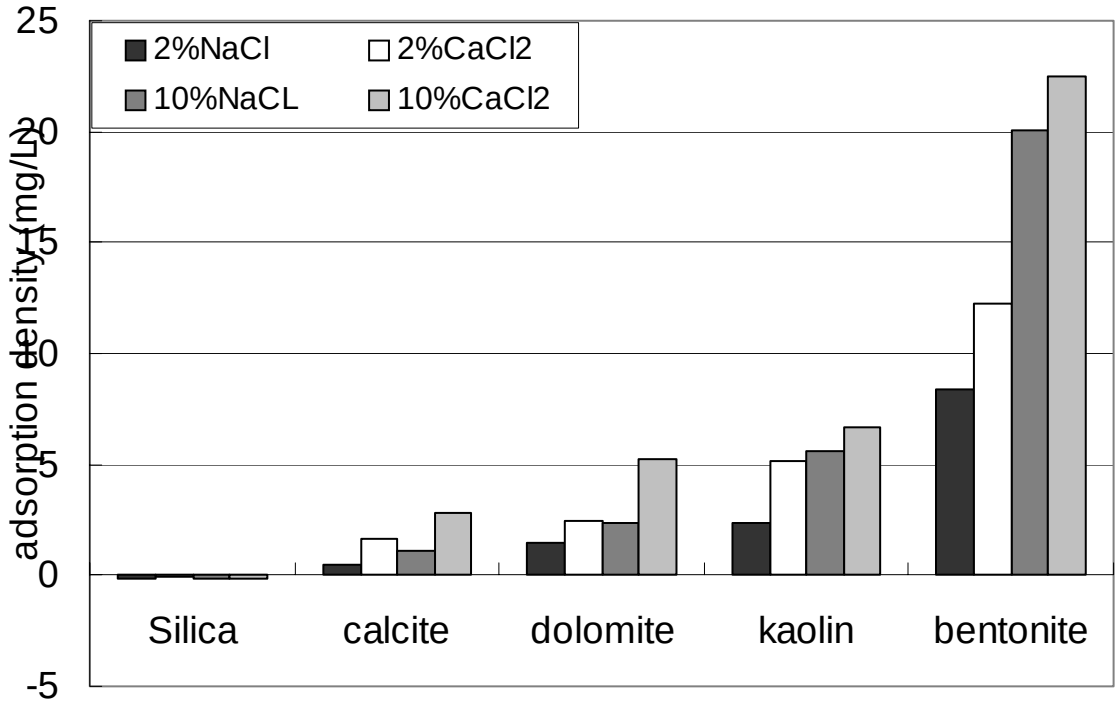

Fig. 3-7. Effect of brine on different adsorption system minerals
(10000 ppm CLS in 2%brine, 30ºC).

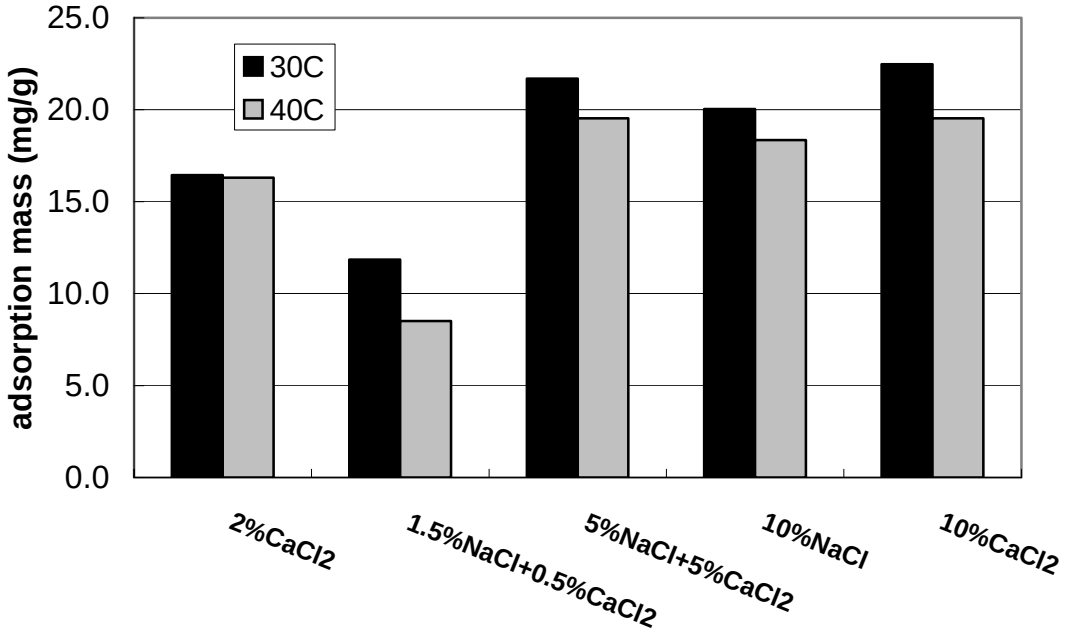

Fig. 3-8. Effect of temperature on CLS adsorption onto bentonite for different brine solution
(10000 ppm CLS).

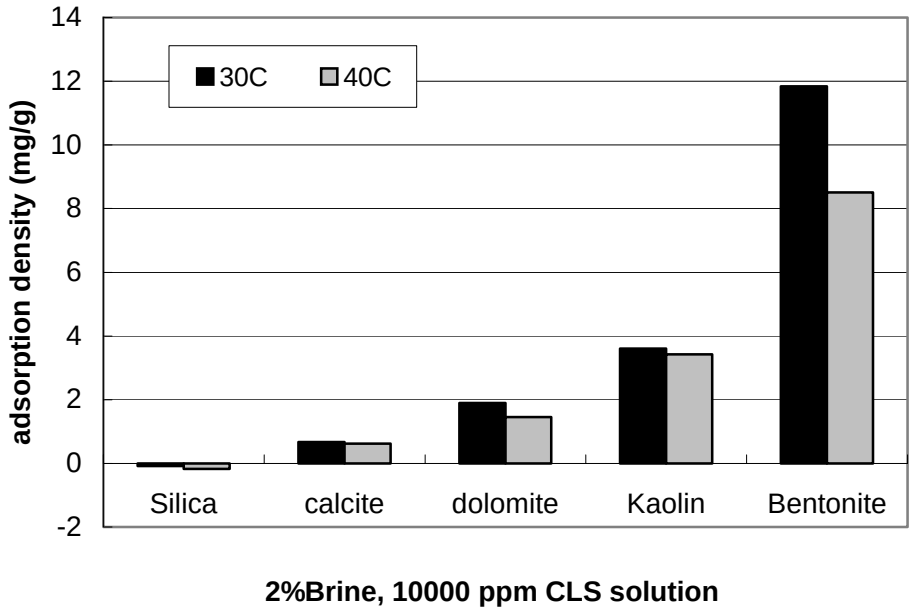

Fig. 3-9. Effect of temperature on CLS adsorption density onto five minerals.

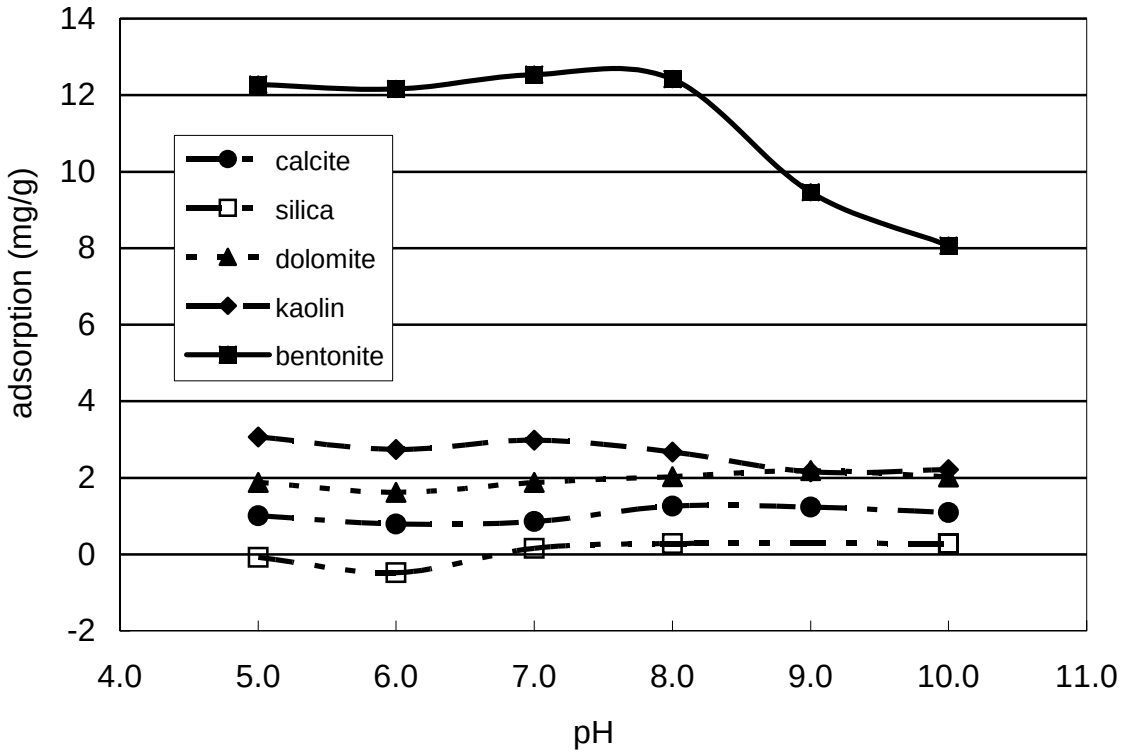

Fig. 3-10. Effect of pH on CLS adsorption for five adsorption systems.

CHAPTER 4. CO-INJECTED CO_2-BRINE INTERACTIONS WITH INDIANA LIMESTONE

Abstract

This chapter reports findings of coreflooding limestone with co-injected carbon dioxide (CO_2) and brine at reservoir pressure and temperature. Metal chlorides were added as tracer components to the injection brine and appeared in quantities well above natural levels in deposited carbonates. Core segment porosity and permeability were reported to indicate dissolution and deposition. Finally, the core was sectioned and analyzed by chemical and back-scattered electron imaging (BSEI) and chemical titration for compositional changes.

Porosity and permeability increased and decreased corresponding to suspected dissolution and precipitation. Qualitative and quantitative analyses confirmed the deposition of trace metals within deposited carbonate material, providing direct evidence of deposition. These phenomena can occur during CO_2 injection into carbonate geological formations, whether for improved oil recovery (IOR) or greenhouse gas sequestration. With IOR the concern is for injectivity changes, while the issues for sequestration are long-term storage capacity and seal integrity.

Introduction

Injectivity abnormalities in water-alternating-gas (WAG) IOR processes seem to mystify the petroleum industry [1]. A survey on CO_2 flooding indicated that loss of injectivity on WAG cycles is a crucial limiting factor in many projects[2]. Based on the fluid flow properties of CO_2, one intuitively expects gas injectivity to be greater than the waterflood brine injectivity[3]. However, in practice, this behavior is not always observed. Also, water injectivity during WAG cycles has been reported to be higher in some projects[4-8] and lower in other projects[9-12] than waterflood injectivity. It is perplexing that some reservoirs lose injectivity and others increase injectivity after the first slug of CO_2 is injected, and that this phenomenon may occur on a local or field-wide scale. Injection wells in the same field and reservoir may behave with significant difference. The change of injectivity has been investigated in the laboratory by several research groups with mixed results[6,13,14]. Change in rock properties due to fluid/rock interactions can account for some of the field injectivity behavior[15-18].

Following injection, some mineral or aqueous trapping may occur[19], transforming CO_2 into less mobile forms and possibly decreasing permeability in some areas of the reservoir, thus providing permanent sequestration. However, at least near the wellbore, as in-situ pH decreases and the water is undersaturated in many components such as carbonates, dissolution of the rock matrix is likely to occur, increasing permeability and thus fluid mobility. Inversely, deposition may occur as the fluid proceeds through the reservoir, which becomes saturated. Reservoir pressure subsequently decreases, reducing solubility in the brine. This can result in reduced permeability and CO_2 mobility. One motivation for this study is to gather information that can be used to calibrate and verify aspects of a new reactive transport model. This model and some of the preliminary results have been previously discussed in publications and presentations[20,21].

In earlier work quarried Indiana (Salem) limestone core was tested in order to investigate the relationship between WAG fluids and the formation rock[14]. Pressure transient data was collected from these cores for calculation of permeability and injectivity. Coreflooding was conducted in the WAG sequence at in-situ conditions. BSEI was performed on pre- and post-flood samples to detect changes in the cores. Macroscopic and microscopic dissolution features were observed in all cores exposed to WAG fluids. Carbonate dissolution caused changes in core permeability and porosity.

In the earlier study, carbonate deposition was indicated by permeability decreases downstream and suggested by the depositional structures seen using BSEI[14]. This is discussed in some detail in the earlier study, but results were not satisfactory because the compositions of the original rock and apparent deposits were essentially identical[14]. In the present study the brine has been modified with components that form carbonates and are found as trace impurities in limestone. These will aid in quantifying fluid-mineral interactions by providing a compositional contrast between the original rock and any new deposits.

Experimental

Indiana limestone, a bioclastic grainstone composed primarily (>99%) of calcite (calcium carbonates, $CaCO_3$), was used in the coreflood experiment. Figure 4-1 shows the structure of the limestone, where the calcite occurs as rounded grains, crystalline cement and overgrowths. Quartz and pyrite occur as very minor trace components. This rock has sufficient permeability and porosity for our laboratory measurements and is a compositionally simple carbonate rock.

The apparatus (shown in Fig. 4-2) used for the coreflooding experiments is similar to the one used in previous work[14]. Selected reservoir conditions were 100ºF and a minimum (core outlet) pressure of 2000 psig. These conditions, used in previous experiments, are similar to conditions in many Permian Basin Reservoirs[14]. Both are above the critical conditions of CO_2 and are in a pressure-temperature region where physical conditions do not change rapidly with respect to temperature or pressure, and physical parameters are similar to liquid CO_2.

The flooded core was a composite core composed of two sequential pieces of Indiana limestone, referred to as segment A and segment B. The fluid inlet was located on segment A, segments A and B were in direct contact, and the fluid outlet was located on segment B. To insure a good seal of the core sleeve and to force the two core segments into close contact an overburden (radial and axial) pressure of 4000 psig was maintained with an effective stress of about 2000 psi. No foreign material such as filter paper was placed between the two core segments to promote capillary contact because previous experience during corefloods of long duration saw contact material degrade and cause surface plugging. Also, dissolution at the segment juncture appeared to be continuous across the two core segments with no visual discontinuities due to the juncture.

Physical parameters of the core segments are listed in Table 4-1. The injection scheme was a constant ratio (1:1) brine with CO_2 co-injection. The initial combined flow rate was 80cc/hr (18.28ft/d), but was reduced to 40cc/hr (9.14ft/d). The cores were periodically cleaned with tetrahydrofuran and dried, then removed from the core holder for inspection and brine permeability and porosity measurements. Tetrahydrofuran is used for its properties that enable removal of both aqueous and hydrocarbon phases with one application without dissolution of inorganic core material. Finally, the core was reassembled into the same orientation, whole core brine permeability determined, and the co-injection of brine and CO_2 continued. The whole core brine permeability was also determined before the first co-injection.

The brine formula used in the experiment was composed of five salts, all chlorides, with composition as listed in Table 4-2. The brine total dissolved solids (tds) of 30,000 ppm was used with emphasis on selected trace metals: manganese (Mn), magnesium (Mg), and strontium (Sr). They are each known to occur in calcite as impurities (see fresh core analysis in Table 4-3). 30,000 ppm tds brine was selected to represent typical Permian Basin waterflood brine. The exact composition was 10,000 ppm sodium chloride (NaCl) with 5,000 ppm each of Ca, Mn, Mg, and Sr chlorides. These were selected to have equal concentration as a first attempt to test the

concept of trace metals in any carbonate precipitate. By BSEI and quantitative measurements the locations along the core that were enriched with respect to these elements could be identified. BSEI would allow us to identify the mode of deposition on the original rock matrix.

Results and Discussion

Core Flood Data Trends. Over the course of the experiment, 15.1 liters of each phase (brine and CO_2) were co-injected; the total volume of fluid co-injected was 30.2 liters. An additional 5 liters of brine was used in single-phase injection during CO_2 desaturation and brine permeability and porosity measurements. Since the original pore volume of the core totaled 195 cc, these yielded a total of 155 pore volumes (PV) of fluid co-injected.

Measurable changes occurred in the permeability and porosity of both core segments. Figure 4-3 shows the trend in core porosity. Note that both core segments show an initial decrease in porosity until about 55 PV injected, when porosity begins to increase. This interval corresponds to the injection of a combined rate of 80 cc/hr. The change was strongest in segment A, which was the upstream side of the composite core. The pore space of segment A was observed to decrease from 57.64 cc to 53.61 cc (-7.0%) during the first 55 PV of injection. During the same period the pore space of segment B decreased from 137.2 cc to 129.72 cc (-5.5%). During the next 100 PV of co-injection (55 PV to 155 PV), at a combined injection rate of 40 cc/hr, porosity was observed to increase in both core segments. Pore space in segment A increased substantially from 53.61 cc to 66.9 cc (+24.8%) and pore space in segment B increased modestly from 129.72 cc to 135.54 cc (+4.5%).

Core permeability to brine is shown in Fig. 4-4. Permeabilities of individual segments A and B were unavailable until midway through the experiment because of instrumental failures during the first interval of data acquisition. However, the whole core permeability decreased monotonically during the first half of the experiment. During the early part of the flood, while whole core permeability was decreasing, the formation of a solution channel was observed at the injection face during periodic visual inspection of the core. The solution channel is shown in Fig. 4-5. At 10 PV co-injected the core inlet surface on segment A was slightly roughened by dissolution of the co-injected fluids. When the core was inspected after 56 PV of co-injection a small solution channel had begun to form, apparently extending only several millimeters into the core. By 84 PV of co-injection a solution channel was clearly established, extending tortuously

into the core and out of view. Termination of the experiment was triggered by the very high permeability of 1978 md measured on segment A after 155 PV of co-injection.

Upon sectioning the flooded core the channel was found to extend nearly to the end of segment A. Figure 4-6 shows the longitudinally sectioned core segments. Flow direction is indicated on the figure by the arrows. The tortuous path of the solution channel is clearly visible in segment A. Near the end of the channel it appears to broaden and terminate into a region of solution enhanced porosity that extended to the end of segment A. On the adjacent face of segment B there also appears to be a region (highlighted by the oval) of solution-enhanced porosity. These two regions were in contact when the core segments were installed in the core holder during flooding. There are no visible solution or deposition features in the remainder of segment B.

The permeability plot (Fig 4-4) shows that the composite core and segment permeabilities during the mid-run times were decreasing while a solution channel (an intrinsically very high permeability feature) was progressing through segment A into the first of segment B (Fig 4-6). Therefore another process was taking place simultaneously, which was capable of reducing core permeability in part of the core while the process of dissolution was increasing permeability in another part. Factors that might have affected core permeability in this way are fines migration with pore plugging or occlusion of pores by the deposition of new mineral material. The introduction of any foreign external particles was prevented by filters (0.5 μ) at the core inlet.

Chemical and BSE Analysis. The sectioned core segments were sampled by removing 0.5 in. diameter core plugs at a point 1 cm from the inlet face and at regular 5 cm intervals thereafter to the outlet face of the core. Each core plug was cut in half, with one piece used for the chemical analysis and the other used for BSEI. Sample locations and core plugs are shown in Fig. 4-7. Chemical samples were pulverized to powder and dissolved in acid, then analyzed by the inductively coupled plasma–mass spectrometer (ICP-MS) method for Mg, Mn, and Sr. Samples were analyzed for Ca by EDTA titration. Fresh rock samples trimmed from the core segments before flooding were used to establish baseline rock properties. The results of the chemical analysis are presented in Table 4-3.

There is no significant trend in the Ca and Mg data. The data for Mn and Sr are plotted in Fig. 4-8. The Mn values are elevated up to 500 times above the baseline. The trend peaks at 15 cm and trails off toward the end of the core. This trend is also seen in the Sr data. The Sr peak is

about twice the baseline and also occurs at 15 cm and trails off toward the end of the core. In the case of Mn and Sr the peaks correspond, within sampling spatial resolution, to the final position of the solution channel, which had reached approximately 17 cm into the core at the end of the coreflooding experiment.

The post-flood chemical quantitative data obtained by BSEI is found in Table 4-4 and is presented with pre-flood composition data of original core using ICP-MS and BSEI methods. At several distances in the sectioned core the sample was surveyed and several point (10 to 20 micron diameter) measurements were averaged to obtain the table entry. The flooded core data is separated into two parts: those regions which appear identical with the original rock texture and those that appear to be newly deposited material by virtue of a significant contrast in atomic number (Z). As seen in the table, this contrast in Z is caused primarily by strong enrichment with respect to Mn and secondarily, Sr.

Referring back to Fig. 4-1, some grains in the pre-flood core show varying degrees of solution which apparently occurred sometime in the rock's history after the deposition of the calcite overgrowths. This is most easily seen where the grain has retreated from the adjacent smooth overgrowth boundary. Since these solution features are present in the pre-flood rock it is important not to confuse these diagenetic artifacts for diagnostic features in the post-flood images.

The distribution of the deposited material in the flooded core is shown in the BSEI images in Fig. 4-9. The images show a wide view (500 micron scale) of the rock matrix at several points along the flooded core, where the distances are measured from the injection face. The calcite grains and cement appear as grey, pore space is black, and the new Mn-rich deposits are white. The new deposits are scattered throughout the region and show a tendency to form at grain boundaries rather than on the cement walls in the larger pores. Deposits are also found within the porous grains. The abundance of Mn-rich deposits appears to follow the trend of the chemical data rather well, with a higher occurrence on the upstream side of the core and a decreasing abundance toward the core outlet.

Figure 4-10 shows a 200 micron overview and 20 micron inset image of the sample taken from 15 cm from the injection face. A Mn-rich deposit has filled in or replaced material at the boundary of the carbonate grain and cement. The deposit is coarsely crystalline and shows porosity that could be original to the mode of deposition or might be due to solution after deposition. BSE quantitative sample locations are indicated as points numbered 1 and 2. Data for

Ca, Mg, Mn, Sr are reported in the accompanying table as percent as carbonate. The very strong contrast in composition is most evident in the Ca and Mn. In the deposit Ca has dropped to 30% and Mn carbonate has increased to 68%.

Figure 4-11 shows a 200 micron overview and 20 micron inset image of the sample taken from 35 cm from the injection face. This deposit has formed on the calcite cement (grey) rather than a grain. It can be clearly seen that the deposit shows essentially the same euhedral growth structure that is evident in the cement. Also a zonation in the deposit due to a contrast in the Mn/Ca ratio during growth is distinctly visible. The inner areas with a higher Mn to Ca content appear brighter than the rims. Data for Ca, Mg, Mn, Sr are reported in the accompanying table as percent as carbonate. In the high Z zone of the deposit that was measured Ca has dropped to 35% and Mn carbonate has increased to 64%.

In an earlier paper,[14] we reported that dissolution could be seen on a macroscopic as well as microscopic scale. Deposits downstream were evident from decreased permeability and what appeared to be fresh deposits were viewed using BSEI. Suspected deposits with composition and structures similar to the original carbonates were therefore not diagnostic. The Mn and Sr carbonate are more and less soluble in brine, respectively, than is calcite. The purpose of the tracer components was to provide a compositional contrast to the original limestone in new deposits.

The porosity and permeability of the system decreased at first, and then increased above the original value by the end of the flood. For segment A the porosity and permeability became much higher by the end of the tests. A solution channel developed in segment A. The evolution of the solution channel entrance is shown in Fig. 4-5 at three different times during the test as a function of PV injected. This, with the increasing roughness at the injection surface, shows dissolution. The full extent of the dissolution was revealed when segments A and B were cut longitudinally after termination of the experiment (Fig. 4-6). The solution channel advanced most of the distance across segment A. The beginning of some apparent dissolution is seen near the injection face of segment B.

Results of BSEI identification in Table 4-4 show a contrast in core properties between pre-flood and post-flood states. Within the post-flood core are areas of original rock texture (no detectable alterations) and new deposits. In Fig.4-9 the new deposits show as white or high Z areas and the original rock (grain and cement) as grey. Mg and Ca concentrations in the new deposits were less than half the concentration in the original core. Mn concentrations increased

by at least three orders of magnitude and Sr increased 4–8 times in the new deposits. The apparent enrichment of the post-flood original rock texture with respect to Mn, seen in Table 4-4, may be caused by the sampling method when the BSI microscope was used in the quantitative mode. The instrument is capable of measuring composition in 20, 10, or 5 micron diameter circles that are chosen at certain coordinates on the sample as images are obtained. Many of the features of interest were little larger then the sampling area that could be used. Repeatability of the BSE coordinate system was a factor in several measurements, for instance when a measurement of the rock matrix returned less than 100% mass in the sample area it was obvious that the instrument had included some pore space. However, if the sample area inadvertently include some adjacent but contrasting grain this error is less obvious

An active area of deposition at the leading edge of the solution channel was indicated when simulating calcite dissolution and deposition using a transport-reactive model.[20,21] This corresponds to the measured Mn and Sr peaks in the vicinity of the termination of the solution channel, see Fig. 4-8 and Table 4-3. This is supported by the BSEI images, where the abundance of high Z deposits increases from the injection face, peaking at about 15 cm and then decreases to the end of the core system.

Using the 15 cm value for the deposit composition would yield a molar composition of about 66% Mn-carbonate, see Table 4-4. If the total composition at 15 cm is taken to be 8.9% Mn-carbonate, see Table 4-3, then the new deposit would represent about 13.5% of the total carbonates at this point in the core. If there had been no dissolution in this area this would indicate a reduction of porosity to about 6% of total volume from the original of about 17%. This is the most likely cause of permeability reduction across the core, even though major dissolution is occurring upstream in the core.

As discussed earlier, injectivity increases and decreases occur in field WAG projects. The dissolution and deposition seen in this study are possible mechanisms for these changes. An unanticipated aspect of this work is the discovery that significant deposition can be occurring in the vicinity of major dissolution. The scaling aspect of this work to the reservoir has not yet been considered. The processes occurring within centimeters may translate to tens of meters in the reservoir, dependent on the scaling of pressure and chemical gradients.

Conclusions

Injectivity losses in WAG have had a significant negative impact on major CO_2 injection projects. The results found in Chapter 4 demonstrate the extent and location of dissolution and precipitation of carbonates. This work indicates a probable cause for at least part of the permanent injectivity changes found in WAG operations. The metal tracers used in this work will provide the fundamentals for designing future laboratory tests to improve our understanding of these phenomena. Also, understanding these phenomena will aid in developing strategies to avoid and/or minimize the effects of dissolution/precipitation of carbonates. Listed below are specific conclusion that can be drawn from the work presented in this chapter:

1. Dissolution of carbonates at reservoir conditions during co-injection of CO_2 and brine was confirmed visually, and by porosity and permeability increases.
2. Deposition of carbonates was indicated by porosity and permeability reduction.
3. Deposition was determined by BSEI identification of high Z areas and reached a maximum near the end of the solution channel.
4. The composition of deposits was strongly influenced by the tracer brine composition.
5. Deposition and dissolution were found to occur in close proximity.

References

1. Rogers, J. D. and Grigg, R.B.: "A Literature Analysis of the WAG Injectivity Abnormalities in the CO_2 Process," *SPERE*, Oct. 2001, 375-386.
2. Grigg, R.B. and Schechter, D.S.: "State of the Industry in CO_2 Floods," paper SPE 38849 presented at the 1997 SPE ATCE, San Antonio, Oct. 6-9.
3. Hadlow, R.E.: "Update of Industry Experience with CO_2 Injection," paper SPE 24928 presented at the 1992 SPE ATCE, Washington D.C., Oct. 4-7.
4. Winzinger, R., *et al*.: "Design of a Major CO_2 Flood, North Ward Estes Field, Ward County, Texas," *SPERE* (Feb. 1991) 11.
5. Ring, J.N. and Smith, D.J.: "An Overview of the North Ward Estes CO_2 Flood," paper SPE 30729 presented at the 1995 SPE ATCE, Dallas, Oct. 22-25.

6. Prieditis, J., *et al.*: "A Laboratory and Field Injectivity Study: CO_2 WAG in the San Andres Formation of West Texas," paper SPE 22653 presented at the 1991 SPE ATCE, Dallas, Oct. 6-9.
7. Christman, P.G., and Gorell, S. B.: "A Comparison of Laboratory and Field-Observed CO_2 Tertiary Injectivity," paper SPE 17335 presented at the 1988 SPE/DOE Enhanced Oil Recovery Symposium, Tulsa, April 17-20.
8. Good, P.A. and Downer, D.G.: "Cedar Creek Anticline Carbon Dioxide Injectivity Test: Design, Implementation, and Analysis," paper SPE 17326 presented at the 1988 SPE/DOE Enhanced Oil Recovery Symposium, Tulsa, April 17-20.
9. Henry, R.L., *et al.*: "Utilization of Composition Observation Wells in a West Texas CO_2 Pilot Flood," paper SPE 9786 presented at the 1981 SPE/DOE Enhanced Oil Recovery Symposium, Tulsa, April 5-8.
10. Patel, P.D., *et al.*: "An Investigation of Unexpectedly Low Field-Observed Fluid Mobilities during Some CO_2 Tertiary Floods," paper SPE 14308 presented at the 1985 SPE ATCE, Las Vegas, Sept. 22-25.
11. Potter, G.F.: "The Effects of CO_2 Flooding on Wettability of West Texas Dolomitic Formations," paper SPE 16716 presented at the 1987 SPE ATCE, Dallas, Sept. 27-30.
12. Schneider, F.N., and Owens, W. W.: "Relative Permeability Studies of Gas-Water Flow Following Solvent Injection in Carbonate Rocks," *SPEJ* (Feb. 1976) 23.
13. Kamath J., *et al.*: "Laboratory Investigation of Injectivity Losses During WAG in West Texas Dolomites," paper SPE 39791 presented at the 1998 SPE Permian Basin Oil and Gas Recovery Conference, Midland, March 25-27.
14. Svec, R.K. and Grigg, R.B.: "Physical Effects of WAG Fluids on Carbonate Core Plugs," paper SPE 71496 presented at the 2001 SPE ATCE, New Orleans, Sept. 30–Oct. 3.
15. Ross, G.D., *et al.*: "The Dissolution Effects of CO_2-Brine Systems on the Permeability of U.K. and North Sea Calcareous Sandstones," paper SPE 10685 presented at the 1982 SPE/DOE Symposium on Enhanced Oil Recovery, Tulsa, April 4-7.
16. Mathis, R.L. and Sears, S.O.: "Effect of CO_2 Flooding on Dolomite Reservoir Rock, Denver Unit Wasson (San Andres) Field," paper SPE 13132 presented at the 1984 SPE ATCE, Houston, Sept. 16-19.
17. Sayegh, S.G., *et al.*: "Rock/Fluid Interactions of Carbonated Brines in a Sandstone Reservoir: Pembina Cardium, Alberta, Canada," *SPEFE* (Dec. 1990) 399.

18. Bowker, K.A. and Shuler, P.J.: “Carbon Dioxide Injection and Resultant Alteration of the Weber Sandstone, Rangely Field, Colorado,” The American Association of Petroleum Geologists Bulletin, V. 75, No. 9 (Sept. 1991) 1489.
19. Wawersik, R., W., *et al*.: “Terrestrial Sequestration of CO_2: An Assessment of Research Needs,” *Advances in Geophysics* **43,** (2001).
20. Wellman, T.P.: *Concatenation of Reactive Transport Model to Simulate CO_2 Sequestration in Geologic Media*, Thesis, New Mexico Institute of Mining and Technology, (2002).
21. Wellman, T.P, *et al*.: “Evaluation of CO_2-Brine-Reservoir Rock Interaction with Laboratory Flow Tests and Reactive Transport Modeling,” paper SPE 80228 presented at the 2003 SPE Oilfield Chemistry Symposium, Houston, Feb. 5-8.

Table 4-1. Initial Core Parameters

	D., cm	**L., cm**	**Por., %**	**PV, cc**
Seg.-A	5.03	17.15	16.91	57.6
Seg.-B	5.03	39.37	17.54	137.2
Core	5.03	56.52	17.35	194.8

Table 4-2. Brine Composition

Salt	**Conc(ppm)**	**Molar(M)**
NaCl	10000	0.1710
$CaCl_2$	5000	0.0450
$MnCl_2$	5000	0.0397
$MgCl_2$	5000	0.0525
$SrCl_2$	5000	0.0315

Table 4-3. Chemical Analysis (bulk core)

Pos. [cm]	*Mg [ppm]*	*Ca [ppm]*	*Mn [ppm]*	*Sr [ppm]*	**Pos. [cm]**	*Mg [ppm]*	*Ca [ppm]*	*Mn [ppm]*	*Sr [ppm]*
1	3000	399000	4800	380	**30**	4040	393000	5460	303
5	3390	390000	7370	299	**35**	4070	394000	5080	325
10	3530	389000	14700	353	**40**	3220	393000	3620	282
15	3620	388000	53100	523	**45**	3400	396150	4000	280
20	3470	391000	20800	367	**50**	3370	393000	3170	258
25	3480	400500	6760	307	**55**	3500	392500	3100	289

Table 4-4. Composition Results by Quantitative BSEI (points in the core)

State	Texture	Position [cm]	Mg [ppm]	Ca [ppm]	Mn [ppm]	Sr [ppm]	# of points	Method
Pre-flood	Original	NA	3053	391940	43	220	4	ICP-MS
Pre-flood	Original	NA	2364	396256	119	237	24	BSE
Post-flood	Original	5	1597	401479	82	211	4	BSE
Post-flood	Original	15	1953	401845	1393	109	7	BSE
Post-flood	Original	25	2717	393447	1279	235	14	BSE
Post-flood	Original	35	1591	404066	1354	101	3	BSE
Post-flood	Original	55	2926	397165	241	402	3	BSE
Post-flood	Deposit	5	1240	140821	302176	1721	3	BSE
Post-flood	Deposit	15	1096	119559	325784	1662	14	BSE
Post-flood	Deposit	25	951	97577	349775	1662	9	BSE
Post-flood	Deposit	35	721	105826	334769	1662	4	BSE
Post-flood	Deposit	55	1297	169289	224613	1424	4	BSE

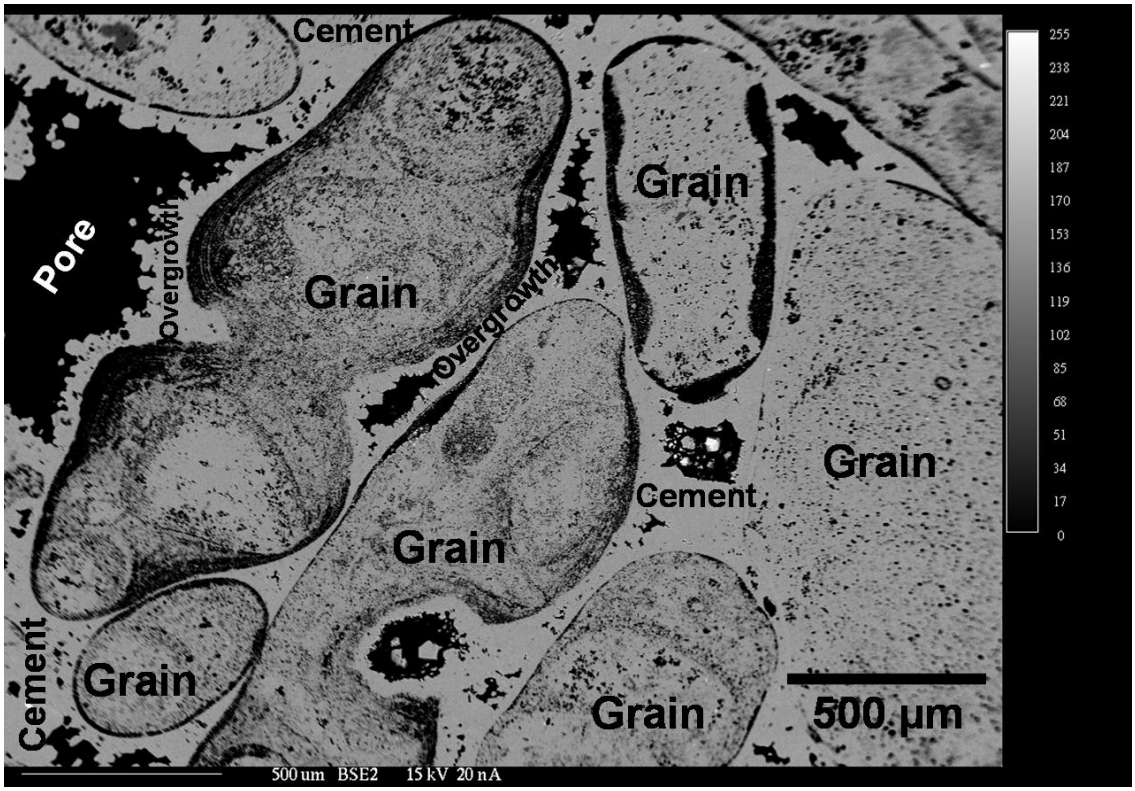

Fig. 4-1**.** Indiana limestone in the pre-flood state.

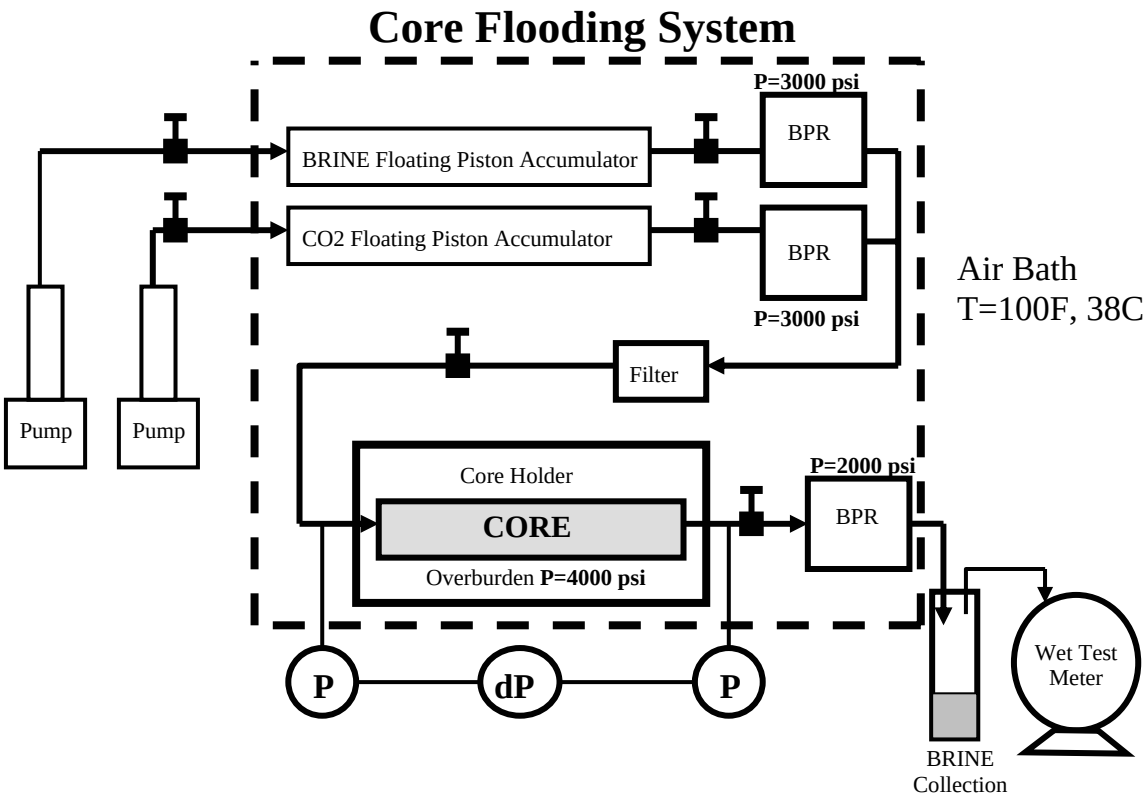

Fig. 4-2. The core flooding apparatus.

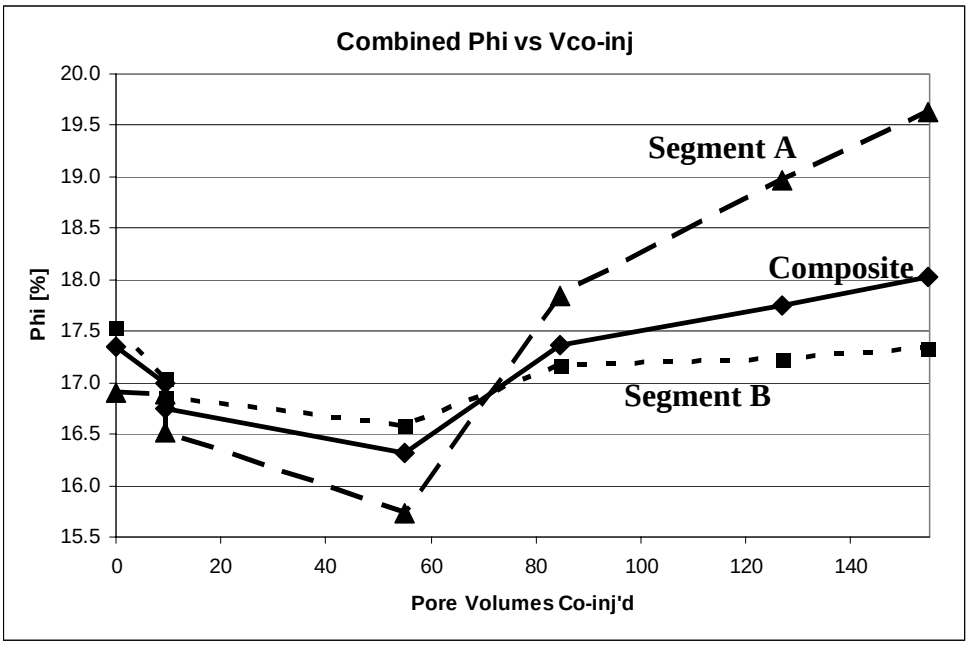

Fig. 4-3. Core porosity.

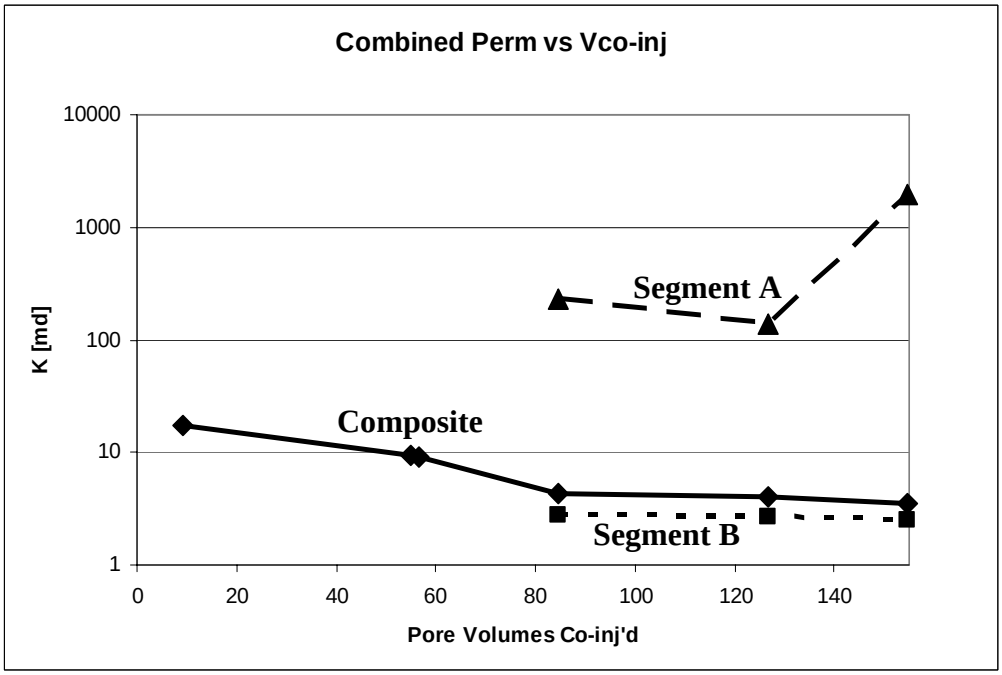

Fig. 4-4. Core permeability.

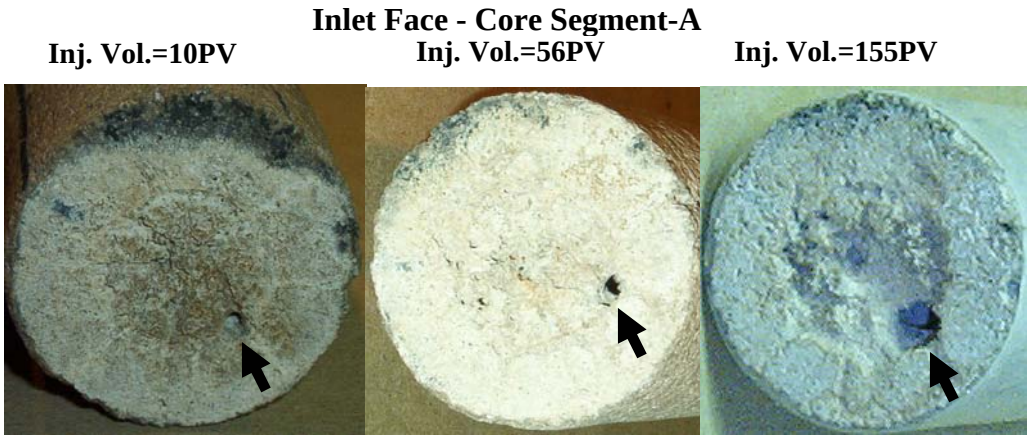

Fig. 4-5. Solution channel progress at the injection face vs. pore volumes injected.

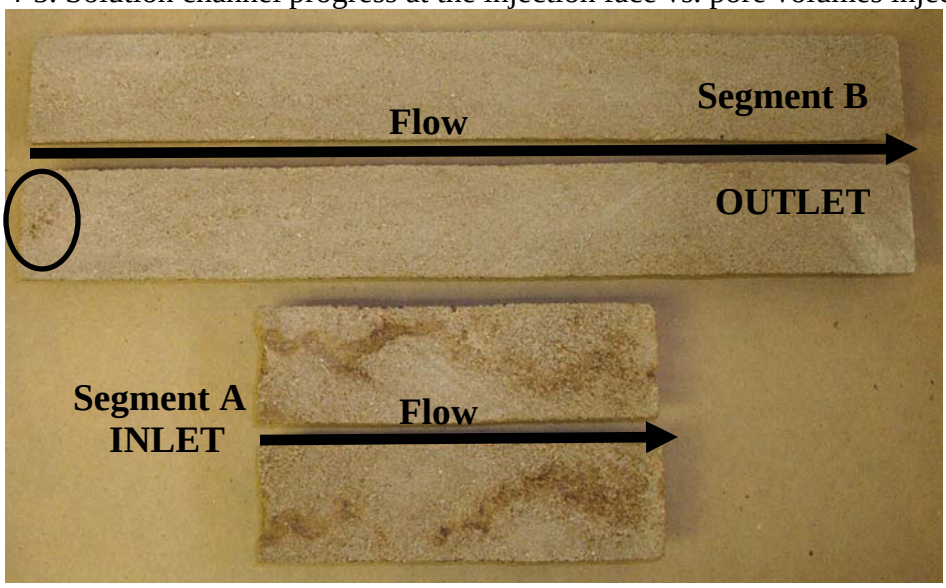

Fig. 4-6. Core segments cut in half longitudinally after the end of the flood.

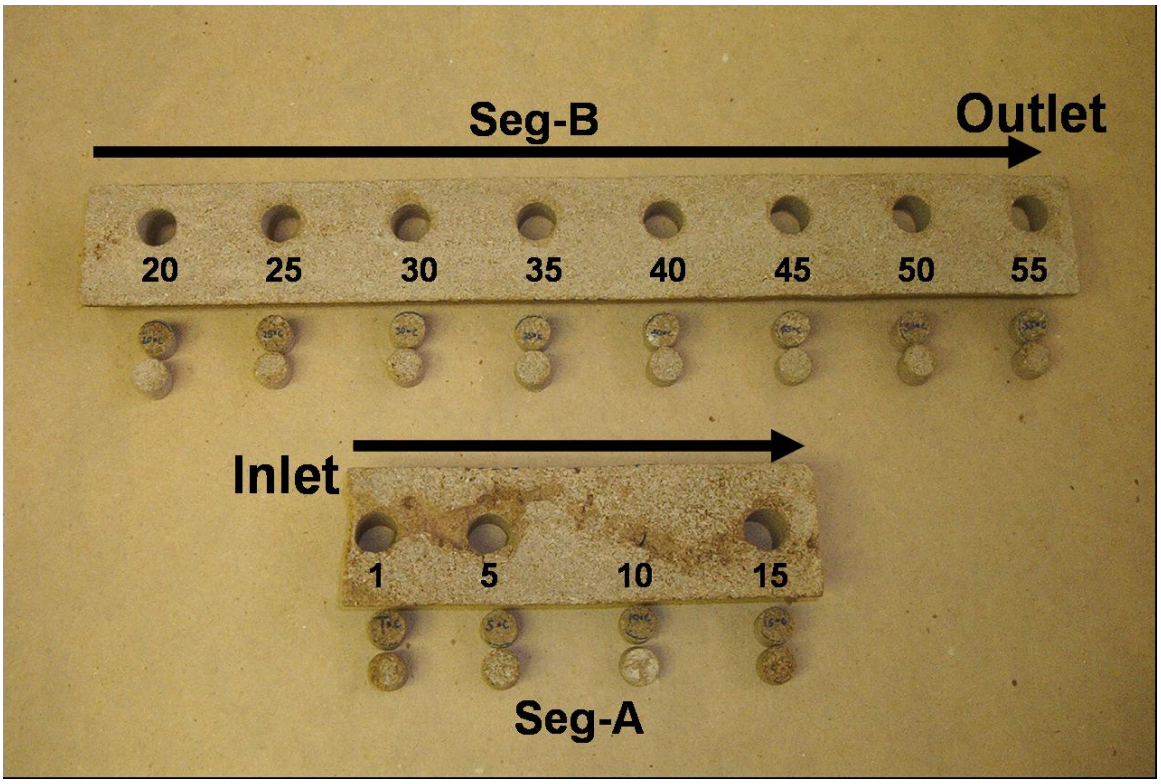

Fig. 4-7. Chemical and BSE core plug sample locations.

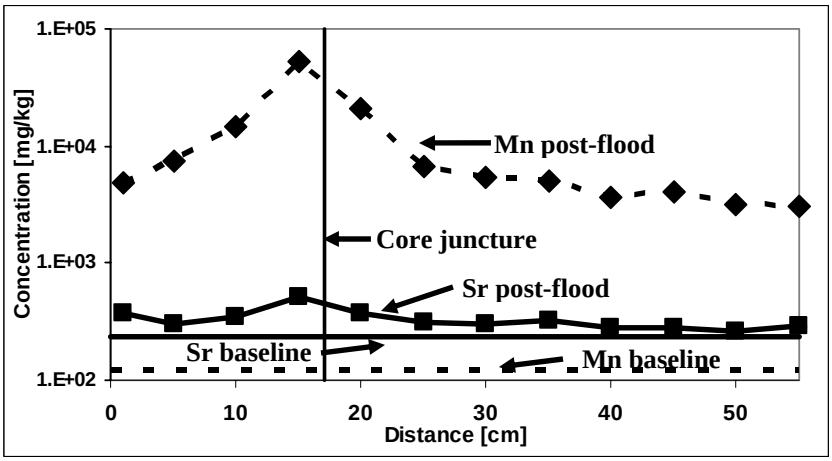

Fig. 4-8. Concentration of Mn. and Sr. along the length of the flooded core as determined by bulk chemical analysis.

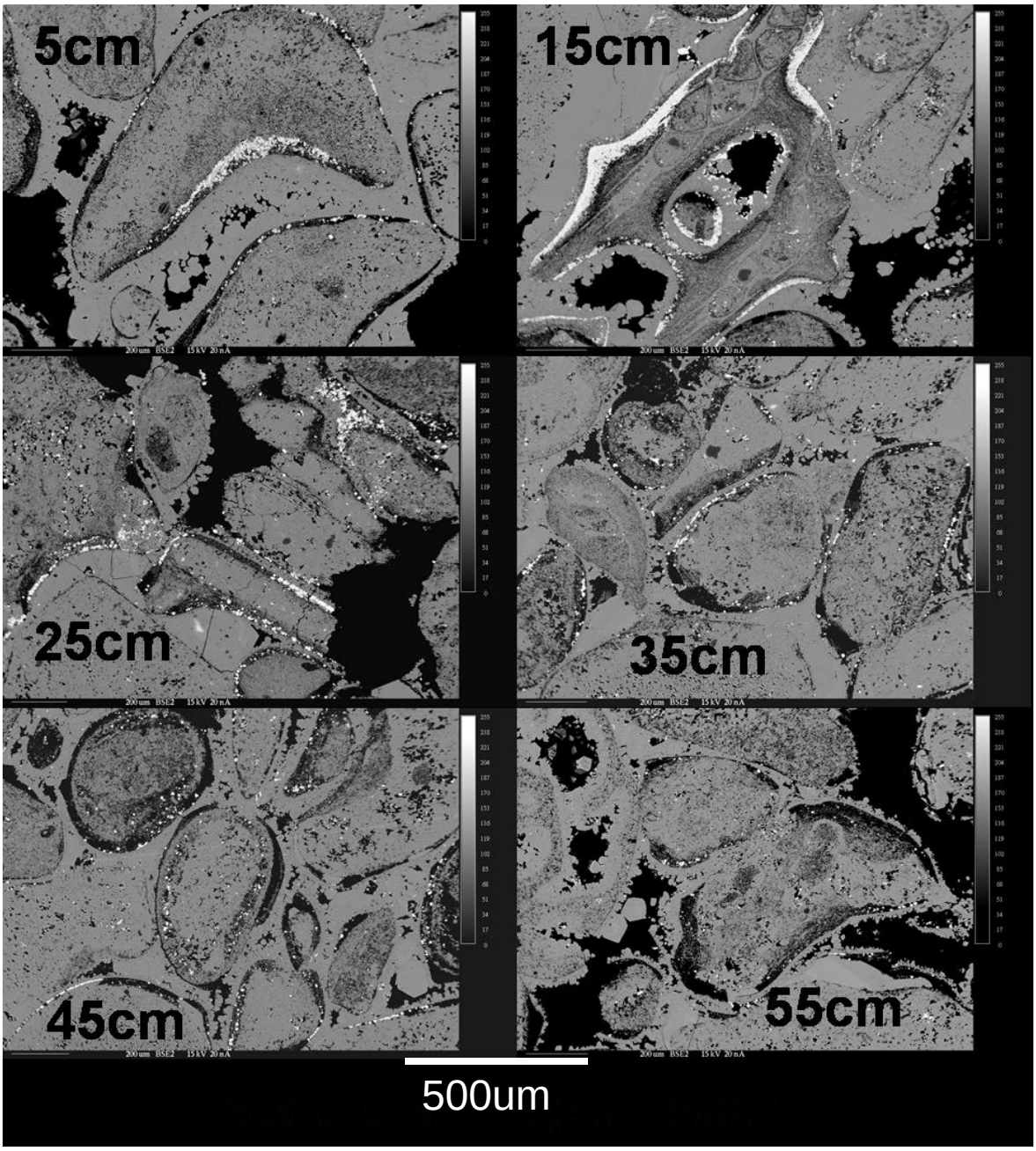

Fig. 4-9. BSE images at several points in the flooded core, all on the same 500 micron scale.

BSE Quantitative analysis [% as carbonate]

	Ca	Mg	Mn	Sr
1.	98.9	0.94	0.05	0.00
2.	30.5	0.47	68.6	0.26

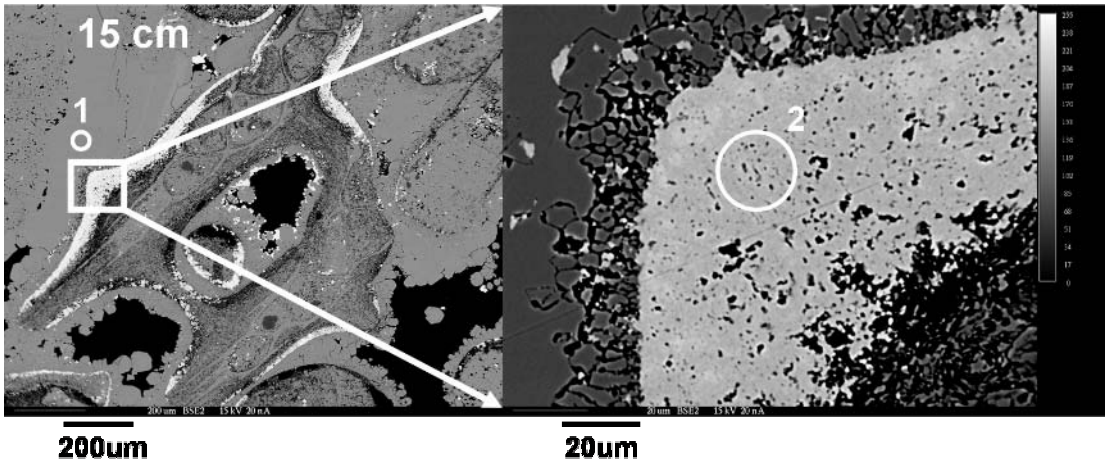

Fig. 4-10. New deposits at 15 cm into the flooded core.

BSE Quantitative analysis [% as carbonate]

	Ca	Mg	Mn	Sr
1.	98.7	0.65	0.62	0.00
2.	35.2	0.32	64.1	0.20

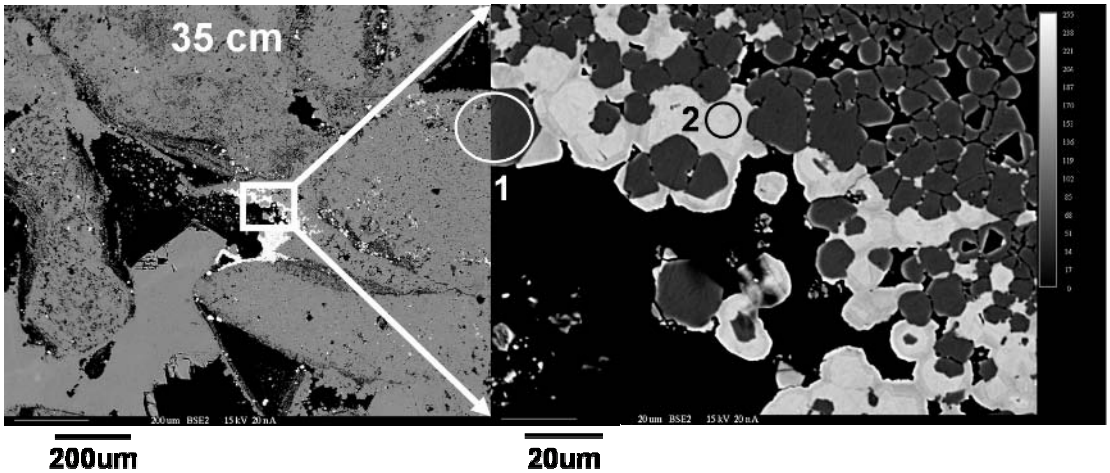

Fig. 4-11. New deposits at 35 cm into the flooded core.

CHAPTER 5. INJECTIVITY LOSS: FLOW RATE AND STRESS SENSITIVITY

Abstract

Water injection alternating with gas (*WAG*) is a routinely used technique for mobility control during CO_2 flooding. The WAG process often suffers more severe injectivity loss than expected. Knowing the mechanisms responsible for this WAG injectivity loss (*WAGIL*) is very important to improving CO_2 efficiency for recovering oil in heterogeneous reservoirs.

One of the several proposed mechanisms for WAGIL is the non-Darcy behavior at the near-wellbore region due to high flow rates. Numerical simulation and field observations have shown that non-Darcy behavior plays significant role on well performance in causing rapid pressure drop at the new-wellbore region. An accurate determination of non-Darcy flow parameters is critical to the accurate description and prediction of well performance. This requires to measure the parameters under restored reservoir flowing conditions, and to establish relationships to predict the variation of the parameters in corresponding to the change of reservoir pressures and in-situ stresses induced by petroleum activities such as production and injection.

This part of the projects focuses on (1) confirming the effects of non-Darcy flow behavior, (2) investigating the non-Darcy flow parameters of five representative rocks under varied reservoir conditions, and (3) developing equations to predict the change of these non-Darcy flow parameters under changed reservoir conditions. Along with solving these problems, related hardware and software have also been developed.In this work the experimental system has been upgraded, over two hundred test series using different rocks, several temperatures, several pore pressures, and overburden pressures each over a wide range of flow rates have been complete. The correlation or lack of between normal and shear stress with non-Darcy parameters are developed.

Introduction

WAG and WAGIL. Water injection alternating with gas (WAG) is a routinely used technique for mobility control during CO_2 flooding. The WAG process often suffers more severe injectivity loss than expected. The mechanisms responsible for this WAG injectivity loss (WAGIL) are not

clearly understood yet. One of the several proposed mechanisms for WAGIL is the non-Darcy behavior at the near-wellbore region due to the high flow rates**.**

Importance of Non-Darcy Behavior. Non-Darcy behavior has shown significant influence on well performance. Holditch and Morse[1] numerically investigated the non-Darcy effect on the effective fracture conductivity and gas well productivity. Their results show that non-Darcy flow can reduce the effective fracture conductivity at the near-wellbore region by a factor of 20 or more, and the gas production by 50%. Non-Darcy effect on hydraulically fractured wells was also confirmed by others.[2,3] Ewing et al investigated non-Darcy effects on production and injection well performance.[4] They found that non-Darcy effect is very important, especially for injection wells. For example, for a well with radius of 0.35 ft injection rate of 0.05 MM scf/day, the injection pressure at the wellbore would be 5263 psi for Darcy behavior ($\beta = 0$), and 7560 psi for non-Darcy behavior ($\beta = 5.61 \times 10^9$ cm^{-1}), a 44% increase. Papavassiliou presented the pressure difference between Darcy behavior and non-Darcy behavior at the near-wellbore region in an injection and production wells (Fig. 5-1).[5] He also presented the importance of an accurately determined non-Darcy flow coefficient to the proper description of the well performance (Fig. 5-2).

From these studies, it can be seen that non-Darcy behavior causes rapid change of pressure drop at the near-wellbore region, and an accurately determined non-Darcy flow coefficient is very important to the accurate description of the well performance.

Objectives. An accurate measurement of the non-Darcy flow coefficient must incorporate two important aspects of reservoir conditions. First, the non-Darcy parameters need to be measured under restored reservoir flowing conditions. Second, a relationship between the non-Darcy flow parameters and in-situ stresses is needed because production operations change the reservoir pressure, which in turn changes the in-situ stresses, and hence the non-Darcy flow parameters. The following are the objectives of this study:

- To select experimental conditions for laboratory measurement of non-Darcy parameters through survey of field CO_2 floods;
- To upgrade hardware for the laboratory measurement of the non-Darcy parameters;
- To develop a data processing method for this study;

- To measure the non-Darcy flow parameters of five different representative rocks under restored reservoir conditions;
- To investigate the flow-rate effect on non-Darcy flow parameters;
- To propose a criterion for the consideration of the non-Darcy effect;
- To establish effects of effective stresses on non-Darcy flow parameters for the five rocks under different temperatures.

Experimental

Non-Darcy behavior has been mentioned in many works on gas production.[6,7] Determination of the non-Darcy flow coefficient for different porous media has been attempted in the laboratory by many researchers.[8] Different correlations have been developed based on these experimental investigations.[9] However, no comparison has been made on how close these experiments were to the real field conditions. As a starting point, several field CO_2 project parameters have been surveyed for the proper selection of experimental parameters.

Selection of Experimental Parameters. *Depth and Temperature of Field CO_2 Projects:* In order to reflect the practical reservoir conditions, a statistical survey of 75 currently active CO_2 flooding projects was conducted based on data from a recent publication.[10] The percentage of the distribution of depth and temperature of these CO_2 projects has been analyzed. The results are shown in Figs. 5-3 and 5-4.

The results show that: (1) presently most (61%) of the CO_2 floods are found in formations at depths between 4000 and 6000 ft, with 5% in formations deeper than 10,000 ft; and (2) the majority (71%) of the CO_2 flooded formations have a temperature between 100 and 150ºF, with 5% over 200ºF.

In-Situ Stress Fields: One of the objectives of this project is to investigate the stress sensitivity of the non-Darcy flow parameters. An overview of the practical stress fields at the near-wellbore region would be helpful to the proper selection of stress conditions in the experimental design.

Conventionally, reservoir rock permeability and non-Darcy flow coefficient are measured under hydrostatic pressures. However, reservoir formation is usually under differential in-situ stresses, i.e., the vertical pressure (overburden pressure) is different from the horizontal stresses.

For example, assume a simple reservoir where no tectonic stresses exist and the formation property can be simplified as homogeneous, isotropic and elastic. At the depth, h, in such a reservoir formation, the overburden pressure, or total vertical in-situ stress, σ_z, and the total horizontal stresses, σ_H and σ_h, can be expressed as

$$\begin{cases} \sigma_v = \rho g h \\ \sigma_H = \sigma_h = \dfrac{\nu}{1-\nu}\sigma_v = \dfrac{\nu}{1-\nu}\rho g h \end{cases} \quad \text{..... (5-1)}$$

where ρ - rock density, g – acceleration of gravity, and ν – Poisson's ratio of the formation rock.

When there is fluid in the formation, part of the total stresses is supported by the fluid, and the effective stresses on the rock matrix is the total stress minus the fluid pressure. Assuming that the reservoir pressure is p_r at the specific depth, the effective stresses can be calculated as

$$\begin{cases} \sigma_v' = \rho g h - p_r \\ \sigma_H' = \sigma_h' = \dfrac{\nu}{1-\nu}\sigma_v' = \dfrac{\nu}{1-\nu}\left(\rho g h - p_r\right) \end{cases} \quad \text{..... (5-2)}$$

Because petrophysic properties of the formation matrix are affected by the effective stresses, not by the total stresses, Eq. (5-2) should be used in addressing the stress effect on permeability and non-Darcy flow coefficient.

If a vertical well is drilled in this formation, the effective stresses at the near-wellbore region are disturbed and redistributed. Assuming that the pressure in the wellbore is now p_w, the effective stresses calculated in Eq. (5-2) are now considered as far-field stresses, and the redistributed, effective stresses, σ_z, σ_r and σ_θ, at the near-wellbore region (Fig. 5-5), can be calculated as follows:[11]

$$\begin{cases} \sigma_z = \rho g h - p_w \\ \sigma_r = \sigma_h' - \left(\sigma_h' - p_w\right)\left(\dfrac{r_w}{r}\right)^2 \\ \sigma_\theta = \sigma_h' + \left(\sigma_h' - p_w\right)\left(\dfrac{r_w}{r}\right)^2 \end{cases} \quad \text{..... (5-3)}$$

For example, assuming an oil pay zone at 8000 ft depth with average reservoir pressure of 3500 psi and wellbore pressure of 1500 psi, the effective stresses at the near-wellbore region can be calculated using Eqs (5-1) through (5-3). Figure 5-6 shows the effective stresses at the near-wellbore region under three different wellbore pressures, 500, 1000 and 2000 psi.

From this example, it can be seen that, for a vertical well, (1) the vertical effective stress is always larger than the horizontal effective stresses; (2) the vertical effective stress does not change with the distance from the wellbore, but the horizontal stresses change rapidly at the vicinity of the wellbore, and converges to a constant value (average far-field horizontal effective stress) at a certain distance (about six times of the well radius) from the wellbore; (3) the lower the wellbore pressure is, the larger is the difference from the average far-field horizontal stress.

In addition, the in-situ stresses change with the reservoir activities: for example, production reduces reservoir pressure, which will increase effective in-situ stresses; for the same reason, injection of fluids into the reservoir will decrease the effective in-situ stresses.

Based on this study and the survey in the previous section, it can be seen that total in-situ stress of 2000 to 10000 psi would cover the in-situ stress range at the depth of most formations in the active CO_2 projects.

CO_2 Superficial Velocity: Calculation Procedures: The following steps were followed in the calculation of the superficial velocity of CO_2 in the field projects.

(1) Find pressure and temperature at the surface and at the near-wellbore region.
(2) Determine gas density at these locations.
(3) Find volumetric rate at surface.
(4) Find mass rate at surface.
(5) Find volumetric rate at wellbore.
(6) Calculate cross-sectional area at (a) the borehole, (b)1 ft away, and (c) 5 ft away.
(7) Determine superficial velocity at these locations.

Case 1 - Goldsmith Unit, Permian Basin:

Given:

Net pay =100 ft,

Depth = 4200 ft,

T = 94º–111ºF,

φ =11.6%,

k = 32 md,

ID = 7.875 in,

Injection rate Q_{sc} = 15 MM scf/d /100_ft/9_well

Find:

Superficial velocity at near-wellbore region

Solution:

(1) Pressure and temperature at the surface and near-wellbore regions

$P_{surface}$ = 1 atm = 14.7 psi

$P_{wellbore1}$ = 1200 psi (Assumed)

$P_{wellbore2}$ = 2000 psi (Assumed)

$T_{surface}$ = 60ºF

$T_{wellbore}$ = 102.5ºF

(2) Gas density at these locations

ρ (14.7 psi, 60ºF) = 0.1167 lb / cf

ρ (1200 psi, 102.5ºF) = 20.81 lb/ cf

ρ (2000 psi, 102.5ºF) = 45.44 lb / cf

(3) Volumetric rate at surface

Qsc = 15 MM scf/d/100_ft/9_well = 1.67 MM scf/d_well

(4) Mass rate at surface

W = ρ (14.7 psi, 60ºF) Qsc=0.1167 lb / cf * 1.67 MM scf/d_well=0.1949 MM lb/d_well

(5) Volumetric rate at wellbore

$Q_{wb1}=W/\rho_{wb1}$ = 0.1949 MM lb/d/20.81 lb/cf = 9366 cf/d

$Q_{wb2}=W/\rho_{wb2}$ = 0.1949 MM lb/d/45.44 lb/cf = 4289 cf/d

(6) Cross-sectional area at (a) the borehole, (b)1-ft away, and (c) 5-ft away

$A_{wb} = \pi Dh = 3.14 * (7.875/12) *100 = 206\ ft^2$

$A_{1ft} = \pi(D+2)h = 3.14 * (7.875/12+2) *100 = 834\ ft^2$

$A_{5ft} = \pi(D+10)h = 3.14 * (7.875/12+10) *100 = 3346\ ft^2$

(7) Superficial velocity at these locations

$V_{wb1} = Q_{wb1} / A_{wb} = 9366/206 = 45$ ft/d

$V_{wb2} = Q_{wb2} / A_{wb} = 4289/206 = 21$ ft/d

$V_{1ft\_1} = Q_{wb1} / A_{1ft} = 9366/834 = 11$ ft/d

$V_{1ft\_2} = Q_{wb2} / A_{1ft} = 4289/834 = 5$ ft/d

$V_{5ft\_1} = Q_{wb1} / A_{5ft} = 9366/3346 = 3$ ft/d

$V_{5ft\_2} = Q_{wb2} / A_{5ft} = 4289/3346 = 1$ ft/d

Case 2 - Central Vacuum, San Andrews:

Given:

Net pay =5 ~ 40 ft,

Gross = 600 ft,

Depth = 4200 ft,

T = 101º–105ºF,

φ =11.9%,

Injection rate:

$Q_{water\_1} = 3000$ bbl/d at $P_{surf\_inj\_1} = 1000$ psi

$Q_{water\_2} = 1700$ bbl/d at $P_{surf\_inj\_2} = 1500$ psi

$Q_{CO2} = 1 \sim 1.3\ Q_{water}$

ID = 7.875 in (assumed)

Find:

Superficial velocity at near-wellbore region

Solution:

(1) Pressure and temperature at the surface and near-wellbore regions

$P_{surface}$ = 1 atm = 14.7 psi

$T_{surface}$ = 60ºF

ρ (14.7 psi, 60ºF) = 0.1167 lb / cf

$P_{wellbore1}$ = 1200 psi (Assumed)

$P_{wellbore2}$ = 1500 psi (Assumed)

$P_{wellbore3}$ = 2000 psi (Assumed)

$T_{wellbore}$ = (101+105)/2 = 103ºF

(2) Gas density at these locations

ρ (14.7 psi, 60ºF) = 0.1167 lb / cf

$\rho_{surf\_inj\_1}$= ρ (1000 psi, 60ºF) = 50.72 lb/ cf

$\rho_{surf\_inj\_-2}$= ρ (1500 psi, 60ºF) = 54.67 lb/ cf

ρ_{wb1}= ρ (1200 psi, 103ºF) = 20.49 lb/ cf

ρ_{wb2}= ρ (1500 psi, 103ºF) = 37.34 lb / cf

ρ_{wb3}= ρ (2000 psi, 103ºF) = 45.27 lb / cf

(3) Volumetric rate at surface

$Q_{sc\_CO2\_surf}$ = 1.3 Q_{water_1}=3900 bbl/d *5.615 cf/bbl= 21899 scf/d

(4) Mass rate at surface

$W=\rho_{surf\_inj\_1} Q_{sc\_CO2\_surf}$ = 50.72 lb / cf * 21899 scf/d =$1.111*10^6$ lb/d

(5) Volumetric rate at wellbore

$Q_{wb1}=W/\rho_{wb1}$ = $1.111*10^6$ lb/d /20.49 lb/cf = 54222 cf/d

$Q_{wb2}=W/\rho_{wb2}$ = $1.111*10^6$ lb/d /37.34 lb/cf = 29754 cf/d

$Q_{wb3}=W/\rho_{wb3}$ = $1.111*10^6$ lb/d /45.27 lb/cf = 24542 cf/d

(6) Cross-sectional area at (a) the borehole, (b) 1-ft away, and (c) 5-ft away

$A_{wb} = \pi Dh$ = 3.14 * (7.875/12) *22.5 = 46.36 ft^2

$A_{1ft} = \pi(D+2)h$ = 3.14 * (7.875/12+2) *22.5 = 187.66 ft^2

$A_{5ft} = \pi(D+10)h = 3.14 * (7.875/12+10) *22.5 = 752.86\ ft^2$

(7) Superficial velocity at these locations

$V_{wb1} = Q_{wb1} / A_{wb} = 54222\ cf/d / 46.36\ ft^2 = 1170\ ft/d$

$V_{wb2} = Q_{wb2} / A_{wb} = 29754 / 46.36 = 642\ ft/d$

$V_{wb3} = Q_{wb3} / A_{wb} = 24542 / 46.36 = 529\ ft/d$

$V_{1ft\_1} = Q_{wb1} / A_{1ft\_1} = 54222\ cf/d / 187.66\ ft^2 = 289\ ft/d$

$V_{1ft\_2} = Q_{wb2} / A_{1ft\_1} = 29754 / 187.66 = 158\ ft/d$

$V_{1ft\_3} = Q_{wb3} / A_{1ft\_1} = 24542 / 187.66 = 131\ ft/d$

$V_{5ft\_1} = Q_{wb1} / A_{5ft\_1} = 54222\ cf/d / 752.86\ ft^2 = 72\ ft/d$

$V_{5ft\_2} = Q_{wb2} / A_{5ft\_1} = 29754\ cf/d / 752.86\ ft^2 = 40\ ft/d$

$V_{5ft\_3} = Q_{wb3} / A_{5ft\_1} = 24542\ cf/d / 752.86\ ft^2 = 32\ ft/d$

Case 3 - SACROC

Given:

Net pay = 166 ft

ID = 7.875 in (assumed)

Injection rate: Q_{CO2_surf} = 2~3 MMcf/d/well

Find:

Superficial velocity at near-wellbore region

Solution:

(1) Pressure and temperature at the surface and near-wellbore regions

$P_{surface}$ = 1 atm = 14.7 psi

$T_{surface}$ = 60ºF

ρ (14.7 psi, 60ºF)= 0.1167 lb / cf

$P_{wellbore1}$ = 1200 psi (Assumed)

$P_{wellbore2}$ = 1500 psi (Assumed)

$P_{wellbore3}$ = 2000 psi (Assumed)

$T_{wellbore}$ = 100ºF (Assumed)

(2) Gas density at these locations

ρ (14.7 psi, 60ºF) = 0.1167 lb / cf

ρ_{wb1}= ρ (1200 psi, 100ºF) = 22.94 lb/ cf

ρ_{wb2}= ρ (1500 psi, 100ºF) = 39.06 lb / cf

ρ_{wb3}= ρ (2000 psi, 100ºF) = 46.26 lb / cf

(3) Volumetric rate at surface

$Q_{sc\_CO2\_surf}$ = 2.5 MMscf /d

(4) Mass rate at surface

W=ρ (14.7 psi, 60ºF) $Q_{sc\_CO2\_surf}$ = 0.1167 lb / cf * 2.5 *10^6 scf/d =2.9175*10^5 lb/d

(5) Volumetric rate at wellbore

$Q_{wb1}=W/\rho_{wb1}$ = 2.9175*10^5 lb/d /22.94 lb/cf = 127180 cf/d

$Q_{wb2}=W/\rho_{wb2}$ = 2.9175*10^5 lb/d /39.06 lb/cf = 74693 cf/d

$Q_{wb3}=W/\rho_{wb3}$ = 2.9175*10^5 lb/d /46.26 lb/cf = 63067 cf/d

(6) Cross-sectional area at (a) the borehole, (b)1 ft away, and (c) 5 ft away

$A_{wb} = \pi Dh$ = 3.14 * (7.875/12) *166 = 342 ft^2

$A_{1ft} = \pi(D+2)h$ = 3.14 * (7.875/12+2) *166 = 1385 ft^2

$A_{5ft} = \pi(D+10)h$ = 3.14 * (7.875/12+10) *166 = 5554 ft^2

(7) Superficial velocity at these locations

$V_{wb1} = Q_{wb1}/ A_{wb}$=127180 cf/d /342 ft^2 = 372 ft/d

$V_{wb2} = Q_{wb2}/ A_{wb}$=74693/342 = 218 ft/d

$V_{wb3} = Q_{wb3}/ A_{wb}$=63067/342 = 184 ft/d

$V_{1ft\_1} = Q_{wb1}/ A_{1ft\_1}$=127180 cf/d /1385 ft^2 = 92 ft/d

$V_{1ft\_2} = Q_{wb2}/ A_{1ft\_1}$=74693/1385 = 54 ft/d

$V_{1ft\_3} = Q_{wb3}/ A_{1ft\_1}$=63067/1385 = 46 ft/d

$V_{5ft\_1} = Q_{wb1} / A_{5ft\_1} = 127180$ cf/d /5554 ft^2 = 23 ft/d

$V_{5ft\_2} = Q_{wb2} / A_{5ft\_1} = 74693/5554$ = 13 ft/d

$V_{5ft\_3} = Q_{wb3} / A_{5ft\_1} = 63067/5554$ = 11 ft/d

Summary. Superficial velocity of CO_2 in the three field cases are summarized in Table 5-1. During the calculation, the wellbore pressure has been assumed at a relatively high value. If that value is lower, the superficial velocity will be higher. Also, this work assumes uniform permeability. In many cases there are high permeability zones. For example in the Central Vacuum Field in New Mexico the average permeability is in the 20 to 25 mD range while the permeability in the pay zone can range from essentially zero to 500+mD. It is not uncommon for 90% of flow to be in 10% of the pay. Thus flow rates can be tenfold greater in the high permeability zones than those calculated in the previous section.

Selected Experimental Parameters. Based on the above survey and calculation with the consideration of existing laboratory facilities, the experimental conditions listed in Table 5-2 were examined.

Upgrade and Development of Experimental Facilities. In order to fulfill the project's research objectives with the experimental parameters listed in Table 5-2, a previous high pressure/high temperature gas flooding system was upgraded. The test apparatus was designed, assembled, and calibrated for determining permeability and non-Darcy flow coefficient under varying conditions of overburden pressures, temperatures, and flow rates. This equipment was designed to work at up to 10,000 psi working pressure and 200°F. A schematic of the system is shown in Fig. 5-7.

The equipment was assembled using high-pressure stainless steel tubing, fittings, accumulator, and pumps to ensure safe and sound performance of the equipment at elevated temperatures and pressures. All possible efforts were made to keep the system at a constant temperature. Most of the tubing was installed inside the constant temperature air bath; only a few inches of the tubing was outside the air bath. All valves were placed inside the hot air bath with their valve stems extending out to avoid effects of temperature variation on flow properties.

In this setup, one accumulator was used for gas (nitrogen, (N_2) or carbon dioxide, (CO_2)). The gas was equilibrated to air bath temperature. Nitrogen was used to charge dome pressures of inlet and outlet backpressure regulators (BPR_{in} and BPR_{out}) that were placed downstream of the ISCO piston pump and the core holder to regulate a constant mass flow and outlet pressure, respectively. A core holder assembly was placed between the two BPRs. The core holder was designed to hold a core sample of 1 in. in diameter and from 1 to 2 in. in length with provisions for triaxial loading of the sample.

A high-pressure positive displacement pump was used to obtain a desired axial and radial overburden pressure (up to 10,000 psi) independently on the core sample in the core holder. Distilled water was used as a confining fluid and a nitrile rubber sleeve separating it from the core sample. Because the end plugs were mobile, both axial and radial confining loads were simultaneously applied on the core, each from 0 to 10,000 psi.

The new system was superior to a previous apparatus because of better temperature control, increased percentage of plumbing that was placed within the constant temperature bath, and the insulation of the small volume of plumbing located outside the air bath. All efforts were made to keep the operating area inside the air bath free from obstacles to give more room for operational use. The equipment was tested and calibrated to the rated pressure to ensure safe operation.

Core Sample Preparation. *Sample Preparation:* Five different samples from three different rock types were prepared for the experiments. Prior to the installation of any core sample into the core holder, the core sample was ascertained to be free of any chips or cavities. Also, the core sample ends were trimmed to ensure a square end. This was important in order to prevent the extrusion of the sleeve into these cavities. Excessive extrusion causes the sleeve to rupture and fail. The extrusion problem becomes more critical at higher temperatures and pressures. Core samples approximately 1 in. in diameter and 2 in. long were prepared. First these core samples were placed in a coreholder and cleaned using tetrahydrofuran (THF) under a sufficient radial load to ensure that THF flowed through the core. Then these cores were removed from the coreholder and were baked at 150ºF in an oven for 24 hours to remove any residual water and THF. Table 5-3 lists the specifications of the core samples used for the experimental work.

Instructions for Use of Core Holder: TEMCO's RCHT-series core holder is a standard triaxial-type core holder, which is capable of independent radial and axial loading. The core sample is held within a nitrile rubber sleeve by confining or radial pressure. The radial pressure simulates reservoir overburden pressures. Independent axial pressure is applied by using an axial loading valve. Inlet and outlet valves allow fluids and gases to be injected through the core sample. All efforts should be made to keep flow lines and internal volumes to a minimum so that accurate flow data can be determined.

A unique feature of this core holder assembly is that a core sample can be replaced without completely disassembling the core holder. Simply by releasing the confining radial and axial pressure and unscrewing the end plug, a core sample can be removed easily without exposing it to the annulus fluid. It is important to release any pressure trapped inside the core to avoid damage to the rubber sleeve. This allows the core sample to be installed or removed easily during the experiment without exposing the assembly to ambient temperatures for long periods of time. This is helpful while performing temperature-sensitive experiments.

Core Assembly: The coreholder assembly was completely disassembled and all parts were cleaned with THF. O-rings were greased with standard O-ring grease and were installed as per the assembly drawings. (All parts are shown in the assembly drawing in Fig. 5-8.)

First, the triaxial end was installed. Next, the piston was installed in the cylinder and after that, the ferrule was installed in the cylinder. Three screws were installed into the cylinder until they bottomed out, and then were backed out for one or two turns. This was necessary to ensure that they did not contact the groove in the ferrule nor extend outside the cylinder. If screws are too far in or too far out, they can cause galling damage to the ferrule and/or to the sealing surface in the body.

The other ferrule end was installed into the cap. Three screws were installed into the end cap until they bottomed out. These screws were also backed out one or two turns. The rubber sleeve was installed around both ferrules. A small amount of grease around the ferrule's outer diameter helped in sliding the sleeve over the ferrule. Every precaution was taken to keep dust or metal chips from entering the coreholder assembly.

The sleeve and triaxial ferrule assembly was carefully installed into the core holder body. It is important not to over-torque the assembly since the o-ring makes the seal and over-tightening can make later removal more difficult. Then, the loading bar was assembled through

the sleeve and against the piston. Finally, the ferrule assembly was installed and the end cap was tightened until it was flush with the body.

To install a new core sample, the end cap was removed and a properly prepared core slid into the rubber sleeve. If the end cap is very tight, it is advisable to make sure that the pressure on the system is released. The core sample should make a firm contact with the distribution plug installed earlier. The ferrule inner diameter is slightly enlarged for effective sealing. Then the other distribution plug assembly was installed through the ferrule and against the core face. Finally, the other retainer was installed into the end cap and tightened. Both retainers were tightened equally until the core was firmly located between the distribution plugs.

Pressurization: Various tubes were connected for gas flow and to confine stress applications to the coreholder as shown in Fig. 5-7. Then the annulus around the sleeve was filled with water, using the low pressure, high discharge (LPHD) option of the positive displacement pump. It is necessary to observe pressure gauges carefully while filling water because the system will pressurize suddenly to a pressure that is too high. Distilled water was used as a confining fluid. Distilled water cannot be used at elevated temperatures, because steam formation will rapidly pressurize the system to very high pressure. In the event of a failure, the gas could be dangerous. Hydraulic oil is recommended for experiments at elevated temperatures.

Once the annulus was full, the axial chamber was pressurized first to approximately 500 psi. This eliminated any gap between the distribution plug and the core face, which could rupture the sleeve if axial pressure is applied first. Next, the annulus was pressurized, or radial stresses were applied. The radial overburden pressure should always be several hundred psi greater than the maximum flowing pressure to prevent leakage between the sleeve and distribution plug. Pressurization was continued until the desired pressure is achieved. Pressure was increased in 500-psi increments to check for leaks.

Care should be taken during de-pressurization; the operator must always reduce the pressure slowly and uniformly between the radial and axial loads to prevent any core damage because of uneven loading.

Porosity Measurement: Core porosity is an important parameter required for the proper analysis of the experimental work. A special attachment was fabricated and used to measure the porosity of the core samples. The test apparatus was initially flushed with THF and then flushed with nitrogen. The inlet and outlet BPR dome pressures were set to 2000 psi and 500 psi,

respectively. A calibration core was prepared from brass stock, and placed carefully in the coreholder. The assembly was then connected to the test apparatus. The calibration core was subjected to an initial pressure using nitrogen gas. All volumes were determined before the test. After stabilization, the source was disconnected and the valve to the air bottle of known volume was opened. Once the temperature was stabilized, the final pressure readings were taken. Using Boyle's law, the porosity of the brass calibration sample that had a hole and whose porosity was known was calculated. This process was repeated on all core samples to determine the porosity of each core sample, given in Table 5-3.

Completed Experiments. The test apparatus was initially flushed with THF and then dried with nitrogen. The inlet and outlet BPR dome pressures were set to desired pressures to represent field and bottomhole pressures, respectively. The core sample was placed carefully in the core holder, and the assembly was connected to the test apparatus. The core was first subjected to approximately 500 psi of axial pressure. Then it was subjected to similar radial load. This seated the core properly inside the coreholder. The core was then subjected to the pre-set axial and radial loads.

Flooding fluid was supplied through an ISCO pump, which was placed in the second controlled temperature system. The fluid was injected at a constant flow rate. Gradual flow of fluid into the core started as soon as the ISCO pump pressure approached the inlet BPR dome pressure. The outlet BPR dome pressure was set lower than the inlet pressure, and the flooding fluid was released to the atmosphere after passing through the outlet BPR. The complete test assembly was situated in a higher temperature air bath except for the ISCO pump, due to temperature limitations.

Experimental Procedure: After the core was installed and the core holder was ready, required axial and radial stresses were applied using a high-pressure pump. Sufficient time was allowed for the core holder assembly and core to reach the equilibrium temperature. An ISCO piston pump was used to receive and preheat the nitrogen in the low temperature air bath. Nitrogen was programmed to flow through the core from the piston at specific flow rate from 25 cc/hr to 10,000 cc/hr at a BPR of 2000 psi and 80ºF. Every experiment was performed at different flow rates. The nitrogen was released to the atmosphere after it passed through the outlet BPR.

Five temperature thermocouples were used to track the temperature and ensure isothermal process in the core holder. Thermocouples were placed at the inlet as well as the outlet of core assembly and temperatures were monitored throughout the experiment.

Tests Conducted: To accomplish the objectives of this study, 206 sets of experiments were performed at different combinations of temperature, in-situ stresses, and outlet pressures, using either N_2 or CO_2, as summarized in Table 5-4.

During each test, the temperature, the stresses and the BPR pressures were kept unchanged. The gas was flooded through the sample at different flow rate. At each flow rate, the flooding continued until the flow reached equilibrium. When flow equilibrium was reached, the pressure and temperature at the inlet and outlet of the sample and at the injection pump were measured. The pressure difference between the inlet and outlet of the sample was also measured for redundancy. During the flooding process, the temperatures at the heating coil of the inner bath, and in the middle of the coreholder were monitored to warrant the isothermal process. When the test of one flow rate was finished, the injection pump went to the next flow rate and pressures and temperatures were measured at the equilibrium under this new flow rate;. This process continued until all scheduled flow rates were competed.

When a series of scheduled flow rates were finished, the axial and radial stresses were changed to the next combination and the flooding test series started again, with flow rate from low to high. When all the planned combinations of axial and radial stresses were finished, the temperature was changed to the next stage. When a cycle of tests under different flow, pressure, and temperature conditions were finished, repeated tests were conducted at initial experimental conditions of the cycle, to check for hysteresis.

Theory and Methods for Data Processing

Overview of Darcy's Law. Non-Darcy behavior results from the inapplicability of Darcy's law. Thus, it is helpful to present an overview on Darcy's law.

Darcy's Law for Liquids: For liquid flow through porous media, Darcy's law has been widely used to describe the relationship between flow rate, pressure gradient, properties of the porous

media and the fluid. According to Darcy's law, the liquid flow rate is linearly proportional to the pressure gradient, as shown in Eq. (5-4).

$$q = \frac{kA}{\mu}\left(-\frac{dP}{dL}\right) \quad \text{.....(5-4)}$$

or

$$\left(-\frac{dP}{dL}\right) = \frac{q\mu}{kA} \quad \text{..... (5-4a)}$$

where

q- flow rate in the sample , cm^3/s

k- permeability of the sample, darcy

μ - viscosity of the gas, cp

-dP/dL- pressure gradient, atm/cm

A- cross-sectional area of the sample, cm^2

If the fluid is gas, Darcy's law needs to be adjusted due to gas compressibility. Depending on the assumptions, it can be modified to several different forms.

Darcy's Law for Ideal Gas with Constant Viscosity: If the gas is assumed to have ideal gas behavior and constant viscosity, Darcy's law can be rewritten as

$$k = \frac{2QL\mu P_b}{A\left(P_1^2 - P_2^2\right)} \quad \text{..... (5-5)}$$

where

A- cross-sectional area of the sample, cm^2

k- permeability, Darcy

L- sample length, cm

P_b- base pressure, e.g. at the pump, atm

P_1- pressure at the inlet of the sample, atm

P_2- pressure at the outlet of the sample, atm

Q- flow rate under P_b, cm^3/s

μ - gas viscosity, cp

The implicit assumption is that the pressure declination of pressure in the sample is linear, which gives the average pressure as (P1+P2)/2. Also, $P_b \times Q = 0.5 \times (P_1+P_2) \times q$, with q as the flow rate in the sample. The assumption of an ideal gas means that the z-factor is constant at P_b, P_1, and P_2.

Darcy's Law for Real Gas Behavior: In most cases, the ideal gas behavior assumption is invalid. In these cases, the real gas model, or pseudo-pressure approach, can be used to rewrite the Darcy's law as follows:

$$k = \frac{2QLP_b}{A\left[m(P_1) - m(P_2)\right]} \quad \text{..... (5-6)}$$

where

k- permeability, Darcy

Q- flow rate under P_b, cm^3/s

P_b- base pressure, e.g. at the pump, atm

P_1- pressure at the inlet of the sample, atm

P_2- pressure at the outlet of the sample, atm

A- cross-sectional area of the sample, cm^2

m(P) – pseudo-pressure, atm^2/cp, which can be calculated by Eq. (5-7)

$$m(P) = 2\int_0^P \left(\frac{P'}{\mu z}\right) dP' \quad \text{..... (5-7)}$$

where

μ - gas viscosity, cp

z- gas compressibility factor

P'- dummy variable for the integration

Non-Darcy Flow: Forchheimer's Equation. *Forchheimer's Equation for Liquids:* Darcy's law was based on the assumption that the fluid in the porous media is laminar flow in which the pressure drop is mainly caused by viscous resistance. When the flow rate, i.e., the superficial fluid velocity, is high, Darcy's law no longer holds. Under this situation, Darcy's law cannot describe the pressure drop properly because part of the energy is consumed by the inertial activities and other processes. An extra term to count the pressure drop in these processes was

added to the Darcy's equation by Forchheimer,[12] resulting in Forchheimer's equation, as shown in Eq. (5-8)

$$\left(-\frac{dP}{dL}\right)=\frac{\mu}{k}\left(\frac{q}{A}\right)+\beta\rho\left(\frac{q}{A}\right)^2 \quad \text{..... (5-8)}$$

or, in terms of gas velocity, v:

$$\left(-\frac{dP}{dL}\right)=\frac{\mu}{k}v+\beta\rho v^2 \quad \text{.....(5-8a)}$$

where

P-pressure, atm

L-length, cm

μ -viscosity, cp

v - gas velocity, cm/s

k - permeability, Darcy = sq cm-cp/(atm*s)

ρ - gas density, g/cm^3

β – Non-Darcy flow coefficient, atm-s^2/g

Forchheimer's Equation for Gas Flow: Similarly to the modification of Darcy's law for gas flow, the Forchheimer's equation for gas flow can be modified as follows.

$$W=\rho q \quad \text{..... (5-9)}$$

where W is the mass flow rate of the gas and

$$q=Av \quad \text{..... (5-10)}$$

so that

$$W=\rho Av \quad \text{.....(5-11)}$$

and

$$\frac{W}{A}=\rho v \quad \text{..... (5-12)}$$

Rearranging Eq.(5-8) as

$$\rho\left(-\frac{dP}{dL}\right)=\frac{\rho\mu}{k}v+\beta\rho^2v^2 \quad \text{..... (5-13)}$$

Applying Eq. (5-12) into Eq. (5-13) results in

$$\rho\left(-\frac{dP}{dL}\right)=\frac{\mu}{k}\frac{W}{A}+\beta\left(\frac{W}{A}\right)^2 \quad \text{..... (5-14)}$$

But

$$\rho = \frac{MP}{zRT} \quad \text{..... (5-15)}$$

so

$$\frac{MP}{zRT}\left(-\frac{dP}{dL}\right) = \frac{\mu}{k}\frac{W}{A} + \beta\left(\frac{W}{A}\right)^2 \quad \text{..... (5-16)}$$

Integrating Eq. (5-16) over the sample length gives Eq. (5-17) that is Forchheimer's equation for gas flow in porous media.[13]

$$\frac{M\left(P_1^{\,2} - P_2^{\,2}\right)}{2zRT\mu L\left(\frac{W}{A}\right)} = \frac{1}{k} + \beta\left(\frac{W}{\mu A}\right) \quad \text{..... (5-17)}$$

where:

M = molecular weight, g/(g-mole)

z = compressibility factor

R = gas constant

T = absolute temperature,

P-pressure, atm

L-length, cm

μ -viscosity, cp

v - gas velocity, cm/s

k - permeability, Darcy, = (cm^2-cp)/(atm-s)

ρ - gas density, g/cm^3

β – non-Darcy flow coefficient, atm-s^2/g

In Eq. (5-17), M and R are constants; L and A are known from sample geometry; P_1 and P_2 are the measured pressures at the inlet and outlet of the sample at temperature, T under mass flow rate, W. z and μ are available from flash test results or from other resources, such as pressure-volume-temperature (PVT) Simulator, PVTsim™,[14] for the specific gas, once the average pressure and temperature are known. Therefore, Eq. (5-17) has only two unknowns: 1/k and β. Eq. (5-17) has the same format as a simple linear equation,

$$Y = aX + b \quad \text{.....(5-17a)}$$

Therefore, under constant temperature T, these two unknowns, 1/k and β, can be determined by measuring the pressures at the inlet and outlet of the sample under different flow rates. This is the foundation of the data process.

Calculation of z and μ for N_2 and CO_2: Based on simulation of z and μ, values for N_2, results listed below were obtained and checked against experimental literature values for consistency. Based on these tested data, the relationships between compression factor and pressure at each temperature are obtained as follows:

$$\begin{cases} z_{100} = 3\times10^{-5}\,p + 0.9953 & (R^2 = 1.00) \\ z_{150} = 3\times10^{-5}\,p + 0.9932 & (R^2 = 0.99) \\ z_{200} = 2\times10^{-5}\,p + 0.9913 & (R^2 = 0.98) \end{cases} \quad \text{(5-18)}$$

Similarly, the relationships between viscosity and pressure are obtained:

$$\begin{cases} \mu_{100} = 5\times10^{-5}\,p + 0.5928 & (R^2 = 1.00) \\ \mu_{150} = 5\times10^{-5}\,p + 0.5858 & (R^2 = 1.00) \\ \mu_{200} = 4\times10^{-5}\,p + 0.5867 & (R^2 = 1.00) \end{cases} \quad \text{(5-19)}$$

Using these equations, the z-factor and the viscosity are calculated at each corresponding pressure and temperature.

The calculation of CO_2 phase properties under test conditions were generated using a PVT simulator.[14] Using the above mentioned experimental apparatus and the method of data processing, more than 200 gas flooding experiments have been conducted on the five core samples. Both N_2 and CO_2 have been used. The following section presents the results.

Dimensional Analyses. During the development of Darcy's law and the Forchheimer's equation, different unit systems have been used, as shown in Eqs. (4) to (17). A dimensional analysis will help simplify the complexity.

Unit of the Y-Axis: In Eq.(5-17), the final unit in the left-hand-side can be simplified as follows:

$$\left[\frac{M\left(P_1^2 - P_2^{\,2}\right)}{2zRT\mu L\left(\frac{W}{A}\right)}\right] = \{[\text{g/(g-mole)}][\text{atm}^2]\}/\{[(\text{atm}\times\text{cm}^3)/(\text{g-mole}\times\text{K})][\text{K}\times\text{cp}\times\text{cm}][(\text{g/s})/\text{cm}^2]\}$$

$$= \{\text{atm}\times\text{s}\}/\{\text{cm}^2\times\text{cp}\}$$

Using the conversions

1 atm = 14.7 psi

1 psi = 6895 Pa

1 cp = 0.001 Pa-s

this becomes

$$[\frac{M\left(P_1^2 - P_2^2\right)}{2zRT\mu L\left(\frac{W}{A}\right)}] = \{[\text{atm}\times\text{s}]\}/\{[\text{cm}^2\times\text{cp}]\} = 1.013565\text{E}8 / [\text{cm}^2]$$

and since 1 μm = 10^{-4} cm, 1 $\text{cm}^2 = 10^8\ \mu\text{m}^2$ therefore

$$[\frac{M\left(P_1^2 - P_2^2\right)}{2zRT\mu L\left(\frac{W}{A}\right)}] = 1.013565\text{E}8 / [\text{cm}^2] = 1.013565\text{E}8 / [10^8\ \mu\text{m}^2] = 1.013565 / [\mu\text{m}^2]$$

also 1 Darcy = 0.9869 μm^2, thus

$$[\frac{M\left(P_1^2 - P_2^2\right)}{2zRT\mu L\left(\frac{W}{A}\right)}] = 1.013565 / \{[1\ \mu\text{m}^2] \times [1\ \text{Darcy} / 0.9869\ \mu\text{m}^2]\} = 1.0003\ 1/\text{Darcy}$$

So the simplified unit on the left-hand-side is about 1/Darcy.

<u>*Unit on the X-Axis*</u>:

$$[\left(\frac{W}{\mu A}\right)] = [(\text{g/s})]/\{[\text{cp}\times\text{cm}^2]\} = [(\text{g/s})]/\{[1\text{cp}\times(0.001\ \text{Pa-s/cp})][\text{cm}^2]\}$$

$$= 1000\ [\text{g/s}] / \{[\text{Pa-s}][\text{cm}^2]\}$$

Using the conversions

1 Pa = 1 N /m^2

1 N = 1 kg × 1 m/s^2

1 kg = 1000 g

this becomes

$$[\left(\frac{W}{\mu A}\right)] = 1[\text{kg/s}] / \{[1\ \text{N}/\text{m}^2\text{-s}][\text{cm}^2]\} = 1\ [\text{kg/s}^2] / \{[1\ \text{N}/\text{m}^2][\text{cm}^2]\}$$

$$= [1\ \text{kg/s}^2] / \{[1\ \text{N} \times (1\ \text{kg} \times 1\ \text{m/s}^2)/1\text{N}]/\text{m}^2\}[\text{cm}^2]\}$$

$$= 1.0 /\{[1/\text{m}][\text{cm}^2]\} = 1\ [\text{m}] / [\text{cm}^2]$$

$$= 100\ 1/\text{cm}$$

Therefore, the simplified unit on the right-hand-side is 100/cm, or 100 1/cm.

Units of k and β:

(a) Unit of k

Because the unit in the LHS is 1/Darcy, which correspondent to 1/k, therefore, the unit of k in Eq. (5-17) is Darcy.

(b) Unit of β

$$\beta = \left[\frac{M\left(P_1^2 - P_2^2\right)}{2zRT\mu L\left(\frac{W}{A}\right)}\right] / \left[\left(\frac{W}{\mu A}\right)\right]$$

$= [\text{Darcy}^{-1}] / [100/\text{cm}] = 100 \text{ cm / Darcy}$

$= 100 \text{ cm} / [0.9869\ \mu\text{m}^2]$

$= 100 \text{ cm} / [0.9869\ \mu\text{m}^2 \times (10^{-8}\ \text{cm}^2 / \mu\text{m}^2)]$

$= 1.013 \text{ E6 / cm}$

$\approx 1.0 \text{ E6 / cm}$

therefore the unit of β in Eq. (17) is 10^6 /cm.

Summary of Units: From the above analyses, it can be concluded that

(1) Based on the units used in the data process, the experimental data plot has the following units

Y: $\left[\frac{M\left(P_1^2 - P_2^2\right)}{2zRT\mu L\left(\frac{W}{A}\right)}\right] = [\text{atm}][\text{s}]\}/\{[\text{cm}^2][\text{cp}] = 1/\text{Darcy}$

X: $\left[\left(\frac{W}{\mu A}\right)\right] = [(\text{g/s})]/\{[\text{cp}][\text{cm}^2]\} = 100/\text{cm}$

(2) k = Darcy

(3) $\beta = 10^6$ 1/cm

So when the trend line equation is displayed on the excel plot, the calculated *k* is in Darcy and β in 10^6 cm^{-1}.

Results and Discussion

Measured Calculation of k and β. *An Example of Test Recordings and Calculation of k and β*: In the experiments previously discussed, the inlet and outlet pressures at the core (P_{cin} and $P_{cout)}$, the pressure difference between the inlet and outlet (ΔP), and the pressure at the injection pump (P_p), are measured when the gas flow reaches equilibrium at each specific flow rate. All measurements are taken under constant temperature, axial and radial stresses. When ΔP is different from (P_{cin} - P_{cout}), (P_{cout} + ΔP) is used to replace P_{cin} because the gauge for the differential pressure has a better resolution than the one for P_{cin} and P_{cout}.

The average pressure at the core, P_{cavg}, is then calculated from P_{cin} and P_{cout}. The z-factor and the viscosity are calculated using Eqs. (5-18) and (5-19), or from other resources such as a PVT simulator. The gas densities at the pump and in the core are calculated using Eq. (5-15). The mass flow rate, W, which is the same in the pump and in the core, is calculated using Eq. (5-9). The volumetric flow rate and the superficial gas velocity in the core, Qc and v_c, are calculated using Eqs. (5-9) and (5-10).

With these measured values and the known temperature and sample geometry, the permeability from Darcy's law, k_{ps}, at each different flow rate is calculated using Eq. (5-6). On the other hand, $[W/(\mu A)]$ and $[M(P_1^2-P_2^2)]/[2zRT\mu L(W/A)]$ in Eq. (17), i.e. X and Y in Eq. (5-17a) are calculated using the previously known, measured or calculated values. Table 5-6 shows the calculation of a complete series of experiment of N_2 flooding through Dakota sandstone under 100ºF and axial and radial pressures at 4000 psi.

Using Forchheimer's equation, Eq. (5-17), the permeability, k, and non-Darcy flow coefficient, β, at high velocity are calculated using the X and Y values under different flow rates shown in Table 5-6. Figure 5-9 shows the calculated results.

Compilation of All Measured k and β: Table 5-7 shows the compilation of the measured permeability and non-Darcy flow coefficient of all five rock samples under different conditions. This provides the basis for further analysis.

Flow Rate Influence on Flow Behavior. From Table 5-6, it can be seen that the permeability calculated using Darcy's law decreases with increased flow rates, as shown in Fig. 5-10. In this

specific case, the permeability at high flow rate (6000 cc/hr) is 1.37 mD, about 39% of that at low flow rate (e.g. 3.54 mD at 25cc/hr). Similar situations exist in other rocks under different testing conditions, as discussed below.

Dakota Sandstone: HT/HP gas flooding experiments have been conducted on Dakota sandstone in as the manner described previously.[15] Similar to that in Table 5-6, apparent permeability was calculated using Eq. (5-5). It was found that the apparent permeability decreases with the increase of flow rate, as shown in Fig. 5-11. This picture shows that the apparent permeability decreases rapidly at the initial stage when pump flow rate increases from 25 cc/hr to 2000 cc/hr. The apparent permeability keeps decreasing as the flow rate goes up. But the rate of decrease becomes slower and slower. This can be better demonstrated from the percentage change of the permeability.

Taking the apparent permeability at low flow-rate as reference, the percentage of the permeability change has been calculated, as shown in Fig. 5-12. From this figure, it is seen that the apparent permeability decreases 40% when the flow rate increases from 25 cc/hr to 2000 cc/hr. For flow-rate increases from 2000 cc/hr to 4000cc/hr, the change of the apparent permeability is 15%. The change of the apparent permeability is even smaller when the flow-rate increases to higher levels, as shown in Table 5-8. This indicates that the flow-rate effects mainly occur at low to intermediate flow rates.

Berea Sandstone 1: From Eq. (5-5) it can be seen that if Darcy's law is valid, the measured pressure drop, $(P_1^2-P_2^2)$ will be linearly proportional to the flow rate. However, the experimental results in Berea sandstone do not support that, as shown in Fig. 5-13.

Analysis of experimental data indicated that at low flow rates, the non-Darcy component is negligible but with the increase in flow rates, the inertial effect causes a higher non-Darcy flow behavior contribution. The flow rate is an important parameter that affects the permeability and non-Darcy flow coefficient. It can be seen in Fig. 5-13 that the Darcy flow and measured curves overlap each other only at low flow rates, which indicates a Darcy flow region which results in flow rate being proportional to $(P_1^2-P_2^2)$. With the increase in flow rate, there is an increase in the non-Darcy flow contribution; experimental results deviate increasingly from Darcy flow. This effect was seen in experimental results on core samples of Berea sandstone,

Dakota sandstone and Indiana limestone. At low flow rates the pressure drop followed Darcy flow and as the flow rate increased, the pressure drop increased proportionally.

Obviously, under high flow rate condition, the conventional Darcy flow permeability does not describe the flow behavior properly. Therefore, permeability and non-Darcy flow coefficient were calculated for each series using a Forchheimer plot as described earlier in Fig.5-9. To examine the goodness of fit over the entire flow regime, differential pressures, dP_{cal}, were calculated using Eq. (5-16); then the measured differential pressures, dP_{exp} were subtracted from the calculated differential pressure, dP_{cal} and divide this by dP_{cal} for a fraction deviation. Figure 5-14 is a plot between $[(dP_{cal} - dP_{exp})/dP_{cal}]$ vs. pump flow rate for a system at 100ºF and hydrostatic pressure of 2000 psig for Berea sandstone. It indicates that fraction change fluctuates around ±2% except at very low flow rates. This is a good indication of the validity of the Forchheimer's equation to represent flow behavior for this case. Initially, the calculated dP is higher but with increase in flow rate, it becomes less than the experimental dP_{exp}. It was observed that around 6000 cc/hr flow rate, calculated dP_{cal} increased by about the same amount as in the experimental work. Similar behavior was seen in all other rocks. Scatter was initially seen at low flow rates. In Fig. 5-14 the diamond shape points are the plot of points with data at low flow rates and very high flow rates excluded due to scatter. The points at higher flow rates can be further adjusted by determining more accurate values of k and β.

Defining the deviation factor as the ratio of pressure drop due to non-Darcy behavior to the total pressure drop, i.e., $dP_{non\text{-}Darcy}/dP_{total}$, provides an indicator for flow behavior deviated away from Darcy flow. Changes of such defined deviation factors with flow rate in this rock under overburden pressures of 2000 to 10000 psi are shown in Fig. 5-15.

Obviously, at low flow rate, the deviation factor is close to zero, meaning very full Darcy behavior. However, with the increase in flow rate, the deviation factor increases rapidly. For example, at the flow rate of 10,000 cc/hr, the deviator factor is about 0.75, meaning a prevailing effect of non-Darcy behavior. In this situation, if the non-Darcy effect is ignored, an error of 75% would result.

Berea Sandstone 2: Berea sandstone 2 (sample # BSSH 301, a higher permeability Berea) was run after BSSL 301 (lower permeability Berea) core sample. The behavior of this core sample was quite different from that of BSSL301. This core sample was of higher porosity and accordingly, had a higher permeability. Analysis of experimental data indicated that at low flow

rates, the non-Darcy component was negligible, but with the increase in flow rates, the inertial effect caused higher non-Darcy flow behavior as in the earlier case. Fig. 5-16 shows the Darcy, and non-Darcy curves overlapping each other only at low flow rates, where the flow is Darcian and dP increase is proportional to flow rate increase. Here also it is seen that with the increase in flow rate, there is an increase in the non-Darcy flow contribution and experimental results deviate increasingly from the Darcy flow.

Figure 5-17 is a plot of $[(dP_{cal} - dP_{exp}/dP_{cal}]$ vs. pump flow rate at 100ºF for core sample BSSH 301. This plot is similar to Fig. 5-14; it indicates that the percentage change in calculated dP and experimental dP with respect to calculated dP fluctuates around 1% in comparison to the BSSL301 sample, where it was fluctuating around ±2%. Initially, calculated dP was higher with a little scatter at low flow rates but after about 3500 cc/hr flow rate, there was a gradual increase in this ratio. Figure 5-18 depicts the behavior of calculated dP vs. experimental dP. This figure indicates the agreement between calculated and experimental dP.

Figure 5-19 shows the deviation factor versus pump flow rate for the BSSH301 core sample. The deviation factor of this core sample increases from being mostly Darcy flow at low flow rates to less than 0.2 Darcy flow contribution at the high flow rates.

Figure 5-20 is a plot of the deviation factor vs. the pump flow rate at various overburden stresses. A specific pattern in the change of Darcian permeability is seen with the change in overburden stresses and temperature. As shown in Fig. 5-20, deviation factor increase with an increase in overburden stresses and flow rates. As stated earlier, the non-Darcy flow coefficient increases with a decrease in permeability. The analysis of this series of tests is given in Table 5-7. It is shown that the permeability and non-Darcy flow coefficient changes from 1.079 Darcy and 1.02E+6 cm^{-1}, respectively, at 100ºF and 2000 psi overburden pressure to 0.577 Darcy and 2.55E+6 cm^{-1} at 200ºF and 10,000 psi overburden pressure, respectively.

Figure 5-21 is a plot of $[(dP_{cal} - dP_{exp})/dP_{cal}]$ versus flow rate at different confining stresses and at 100ºF temperature. This plot also indicates that there is scatter at the low flow rates but after that there is about 2% difference between calculated and experimental dP.

Indiana Limestone 1: An Indiana limestone core was run after the experimental work on Berea sandstone was completed. The porosity of this core was about 14.57%. Analysis of the data revealed that the permeability varied from 23 md at a 2000-psi overburden pressure and 100ºF to 17 md at 10000 psi overburden pressure and 200ºF. The non-Darcy flow coefficient increased

from 34.1E+6 cm^{-1} to 47.1E+6 cm^{-1}. Results indicated that at low flow rates, the non-Darcy component was negligible but with the increase in flow rates, the inertial effect caused significant non-Darcy flow effects. Figure 5-22 shows that the curves from Darcy and Forchheimer flow equations overlapping each other at low flow rates, where the flow is Darcian and flow rate is proportional to dP. As with the Berea sandstone, with the increase in flow rate, there is an increase in the non-Darcy flow contribution.

Figure 5-23 is a plot for IL301 core sample between $[(dP_{cal} - dP_{exp})/dP_{cal}]$ and flow rate at the pump at 100ºF. This plot indicates the percentage change in calculated dP and experimental dP with respect to calculated dP. It is seen that percentage change averages around 8%. Figure 5-24 shows the behavior of calculated dP and experimental dP. Figure 5-24, for core sample IL301 plotted for dP_{exp} vs. dP_{cal} at 100°F shows that the rate of change on calculated dP is much more than the change in experimental dP. Also, there is a fair amount of curvature in the plot indicating deviation from a one to one relationship.

The deviation factor vs. pump flow rate for the IL301 core sample is shown in Fig. 5-25. The deviation factor of this core sample decreased from 100% Darcy flow to less than 25%. On plotting different curves for this core at different confining stresses (Fig. 5-26), it was found that the change in deviation factor was almost the same as that shown in Fig. 5-25. All the curves for different confining stresses follow almost the same curve.

Indiana Limestone 2: Figure 5-27 is similar to Fig. 5-22. On this second Indiana limestone core the tests were done with axial and radial confining pressures different. This was to aid in the determination of stresses similar to those that are uneven and are the rule in nature. This experiment was conducted on IL302 core sample.

Figure 5-28 is similar to Fig. 5-24. The explanation for all these plots has been given in the earlier discussion. Calculated dP is higher than measured dP in the IL302 core sample.

Figure 5-29 shows the plot between the deviation factor and pump flow rate. In all the experimental analysis, the permeability at the low flow rates was the actual permeability due to the Darcian flow, and with the increase in flow rate the fraction of Darcian contribution decreased with flow rate.

Figure 5-30 shows the change of deviation factor with flow rate under different stress conditions. It is seen that an increase in deviation factor is greater at low flow rates. The deviation factor is reduced with an increase in flow rate. There was a small increase in deviation

factor at very low flow rates; otherwise the deviation factor was almost the same under varying axial pressure with constant radial pressure, as shown in Fig. 5-31.

Summary of Flow Rate Influence: It can be seen that the flow rate has significant influence on permeability and non-Darcy behavior. In general, with the increase of flow rate, the apparent permeability decreases, the deviator factor increases, and the relative error experiences a complex variation. The relative error level is within 8% in most cases.

As the comparison of the flow effects on different rocks shows, the magnitude of the flow rate influence is different in different cases. Although the general trends are similar, the influence on each specific rock is different. A universally applicable criterion is needed to quantify the non-Darcy effect due to the flow-rate increase in different rocks. This is the topic of next section.

Proposed Criterion for Flow Rate Effect. As demonstrated above, there is a need to consider flow rate effect on flow behavior, that is, a criterion is need to quantify when the flow rate effect, or in other words, non-Darcy behavior, must be considered, and what the error would be if ignored. This section recommended such a criterion based on theoretical analysis and experimental verification of different rocks.

Review of Previous Work: The earliest work on the criterion for non-Darcy flow behavior in porous media was probably published by Chilton and Colburn.[16] They conducted fluid flow experiments on packed unconsolidated particles, and modified Reynolds number to

$$\mathrm{Re} = \frac{\rho D_p v}{\mu} \quad \text{..... (5-20)}$$

as a criterion for non-Darcy flow. From their experiments the critical Reynolds number for non-Darcy flow is *40* to *80*.

Fanch and Lewis[17] flowed crude oil, water, and air through unconsolidated sands, lead shot, and consolidated sandstones to investigate the non-Darcy flow behavior in porous media. Using Chilton and Colburn's definition of Reynolds number,[16] their experiment results show that non-Darcy flow occurs at $Re = 10 \sim 1000$ in unconsolidated porous media and at $Re = 0.1 \sim 10$ in loosely consolidated rocks. The major disadvantage of this definition is that the use of particle diameter to represent the pore diameter does not have a sound physical foundation.

Green and Duwez[18] addressed this problem by redefining the Reynolds number for fluid flow in porous media as

$$\mathrm{Re} = \frac{\beta G_w}{\alpha \mu g} \quad \text{..... (5-21)}$$

They conducted N_2 flooding experiments through four different porous media of metal. Results show that non-Darcy behavior started at *Re = 0.1* and became dominant at *Re >10*.

Ergun[19] included porosity in his definition of Reynolds number as follows

$$\mathrm{Re} = \frac{D_p G}{\mu} \frac{1}{1-\varphi} \quad \text{..... (5-22)}$$

From the experiments of fluid flow in packed particles, he observed a critical value of Re = 10, and a transitional zone of *Re = 10 ~1000*.

Cornell and Katz[20] included a electrical resistivity factor in the formula and defined the Reynolds number as

$$\mathrm{Re} = \frac{D_E G_s \sqrt{F} k_1}{\mu k_2 \sqrt{\varphi}} \quad \text{..... (5-23)}$$

They repeated Green and Duwez's[18] experiments on sandstones, dolomites and limestones and had similar results as Green and Duwez on metals. However, different results continued to appear. Critical values from *0.1* to *75* were reported, which initiated an uncertainty by a factor of *750*.[21]

Hassanizadeh and Gray[22] believed critical value *Re = 1 ~ 15*, and used *Re = 10* as a critical value for non-Darcy flow. From this assumption they concluded that non-Darcy flow behavior is due to the increase of the so-called microscopic viscous force at high velocity.

Blick and Civan[23] used a capillary-orifice model[24] to simulate the fluid flow in porous media. Based on that model, the critical Reynolds number for non-Darcy behavior is *100*, below which Darcy's law is valid. Ruth and Ma[25] used a periodical model, similar to the capillary-orifice model,[24] to simulate non-Darcy flow behavior in porous media. They defined a new dimensionless number, the Forchheimer number, as

$$F_o = \frac{\beta k_0 \rho v}{\mu} \quad \text{..... (5-24)}$$

and correlated it to the conventional Reynolds number. Their results showed that for a transitional zone of *Re = 3 ~ 5*, *Fo* is about *0.02*. However, there is a major shortcoming in this definition: they used the traditional permeability measured at "zero" (low) velocity according to Darcy's law to describe high-velocity, non-Darcy behavior.

Andrade et al[26] numerically simulated the inertial effect of fluid flow through porous media. Their results show that for porous media with different porosities, non-Darcy behavior occurs similarly when *Re = 0.01 ~ 0.1*. This result indicates that the occurrence of non-Darcy behavior is independent of porosity, contradicting the earlier formulas.[19,20]

Non-Darcy behavior has shown significant influence on well performance. Holditch and Morse[1] numerically investigated the non-Darcy effect on the effective fracture conductivity and gas well productivity. Their results show that non-Darcy flow can reduce the effective fracture conductivity at the near-wellbore region by a factor of 20 or more; and the gas production by 50%. Non-Darcy effect on hydraulically fractured wells was also confirmed by others.[2,3]

Due to the importance of the non-Darcy effect, efforts have been made to include it in well performance simulation.[4] However, the inclusion of this non-Darcy effect can be very expensive in numerical simulation with a high order of approximation.[27]

In summary, there are two types of Reynolds number defined to characterize the occurrence of non-Darcy behavior in porous media: Type 1 represented by Eq. (5-20), and Type 2 by Eq. (5-21). Type 1 is characterized by including a un-measurable parameters, such as a geometric length of the porous media, i.e., the diameter of the pore or the particle. Type 2 includes only measurable parameters. Both types of definition have some disadvantages, mainly: (1) the term "Reynolds number" has caused confusion in terminology, because it has been closed related to turbulent flow which has been widely rejected in porous media;[28] (2) the inconsistent range of critical values (Re = 1 ~ 100 for Type-1, and Re = 0.01 ~ 0.1 for Type-2) makes the criteria hard to use; and (3) both have not been explicitly connected to error that would be caused if the non-Darcy behavior were ignored.

The studies included in this project have attempted to overcome these disadvantages. Presented is a recommendation for a new criterion for non-Darcy behavior in porous media, the theoretical analysis of this criterion, and experimental verification using real rocks that have physical properties covering many reservoir rocks.

Recommendation of a Non-Darcy Flow Criterion: From the above review, it can be seen that there has been two types of Reynolds number-based criteria for non-Darcy behavior in porous media. Type 1 includes un-measurable parameters, which makes it lack a sound physics foundation, and hard to use. Type 2 has only parameters that are measurable. Several researchers have expressed their preference for using the Type 2 criterion.[3,29,30] But, in addition to the other shortcomings mentioned above, lack of direct connection to error due to ignoring the non-Darcy effect restricts a wider use of Type 2 criterion in well performance simulation.

Ruth and Ma's[25] establishment of Forchheimer's number, which was first suggested by Lee et al[31] to honor the pioneer in this area, was true progress. But their definition included the traditional permeability measured at "zero" (low) velocity using Darcy's law, an obvious contradiction to the theme of non-Darcy behavior that occurs at high-flow velocity. In order to correct this shortcoming, Forchheimer's number is proposed to characterize the non-Darcy behavior for fluid flow in porous media, and is redefined as

$$F_o = \frac{\beta k \rho v}{\mu} \quad \text{..... (5-25)}$$

The physical meaning and its relation to error of ignoring non-Darcy behavior will be analyzed in the following section.

Theoretical Analysis of the Proposed Criterion: The non-Darcy flow behavior in porous media is usually described by the well-known Forchheimer's equation, Eq. (5-8a). The first term on the right-hand-side of Eq. (8a) is the pressure gradient caused by viscous force, and the second term by the inertial force. So the physical meaning of Eq. (8a) is that the total pressure gradient for fluid flow in porous media is contributed by the viscous resistance and the inertial force.

The Forchheimer's number defined in Eq. (5-25) is then the ratio of the second term to the first term on the right-hand side of Eq. (5-8a). Therefore, physically, it represents the ratio of the inertial force to the viscous force.

Because Darcy's law is based on viscous flow, using Darcy's law assumes that pressure gradient is 100% caused by viscous resistance. In other words, non-Darcy effect, or the error caused by ignoring the non-Darcy behavior, is zero in the case of applying Darcy's law. Therefore, non-Darcy effect can be quantified by the portion of the pressure gradient caused by the inertial force in the overall pressure gradient in Eq. (5-8a), which leads to the definition of the theoretical non-Darcy effect, f_{ND_T}

$$f_{ND\_T} = \frac{\beta \rho v^2}{-\frac{dp}{dl}} \quad \text{..... (5-26)}$$

Combining Eqs. (5-25) and (5-26) gives

$$f_{ND\_T} = \frac{Fo}{1+Fo} \quad \text{..... (5-27)}$$

Thus from Eq. (5-27), it can be seen that Forchheimer's number is directly connected to the error of ignoring non-Darcy behavior. Such a connection will be useful to well performance simulation, in which a trade-off is often needed on whether to include the non-Darcy behavior or not.

From the above analysis, it is seen that the proposed criterion, the Forchheimer's number has two advantages: (1) all parameters involved have clear physical meaning, and are all measurable; and (2) knowing the Forchheimer's number can estimate the non-Darcy effect, an indicator of error for ignoring non-Darcy behavior. Table 5-9 shows several values of Forchheimer's number, and the corresponding non-Darcy effect.

Experimental Verification: Theoretical analysis has shown the physical meanings of the proposed criterion and its relationship to non-Darcy effect. In order to verify the proposed criterion and the theoretical analysis, gas flooding experiments have been designed and carried out in laboratory. Using a high-pressure, high-temperature gas flooding system, nitrogen flooding experiments were conducted on Dakota sandstone, Indiana limestone, and Berea sandstone, each representing typical reservoir rocks with a wide range of permeabilities (~ 3 to 200 mD). Details of the experimental system have been introduced elsewhere.[15] The samples used in the verification experiments are 1-in. in diameter by 2-in. long. Pump flow rates used in the experiments range from 25 to 10,000 cc/hr. The starting flow rate corresponds to the condition where the induced pressure drop is large enough to be accurately measured at equilibrium. The ending flow rate is limited by the pump capacity. Boundaries of the related parameters in the verification experiments are shown in Table 5-10.

Under gas flooding conditions, Forchheimer's equation becomes Eq. (5-17). By flooding gas through the sample at different flow rates and measuring the inlet pressure (p_1) and outlet pressure (p_2) under controlled backup pressure and temperature, the permeability, k, and non-Darcy flow coefficient, β, can be determined using Eq. (5-17). Figure 5-9 shows an example of

determining k and β for the Dakota sandstone. Measured permeability and non-Darcy flow coefficient of all three rocks are shown in Table 5-11.

In order to verify the proposed criterion, the measured non-Darcy effect can be calculated from Eq. (5-17) as follows. Rewrite Eq. (5-17) as

$$\left(p_1^{\,2} - p_2^{\,2}\right) = \frac{1}{k}\frac{2zRT\mu l}{M}\left(\frac{W}{A}\right) + \beta\frac{2zRTl}{M}\left(\frac{W}{A}\right)^2 \quad \text{.....(5-28)}$$

In Eq. (28), the left-hand-side term represents the total nominal pressure drop; on the right-hand-side, the first term represents the viscous nominal pressure drop, i.e., the Darcy effect, and the second term the inertial nominal pressure drop, i.e., the non-Darcy effect.

Similar to the definition of the theoretical non-Darcy effect, the measured non-Darcy effect, f_{ND_M} can be defined as

$$f_{ND\_M} = \frac{\beta\dfrac{2zRTl}{M}\left(\dfrac{W}{A}\right)^2}{\left(p_1^{\,2} - p_2^{\,2}\right)} \quad \text{.....(5-29)}$$

Now from the experiments and Eq. (5-17), k and β have been determined as shown in Table 5-11. Using these k and β, the Forchheimer number, Fo, can be calculated for each flow rate; further, the theoretical non-Darcy effect, f_{ND_T}, can be calculated using Eq. (5-27). On the other hand, the measured non-Darcy effect, f_{ND_M}, can be calculated using Eq. (5-29). Comparing of the theoretical and measured non-Darcy effect would verify the validity of the proposed criterion. Table 5-12 shows the verification results in the Dakota sandstone. Figures 5-32–5-34 graphically show the comparisons of the measured and the theoretically calculated non-Darcy effects in each of the three rocks.

From these verification and comparisons, it is seen that the theoretical and measured non-Darcy effects are very close in the tested range of the flow rates. In fact, it is very hard to distinguish the two effects in Figs. 5-32–5-34. As shown in Table 5-12, the maximum relative error is about 8% in the case of Dakota sandstone. Therefore, it can be concluded that the proposed criterion of non-Darcy flow behavior and the related formula of non-Darcy effect have successfully passed the experimental verifications.

Because the petrophysical properties of the tested rocks are similar to those of common reservoir rocks, it is assumed that the proposed criteria can be used for field purposes.

Critical Value of Fo: One of the reasons that a new criterion is needed is due to the inconsistency of critical value for the beginning of non-Darcy flow behavior from existing criteria. From an engineer's point of view, if a critical value can be given, it would be very helpful to such application as reservoir simulation.

Previous efforts have been focused on finding the start point of the departure of the linear Darcy prediction from the observed, non-linear performance in different forms. The most commonly mentioned ones include friction factor-Reynolds number curve, and the pressure drop-flow rate curve. Because of the restriction of resolution, the optical identification of the critical point for the starting of non-Darcy behavior is usually not accurate, and thus less dependable.

Figure 5-35 shows the flow rate vs. pressure drop and Forchheimer's number for the gas flooding experiment in the Dakota sandstone. The dashed line is the pressure drop predicted according to Darcy's law. It can be seen that non-Darcy behavior occurs at a very low flow rate. Optically, point A may be selected as the start for the non-Darcy behavior, which corresponds to a critical value of Fo = 0.235. From Eq. (5-27), this corresponds to a non-Darcy effect of 19%. On the other hand, a 10% non-Darcy effect would be numerically large enough for consideration in engineering practice, which corresponds to Fo ≈ 0.1, or point B in Fig. 5-35. Obviously, the non-Darcy effect-based critical value of Fo would be more reasonable than the optical selection. Therefore, Fo = 0.1 is recommended as the critical point for the beginning of non-Darcy flow behavior.

Summary of Recommended Criterion: Based on the research results presented in this section, the following conclusions can be obtained.

1. Reynolds number-based criteria for characterizing flow rate effect, or non-Darcy flow behavior in porous media are not satisfactory. New criteria defined by measurable parameters and with direct connections to non-Darcy effect are needed.
2. A Forchheimer's number, defined as $Fo = k\beta\rho v/\mu$, is recommended to replace the Reynolds number as the criterion for describing non-Darcy flow behavior.
3. A relationship between the non-Darcy effect and the Forchheimer's number is derived, which, in physics, means the error induced if the non-Darcy behavior is ignored at the corresponding Fo.

4. The proposed criterion and the derived non-Darcy effect formula have been experimentally verified using three different rocks in laboratory gas flooding tests.
5. A critical value of Fo = 0.1 is proposed for the consideration of non-Darcy behavior, which is more accurate than the optical identification.

Influence of In-Situ Stress on K and β. The previous section recommended a criterion to quantify the influence of flow rate on permeability and non-Darcy flow behavior, which depends on an accurate result of the permeability and non-Darcy flow coefficient. Results in previous sections have also shown that the permeability and non-Darcy flow coefficient are also affected by in-situ stresses and temperatures.

However, most existing experimental results were measured under hydrostatic pressure, an in-correct restored reservoir condition in most cases. In addition, reservoir in-situ stresses are undergoing changes continuously during reservoir operations, such as production and injection. Also the reservoir temperature plays a role on the non-Darcy flow behavior. Therefore, relations between in-situ stress and permeability as well as non-Darcy flow coefficient under different temperatures are not only needed to the adequate address of flow rate effect revealed in the previous section, but also useful to the proper characterization of the reservoir under varying conditions.

This section presents some of the relationships between in-situ stress and permeability aw well as non-Darcy flow coefficient under different conditions.

Brief Review: As stated in previous sections, Darcy's law has been widely used to describe the fluid flow though porous media in petroleum science and other disciplines. This law is based on experimental observations of fluid flow through porous media under laminar conditions, that is, under low flow velocity. But, in the near-wellbore region, fluid velocity can be very high due to the high pressure gradient.

Forchheimer[12] noticed that at high velocity in porous media, the pressure drop is higher than predicted by Darcy's law. Non-linear terms of second and third power of the fluid velocity were added to Darcy's law to correlate the pressure drop and the flow velocity. Later Green and Duwez[18] analytically derived the one-dimensional differential form of Forchheimer's equation (Eq. (5-8a)). They also determined the non-Darcy flow coefficient, β, for gas through sintered

porous media. Cornell and Katz[20] extended Green and Duwez's[18] work to consolidated rocks, and established the widely-used method of determining permeability, k, and non-Darcy flow coefficient, β, from experimental data. Since then, considerable effort has been expended to address non-Darcy behavior in porous media. Several papers have presented very good reviews from different aspects on research about non-Darcy behavior of fluid flow through porous media.[8,9,28,32,33]

Several issues still remain to be addressed related to the experimental research on overburden and in-situ stress effects on non-Darcy behavior of gas flow through porous media. It has been noted that the Klinkenberg[34] effect exists in non-Darcy flow if the average pore pressure is not sufficiently high, but the Forchheimer equation does not account for this effect.[8] The stress effect on permeability under Darcy flow conditions has been investigated extensively.[35-38] Several studies have investigated the effect of overburden pressures on the non-Darcy flow coefficient.[8,39] However, quantitative equations were not generated, and those experiments were conducted under hydrostatic overburden pressures; which are usually different from the natural stress distribution in the near-wellbore region.[40] A recent paper reported the efforts of measuring the non-Darcy coefficient under in-situ reservoir conditions using a triaxial set-up.[41] However, the permeability was determined using Darcy's law and the non-Darcy coefficient using the Forchheimer's equation; an inherent conflict. This mixing of terms seems common, that is the permeability in the correlations between the non-Darcy flow coefficient and other rock properties (mainly permeability and porosity) are determined using Darcy's law.[9,33,42]

This section is based on the results shown in Table 5-7. Experimental conditions are also shown in the same table. Results has been published in a recent paper[15] and several Master of Science works by Ganda,[43] Gupta,[44] and Bethapudi.[45]

Data Processing: Calculation of σ_{oct_eff} and τ_{oct} : Because most of the previous studies by other researchers were conducted under hydrostatic stress conditions (hydrostatic overburden pressures), and because by nature the vertical and horizontal stresses are normally different, both hydrostatic and differential stress conditions have been included in this section. These tests are summarized in Table 5-7. The effect of overburden and stresses on permeability and non-Darcy flow coefficient is due to the compaction and deformation of the pores and change of the tortuosity of the porous rock.

According to rock mechanics, effective normal stresses cause compaction and shear stresses generate deformation. Under triaxial stress conditions, the overall compaction is proportional to the average effective normal stresses, σ_{eff}; and the overall deformation is proportional to the average shear stresses, τ; which are expressed as:[46]

$$\begin{cases} \sigma_{eff} = \dfrac{1}{3}(\sigma_{1eff} + \sigma_{2eff} + \sigma_{3eff}) \\ \tau = \dfrac{\sqrt{(\sigma_{1eff} - \sigma_{2eff})^2 + (\sigma_{2eff} - \sigma_{3eff})^2 + (\sigma_{3eff} - \sigma_{1eff})^2}}{3} \end{cases} \quad \text{..... (5-30)}$$

where σ_{1eff}, σ_{2eff}, and σ_{3eff} are the effective principal stresses calculated as follows for the triaxial experiments in this study:

$$\begin{cases} \sigma_{1eff} = \max\{\sigma_a - p_{c\_avg}, \sigma_r - p_{c\_avg}\} \\ \sigma_{2eff} = \sigma_r - p_{c\_avg} \\ \sigma_{3eff} = \min\{\sigma_a - p_{c\_avg}, \sigma_r - p_{c\_avg}\} \end{cases} \quad \text{..... (5-31)}$$

where p_{c_avg} is the average core pressure that corresponds to an average of the average pore pressure of the lowest and highest flow rates in the same series of test. These are listed in Table 5-7 with the values of σ_{eff} and τ that have been calculated for each test series.

Results and Discussions: General Observation: Using the data shown in Table 5-7, the influence of overburden and in-situ stress on permeability and non-Darcy flow coefficient is investigated. Figures 5-36(a) and 36(b) show the change of k and β, respectively, with radial stresses while axial stress is constant during the flooding of N_2 through Dakota sandstone at 100°F. Holding radial stress constant while changing axial stress will give similar changes but with a lower magnitude. Overall, the following general features have been observed:

(1) At the same axial stress, k and β change in opposite trends: k decreases with increased radial stress while β increases;

(2) At the same radial stress, k and β also change in opposite directions: k decreases with axial stress while β increases; and

(3) The rate of change for k and β seem to be greatest when both radial and axial stresses are low.

(4) When CO_2 is flooding through the core, several features have been observed and need to be handled properly:

a. Flooding at the near critical point: when the outlet pressure was set to 1000 psi in the system, the experiments could not be completed due to difficulty in reaching flow equilibrium, as shown at the end of Table 5-7. A possible reason for this might be phase change within the core, because, from the inlet to the outlet, the pore pressure overlapped with the critical point, at which CO_2 undergoes phase change.

b. Cooling effect at high flow rate: Drastic change of temperature in the tubing system was observed when flow rate was higher than about 1500 cc/hr. This effect brought further change in the pressures and equilibrium could not be reached. The method used in this investigation to solve this problem was to keep the system at low flow rate and to let the automatic heater re-heat the system to re-establish the thermal equilibrium.

c. In the outlet tubing, the condensation of CO_2 would block the tubing. If this dry ice were not removed immediately, an explosion would occur once the pressure built up to a certain level. The method used in this research was to put the outlet tubing into hot water, which had been pre-heated to a temperature above the condensation point.

Quantitative Correlations: Figs. 5-37(a) and 37(b) show the effect of average effective normal stress on k and β respectively, under hydrostatic and differential stress conditions. It can be seen that under hydrostatic stress conditions, permeability and non-Darcy flow coefficient have very good linear relationship with the average effective normal stresses. For the Dakota sandstone investigated in this study, (Fig. 5-37(a)), the correlations, when the variables are in the specified units, i.e., k in mD, β in 10^6 cm^{-1}, and σ_{eff} in psi, are as follows:

$$\begin{cases} k = -5.0\times10^{-5}\sigma_{oct\_eff} + 3.48 & (R_k^2 = 0.92) \\ \beta = 5.6\times10^{-3}\sigma_{oct\_eff} + 154.33 & (R_\beta^2 = 0.92) \end{cases} \quad \text{..... (5-32)}$$

Under differential stress conditions shown in Fig. 5-37 (b), the average effective normal stress has a similar effect on permeability and the non-Darcy flow coefficient. Compared to the hydrostatic case, the correlation is less. This can be seen in the data scatter in Fig. 5-37(b) and the data fit in Eq. (5-33) below:

$$\begin{cases} k = -4.0\times10^{-5}\sigma_{oct\_eff} + 3.36 & (R_k^2 = 0.87) \\ \beta = 5.4\times10^{-3}\sigma_{oct\_eff} + 158.04 & (R_\beta^2 = 0.84) \end{cases} \quad \text{..... (5-33)}$$

The effect of average shear stress on k and β are shown in Figs. 5-38(a) and 38(b), respectively. It can be seen that the average coefficient between the average shear stress and k and β are either zero or close to zero. Therefore, average shear stress does not appear to influence permeability and non-Darcy flow coefficient, and thus deformation is not a dominant factor for the overburden and in-situ stress effect on k and β.

Similarly, correlations of k and β with respect to effective stress and shear stress have also been developed, as shown in Table 5-13.

Discussion of Limitations of Forchheimer's Method: Forchheimer's plots using Eqs. (5-8a) and (5-17) do not fit the data as well as expected. When examining Fig. 5- 9 closely, it can be seen that the plot is not linear. In fact, the data in this study better fit a second order polynomial. There are a number of assumptions that would account for deviations or simply invalidate the Forchheimer type equation as an exact equation. These include but are not limited to the following:

1. The assumption that permeability does not change with flow rate. The effective stress decreases as the flow rate increases, due to the increase in pore pressure. For instance, in the case of Dakota sandstone, the pressure drop going from the lowest to highest flow rate increases from as low as 2 psi to as high as 1,800 psi, resulting in a similar change in effective stress, which has shown to change permeability and thus the non-Darcy flow coefficient.
2. Stress is not constant across the core in the same test. It can vary by as much as 1,800 psi across a 2-in. core. What does this do to the permeability?

3. It is assumed that the core is homogeneous, and thus the flow path and average permeability are assumed to be constant. However, it is not homogeneous, and thus the other assumptions would not hold with flow rate.
4. The mass flow rate is constant across the core, but the volume flow rate can change by as much as threefold with similar changes in density and, to a lesser extent, in viscosity. This expansion can also change the temperature locally and affect again the density, volume, and viscosity locally.

These parameters, and certainly others not mentioned, will cause deviations from the Forchheimer's equation, even if it was an exact equation. Thus the Forchheimer method is a means to see the relative effects of stress, but can not be considered an exact representation.

Summary of In-Situ Stress Effects: From this study, the following conclusions are derived from the non-Darcy nitrogen flow behavior:

(1) Non-Darcy flow behavior is influenced by overburden/in-situ stresses. The higher the overburden and in-situ stress level, the lower the permeability and the higher the non-Darcy flow coefficient.
(2) Under the same overburden/in-situ stress conditions, the higher the pore pressure (outlet pressure), the higher the permeability, and the lower the non-Darcy flow coefficient.
(3) Sixty linear correlations have been developed between permeability, non-Darcy flow coefficient and overburden/ in-situ stresses in terms of average effective normal stress. Based on these correlations, it is observed that
    a. Permeability decreases while non-Darcy flow coefficient increases with increased effective stresses.
    b. Coefficient of correlation between permeability, non-Darcy flow coefficient and effective stresses are higher under hydrostatic stress conditions than under differential stress conditions, self-evidently meaning compaction is more significant in the former situation.
    c. Shear stresses do not show a significant correlation to the permeability and non-Darcy coefficient, especially in Dakota sandstone and Berea sandstone. This

indicates that in these rocks, compaction is a more dominant process than deformation.

(4) This work confirms previous studies, which indicated that though the Forchheimer equation is useful in describing high velocity flow in porous media, in many cases it is not sufficient.

Conclusions

Near-wellbore flow is always much higher then the rest of the reservoir. Chapter 5 reports the results of work to examine the effects on injectivity and productivity of high flow rate and large pressure gradients near the wellbore. A displacement process depends on the ability to inject and subsequently remove fluid into and out of a reservoir. The processes seem to be reversible in the five systems examined but significant changes in permeability and the non-Darcy flow coefficients all decreasing the injectivity and productivity need to be considered for accurate predictions of fluid injection and production. Through the research completed in this chapter, the following has been achieved:

Through the research completed in this part, the following progress has been made.

1. Upgraded hardware for HPTR flooding,
2. Developed experimental procedures for HPTR flooding, especially for CO_2 flooding,
3. Identified formulas for data process in HPTR flooding,
4. Completed more than 200 series of HPTR flooding experiments,
5. Confirmed non-Darcy behavior in HPTR flooding for five different rock systems,
6. Defined and verified criterion for non-Darcy behavior,
7. Quantified stress effect on permeability and non-Darcy flow coefficient,
8. Verified significant Joule-Thomson cooling effect near the critical point of CO_2.

The next step after this research is to add these results to the numerical simulator and check if the experimental process can be re-simulated.

A long-term plan derived from this research is to install automatic data acquisition system to record the change of temperature and pressure during CO_2 flooding. From those types of recordings, more discoveries related to CO_2 flooding are expected.

References

1. Holditch, S.A. and Morse, R.A.: "The Effects of Non-Darcy Flow on the Behavior of Hydraulically Fractured Gas Wells," *Journal of Petroleum Technology* (October 1976), 1196-1179.
2. Guppy, K.H., Cinco-Ley, H. and Ramey, H.J.: "Pressure Buildup Analysis of Fractured Wells Producing at High Flow Rates," *Journal of Petroleum Technology*, Nov. 1982, pp 2656-2666.
3. Martins, J.P., Milton-Taylor, D. and Leung, H.K.: "The Effects of Non-Darcy Flow in Propped Hydraulic Fractures," paper SPE 20790 presented at the 1990 SPE Annual Conference and Exhibition , New Orleans, Sept 23-26.
4. Papavassiliou, D.V.: "Flow through Porous Media: How Can HPC Improve Our Understanding?" Presentation, University of Oklahoma, Norman, OK, USA (2000).
5. Wattenbarger, R.A. "Chapter 35: Well Performance Equations," *Petroleum Engineering Handbook* (Ed. Bradley), Society of Petroleum Engineers, Richardson, TX, USA (1988).
6. Ewing, R. E., Lazarov, R.D., Lyons, S.L., Papavassiliou, D.V., Pasciak, J. and Qin, G.: "Numerical Well Model for Non-Darcy Flow through Isotropic Porous Media," *Computational Geosciences*, 3 (1999), 185-204.
7. Dake, L.P.*: Fundamentals of Reservoir Engineering*. Elsevier Scientific Publishing Company, Amsterdam, 1978.
8. Tiss, M. and Evans, R. D.: "Measurement and Correlation of Non-Darcy Flow Coefficient in Consolidated Porous Media," *J. Pet. Sci. Eng.* 1989, 3, 19-33.
9. Li, D. and Engler, T.: "Literature Review on Correlations of the Non-Darcy Coefficient," paper SPE 70015 presented at the 2000 SPE Permian Basin Oil and Gas Recovery Conference, Midland, May 15-16.
10. Jarrell, P.M., Fox, C.E., Stein, M. H. and Webb, S.L.: *Practical Aspects of CO_2 Flooding*, SPE Monograph Volume 22, Society of Petroleum Engineers, Richardson, TX, USA, 2002.
11. Thiercelin, M.C. and Roegiers, J.-C.: "Chapter 3: Formation Characterization: Rock Mechanics," *Reservoir Stimulation* (Third ed.) (Eds.: Economides and Notle), John Wiley & Sons, Ltd, New York, 2000.

12. Forchheimer, P.: "Wasserbewegung durch Boden," *Zeit. Ver. Deutsch. Ing.*, 45, 1901, 1781-1788.
13. Katz, D.L. Cornell, D., Kobayashi, R. Poettman, F.H., Vary, J.A., Elenbaas, J.R. and Weinaug, C.F.: *Handbook of Natural Gas Engineering*, McGraw-Hill Book Co., Inc., New York City (1959).
14. PVT software: CALSEP: "PVTsim 13", Calsep A/S, Denmark, 2003.
15. Zeng, Z., Grigg, R.B. and Ganda, S.: "Experimental Study of Overburden and Stress on Non-Darcy Gas Flow in Dakota Sandstone," paper SPE 84069 presented at the 2003 SPE Annual Technical Conference and Exhibition, Denver, Oct. 5–8.
16. Chilton, T.H., and Colburn, A.P., "Pressure Drop in Packed Tubes," *Industrial and Engineering Chemistry*, Vol 23, No. 8, 1931, 913-919.
17. Fanch, G.H. and Lewis, J.A.: "Flow of Simple Fluids through Porous Materials," *Industrial and Engineering Chemistry*, Vol 25,No. 10,1933, 1139-1147.
18. Green, L., Jr. and Duwez, P.: "Fluid Flow Through Porous Metals," *Journal of Applied Mechanics*, (March 1951) 39-45.
19. Ergun, S.: "Fluid Flow Through Packed Columns," *Chemical Engineering Progress*, Vol 48, No. 2, 1952, p.p. 89-94.
20. Cornell, D. and Katz, D. L.: "Flow of Gases through Consolidated Porous Media," *Industrial and Engineering Chemistry*, Vol. 45 No. 10, 2145-2152.
21. Scheidegger, A.E.: *The Physics of Flow through Porous Media* (Third ed.), University of Toronto Press, 1974, 152-170.
22. Hassanizadeh, S.M. and Gray, W.G: "High Velocity Flow in Porous Media," *Transport in Porous Media* 2 (1987), 521-531.
23. Blick, E.F. and Civan F.: "Porous-Media Momentum Equation for Highly Accelerated Flow," *SPERE*, (August 1988).
24. Blick, E.F.: "High Speed Flow through Porous Media," PhD Dissertation, U of Oklahoma, Norman, Oklahoma, 1963.
25. Ruth, D.W. and Ma, H.: "On the Deviation of the Forchheimer Equation by Means of the Average Theorem," *Transport in Porous Media*, 7, 1992, 255-264.
26. Andrade, J.A., Costa, U.M.S., Almeida, M.P., Makse, H.A. and Stanley, H. E.: "Inertial Effects on Fluid Flow through Disordered Porous Media," *Physical Review Letters*, Vol. 82, No. 26, (June 1998), 5249-5252.

27. Garanzha, V.A., Konshin, V.N., Lyons, S.L., Papavassiliou, D.V., and Qin, G.: "Validation of non-Darcy well models using direct numerical simulation," in *Numerical Treatment of Multiphase Flows in Porous Media,* (Chen, Ewing & Shi, editors), pp. 156-169, Lecture Notes in Physics, Vol. **552**, Springer-Verlag, 2000.
28. Firoozabadi, A. and Katz, D.L.: "An Analysis of High-Velocity Gas Flow through Porous Media," *JPT*, February 1979.
29. Geertsma, J.: "Estimating the Coefficient of Inertial Resistance in Fluid Flow through Porous Media," *SPEJ*, (October 1974), 445-450.
30. Gidley, J.L.: "A Method for Correcting Dimensionless Fracture Conductivity for non-Darcy Flow Effect," *SPE Production Engineering* (November 1991).
31. Lee, R. L., Logan, R.W. and Tek, M.R.: "Effects of Turbulence on Transient Flow of Real Gas through Porous Media," *SPEFE*, (March 1987), 108-120.
32. Grigg, R.B. and Hwang, M.K.: "High Velocity Gas Flow Effects in Porous Gas-Water System," paper SPE 39978 presented at the 1998 SPE Gas Technology Symposium, Calgary, March 15-18.
33. Narayanaswamy, G., Sharma, M.M. and Pope, G.A.: "Effect of Heterogeneity on the Non-Darcy Flow Coefficient," *SPE Reservoir Eval. & Eng.* 2(3) (June 1999) 296-302.
34. Klinkenberg, L.J.: "The Permeability of Porous Media to Liquids and Gases," *API Drill and Prod. Prac.,* 1941, p. 200.
35. Gray, D.H., Fatt, I. and Bergamini, G.: "The Effect of Stress on Permeabiliy of Sandstone Cores," *SPEJ*, (June 1963), 95-100.
36. Casse, F.J. and Ramey, H.J, Jr.: "The Effect of Temperature and Confining Pressure on Single-Phase Flow in Consolidated Rocks," *JPT.*, (Aug. 1979), 1051-1059.
37. Bai, M., Meng, F. Roegiers, J.-C., and Green, S.: "Improved Determination of Stress-Dependent Permeability for Anisotropic Formations," Paper SPE/ISRM 78188 presented at the 2002 SPE/ISRM Rock Mechanics Conference, Irving, Oct. 20-23.
38. Jones, C. and Smart, G.D.: "Stress Induced Changes in Two-Phase Permeability," Paper SPE/ISRM 78188 presented at the 2002 SPE/ISRM Rock Mechanics Conference, Irving, Oct. 20-23.
39. Avila, C.E. and Evans, R.D.: "The Effect of Temperature and Overburden Pressure upon the Non-Darcy Flow Coefficient in Porous Media," *Proc. 27th U.S. Symp. Rock Mech.*, Univ. Alabama, 1985, 623-634.

40. Fjaer, E. Holt, R.M., Horsrud, P., Raaen, A.M. and Risnes, R.: *Petroleum Related Rock Mechanics*, Elsevier, Amsterdam, 1992.
41. Belhaj, H.A., Agha., K.R., Nouri, A.M., Butt, S.D., and Islam, M.R.: "Numerical and Experimental Modeling of Non-Darcy Flow in Porous Media," Paper SPE 81037 presented at the 2003 SPE Latin American and Caribbean Petroleum Engineering Conference, Port-of-Spain, Trinidad, West Indies, April 27-30.
42. Ma, H. and Ruth, D.W.: "Physical Explanation of Non-Darcy Effects for Fluid Flow in Porous Media," paper SPE 26150 presented at the 1993 SPE Gas Technology Symposium, Calgary, June 28–30.
43. Ganda, S.: "A Laboratory Study of the Effect of Overburden Pressures, Flow Rates and Temperatures on Permeability and the Non-Darcy Flow Coefficient," Master of Science Thesis, New Mexico Institute of Mining and Technology, 2001.
44. Gupta, D.B.: "The effect of Hydrostatic Stresses, Flow Rate, Temperature and Pore Pressure on Pressure Gradient," Master of Science Thesis, New Mexico Institute of Mining and Technology, 2003.
45. Bethapudi, L.V.: "Comprehensive Literature Review of Foams and a Laboratory Study of CO_2 Flowing in Indiana Limestone versus Rates, Temperatures and Stresses," Master of Science Project, New Mexico Institute of Mining and Technology, 2003.
46. Jaeger, J.C. and Cook, N.G.W.: *Fundamentals of Rock Mechanics*, Third Edition, Chapman and Hall, London, 17-30.

Table 5-1. Superficial Velocity in Several CO_2 Floods

CO_2 floods	$V_{wellbore}$, ft/d	$V_{1\ ft}$, ft/d	$V_{5\ ft}$, ft/d
Goldsmith	21~45	5~11	1~3
Central vacuum, San Andrews	529~1170	131~289	32~72
SAC ROC	184~372	46~92	11~23

Table 5-2. Selected Experimental Parameters

Parameter	Value
Overburden pressure, psi	2000~10000
Axial stress, psi	2000~10000
Radial stress, psi	2000~10000
Reservoir pressure, psi	500~2000
BPR inlet pressure, psi	2000, 2500
BPR outlet pressure	500, 1000, 1500
Temperature, F	100, 150, 200
Flow rate at (80F, 2000 psi) , cc/hr	25 ~10000
Superficial velocity in core, ft/d	4 ~ 6775
Sample size, in	1-in diameter by 2-in length
Permeability range, mD	2~1100

Table 5-3. Sample Specifications

Rock	**Sample**	**Length, in**	**Diameter, in**	**Porosity, %**	**Permeability, mD**	**PV, cc**
Berea sandstone	**BSSH301**	**2.13**	**0.98**	**22.54**	**1109**	**5.9**
Berea sandstone	**BSSL301**	**1.98**	**0.99**	**18.40**	**202**	**5.6**
Dakota sandstone	**DSS201**	**2.00**	**1.00**	**14.00**	**2.02**	**5.8**
Indiana limestone	**IL301**	**2.07**	**0.99**	**14.57**	**22.14**	**5.9**
Indiana limestone	**IL302**	**2.04**	**0.99**	**26.81**	**74.22**	**5.8**

Table 5-4. Summary of All the Tests

Sample	Gas	Temp, F	Stress, psi	Pin, psi	Pout, psi	Tests
BSSH301	N2	100, 150 200	2000~10000	2000	500	15
BSSL301	N2	100, 150 200	2000~10000	2000	500	15
DSS201	N2	100, 150 200	2000~10000	2000	500	78
IL301	N2	100	2000~10000	2000	500	15
IL302	N2	100, 150 200	2000~10000	2000	500	36
IL301	CO2	100, 150 200	2000~10000	2000, 2500	500,1000,1500	45
Total						204

Table 5-5. Flash Test Results

T, ^{o}F	P, psia	z	μ, cp
100	500	1.00374	0.618765
	1,000	1.00994	0.643306
	1,500	1.02196	0.671072
	2,000	1.03481	0.695241
150	500	1.00852	0.607930
	501	1.00854	0.607982
	510	1.00872	0.608453
	600	1.01060	0.613124
	1,000	1.02026	0.632989
	1,500	1.03529	0.655446
	2,000	1.05341	0.675113
200	500	1.01249	0.605126
	501	1.01251	0.605169
	510	1.01276	0.605562
	600	1.01525	0.609455
	1,000	1.02721	0.625978
	1,500	1.04420	0.644682
	2,000	1.06335	0.661167

Table 5-6. Example of Calculation

Q_{pump}	ΔP	P_{cin}	P_{cout}	P_{cavg}	P_p	ρ_p	z_c	ρ_c	μ_c	w	Q_c	v_c	k_{ps}	X	Y
cc/hr	Psi	psi	psi	psi	psi	g/cm^3		g/cm^3	cp	g/hr	cc/hr	cm/s	mD	100/cm	1/Darcy
25	2	490	488	489	2004	0.1442	1.0026	0.0364	0.0186	3.60	99	0.01	3.54	0.01	293.55
50	4	492	488	490	2003	0.1441	1.0026	0.0365	0.0186	7.21	197	0.01	3.54	0.02	292.99
100	9	497	488	492	2001	0.1440	1.0026	0.0367	0.0186	14.40	392	0.02	3.61	0.04	287.47
200	17	507	490	499	2002	0.1440	1.0027	0.0372	0.0186	28.81	775	0.04	3.51	0.08	295.86
300	27	519	492	506	2003	0.1441	1.0027	0.0377	0.0186	43.23	1148	0.06	3.36	0.13	308.66
400	37	530	493	511	2003	0.1441	1.0028	0.0381	0.0186	57.64	1513	0.08	3.26	0.17	318.16
500	47	541	494	518	2004	0.1442	1.0029	0.0386	0.0186	72.09	1870	0.10	3.14	0.21	330.30
600	58	553	495	524	2004	0.1442	1.0029	0.0390	0.0186	86.50	2217	0.12	3.04	0.25	341.15
700	69	564	495	529	2004	0.1442	1.0030	0.0394	0.0186	100.92	2560	0.14	2.95	0.30	351.67
800	80	575	495	535	2004	0.1442	1.0030	0.0398	0.0186	115.34	2895	0.16	2.87	0.34	361.51
900	91	587	496	542	2004	0.1442	1.0031	0.0403	0.0187	129.76	3217	0.18	2.79	0.38	371.61
1000	103	599	496	548	2004	0.1442	1.0032	0.0408	0.0187	144.17	3536	0.19	2.72	0.42	381.22
1500	165	665	500	582	2004	0.1442	1.0036	0.0434	0.0187	216.26	4989	0.27	2.41	0.63	431.15
2000	227	727	500	614	2004	0.1442	1.0039	0.0457	0.0187	288.35	6316	0.35	2.22	0.84	468.45
2500	295	796	501	649	2003	0.1441	1.0043	0.0482	0.0188	360.26	7468	0.41	2.02	1.05	513.75
3000	363	865	502	684	2002	0.1440	1.0046	0.0508	0.0188	432.09	8501	0.47	1.87	1.26	554.11
3500	431	934	503	719	2002	0.1440	1.0050	0.0534	0.0189	504.11	9439	0.52	1.76	1.46	591.29
4000	500	1003	503	753	2001	0.1440	1.0054	0.0560	0.0189	575.83	10291	0.56	1.65	1.67	627.77
4500	568	1072	504	788	2002	0.1440	1.0058	0.0585	0.0189	648.14	11073	0.61	1.57	1.88	661.36
5000	635	1139	504	822	2001	0.1440	1.0061	0.0610	0.0190	719.79	11800	0.65	1.50	2.08	692.39
6000	771	1276	505	891	2002	0.1440	1.0068	0.0661	0.0191	864.18	13079	0.72	1.37	2.48	755.26
7000	905	1411	506	959	2002	0.1440	1.0076	0.0711	0.0191	1008.21	14187	0.78	1.28	2.89	813.91
8000	1040	1546	506	1026	2001	0.1440	1.0083	0.0760	0.0192	1151.67	15150	0.83	1.19	3.28	872.25
9000	1171	1678	507	1093	2001	0.1440	1.0090	0.0809	0.0193	1295.63	16017	0.88	1.12	3.68	925.17
10000	1301	1808	507	1158	2002	0.1440	1.0097	0.0856	0.0194	1440.31	16818	0.92	1.06	4.07	975.13

Table 5-7. Measured k and β

Test	Gas	Rock	T	P_{in}	P_{out}	σ_a	σ_r	σ_{eff}	τ	k	β
			F	psi	psi	psi	psi	psi	psi	md	10^6/cm
1	N_2	DSS201	100	2000	500	2000	2000	1192.99	0.00	3.44	155.51
2	N_2	DSS201	100	2000	500	3000	3000	2179.71	0.00	3.36	165.13
3	N_2	DSS201	100	2000	500	4000	4000	3176.70	0.00	3.30	171.81
4	N_2	DSS201	100	2000	500	5000	5000	4177.93	0.00	3.27	175.84
5	N_2	DSS201	100	2000	500	6000	6000	5167.93	0.00	3.26	183.14
6	N_2	DSS201	100	2000	500	7000	7000	6163.67	0.00	3.16	189.36
7	N_2	DSS201	100	2000	500	8000	8000	7159.66	0.00	3.13	192.59
8	N_2	DSS201	100	2000	500	9000	9000	8161.65	0.00	3.11	194.43
9	N_2	DSS201	100	2000	500	10000	10000	9161.14	0.00	3.07	195.94
10	N_2	DSS201	100	2000	500	2000	3000	1846.63	471.40	3.29	164.26
11	N_2	DSS201	100	2000	500	2000	4000	2522.53	942.81	3.29	170.99
12	N_2	DSS201	100	2000	500	2000	5000	3177.47	1414.21	3.22	175.20
13	N_2	DSS201	100	2000	500	2000	6000	3851.85	1885.62	3.24	176.03
14	N_2	DSS201	100	2000	500	2000	7000	4505.52	2357.02	3.12	179.43
15	N_2	DSS201	100	2000	500	2000	8000	5181.42	2828.43	3.22	180.63
16	N_2	DSS201	100	2000	500	2000	9000	5843.58	3299.83	3.15	184.38
17	N_2	DSS201	100	2000	500	2000	10000	6506.74	3771.24	3.11	186.95
18	N_2	DSS201	100	2000	500	4000	2000	1873.10	942.81	3.33	162.91
19	N_2	DSS201	100	2000	500	4000	6000	4514.75	942.81	3.19	184.41
20	N_2	DSS201	100	2000	500	4000	8000	5849.32	1885.62	3.17	186.90
21	N_2	DSS201	100	2000	500	4000	10000	7176.42	2828.43	3.14	192.61
22	N_2	DSS201	100	2000	500	6000	2000	2549.50	1885.62	3.30	163.74
23	N_2	DSS201	100	2000	500	6000	4000	3862.32	942.81	3.21	178.38
24	N_2	DSS201	100	2000	500	6000	8000	6511.23	942.81	3.10	191.01
25	N_2	DSS201	100	2000	500	6000	10000	7848.30	1885.62	3.10	192.78
26	N_2	DSS201	100	2000	500	8000	2000	3216.41	2828.43	3.29	166.46
27	N2	DSS201	100	2000	500	8000	4000	4529.46	1885.62	3.20	180.79
28	N2	DSS201	100	2000	500	8000	6000	5862.79	942.81	3.17	189.90
29	N2	DSS201	100	2000	500	8000	10000	8521.19	942.81	3.08	199.46
30	N2	DSS201	100	2000	500	10000	2000	3892.55	3771.24	3.24	165.67
31	N2	DSS201	100	2000	500	10000	4000	5205.63	2828.43	3.16	185.53
32	N2	DSS201	100	2000	500	10000	6000	6530.95	1885.62	3.12	192.32
33	N2	DSS201	100	2000	500	10000	8000	7856.27	942.81	3.07	198.00
34	N2	DSS201	150	2000	500	2000	2000	1179.01	0.00	3.25	177.87
35	N2	DSS201	150	2000	500	3000	3000	2161.99	0.00	3.20	186.94
36	N2	DSS201	150	2000	500	4000	4000	3147.99	0.00	3.18	197.98
37	N2	DSS201	150	2000	500	5000	5000	4142.98	0.00	3.16	206.69
38	N2	DSS201	150	2000	500	6000	6000	5140.98	0.00	3.13	210.74
39	N2	DSS201	150	2000	500	7000	7000	6137.97	0.00	3.10	213.03
40	N2	DSS201	150	2000	500	8000	8000	7132.96	0.00	3.07	220.29
41	N2	DSS201	150	2000	500	9000	9000	8129.21	0.00	3.04	223.38
42	N2	DSS201	150	2000	500	10000	10000	9126.20	0.00	3.01	226.72

43	N2	DSS201	150	2000	500	2000	4000	2487.57	942.81	3.20	190.74
44	N2	DSS201	150	2000	500	2000	6000	3815.65	1885.62	3.20	204.47
45	N2	DSS201	150	2000	500	2000	8000	5141.36	2828.43	3.19	210.03
46	N2	DSS201	150	2000	500	2000	10000	6469.07	3771.24	3.16	217.99
47	N2	DSS201	150	2000	500	4000	2000	1830.91	942.81	3.26	103.28
48	N2	DSS201	150	2000	500	4000	6000	4479.57	942.81	3.17	206.14
49	N2	DSS201	150	2000	500	4000	8000	5809.65	1885.62	3.15	209.80
50	N2	DSS201	150	2000	500	4000	10000	7137.23	2828.43	3.12	216.22
51	N2	DSS201	150	2000	500	6000	2000	2494.86	1885.62	3.34	191.32
52	N2	DSS201	150	2000	500	6000	4000	3822.69	942.81	3.27	197.28
53	N2	DSS201	150	2000	500	6000	8000	6481.84	942.81	3.21	205.36
54	N2	DSS201	150	2000	500	6000	10000	7799.40	1885.62	3.07	222.68
55	N2	DSS201	150	2000	500	8000	2000	3160.53	2828.43	3.32	192.60
56	N2	DSS201	150	2000	500	8000	4000	4484.10	1885.62	3.25	202.90
57	N2	DSS201	150	2000	500	8000	6000	5807.41	942.81	3.16	215.15
58	N2	DSS201	150	2000	500	8000	10000	8461.80	942.81	3.04	228.47
59	N2	DSS201	150	2000	500	10000	2000	3826.44	3771.24	3.29	192.82
60	N2	DSS201	150	2000	500	10000	4000	5148.01	2828.43	3.22	205.83
61	N2	DSS201	150	2000	500	10000	6000	6467.82	1885.62	3.13	222.93
62	N2	DSS201	150	2000	500	10000	8000	7793.12	942.81	3.03	231.87
63	N2	DSS201	200	2000	500	2000	2000	986.25	0.00	3.21	202.25
64	N2	DSS201	200	2000	500	4000	4000	3103.75	0.00	3.07	210.77
65	N2	DSS201	200	2000	500	6000	6000	5093.75	0.00	3.02	227.09
66	N2	DSS201	200	2000	500	10000	10000	9079.25	0.00	2.93	245.98
67	N2	DSS201	200	2000	500	2000	6000	3752.92	1885.62	3.05	221.65
68	N2	DSS201	200	2000	500	2000	10000	6413.33	3771.24	2.95	237.85
69	N2	DSS201	200	2000	500	4000	2000	1755.92	942.81	3.18	213.11
70	N2	DSS201	200	2000	500	4000	6000	4417.33	942.81	3.08	234.84
71	N2	DSS201	200	2000	500	4000	10000	7073.00	2828.43	3.02	244.20
72	N2	DSS201	200	2000	500	6000	2000	2425.83	1885.62	3.19	217.75
73	N2	DSS201	200	2000	500	6000	10000	7738.42	1885.62	3.02	253.41
74	N2	DSS201	200	2000	500	8000	2000	3086.00	2828.43	3.19	227.30
75	N2	DSS201	200	2000	500	8000	6000	5750.42	942.81	2.99	234.14
76	N2	DSS201	200	2000	500	8000	10000	8395.08	942.81	2.96	258.16
77	N2	DSS201	200	2000	500	10000	2000	3750.67	3771.24	3.14	223.53
78	N2	DSS201	200	2000	500	10000	8000	7733.42	942.81	2.97	260.76
79	N2	BSSL301	100	2000	500	2000	2000	1450.40	0.00	215.55	2.80
80	N2	BSSL301	100	2000	500	4000	4000	3451.95	0.00	207.20	2.67
81	N2	BSSL301	100	2000	500	6000	6000	5448.35	0.00	207.23	2.76
82	N2	BSSL301	100	2000	500	8000	8000	7456.18	0.00	200.80	2.86
83	N2	BSSL301	100	2000	500	10000	10000	9452.85	0.00	198.85	2.88
84	N2	BSSL301	150	2000	500	2000	2000	1448.80	0.00	196.49	3.02
85	N2	BSSL301	150	2000	500	4000	4000	3451.28	0.00	185.89	2.95
86	N2	BSSL301	150	2000	500	6000	6000	5448.82	0.00	191.61	3.03

87	N2	BSSL301	150	2000	500	8000	8000	7448.53	0.00	183.03	3.20
88	N2	BSSL301	150	2000	500	10000	10000	9446.16	0.00	173.97	3.05
89	N2	BSSL301	200	2000	500	2000	2000	1419.93	0.00	176.43	3.31
90	N2	BSSL301	200	2000	500	4000	4000	3414.32	0.00	171.24	3.29
91	N2	BSSL301	200	2000	500	6000	6000	5414.09	0.00	161.77	3.33
92	N2	BSSL301	200	2000	500	8000	8000	7408.27	0.00	154.36	3.49
93	N2	BSSL301	200	2000	500	10000	10000	9403.93	0.00	154.15	3.32
94	N2	BSSH301	100	2000	500	2000	2000	1463.25	0.00	1079.45	1.02
95	N2	BSSH301	100	2000	500	4000	4000	3463.09	0.00	1133.79	1.12
96	N2	BSSH301	100	2000	500	6000	6000	5462.74	0.00	943.40	1.25
97	N2	BSSH301	100	2000	500	8000	8000	7463.08	0.00	924.13	1.30
98	N2	BSSH301	100	2000	500	10000	10000	9462.88	0.00	879.28	1.34
99	N2	BSSH301	150	2000	500	2000	2000	1450.81	0.00	834.10	1.67
100	N2	BSSH301	150	2000	500	4000	4000	3449.35	0.00	726.90	1.73
101	N2	BSSH301	150	2000	500	6000	6000	5448.88	0.00	702.25	1.78
102	N2	BSSH301	150	2000	500	8000	8000	7448.26	0.00	679.86	1.83
103	N2	BSSH301	150	2000	500	10000	10000	9447.50	0.00	666.40	1.91
104	N2	BSSH301	200	2000	500	2000	2000	1454.05	0.00	607.94	2.27
105	N2	BSSH301	200	2000	500	4000	4000	3452.77	0.00	682.31	1.57
106	N2	BSSH301	200	2000	500	6000	6000	5455.38	0.00	529.38	2.27
107	N2	BSSH301	200	2000	500	8000	8000	7455.55	0.00	586.89	2.38
108	N2	BSSH301	200	2000	500	10000	10000	9454.63	0.00	577.27	2.55
109	N2	IL301	100	2000	500	2000	2000	1342.47	0.00	22.14	36.00
110	N2	IL301	100	2000	500	4000	4000	3337.40	0.00	20.82	36.61
111	N2	IL301	100	2000	500	6000	6000	5333.93	0.00	20.66	37.55
112	N2	IL301	100	2000	500	8000	8000	7332.42	0.00	20.34	38.38
113	N2	IL301	100	2000	500	10000	10000	9328.20	0.00	20.35	40.50
114	N2	IL301	150	2000	500	2000	2000	1376.93	0.00	19.71	40.84
115	N2	IL301	150	2000	500	4000	4000	3372.43	0.00	18.93	42.45
116	N2	IL301	150	2000	500	6000	6000	5369.91	0.00	18.36	43.44
117	N2	IL301	150	2000	500	8000	8000	7367.16	0.00	18.11	44.59
118	N2	IL301	150	2000	500	10000	10000	9344.64	0.00	17.91	47.04
119	N2	IL301	200	2000	500	2000	2000	1333.37	0.00	17.20	43.74
120	N2	IL301	200	2000	500	4000	4000	3347.38	0.00	16.81	45.80
121	N2	IL301	200	2000	500	6000	6000	5345.40	0.00	16.58	47.74
122	N2	IL301	200	2000	500	8000	8000	7317.38	0.00	16.13	48.09
123	N2	IL301	200	2000	500	10000	10000	9314.62	0.00	15.42	48.71
124	N2	IL302	100	2000	500	1500	2000	1239.49	235.70	74.84	25.07
125	N2	IL302	100	2000	500	1000	2000	1073.57	471.40	74.23	24.26
126	N2	IL302	100	2000	500	1000	4000	2406.40	1414.21	75.52	24.31

127	N2	IL302	100	2000	500	1000	6000	3740.25	2357.02	78.22	24.41
128	N2	IL302	100	2000	500	1000	8000	5039.09	3299.83	66.91	26.57
129	N2	IL302	100	2000	500	1000	10000	6205.66	4242.64	93.91	42.14
130	N2	IL302	100	2000	500	2000	4000	2737.64	942.81	72.75	25.42
131	N2	IL302	100	2000	500	2000	6000	4073.85	1885.62	78.25	24.67
132	N2	IL302	100	2000	500	2000	8000	5373.24	2828.43	62.59	25.52
133	N2	IL302	100	2000	500	2000	10000	6699.44	3771.24	56.23	28.82
134	N2	IL302	100	2000	500	3500	4000	3236.75	235.70	75.70	25.89
135	N2	IL302	100	2000	500	3000	6000	4403.56	1414.21	73.02	25.74
136	N2	IL302	100	2000	500	3000	8000	5708.25	2357.02	69.16	26.76
137	N2	IL302	100	2000	500	3000	10000	7033.33	3299.83	61.20	29.12
138	N2	IL302	100	2000	500	4000	6000	4732.64	942.81	62.60	18.48
139	N2	IL302	100	2000	500	4000	8000	6040.58	1885.62	68.01	27.16
140	N2	IL302	100	2000	500	5000	10000	7701.24	2357.02	59.96	28.93
141	N2	IL302	100	2000	500	5000	8000	6374.41	1414.21	67.34	27.30
142	N2	IL302	100	2000	500	5000	10000	7711.49	2357.02	61.64	29.65
143	N2	IL302	100	2000	500	6000	8000	6706.01	942.81	68.01	27.76
144	N2	IL302	100	2000	500	6000	10000	8044.58	1885.62	58.89	29.67
145	N2	IL302	100	2000	1500	2500	6000	3253.10	1649.92	76.12	21.93
146	N2	IL302	100	2000	1500	2000	6000	3086.68	1885.62	81.49	22.18
147	N2	IL302	100	2000	1500	2000	8000	4406.71	2828.43	63.67	24.00
148	N2	IL302	100	2000	1500	2000	10000	5742.51	3771.24	72.29	24.52
149	N2	IL302	100	2000	1500	2000	6000	3085.03	1885.62	78.13	23.32
150	N2	IL302	100	2000	1500	2000	6000	3089.10	1885.62	79.42	22.73
151	N2	IL302	100	2000	1500	3000	8000	4743.67	2357.02	72.58	24.51
152	N2	IL302	100	2000	1500	3000	10000	6077.75	3299.83	71.08	24.66
153	N2	IL302	100	2000	1500	4000	6000	3755.07	942.81	81.21	23.66
154	N2	IL302	100	2000	1500	4000	8000	5082.00	1885.62	71.62	24.74
155	N2	IL302	100	2000	1500	4000	10000	6412.03	2828.43	70.91	24.71
156	N2	IL302	100	2000	1500	5000	8000	5410.16	1414.21	71.35	24.90
157	N2	IL302	100	2000	1500	5000	10000	6742.45	2357.02	70.94	24.74
158	N2	IL302	100	2000	1500	6000	8000	5744.29	942.81	69.95	25.38
159	N2	IL302	100	2000	1500	6000	10000	7085.92	1885.62	70.35	24.81
160*	CO2	IL301	100	2500	1500	6000	2000	1690.26	1885.62	25.01	33.44
162	CO2	IL301	100	2000	1500	6000	3000	2372.83	1414.21	24.01	39.69
163*	CO2	IL301	100	2000	1500	6000	4000	3015.64	942.81	23.67	39.24
165	CO2	IL301	100	2000	1500	8000	2000	2370.82	2828.43	24.24	34.11
166	CO2	IL301	100	2000	1500	8000	4000	3668.63	1885.62	23.94	35.96
167	CO2	IL301	100	2000	1500	8000	6000	5005.68	942.81	23.64	40.80
168	CO2	IL301	100	2000	1500	10000	2000	2988.75	3771.24	24.36	33.80
169	CO2	IL301	100	2000	1500	10000	4000	4324.82	2828.43	23.02	33.19
170	CO2	IL301	100	2000	1500	10000	6000	5671.59	1885.62	22.71	38.83
171	CO2	IL301	100	2000	1500	10000	8000	6927.64	942.81	22.01	44.06
172	CO2	IL301	100	2000	500	4000	2000	2033.51	942.81	13.61	38.28
173	CO2	IL301	100	2500	500	6000	2000	2698.99	1885.62	13.33	37.91

174	CO2	IL301	100	2000	500	6000	3000	3363.29	1414.21	12.65	39.66
175	CO2	IL301	100	2000	500	6000	4000	4025.94	942.81	12.48	41.95
176	CO2	IL301	100	2000	500	8000	2000	3364.87	2828.43	13.77	36.82
177	CO2	IL301	100	2000	500	8000	4000	4690.68	1885.62	12.69	39.71
178	CO2	IL301	100	2000	500	8000	6000	6028.68	942.81	12.17	41.64
179	CO2	IL301	100	2000	500	10000	2000	4028.23	3771.24	13.09	40.91
180	CO2	IL301	100	2000	500	10000	4000	5360.57	2828.43	12.90	41.36
181	CO2	IL301	100	2000	500	10000	6000	6695.83	1885.62	12.21	40.91
182*	CO2	IL301	150	2000	500	6000	2000	2675.36	1885.62	14.27	43.17
184	CO2	IL301	150	2000	500	6000	3000	3344.93	1414.21	12.50	44.68
185*	CO2	IL301	150	2000	500	6000	4000	4011.56	942.81	13.78	42.77
187	CO2	IL301	150	2000	500	8000	2000	3377.19	2828.43	14.61	37.06
188	CO2	IL301	150	2000	500	8000	4000	4702.69	1885.62	14.43	42.72
189	CO2	IL301	150	2000	500	8000	6000	6000.59	942.81	12.62	46.04
190*	CO2	IL301	200	2000	500	6000	2000	2665.67	1885.62	15.43	50.15
192	CO2	IL301	200	2000	500	6000	3000	3333.50	1414.21	14.53	47.60
193*	CO2	IL301	200	2000	500	6000	4000	3991.74	942.81	13.73	50.31
195	CO2	IL301	200	2000	500	8000	2000	3321.42	2828.43	14.31	50.74
196	CO2	IL301	200	2000	500	8000	4000	4654.80	1885.62	13.56	45.27
197	CO2	IL301	200	2000	500	8000	6000	5996.75	942.81	12.66	48.08
198	CO2	IL301	100	2000	500	2000	500	304.63	707.11	19.23	15.28
199	CO2	IL301	100	2000	500	2000	1000	694.37	471.40	22.83	19.65
200	CO2	IL301	100	2000	500	4000	2000	2011.58	942.81	20.80	20.21
201	CO2	IL301	100	2000	500	4000	2000	2038.83	942.81	20.05	24.26
202	CO_2	IL301	100	2000	1000	2000	1000	Incomplete due to cooling effect.			
203	CO_2	IL301	100	2000	1000	4000	2000	Incomplete due to cooling effect.			
204	CO_2	IL301	100	2000	1000	6000	3000	Incomplete due to cooling effect.			
*	Repeated at the end of the cycle to check the hysteresis effect.										

Table 5-8. Change of Apparent Permeability by Percentage

Pump flow-rate, cc/hr	k/k0, %	Change of k/k0 WRT previous flow-rate, %
25	100	
2000	60	40
4000	45	15
6000	37.5	7.5
8000	32	5.5
10000	29	3

Table 5-9. Non-Darcy Effect under Different Forchheimer's Numbers

Frochheimer's number, Fo	non-Darcy effect, f_{ND_T}	Error of ignoring non-Darcy behavior
0.01	0.01	1%
0.05	0.05	5%
0.1	0.09	9%
0.5	0.33	33%
1	0.50	50%
2	0.67	67%
5	0.83	83%
10	0.91	91%
100	0.99	99%

Table 5-10. Boundary Values of Test Conditions

Parameter	Dakota sandstone	Indiana limestone	Berea sandstone
Flow rate at pump, cc/hr	25 ~ 10000	200 ~ 10000	1000 ~ 10000
Forchheimer's number at core	0.006 ~ 2.20	0.07 ~ 3.33	0.21 ~ 5.15
Superficial velocity at core, ft/d	15 ~ 2666	116 ~ 4220	603 ~ 5948

Table 5-11. Measured Permeability and Non-Darcy Coefficient

Parameter	Dakota sandstone	Indiana limestone	Berea sandstone
Permeability, mD	3.36	35.98	195.94
Non-Darcy coefficient, 10^6 cm^{-1}	169.8	21.61	2.95

Table 5-12. Measured and Theoretical Non-Darcy Effects in Dakota Sandstone

Flow rate, cc/hr	Forchheimer Number, Fo	Measured non-Darcy effect, f_{ND_M}	Theoretical non-Darcy effect, f_{ND_T}	Relative error, %
25	0.006	0.62	0.59	5.27
50	0.012	1.24	1.17	6.00
100	0.024	2.52	2.30	8.85
200	0.047	4.91	4.50	8.33
300	0.071	7.06	6.60	6.51
400	0.094	9.13	8.60	5.73
500	0.118	10.99	10.53	4.23
600	0.141	12.77	12.36	3.16
700	0.165	14.45	14.13	2.21
800	0.188	16.06	15.82	1.49
900	0.211	17.57	17.44	0.73
1000	0.235	19.02	19.00	0.12
1500	0.351	25.19	25.96	3.04
2000	0.466	30.87	31.78	2.95
2500	0.580	35.11	36.71	4.53
3000	0.693	38.99	40.93	4.99
3500	0.806	42.56	44.62	4.83
4000	0.917	45.73	47.83	4.61
4500	1.028	48.78	50.70	3.94
5000	1.138	51.67	53.23	3.02
6000	1.357	56.70	57.57	1.53
7000	1.572	61.21	61.12	0.14
8000	1.784	65.06	64.08	1.51
9000	1.994	68.81	66.60	3.22
10000	2.202	72.38	68.77	4.99

Table 5-13. Correlations

Rock	Gas	P_{out}, psi	T, F	Stress state	Correlations	No.
DSS201	N_2	500	100	Hydrostatic	$k = -0.00004\sigma_{eff} + 3.46$ (R_k^2 =0.97)	1
					$\beta = 0.0051\sigma_{eff} + 154.06$ (R_β^2 =0.95)	2
DSS201	N_2	500	100	Differential	$k = -0.00004\sigma_{eff} + 3.37$ (R_k^2 =0.86)	3
					$\beta = 0.0055\sigma_{eff} + 153.97$ (R_β^2 =0.90)	4
					$k = -0.000008\tau + 3.20$ (R_k^2 =0.01)	5
					$\beta = -0.0005\tau + 182.18$ (R_β^2 =0.00)	6
DSS201	N_2	500	150	Hydrostatic	$k = -0.00003\sigma_{eff} + 3.27$ (R_k^2 =1.00)	7
					$\beta = 0.006\sigma_{eff} + 176.41$ (R_β^2 =0.95)	8
DSS201	N_2	500		Differential	$k = -0.00004\sigma_{eff} + 3.39$ (R_k^2 =0.74)	9
					$\beta = 0.0104\sigma_{eff} + 149.76$ (R_β^2 =0.57)	10
					$k = 0.00002\tau + 3.15$ (R_k^2 =0.06)	11
					$\beta = 0.0036\tau + 196.59$ (R_β^2 =0.02)	12
DSS201	N_2	500	200	Hydrostatic	$k = -0.00003\sigma_{eff} + 3.20$ (R_k^2 =0.92)	13
					$\beta = 0.0056\sigma_{eff} + 196.12$ (R_β^2 =0.99)	14
DSS201	N_2	500		Differential	$k = -0.00004\sigma_{eff} + 3.25$ (R_k^2 =0.77)	15
					$\beta = 0.0067\sigma_{eff} + 200.9$ (R_β^2 =0.92)	16
					$k = 0.00001\tau + 3.04$ (R_k^2 =0.02)	17
					$\beta = -0.003\tau + 241.47$ (R_β^2 =0.04)	18
BSSL301	N_2	500	100	Hydrostatic	$k = -0.002\sigma_{eff} + 216.77$ (R_k^2 =0.92)	19
					$\beta = 0.00004\sigma_{eff} + 2.56$ (R_β^2 =0.94)	20
BSSL301	N_2	500	150	Hydrostatic	$k = -0.0024\sigma_{eff} + 199.25$ (R_k^2 =0.78)	21
					$\beta = 0.000004\sigma_{eff} + 3.01$ (R_β^2 =0.97)	22
BSSL301	N_2	500	200	Hydrostatic	$k = -0.0031\sigma_{eff} + 180.25$ (R_k^2 =0.94)	23
					$\beta = 0.00003\sigma_{eff} + 3.23$ (R_β^2 =0.69)	24
BSSH301	N_2	500	100	Hydrostatic	$k = -0.0305\sigma_{eff} + 1158.60$ (R_k^2 =0.78)	25
					$\beta = 0.00004\sigma_{eff} + 0.98$ (R_β^2 =0.96)	26
BSSH301	N_2	500	150	Hydrostatic	$k = -0.0191\sigma_{eff} + 826.13$ (R_k^2 =0.82)	27
					$\beta = 0.00003\sigma_{eff} + 1.62$ (R_β^2 =0.99)	28
BSSH301	N_2	500	200	Hydrostatic	$k = -0.0078\sigma_{eff} + 639.53$ (R_k^2 =0.20)	29
					$\beta = 0.00003\sigma_{eff} + 2.17$ (R_β^2 =0.73)	30
IL301	N_2	500	100	Hydrostatic	$k = -0.0002\sigma_{eff} + 21.95$ (R_k^2 =0.75)	31
					$\beta = 0.0005\sigma_{eff} + 34.93$ (R_β^2 =0.94)	32
IL301	N_2	500	150	Hydrostatic	$k = -0.0002\sigma_{eff} + 19.79$ (R_k^2 =0.92)	33
					$\beta = 0.0007\sigma_{eff} + 39.76$ (R_β^2 =0.97)	34
IL301	N_2	500	200	Hydrostatic	$k = -0.0002\sigma_{eff} + 17.56$ (R_k^2 =0.96)	35
					$\beta = 0.0006\sigma_{eff} + 43.54$ (R_β^2 =0.91)	36
IL302	N_2	500	100	Differential	$k = -0.0026\sigma_{eff} + 81.26$ (R_k^2 =0.64)	37
					$\beta = 0.0008\sigma_{eff} + 22.78$ (R_β^2 =0.81)	38
					$k = -0.0039\tau + 75.26$ (R_k^2 =0.34)	39
					$\beta = 0.0024\tau + 22.48$ (R_β^2 =0.40)	40
IL302	N_2	1500	100	Differential	$k = -0.0026\sigma_{eff} + 86.89$ (R_k^2 =0.78)	41
					$\beta = 0.0006\sigma_{eff} + 20.91$ (R_β^2 =0.72)	42
					$k = -0.0025\tau + 78.65$ (R_k^2 =0.16)	43
					$\beta = 0.0002\tau + 23.56$ (R_β^2 =0.03)	44
IL301	CO_2	1500	100	Differential	$k = -0.0005\sigma_{eff} + 25.51$ (R_k^2 =0.85)	45
					$\beta = 0.0016\sigma_{eff} + 31.78$ (R_β^2 =0.59)	46
					$k = 0.0003\tau + 22.86$ (R_k^2 =0.19)	47

					$\beta = -0.0032\tau + 43.47$ (R_β^2 =0.66)	48
IL301	CO_2	500	100	Differential	$k = -0.0003\sigma_{eff} + 14.15$ (R_k^2 =0.62)	49
					$\beta = 0.0008\sigma_{eff} + 36.45$ (R_β^2 =0.48)	50
					$k = 0.0002\tau + 12.48$ (R_k^2 =0.13)	51
					$\beta = -0.0002\tau + 40.29$ (R_β^2 =0.01)	52
IL301	CO_2	500	150	Differential	$k = -0.0006\sigma_{eff} + 16.10$ (R_k^2 =0.87)	53
					$\beta = 0.0012\sigma_{eff} + 38.03$ (R_β^2 =0.21)	54
					$k = 0.0009\tau + 12.17$ (R_k^2 =0.51)	55
					$\beta = -0.0037\tau + 48.81$ (R_β^2 =0.73)	56
IL301	CO_2	500	200	Differential	$k = -0.0008\sigma_{eff} + 17.09$ (R_k^2 =0.93)	57
					$\beta = -0.0009\sigma_{eff} + 52.12$ (R_β^2 =0.24)	58
					$k = 0.0006\tau + 13.00$ (R_k^2 =0.23)	59
					$\beta = 0.0006\tau + 47.72$ (R_β^2 =0.04)	60

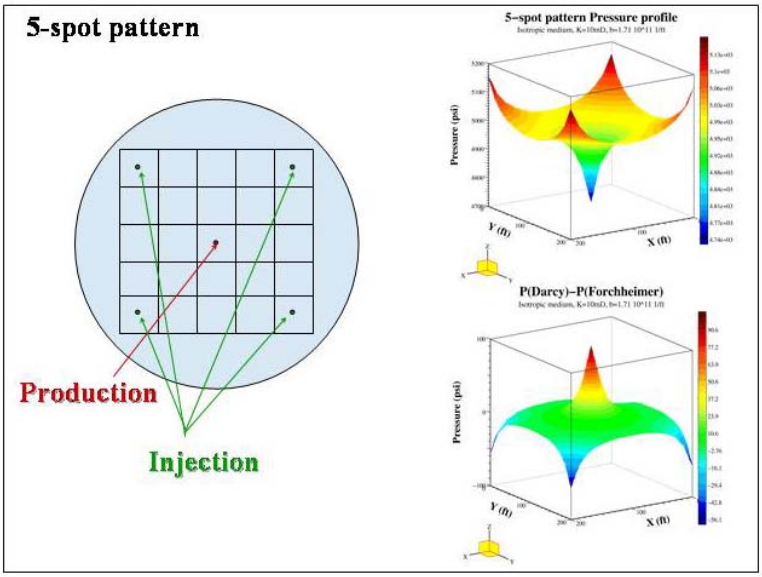

Fig. 5-1. Pressure difference between Darcy behavior vs. non-Darcy behavior at the near-wellbore region in an injection and production well (Papavassiliou, 2000).

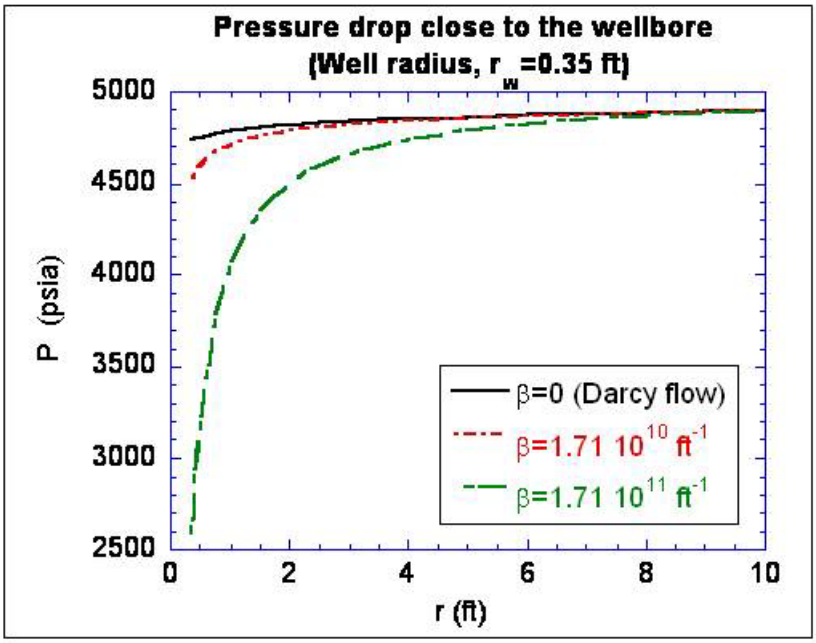

Fig. 5-2. Non-Darcy flow coefficient effects on pressure drop at near-wellbore region.

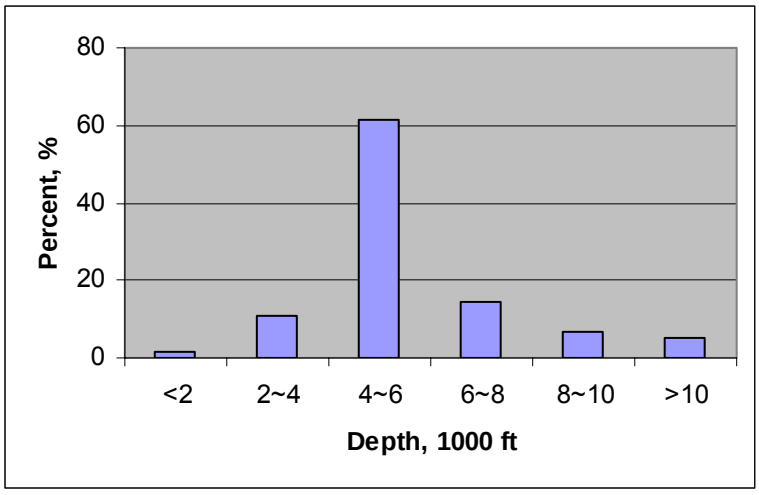

Fig. 5-3. Depth distribution of currently active CO_2 projects.

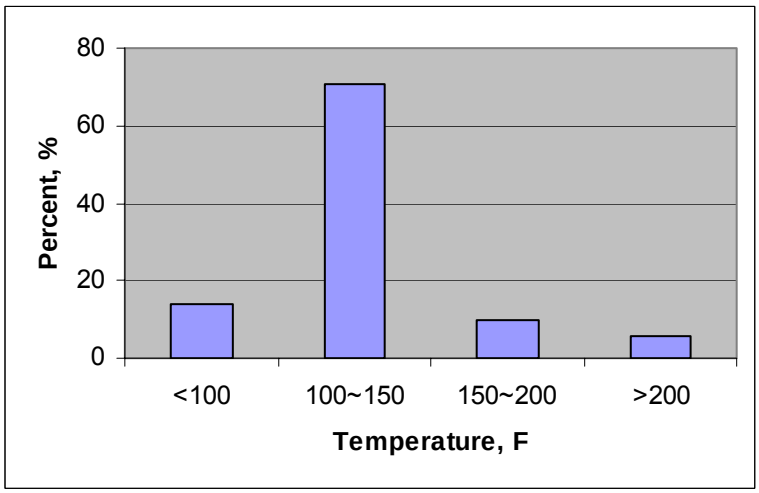

Fig. 5-4. Temperature distribution of currently active CO_2 projects.

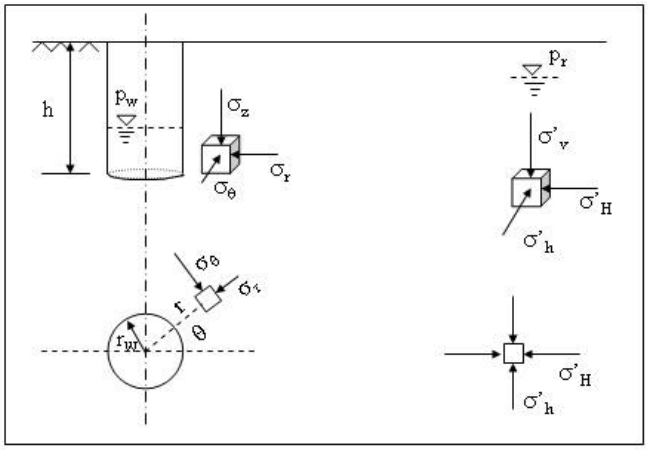

Fig. 5-5. Far-field and near-wellbore effective stresses.

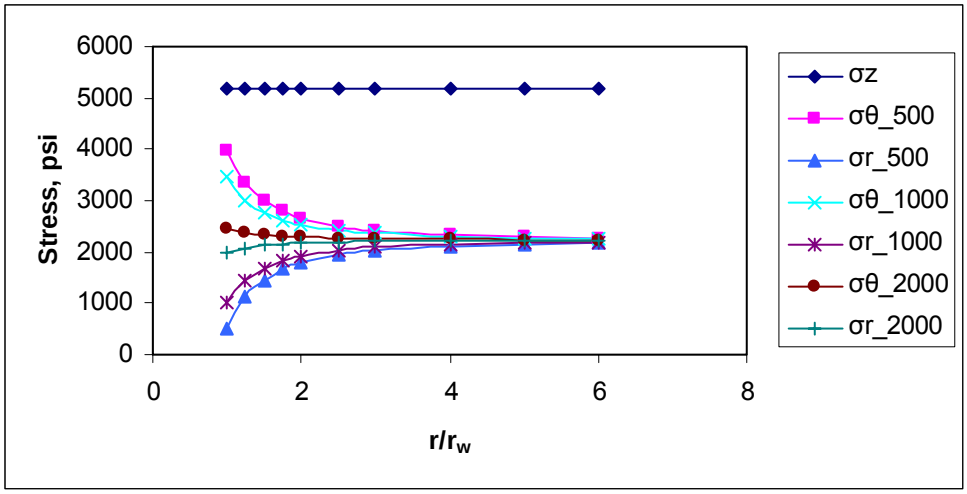

Fig. 5-6. Change of effective stresses at the near-wellbore region.

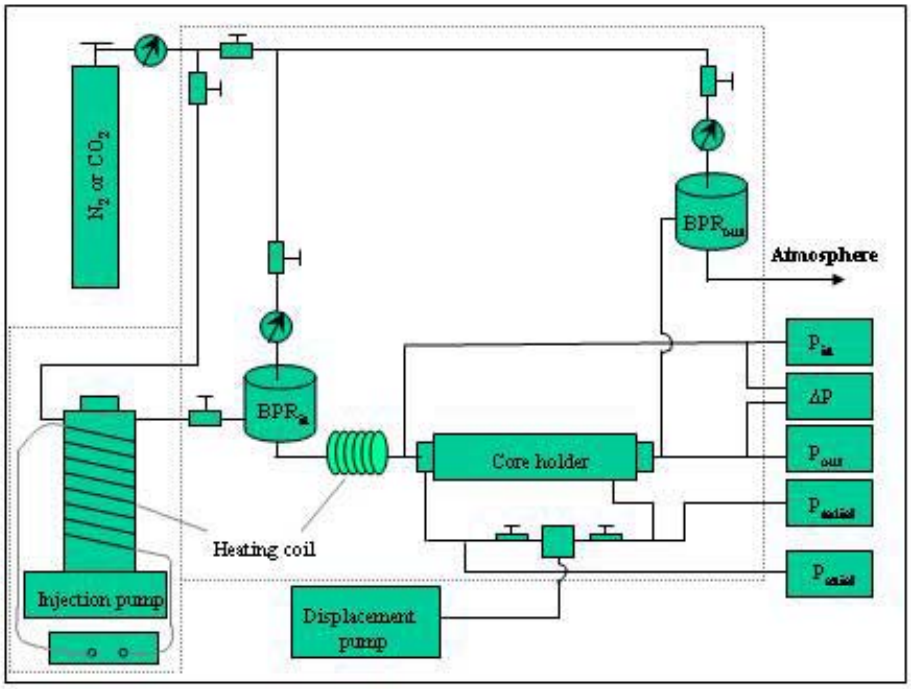

Fig. 5-7. A schematic of the HP/HT gas flooding system.

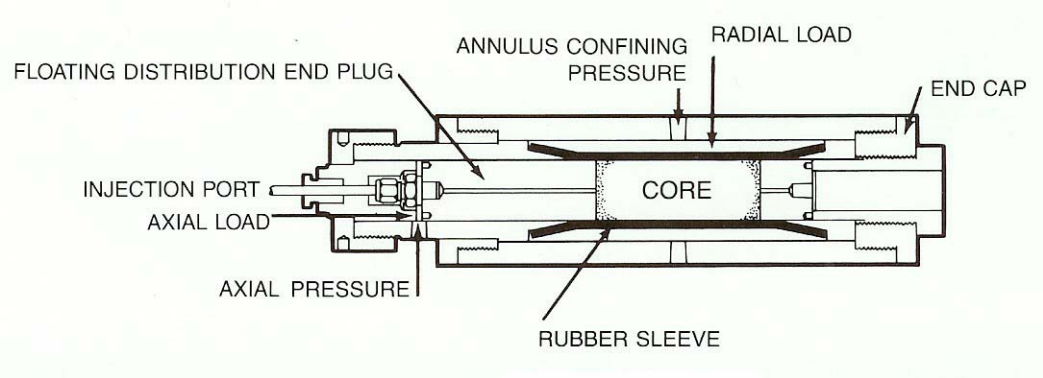

Fig. 5-8. Core holder assembly.

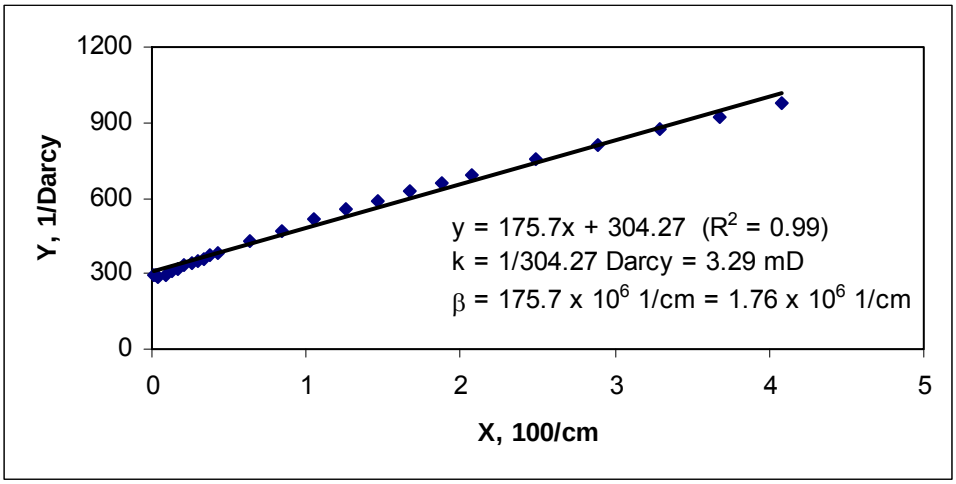

Fig. 5-9. Calculation of k and β from non-Darcy flow experiments.

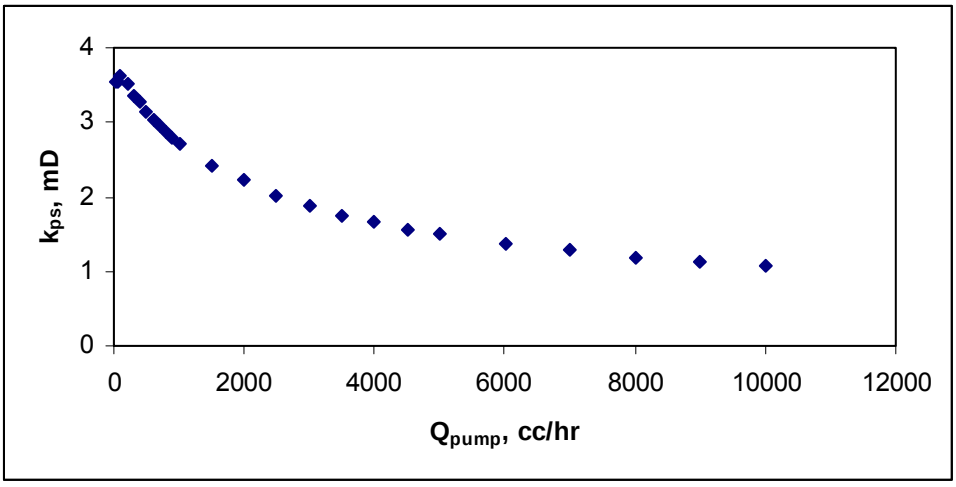

Fig. 5-10. Change of Darcy's law-based permeability measured under different flow rates.

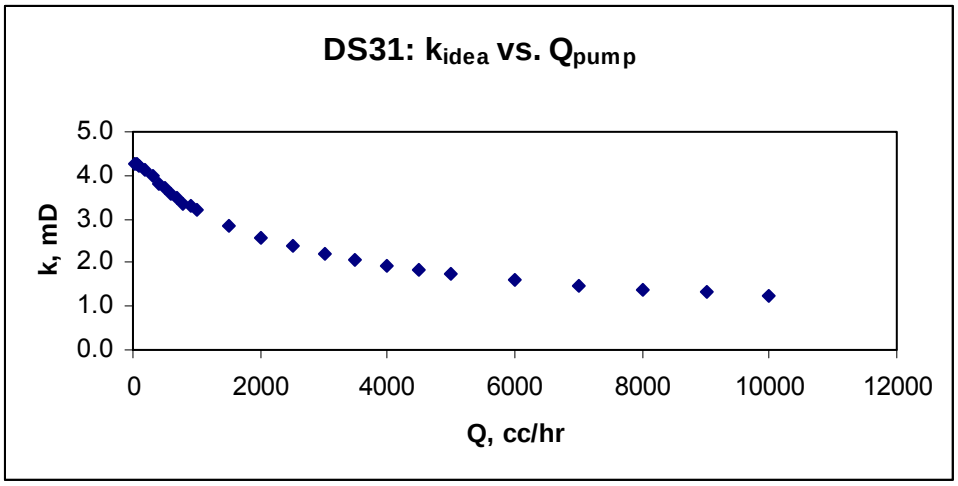

Fig. 5-11. Change of apparent permeability with flow rate in Dakota sandstone at 100°F.

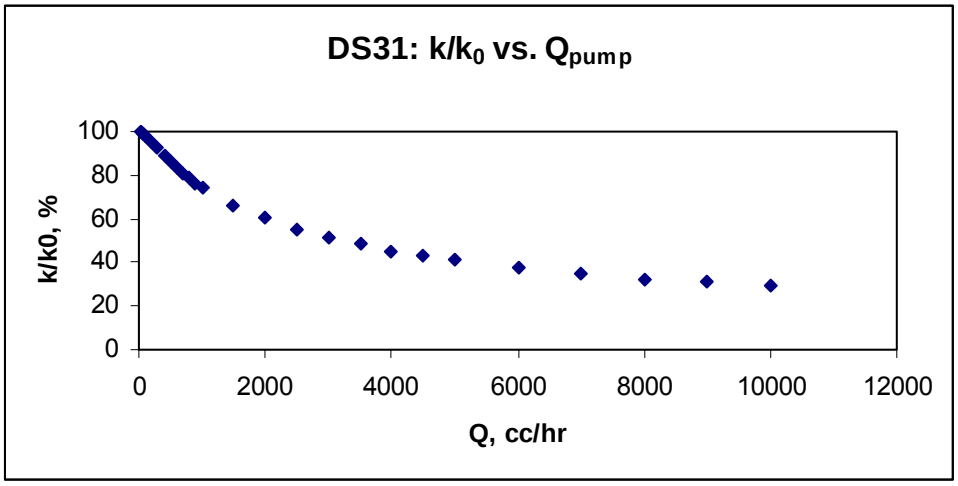

Fig. 5-12. Change of apparent permeability by percentage with flow rate in Dakota sandstone at 100°F.

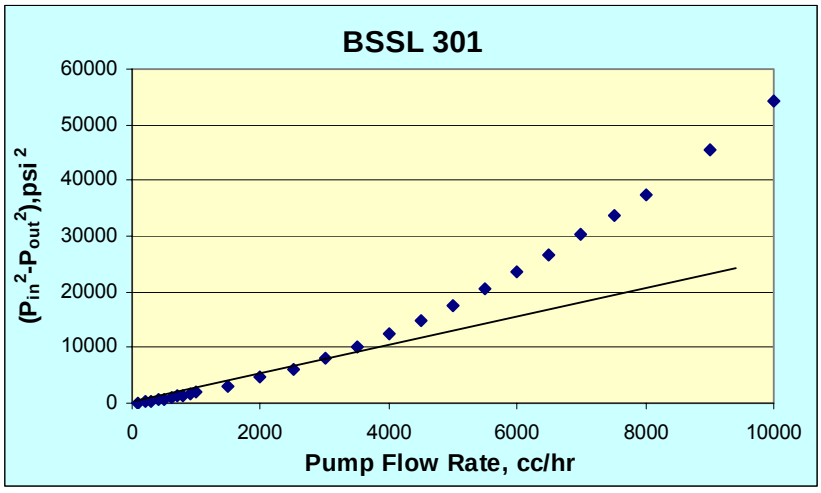

Fig. 5-13. Flow rate vs. pressure drop for Berea sandstone under 2000/2000 psi overburden pressure at 100ºF.

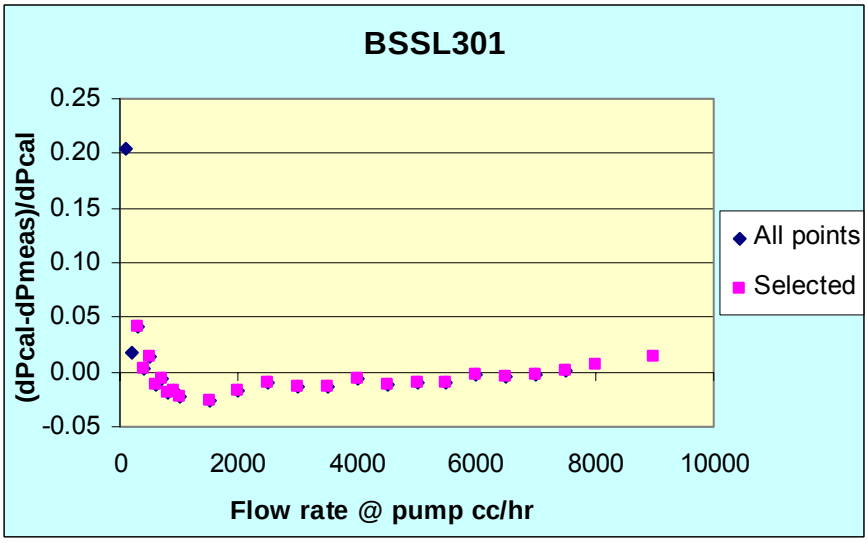

Fig. 5-14. Plot between $(dP_{cal} - dP_{exp})/dP_{cal}$ vs. pump flow rate at 100 ºF for Berea sandstone.

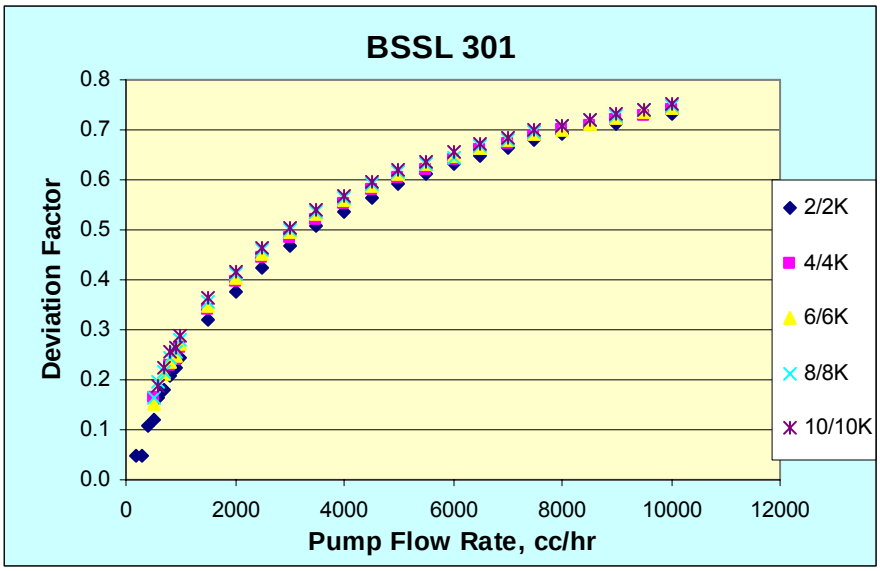

Fig. 5-15. Change of deviator factor vs. flow rate.

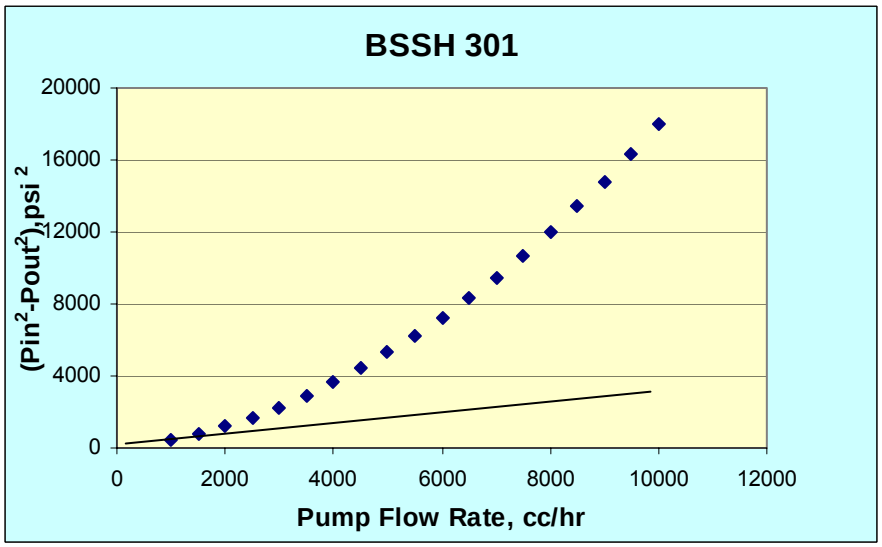

Fig. 5-16. Flow rate vs. pressure drop for Berea sandstone BSSH301 under 2000/2000 psi overburden stresses at 100°F.

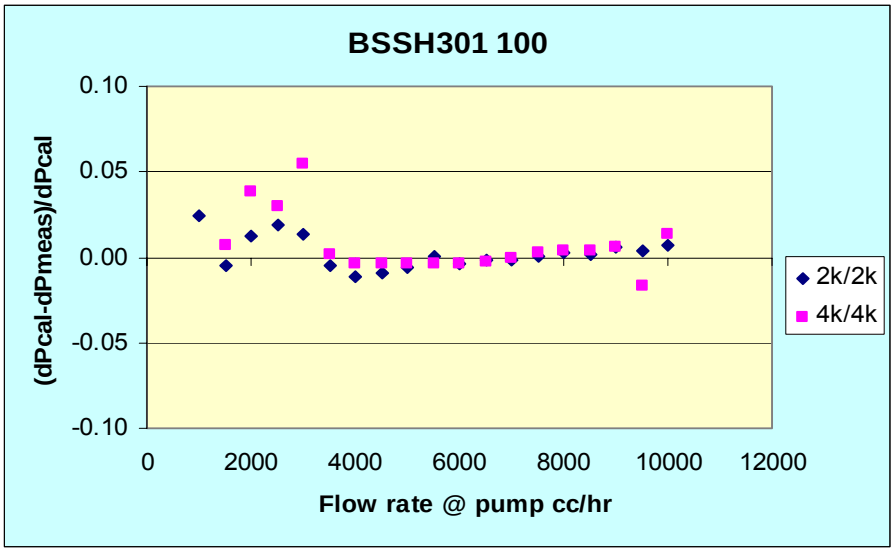

Fig. 5-17. Plot between ($dP_{cal} - dP_{exp}$)/dP_{cal} vs. pump flow rate at 100°F for Berea sandstone(BSSH301) at 2000/2000 psi confining stresses.

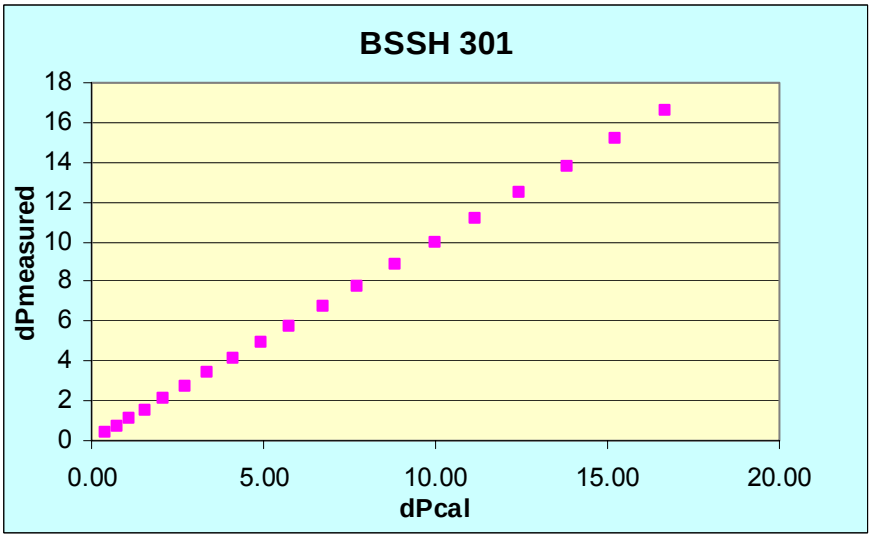

Fig. 5-18. Plot between dP_{exp} vs. dP_{cal} at 100°F for Berea sandstone BSSH301.

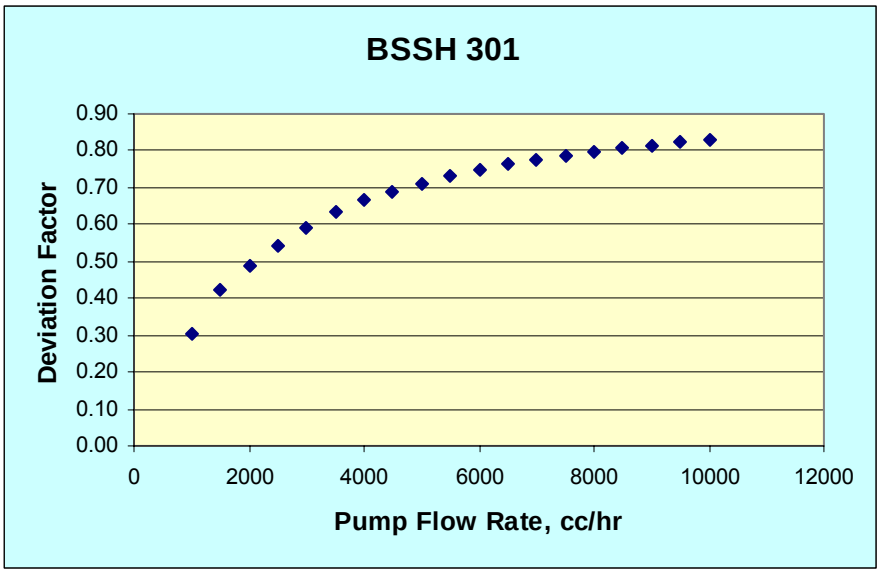

Fig. 5-19. Deviation factor vs. pump flow rate at 100ºF for Berea sandstone BSSH301.

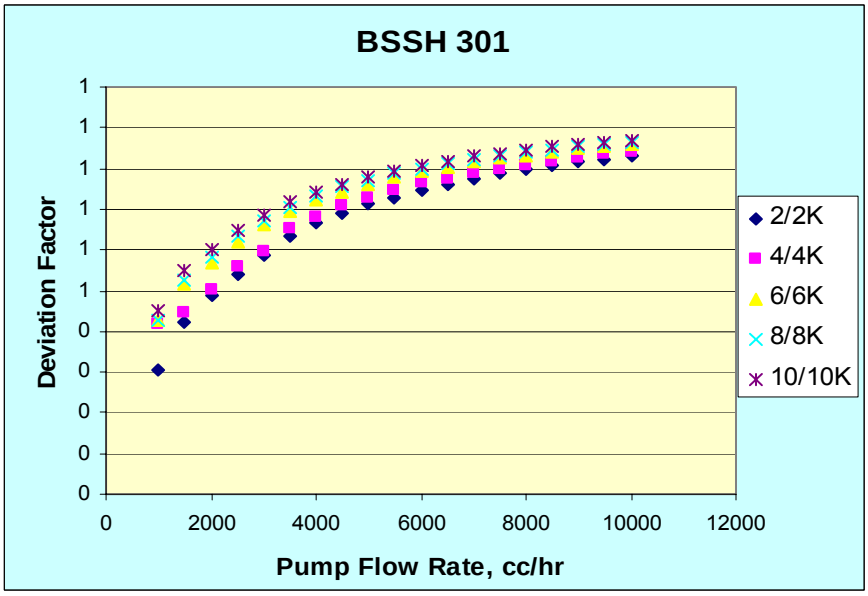

Fig. 5-20. Deviation factor vs. flow rate (at pump) at 100ºF for Berea sandstone BSSH301.

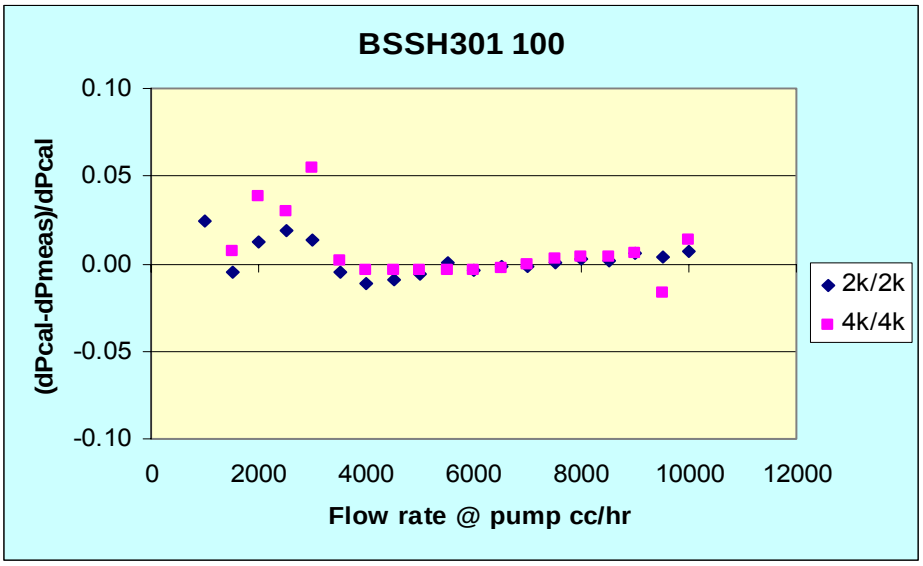

Fig. 5-21. Plot between $(dP_{cal} - dP_{exp})/dP_{cal}$ vs. pump flow rate at 100°F for Berea sandstone BSSH301 at different confining stresses.

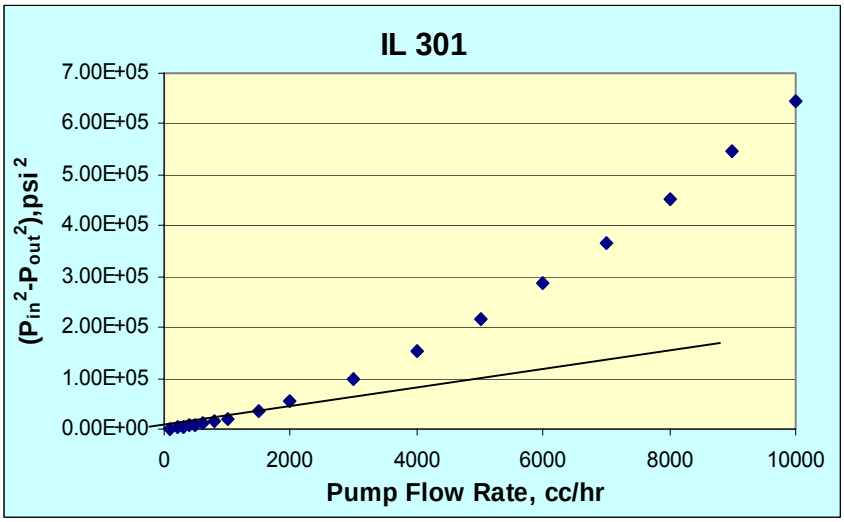

Fig. 5-22. Pump flow rate vs. pressure drop for Indiana limestone IL301 under 2000/2000 psi overburden stresses at 100ºF.

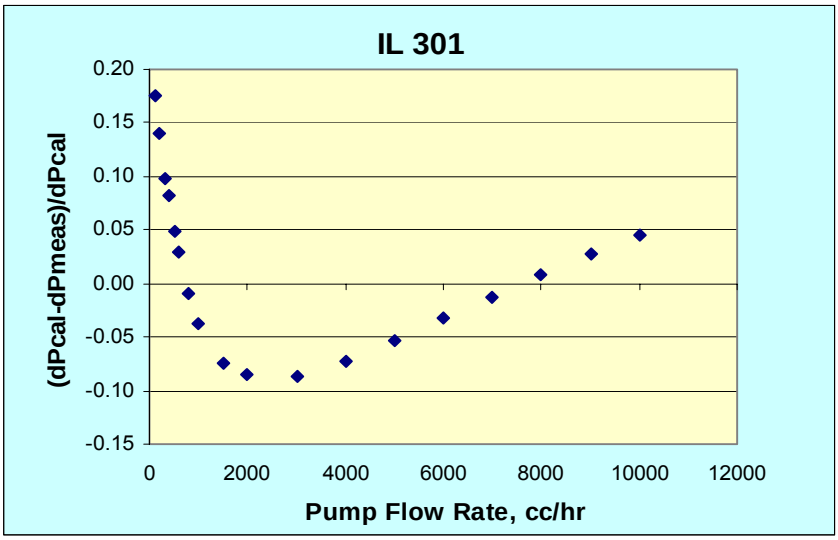

Fig. 5-23. Plot between $(dP_{cal} - dP_{exp})/dP_{cal}$ and pump flow rate at 100ºF for Indiana limestone IL301.

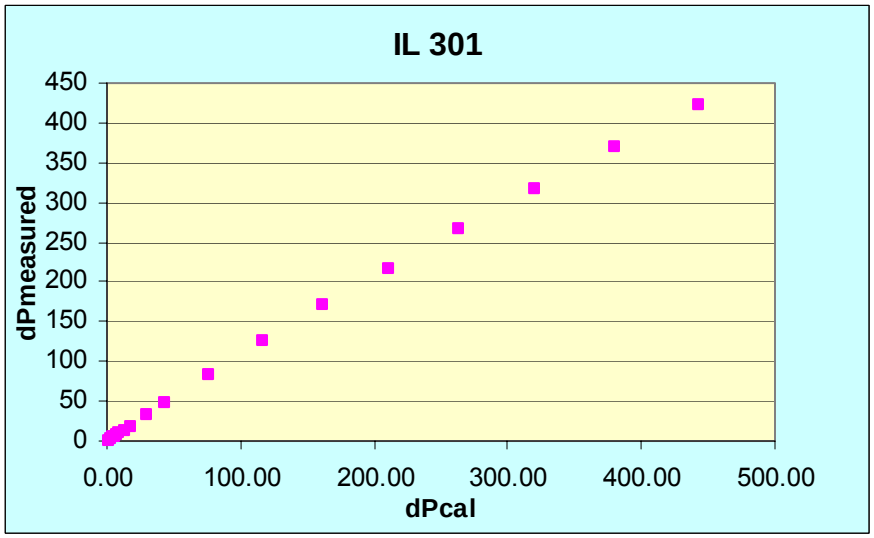

Fig. 5-24. Plot between dP_{exp} vs. dP_{cal} at 100ºF for Indiana limestone IL301.

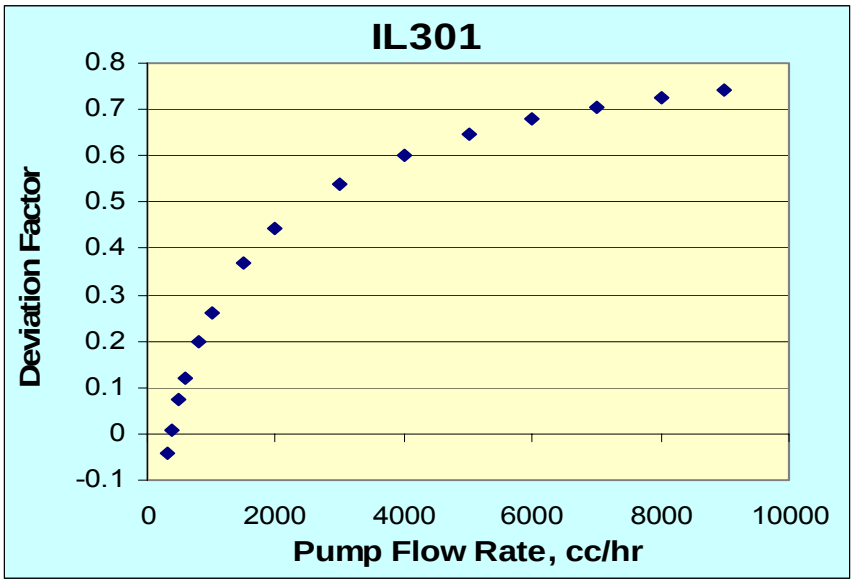

Fig. 5-25. Deviation factor vs. pump flow rate at 100ºF for Indiana limestone IL301.

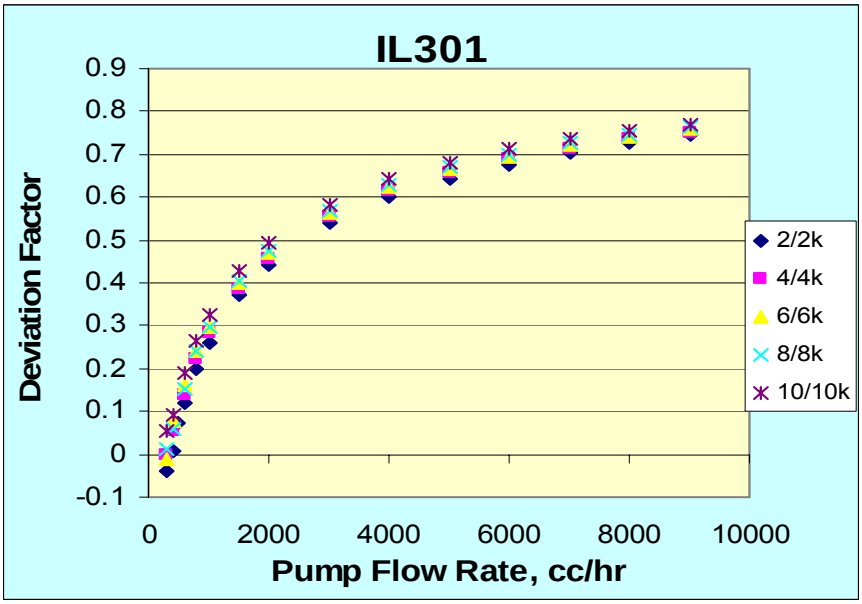

Fig. 5-26. Deviation factor vs. pump flow rate at 100ºF for Indiana limestone IL301.

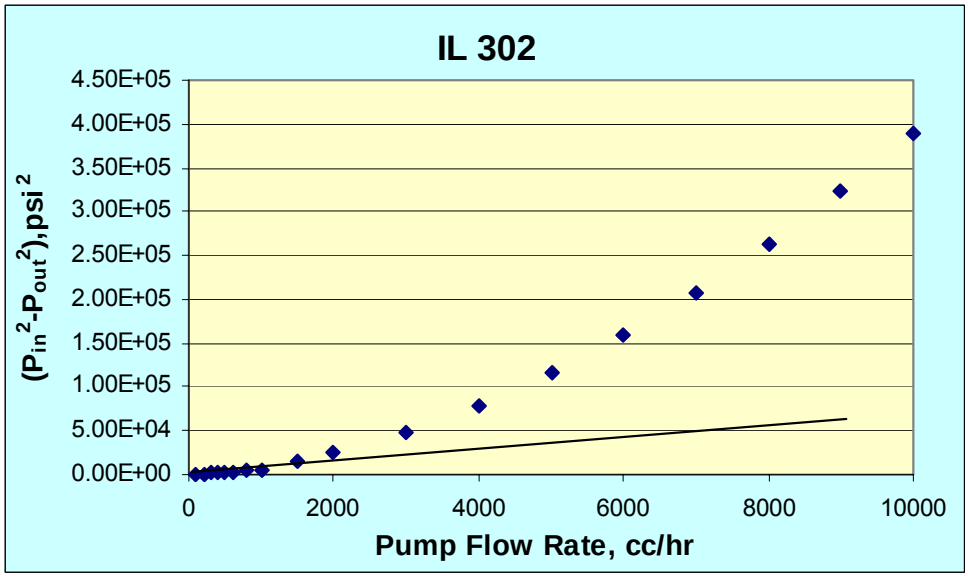

Fig. 5-27. Flow rate vs. pressure drop for Indiana limestone IL302 under 1500axial/2000 radial psi overburden stresses at 100ºF.

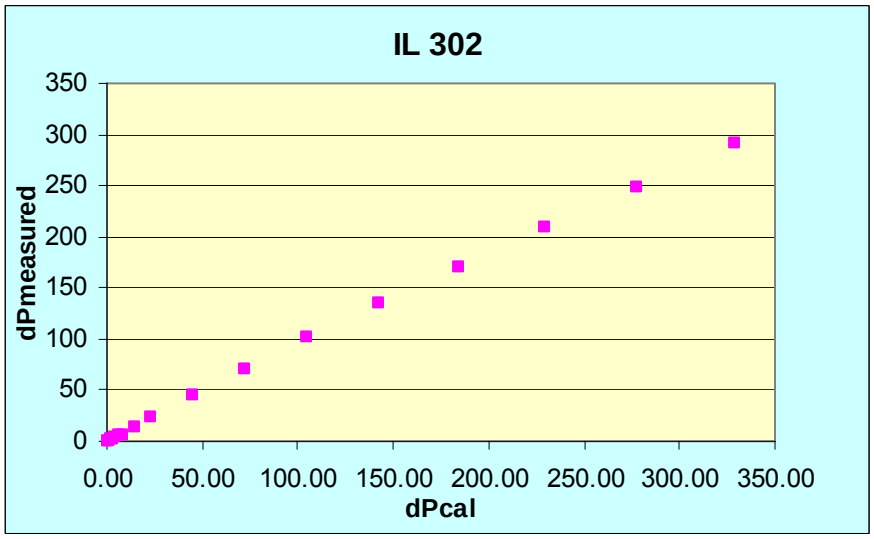

Fig. 5-28. Plot between dP_{exp} vs. dP_{cal} at 100°F for Indiana limestone IL302.

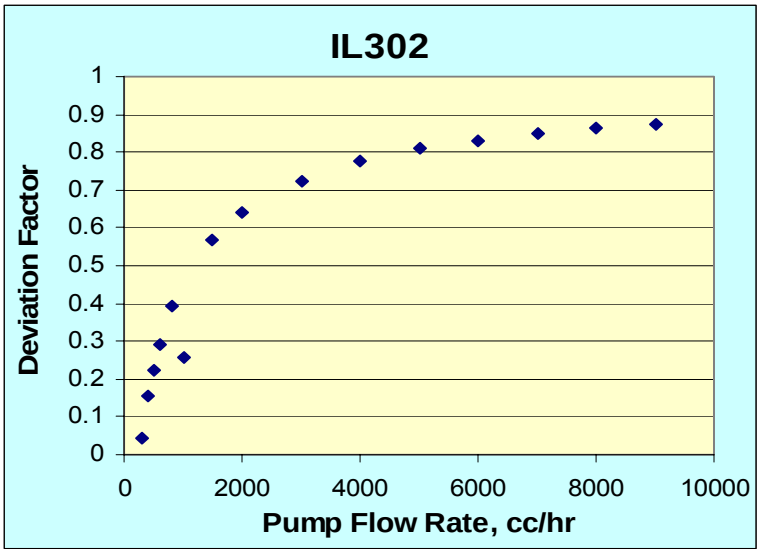

Fig. 5-29. Deviation factor vs. pump flow rate at 100ºF for Indiana limestone IL302.

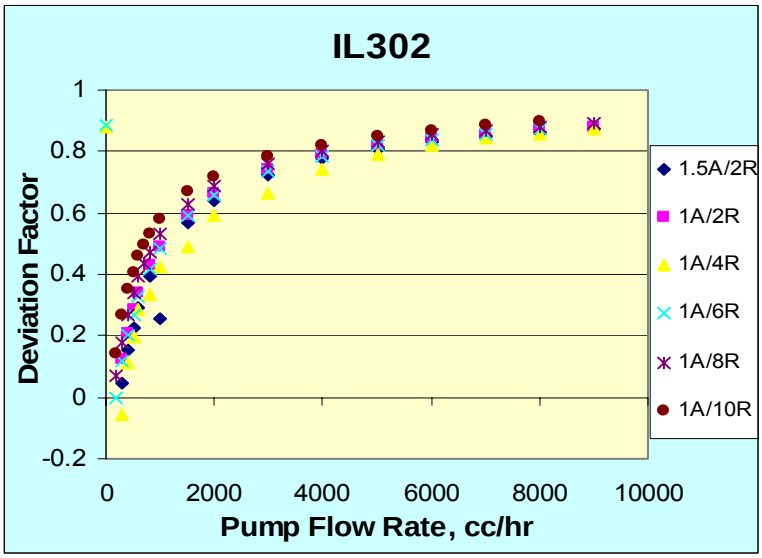

Fig. 5-30. Deviation factor vs. pump flow rate at different radial stresses at 100ºF, 500 psi pore pressure for Indiana limestone IL302.

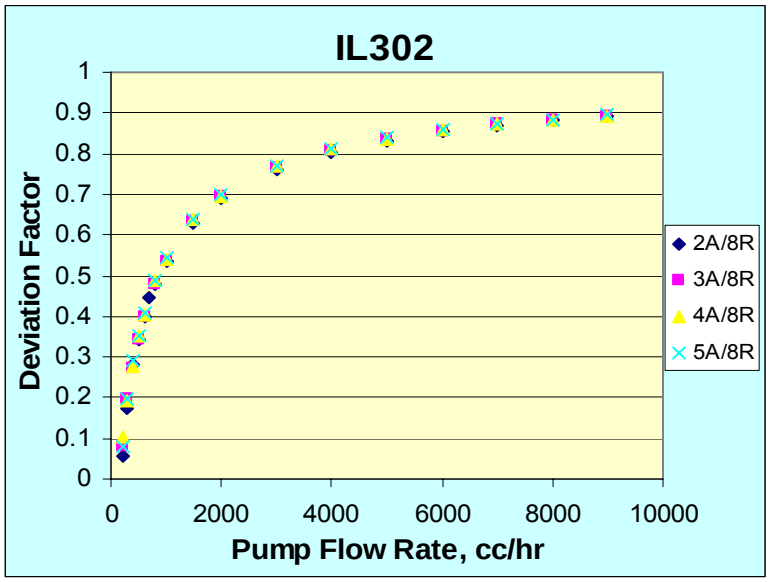

Fig. 5-31. Deviation factor vs. pump flow rate at different axial stresses at 100ºF, 500 psi pore pressure for Indiana limestone IL302.

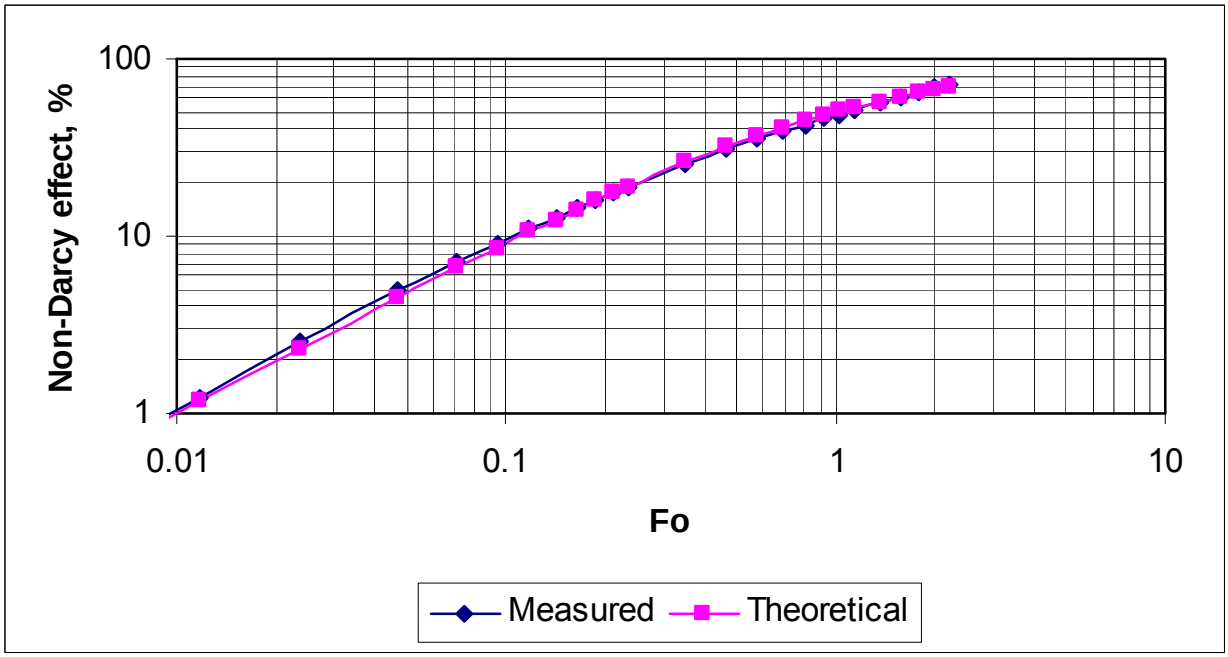

Fig. 32. Comparison of measured and theoretical non-Darcy effects in Dakota sandstone at 100°F, 500 psi pore pressure and 4,000 psi hydrostatic overburden pressure.

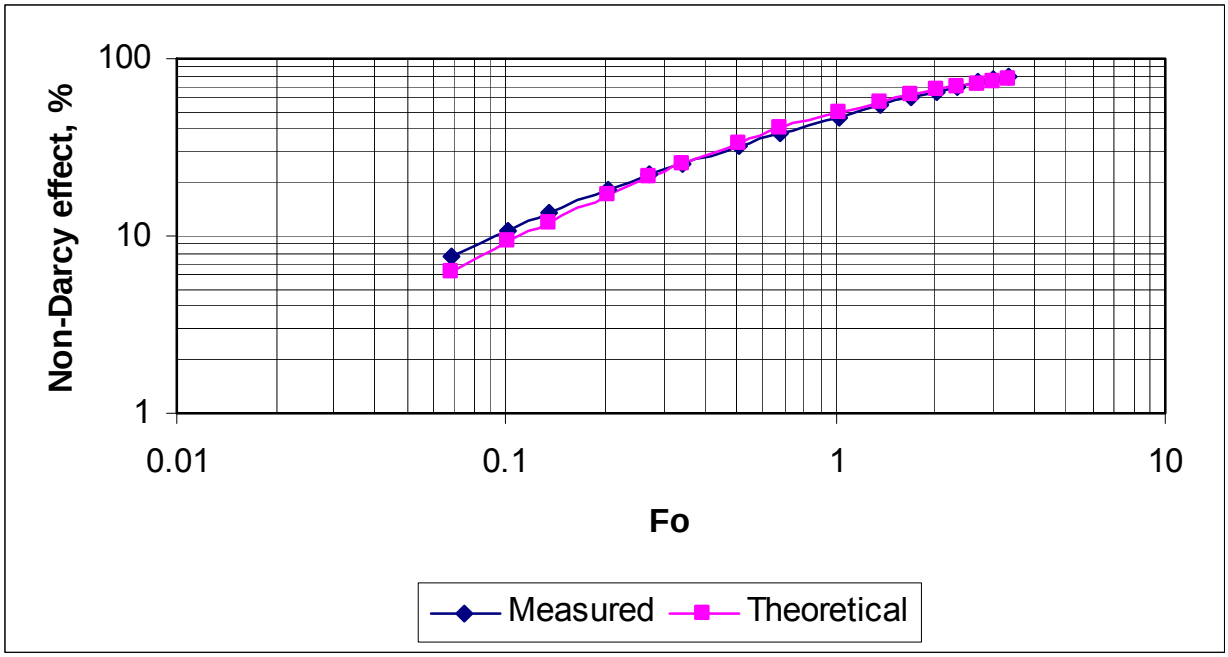

Fig. 5-33. Comparison of measured and theoretical non-Darcy effects in Indian limestone at 100°F, 500 psi pore pressure and 4,000 psi hydrostatic overburden pressure.

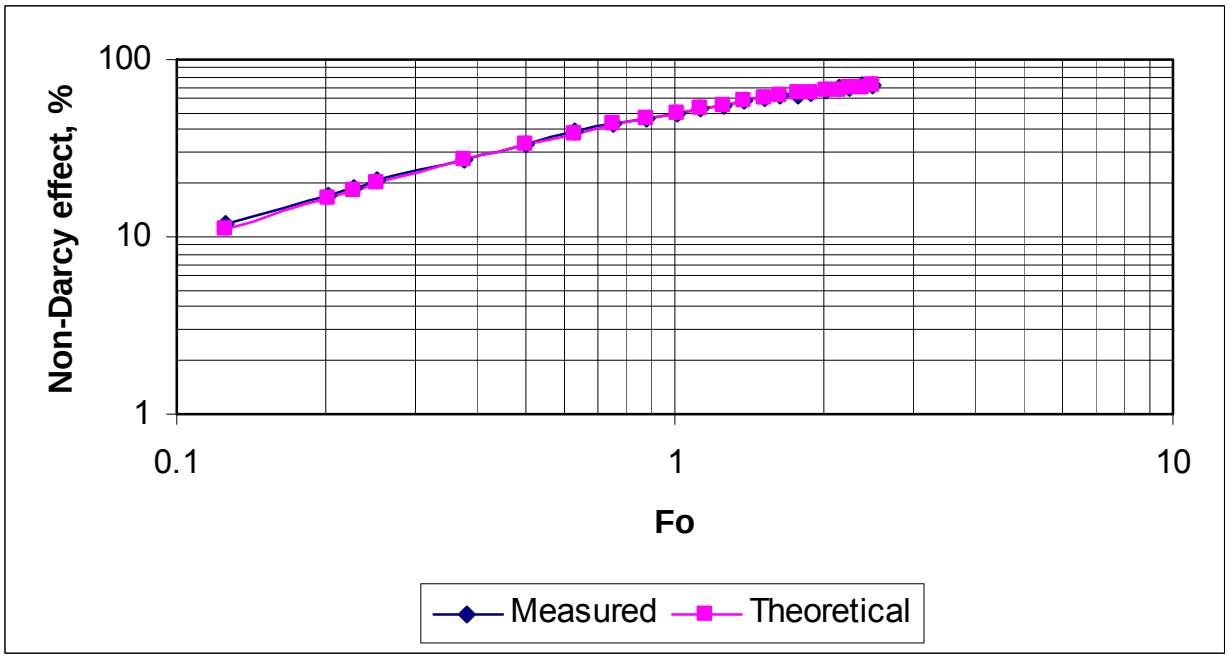

Fig. 5-34. Comparison of measured and theoretical non-Darcy effects in Berea sandstone at 100°F, 500 psi pore pressure and 4,000 psi hydrostatic overburden pressure.

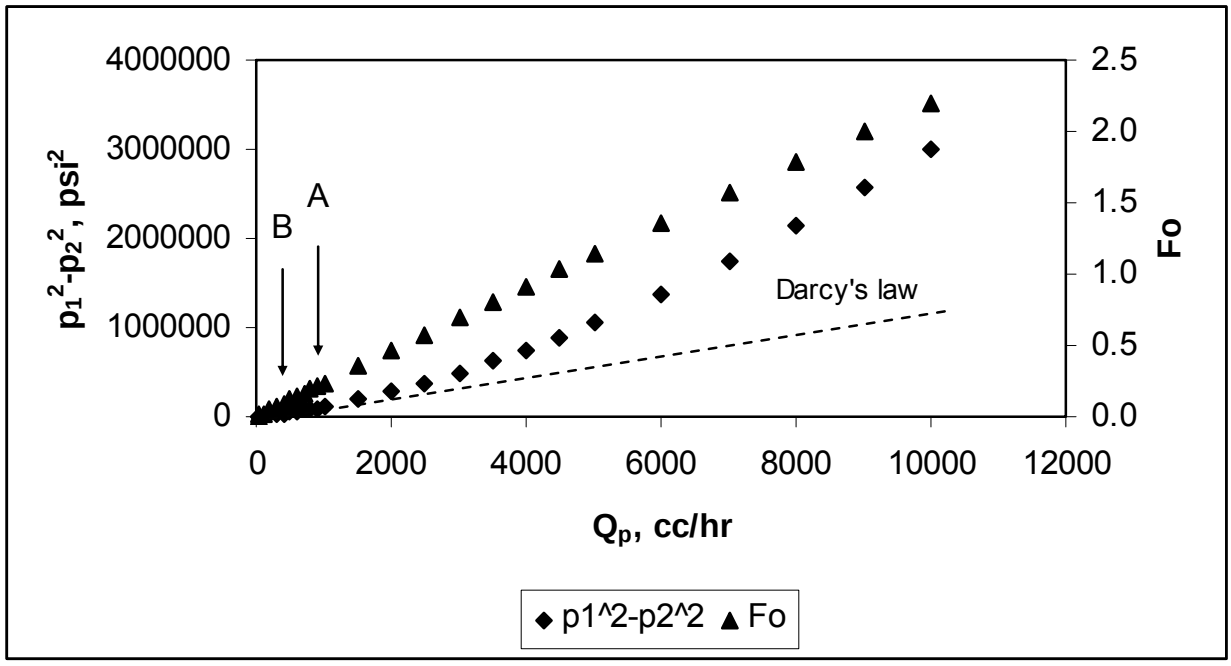

Fig. 5-35. Flow rate vs. pressure drop and Forchheimer's number. Dashed line represents pressure drop predicted by Darcy's law. A and B are optical and accurate start points of non-Darcy behavior, respectively.

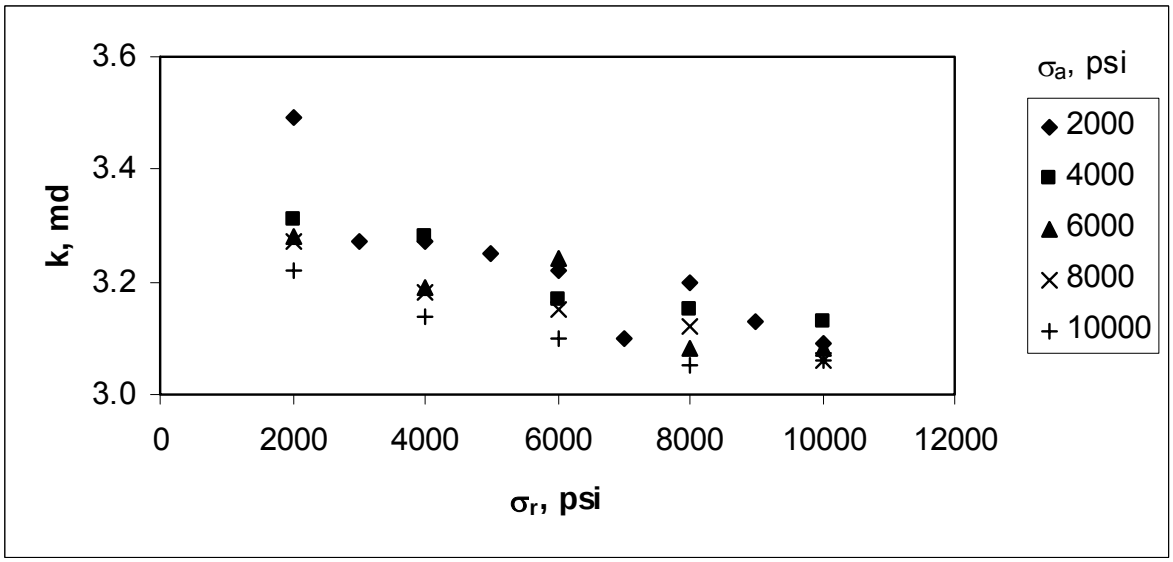

(a)

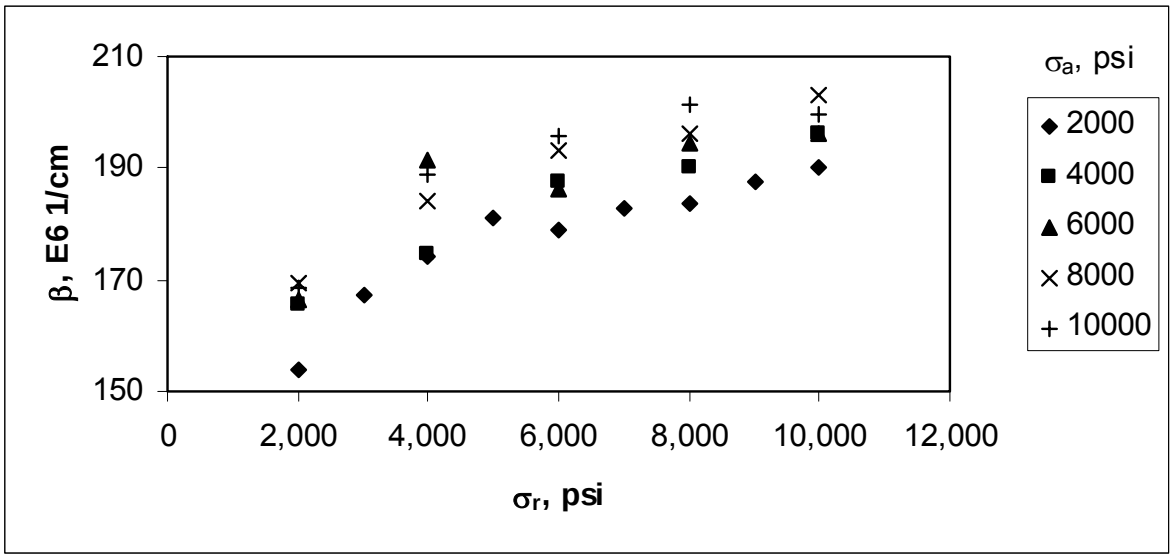

(b)

Fig. 5-36. Change of k and β with radial stresses when axial stresses are constant: k vs. σ_r, (b) β vs. σ_r.

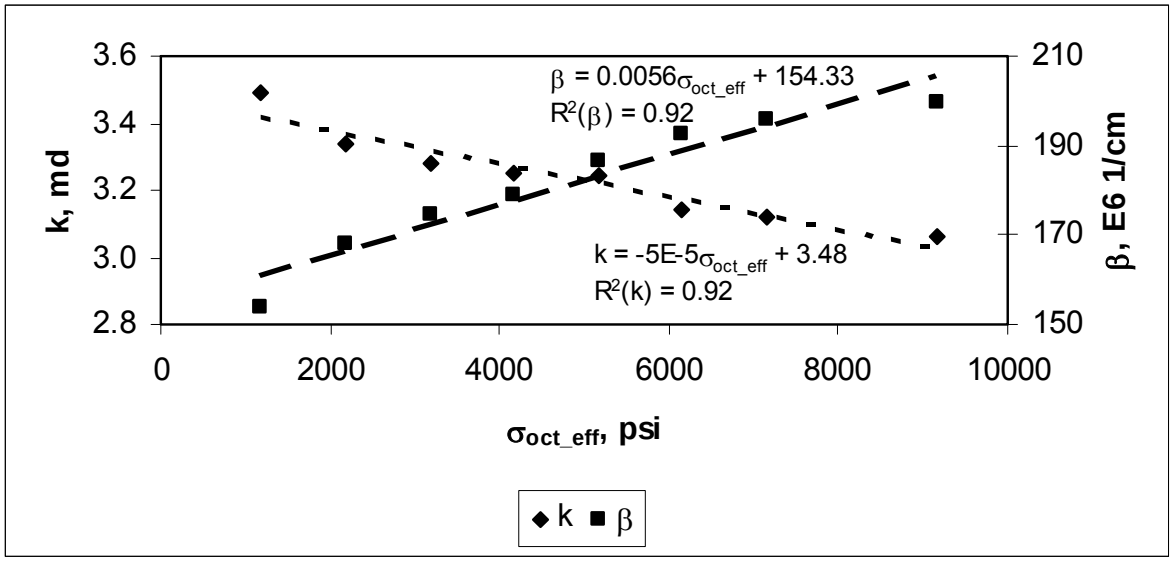

(a)

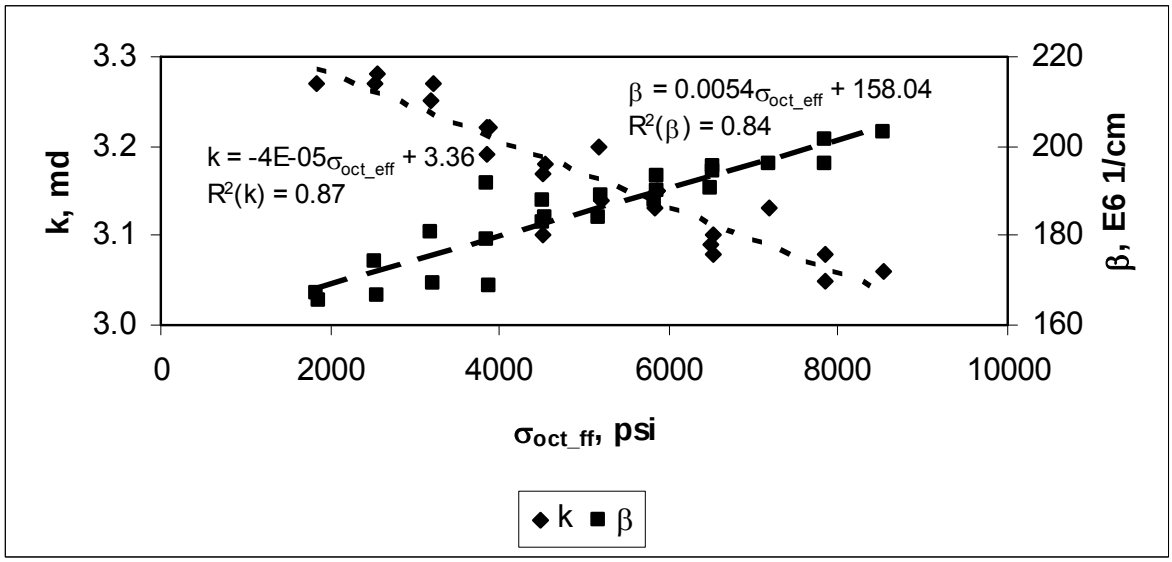

(b)

Fig. 5-37 Influence of average effective normal stress on k and β:
(a) hydrostatic stress condition; and (b) differential stress condition.

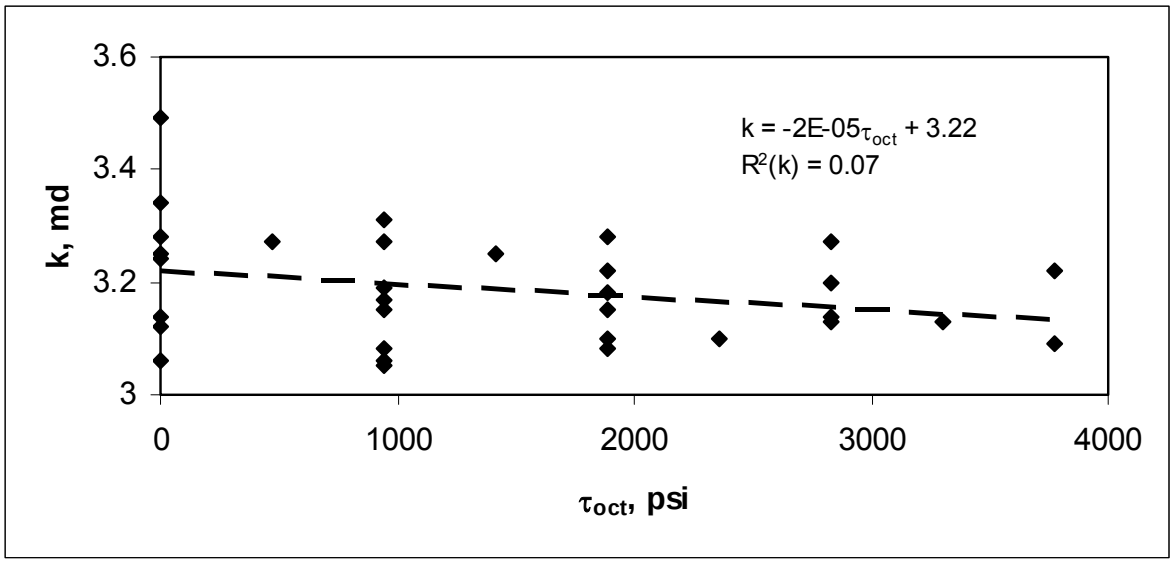

(a)

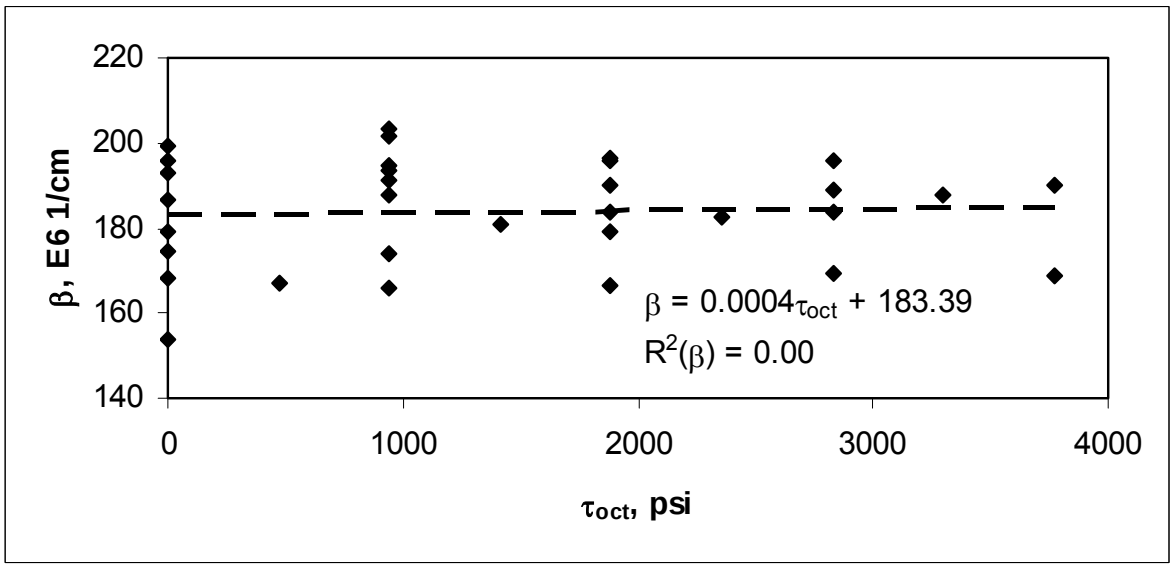

(b)

Fig. 5-38. Shear stress has zero correlation with k and β:
(a) k vs.τ_{oct}; and (b) β vs. τ_{oct}.